Dissertation zur Erlangung des Doktorgrades
der Fakultät für Chemie und Pharmazie
der Ludwig-Maximilians-Universität München

Structural and Biochemical Characterization of the IFT-B Complex Proteins IFT20, IFT38, IFT54 and IFT57

Kristina Simone Weber
aus
Isny im Allgäu, Deutschland

2015

Erklärung

Diese Dissertation wurde im Sinne von §7 der Promotionsordnung vom 28. November 2011 von Frau Prof. Dr. Elena Conti betreut.

Eidesstattliche Versicherung

Diese Dissertation wurde eigenständig und ohne unerlaubte Hilfe erarbeitet.

München, den 11.06.2015

………………………………

Kristina Weber

Dissertation eingereicht am 11.06.2015

1. Gutachterin Frau Prof. Dr. Elena Conti

2. Gutachter Herr Prof. Dr. Karl-Peter Hopfner

Mündliche Prüfung am 30.09.2015

Table of Contents

Preface

This study was performed in the laboratory of Dr. Esben Lorentzen at the Max Planck institute of biochemistry (MPIB). During the last 4½ years I was working on one main project described in this thesis. A detailed description based on the available literature will introduce this study. The result part of the thesis will be presented as three chapters, two of which are of collaborative nature and one that represents my main project (chapter II). All three chapters deal with the investigation of Calponin Homology (CH) domain containing proteins of the intraflagellar transport (IFT) complex. Chapter I contains the research report published in Science with my colleague Sagar Bhogaraju as a lead author with the title: 'Molecular Basis of Tubulin Transport Within the Cilium by IFT74 and IFT81', to which I contributed as an co-author. The results of my main project are summarized in chapter II as a manuscript with the title: 'The CH domain of IFT54 binds tubulin whereas the CH domains of IFT38 and IFT57 interact with IFT80 and IFT172, respectively' that will be finalized for submission. In chapter III, I present a manuscript (Nature communication, under review) from collaborators on ciliopathy disease mutations in the protein IFT54 with the title: 'Hypomorphic mutations in TRAF3IP1/IFT54 reveal a new role for IFT proteins in microtubule stabilization'. I contributed the *in vitro* work on disease variants to this manuscript and I am listed as a co-author on the manuscript. An extended discussion follows the results part in which I discuss topics that were not part of the manuscripts as well as future research directions for the field.

Contributions

Chapter I:

Bhogaraju, S., Cajanek, L., Fort, C., Blisnick, T., **Weber, K**., Taschner, M., Mizuno, N., Lamla, S., Bastin, P., Nigg, E.A., et al. (2013). **Molecular Basis of Tubulin Transport Within the Cilium by IFT74 and IFT81**. Science *341*, 1009–1012.

> For this study I established microscale thermophoresis (MST) measurements for determining K_d's for tubulin-binding domains together with Dr. S. Bhogaraju. Additionally, I carried out the subtilisin treatment of tubulin to remove the E-hooks in preparative scale (Fig. S5A).

Chapter II (in preparation):

Weber K., Taschner M., Stiegler M., Lorentzen E., **The CH domain of IFT54 binds tubulin whereas the CH domains of IFT38 and IFT57 interact with IFT80 and IFT172, respectively**

> I performed all experiments presented in the manuscript apart from the purifications and pull down experiments presented in Fig. 7A and Fig. S4 (done by Dr. Michael Taschner), the analytical ultracentrifugation (AUC) measurement Fig. 2B (done by Dr. Stephan Uebel) and the affinity pull down Fig. 1E (done by Marc Stiegler).

Chapter III (under review):

Albane A. Bizet, Anita Becker-Heck, Rebecca Ryan, **Kristina Weber**, Emilie Filhol, Pauline Krug, Jan Halbritter, Marion Delous, Bolan Linghu, Edward J. Oakeley, Mohammed Zarhrate, Patrick Nitschké, Fabrizio Serluca, Marie-Christine Lasbennes, Fan Yang, Tewis Bouwmeester, Lucile Pinson, Elisabeth Cassuto, Philippe Dubot, Neveen A. Soliman Elshakhs, José A. Sahel, Rémi Salomon, Iain A. Drummond, Marie-Claire Gubler, Corinne Antignac, Salahdine Chibout, Joseph. D. Szustakowski, Friedhelm Hildebrandt, Esben Lorentzen*,* Andreas W. Sailer, Alexandre Benmerah, Pierre Saint-Mezard, Sophie Saunier, **Hypomorphic mutations in TRAF3IP1/IFT54 reveal a new role for IFT proteins in microtubule stabilization**

I performed all *in vitro* studies (Fig. 1g/h and Fig. S4).

Remarks:

The work presented in this study was of course a cooperative achievement of a lot of people. I carried out and performed all experiments mentioned above under the supervision of Dr. Esben Lorentzen. Furthermore, I received technical support and scientific suggestions from the people in the lab.

Summary

Cilia are microtubule (MT)-based appendages projecting from the surface of many different eukaryotic cells. Apart from their known function in motility, cilia on many cell types have been thought to be vestigial remnants that lost their functionality throughout evolution. But it has been shown that cilia not only perform important functions in motility, they are also indispensable for sensory reception and signaling. Non-functional or missing cilia are the cause of various human diseases, referred to as ciliopathies. Given that >600 different proteins function inside the cilium and that the cilium is devoid of ribosomes, a specialized trafficking process known as intraflagellar transport (IFT) is in place to assemble and maintain cilia. The IFT complex consists of 22 proteins identified so far that organize in a ~1.5 MDa complex, subdivided into the IFT-A and IFT-B complex. Nine of the IFT-B proteins have been shown to form a salt-stable core in which the interactions between the proteins have been recently mapped. In contrast, not much is known about the interactions between the remaining seven IFT-B proteins (considered as 'peripheral') either between each other or with the 'IFT-B core'. It has been shown that mutation or deletion of certain IFT-proteins or the motor proteins required for IFT can lead to impairment or disruption of IFT and consequently to non-functional or missing cilia. Recently, disease mutations in IFT proteins have emerged as the cause of ciliopathies although the molecular basis is often not well understood. To better understand the interplay between different IFT proteins as well as to identify possible cargo interaction sites, my project comprised the structural and biochemical characterization of the four IFT-B proteins IFT20, IFT38, IFT54 and IFT57.

During my project work on IFT54 it emerged that both this protein and IFT81 were likely to contain an N-terminal Calponin Homology (CH) domain with potential tubulin-cargo binding affinity. I thus collaborated with another graduate student of the lab who was working on IFT81 (Sagar Bhogaraju) to setup methods to characterize tubulin and MT binding. For this study I specifically contributed proteolysed tubulin lacking the C-terminal E-hooks, which I prepared in large scale and purified to homogeneity. This ΔC form of tubulin was used in several figures of the Science paper shown in chapter I and allowed for the detailed mapping of the interaction between IFT81 and tubulin. Additionally, chapter I describes the high-resolution

structure of the N-terminal part of IFT81 that adopts a CH domain fold. Characterization of the CH domain of IFT81 demonstrated its ability to bind to tubulin and MTs. Furthermore, the binding ability of the CH domain in IFT81 increases significantly in the presence of the positively charged N-terminal stretch of IFT74. Quantification of the binding between IFT81/74 and tubulin revealed a K_d of 0.9 μM. Further examinations demonstrated that the CH domain in IFT81 selectively binds to the globular domain of tubulin whereas the positively charged stretch of IFT74 strengthen the binding via interaction with the negatively charged E-hooks of tubulin. These findings were the first reported tubulin-interaction site at one of the IFT proteins.

In chapter II of the results I present my studies on IFT20, IFT38, IFT54 and IFT57. The reported interaction between IFT20 and IFT54 was confirmed and mapped to the coiled coil regions (CC) of both proteins. Furthermore, a yet unknown interaction between IFT38 and IFT57 was identified, indicating that IFT38 is indeed a member of the IFT-B complex. In addition, the three proteins IFT38, IFT54 and IFT57 contain predicted CH domains at their N-termini. Therefore, the binding ability of IFT20/54 and IFT38/57 to tubulin was tested. Surprisingly, IFT20/54 but not IFT38/57 binds tubulin. Quantification of the binding between tubulin and IFT20/54 revealed a binding affinity of 3 μM. The interaction of IFT20/54 to tubulin was mapped to the predicted CH domain in IFT54. I solved the high-resolution structure of the N-terminal region of IFT54 to demonstrate that it indeed adopts a CH domain fold. All these findings point to the CH domain of IFT54 as a second tubulin-binding site within the IFT complex.

The CH domains in IFT38/57 lost their ability to bind tubulin raising the question of their molecular function. Further examinations of the IFT38/57 complex with proteins of the ‘IFT-B core’ did not reveal any interaction. Thus, the remaining IFT-B proteins were tested in direct interaction assays. An interaction between the CH domains of IFT38 and IFT57 with IFT80 and IFT172, respectively, could be verified. In summary, the CH domains in IFT38 and IFT57 seem to have lost their ability to bind tubulin and have been adapted to mediate the binding to the IFT-B proteins IFT80 and IFT172.

Chapter III of the results contains work from collaborators, to which I contributed the *in vitro* studies. In this study, DNA was sequenced from patients suffering from the ciliopathy Nephronophthisis (cystic kidney disease) to reveal point mutations. Four point mutations (I17S, V125A/M, M520R) were identified in IFT54/Traf3ip1/MIP-T3. Interestingly, the point mutations I17S and V125A/M are located in the N-terminal CH domain of IFT54, of which I solved the crystal structure as described in chapter II. More precisely, both residues are located in hydrophobic pockets, suggesting that mutation of these residues likely impairs proper folding and thereby disrupts the function of the CH domain in IFT54. Point-mutants of the mouse IFT54 CH domain (I17S and V125A/M) were cloned and expressed but as expected from the structure could not be obtained in a soluble form but were instead degraded in our recombinant expression system. Sequence alignments revealed that the valine is evolutionary conserved. Introducing the valine mutations in full-length *Chlamydomonas reinhardttii* IFT54 resulted in soluble IFT20/54$_{\mathrm{V126A/M}}$ complexes. Circular dichroism (CD) spectroscopy showed that both IFT54 mutants are overall folded proteins with a slightly lower α -helical content compared to the WT. Furthermore, thermal unfolding of the IFT20/54 WT and mutant complexes were performed resulting in a 3°C lower melting temperature of both IFT20/54 mutant complexes compared to the WT. This indicates that the mutations in the CH domain in full-length IFT54 lead to a less stable protein and presumably compromise the function *in vivo* in this way.

In addition, the collaborators could show that injection of WT IFT54 RNA in IFT54 deficient zebrafish embryos partially rescued the mutant phenotypes, whereas injection of mutated (V125A/M) IFT54 RNA failed to do so. Furthermore, the V125 mutations impair the localization of IFT54 at cytoplasmic MTs that in turn stabilizes MAP4 (MT-associated protein 4) on MTs, leading to altered cytoplasmic MT dynamics. These findings implicate an extra-ciliary role for IFT54 and thus additional possibilities for the occurrence of certain ciliopathies that have not been studied yet.

1) Introduction

Cilia are hair-like organelles that protrude from the surface of many different eukaryotic cells (figure 1). They are present in unicellular organisms such as the green algea *Chlamydomonas reinhardtii* and *Trypanosoma brucei*, the parasite causing sleeping sickness in human (Morga and Bastin, 2013). Cilia are also found in cells of multicellular organisms ranging from *C.elegans* to higher metazoans but are absent in *Saccharomyces* and *Arabidopsis*. Cells use motile cilia either for motility (sperm cells) or movement of cells or extracellular fluids (cilia facing the female fallopian tubes, the respiratory tract and the ventricles of the brain) (see section 1.2.4). A second type of cilia is the immotile (primary) cilium, first discovered 1898 by the Swiss anatomist K. W. Zimmermann on mammalian kidney cells (Zimmermann, 1898). For a long time it was thought that primary cilia are only evolutionary remnants without any function. But during the last decades it turned out that primary cilia play important roles in sensory reception such as sight and smell but also serve as key organelles in signaling (see section 1.2). Therefore, it is not surprising that nowadays a large number of human diseases, referred to as ciliopathies (primary cilia dyskinesia (PCD), polycystic kidney disease (PKD), retinal degeneration, respectively), are known to be linked with non-functional, misshapen or missing cilia (Badano et al., 2006; Fliegauf et al., 2007; Pazour and Rosenbaum, 2002).

1.1) Architecture of the cilium

The terms cilia and flagella describe the same organelle and will be used interchangeable throughout this thesis. However, the eukaryotic flagellum should not be confused with the prokaryotic flagellum as the two structures have different architectures and evolutionary origins. The bacterial flagellum is an extracellular appendage also used for motility but the main building block is flagellin and the structure is not surrounded by a membrane (reviewed in (Macnab, 2003)). The eukaryotic flagellum has a microtubule (MT)-based axoneme surrounded by a membrane continuous with the plasma membrane and is classified as an intracellular organelle.

Cilia can be categorized in motile and non-motile cilia depending on their inner organization (figure 2). Motile cilia have nine outer MT doublets (A- and B-tubules) with a central MT pair, referred to as ‘9+2’ arrangement. Non-motile cilia (also called primary cilia) have a ‘9+0’ arrangement, missing the central pair of MTs and perform mainly sensory functions (see section 1.2). Two exceptions from the rule above could be identified in humans so far. First, the cilium on nodal cells has a ‘9+0’ arrangement but still contains the motor machinery to perform a unique twirling movement (Nonaka et al., 1998). Second, the cilia in the inner ear (kinocilium) are immotile due to the lack of parts of the motor machinery but have a ‘9+2’ arrangement (Dabdoub and Kelley, 2005; Kikuchi et al., 1989; Sobkowicz et al., 1995).

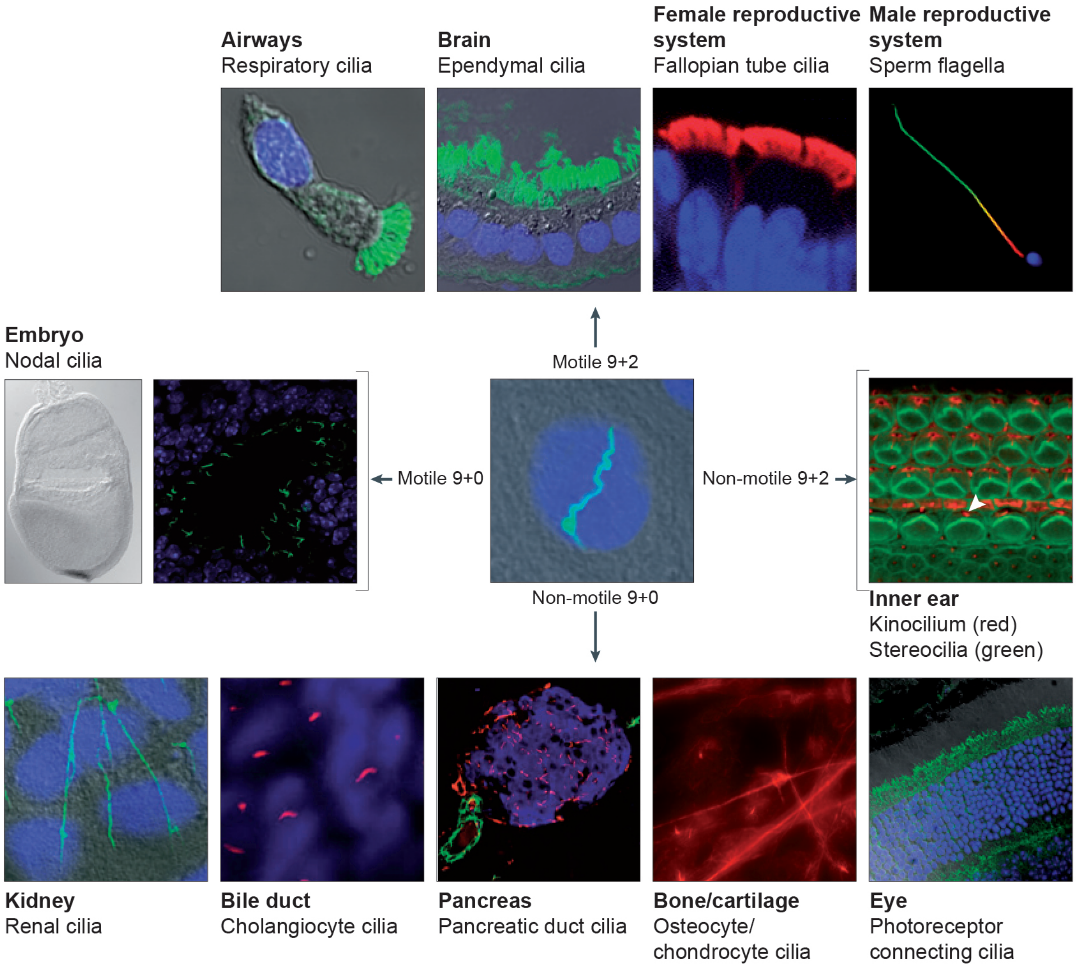

Figure 1: Overview of cilia emerging from a various number of eukaryotic cell types. Cilia are sorted into four groups according to their MT-based axoneme (adapted from (Fliegauf et al., 2007)).

The cilium emanates from a basal body, a modified mother centriole (Bornens, 2012; Nigg and Raff, 2009). The orientation of the basal body in the cell is important for the correct localization of the cilium. Triplet MTs (A-, B- and C-tubules) in the basal body arrange in a cartwheel structure whose symmetry is continued in the outer doublet MT array of the ciliary axoneme (Mizuno et al., 2012; Ringo, 1967). Distal to the basal body is the ‘transition zone’ in which the central pair of MTs originate, the C-tubules terminate and only the A- and B-tubules are continuous through and form the ciliary axoneme (Gilula and Satir, 1972). The MTs are assembled by adding αβ-tubulin dimers (8 nm length) to the ‘plus end’ (Hao et al., 2011; Johnson and Rosenbaum, 1992; Lechtreck et al., 2013; Marshall and Rosenbaum, 2001). The B-tubules consist of 10 protofilaments, whereas the A-tubules and the central pair have 13 protofilaments (Warner and Satir, 1973; Witman et al., 1972). Furthermore, MT-associated structures are necessary to assemble and maintain a functional cilium. The most important structures are discussed here. (1) Two big protein complexes, the inner and outer dynein arms (subcategorized depending on their location), extend from the A-tubules of one MT doublet to the B-tubules of the adjacent MT doublet from motile cilia (Mitchell, 2000; Warner and Satir, 1974). The inner dynein arms (IDAs) are located in the inner periphery of the doublet MTs whereas the outer dynein arms (ODAs) are facing the ciliary membrane. Both complexes consist of several heavy, intermediate and light chains (reviewed in (Porter, 1996)). The heavy chains contain ATPase activity, hydrolyzing ATP to ADP and phosphate providing the driving force for the bending of motile cilia (Gibbons, 1963). The movement is achieved by sliding of adjacent MT doublets located next to each other (Satir, 1968; Summers and Gibbons, 1971). (2) Thin fibers, the nexins, span A- and B-tubules of the adjacent MT doublet (Gibbons, 1963). A later study using cryo electron tomography identified nexins as part of the dynein regulatory complex (DRC), now referred to as N-DRC (Heuser et al., 2009). How this complex stabilizes the ciliary axoneme as well as the exact protein composition are still questions to address. (3) Radial spokes (a complex of at least 23 proteins) connect the A-tubules and the central sheath, surrounding the central MT pair (Gibbons and GRIMSTONE, 1960; Patel-King et al., 2004; Piperno et al., 1981; Warner, 1970; Warner and Satir, 1974; Yang et al., 2006). Additional mutagenesis studies revealed interplay of radial spokes and the central sheath/MT pair in regulating the activity of dynein motors attached to the A-tubules (Mitchell, 2000; Warner and Satir, 1974; Witman et al., 1978), although the detailed mechanism remains elusive.

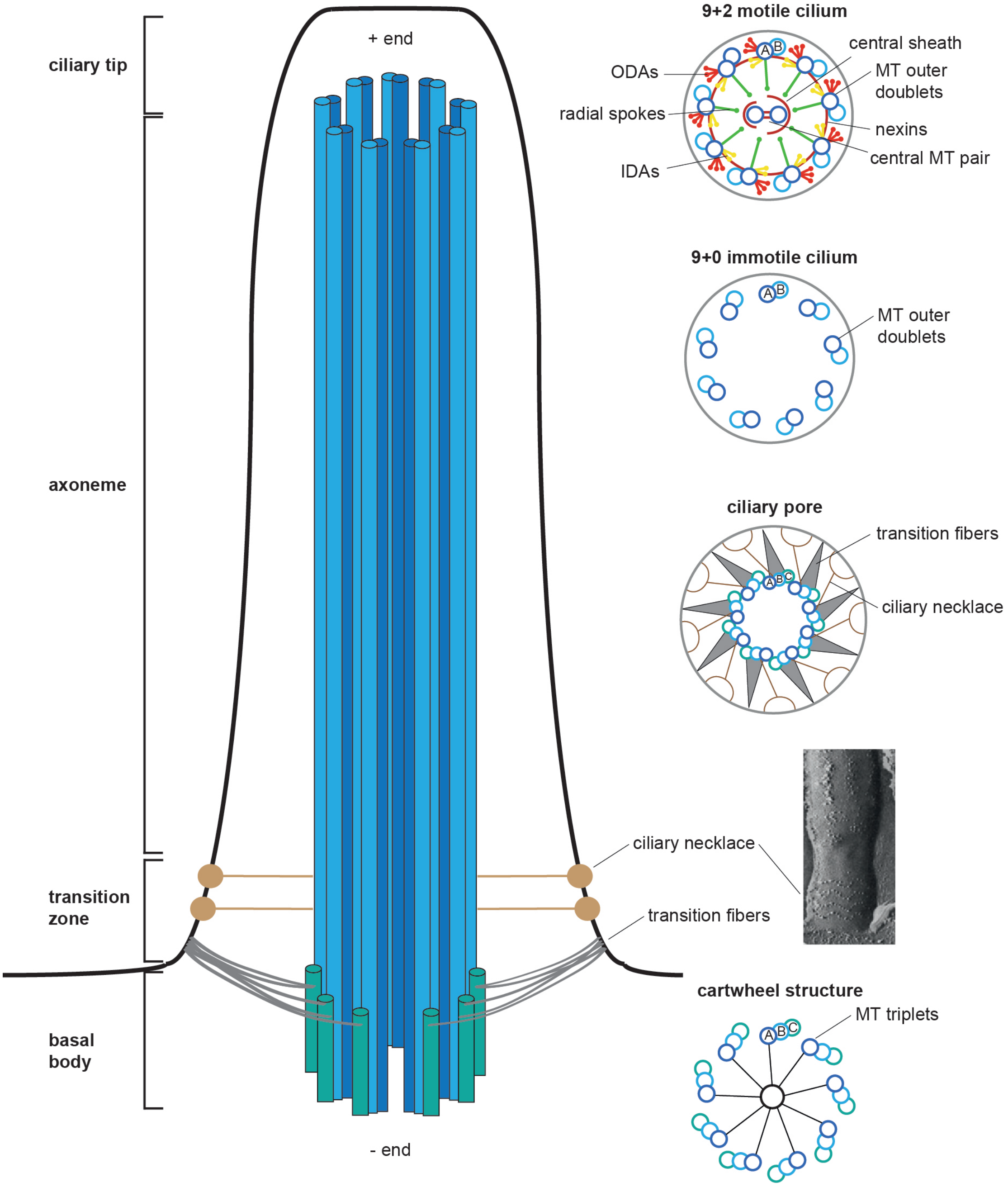

Figure 2: Cartoon representation of a cilium. Cross sections ('9+2' arrangement adapted from (Pedersen and Rosenbaum, 2008)) at various positions of the cilium illustrate the inner organization in more detail. The A- and B-MTs extend from the basal body to form the backbone of the ciliary axoneme. Transition fibers and the ciliary necklace (microscope picture (Czarnecki and Shah, 2012)) are thought to form the ciliary pore to avoid uncontrolled entry into the ciliary compartment. MT: microtubule, ODAs: outer dynein arms, IDAs: inner dynein arms.

As already mentioned above, the ‘transition zone’ is located between the distal end of the basal body and the axoneme. In this region transition fibers (also termed Alar sheets (Anderson, 1972)) form a nine-bladed propeller like structure connecting the ciliary membrane with all nine MT triplets of the basal body (Gibbons and GRIMSTONE, 1960; Gilula and Satir, 1972; O'Toole et al., 2007; Ringo, 1967). Distal to the transition fibers, the ciliary necklace is placed. This is a specialized structure composed of several parallel strands of intramembrane particles (unknown composition) bridging the A- and B-tubules and the ciliary membrane (Gilula and Satir, 1972). The transition fibers and the ciliary necklace are thought to function together as a ciliary pore avoiding uncontrolled entry into the ciliary compartment (Fisch and Dupuis-Williams, 2011; Gilula and Satir, 1972). This gateway keeper function supports the argument to classify cilia as an independent intracellular compartment.

Proteins larger than 9 nm in diameter (~100 kDa) are unable to diffuse through the ciliary pore (Breslow et al., 2013). Therefore, it was speculated that either helper proteins or an active transport system is in place to ensure entry into the cilium. It has been shown that larger proteins or pre-assembled complexes (like radial spokes, dynein arms) are escorted through the ciliary pore through helper proteins (Hou et al., 2007; Qin et al., 2004) but the exact mechanism how this big protein complexes pass the ciliary pore is still enigmatic.

1.2) Functions of cilia

1.2.1) Cilia in development

Embryonic node cells contain one cilium per cell. These nodal cilia perform a unique twirling movement creating an extracellular nodal fluid flow (Nonaka et al., 1998) (figure 3). Non-functional or missing nodal cilia in this early step of development result in an inverted position of the inner organs in the body, a condition known as *situs inversus* (Okada et al., 1999; Pazour et al., 2000). Elegant work in which mouse embryos were cultured under an artificial fluid flow could show that the embryonic nodal fluid flow is essential for the correct left-right-axis determination of the embryo. Whereas embryos exposed to leftward flow showed normal left-right patterning, the body symmetry was reversed in embryos developed under a rightward flow (Nonaka et al., 2002). An explanation for the importance of the nodal flow could be the formation of a gradient of a so far unknown morphogen towards the left side and thereby triggering a signaling cascade responsible for the body symmetry. In line with this, Tanaka and colleagues observed secretion of membrane-sheathed 'nodal vesicular parcels' (NVPs) from the nodal surface carrying Sonic hedgehog (Shh) and retinoic acid molecules, transported leftwards by the fluid flow (Tanaka et al., 2005). Furthermore, the Ca^{2+} channel polycystin-2 (Pkd-2) in cilia of crown cells, placed at the edge of the node, is pivotal in sensing the nodal flow and therefore for correct left-right patterning (McGrath et al., 2003; Yoshiba et al., 2012).

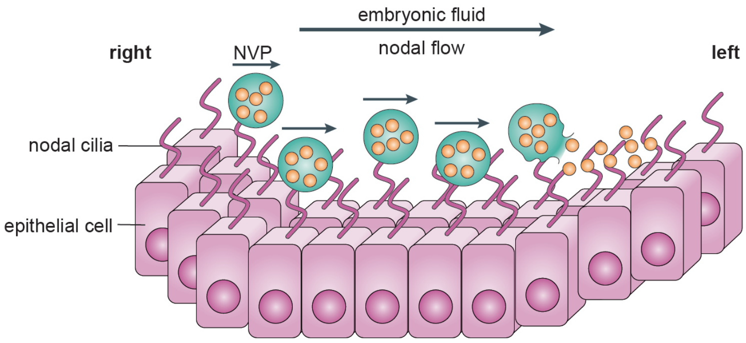

Figure 3: Schematic representation of embryonic nodal cells. 'Nodal vesicular parcels' (NVPs) are secreted from the cells and transported leftwards due to the nodal flow created from beating cilia, determining the left-right-axis pattern of the embryo (adapted from (Fliegauf et al., 2007)).

Sonic hedgehog (Shh) signaling

Another important role of cilia during mammalian development is their involvement in various signaling pathways. Cilia are indispensable for the regulation of Sonic hedgehog (Shh) signaling due to the localization of Shh components, like Smoothened (Smo) (Corbit et al., 2005), Suppressor of fused (Sufu) and the transcription factors Glioma 2 and 3 (Gli2, Gli3) (Haycraft et al., 2005) to cilia. Cells, either lacking cilia or with defective cilia, are unable to induce the pathway in response to exogenous Shh ligands or show impaired Shh, leading to various developmental defects (Badano et al., 2006; Cortellino et al., 2009; Haycraft et al., 2005; Houde et al., 2006; Huangfu et al., 2003; Liem et al., 2012). Since the secreted protein Hedgehog (Hh) binds to its receptor Patched-1 (Ptch-1) the pathway is

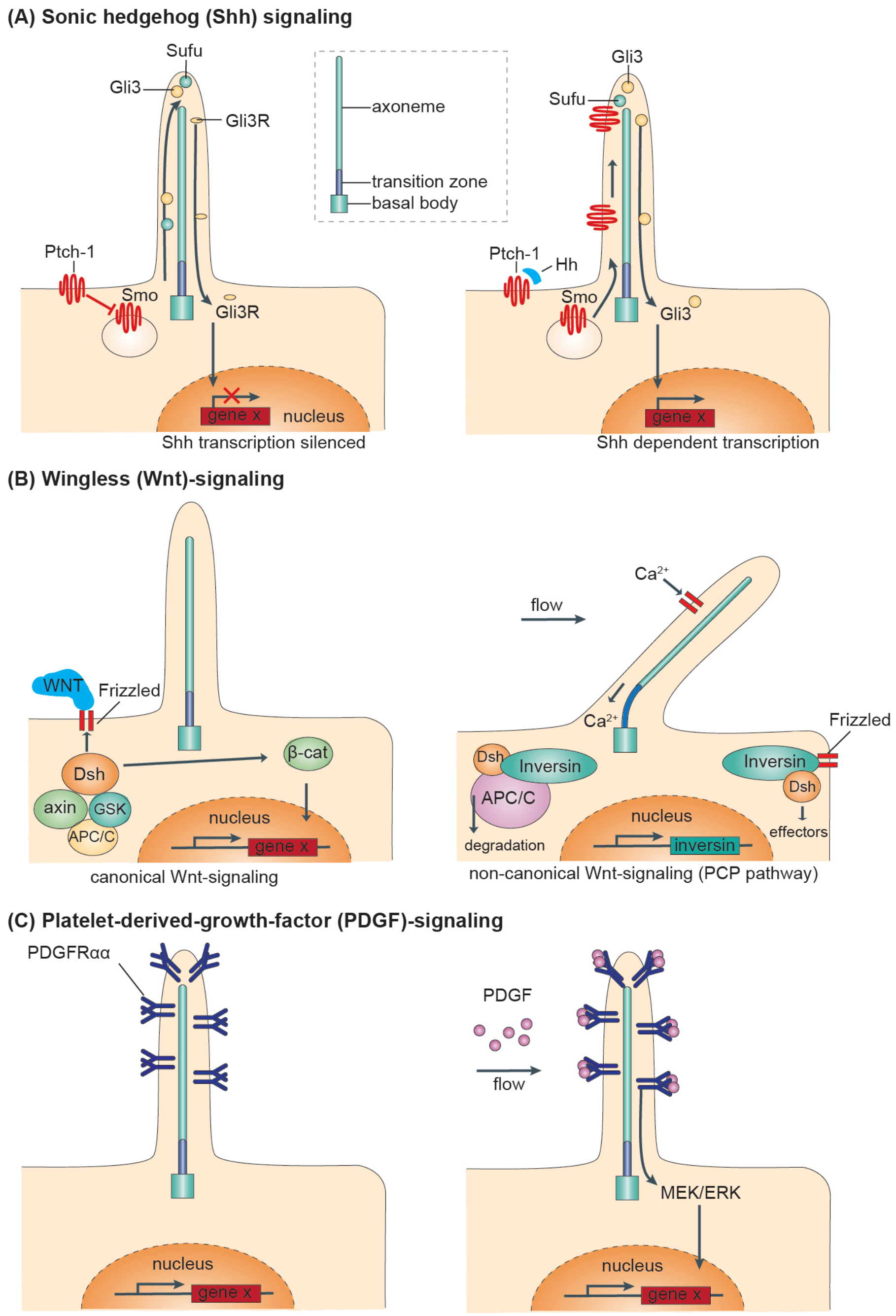

Figure 4: Schematic representation of the role of cilia in various signaling pathways. (A) Shh signaling: Upon ligand binding of Hh to the receptor Ptch-1, Smo is transported into cilia to promote the activation of the transcription factor Gli3. (B) Wnt-signaling: Upon ligand binding, Dsh is recruited to the receptor Frizzled, leading to activation of the transcription factor β*-cat (canonical pathway). Flow-induced* Ca^{2+} *influx promotes Inversin expression that in turn targets cytoplasmic Dsh for degradation. Membrane-bound Dsh activates downstream effectors (non-canonical pathway). (C) PDGF-signaling: Binding of PDGF to PDGFRαα leads to activation of the MEK/ERK cascade. (Figures adapted from (Fliegauf et al., 2007)).*

initiated. In the absence of its ligand, Ptch-1 is located in the ciliary membrane and keeps Smo in an inactive state by an unknown mechanism. After Hh binding Ptch-1 is removed from the ciliary membrane and Smo is released and transported to the ciliary tip (Rohatgi et al., 2007). In the cilium, Smo blocks the processing of Gli3 by interacting with Sufu. Active Gli3 is then transported to the base of the cilium, enters the nucleus and induces the expression of several Shh target genes. In the absence of Smo, full length Gli3 is processed to a transcriptional repressor (Gli3R) (Berbari et al., 2009; Haycraft et al., 2005) (figure 4A).

Wingless (Wnt)- and platelet-derived-growth factor (PDGF)-signaling

Wingless (Wnt)-signaling can be subdivided into canonical and non-canonical pathways (figure 4B). The canonical route is required for cell fate determination and proliferation whereas the non-canonical pathway, also known as planar cell polarity (PCP) pathway, controls cell polarization and gastrulation (Christensen et al., 2008; Sato et al., 2006). Members of both routes can be found at the cell membrane close to the ciliary base as well as within cilia, like Inversin (Morgan et al., 2002), Dishevelled (Dsh) (Park et al., 2008), anaphase-promoting complex/cyclosome (APC/C), β-catenin (β-cat) and glycogen synthase kinase-3β (GSK) (Corbit et al., 2008). The canonical pathway is induced upon ligand binding of WNT to the receptor Frizzled leading to the recruitment of cytoplasmic Dsh to Frizzled and inactivation of GSK. As a consequence, Dsh stabilizes β-cat that translocates to the nucleus and induces transcription of Wnt-target genes. In the absence of a signal β-cat is degraded via a complex of axin, GSK and APC/C (Berbari et al., 2009; Fliegauf et al., 2007). The non-canonical pathway is mediated via flow-induced bending of cilia. This leads to Ca^{2+} influx and thus to an increased Inversin expression. In turn, Inversin targets the cytoplasmic pool of Dsh (not membrane-bound Dsh) for APC/C-dependent ubiquitylation and degradation and thus destabilizes β-cat as well. Membrane-bound Dsh promotes the activation of downstream effectors that in turn affect the cytoskeleton independent of transcription (Fliegauf et al., 2007; Sato et al., 2006).

Signaling via platelet-derived-growth factors (PDGFs) and their receptors (PDGFRs) is pivotal in controlling cell survival, proliferation and embryonic development. In growth-arrested fibroblasts, PDGFRα localizes to the primary cilium (Schneider et al., 2005) where it functions as a homodimer (Fredriksson et al., 2004). After stimulation with its ligand PDGF-AA, PDGFRαα gets auto-phosphorylated at certain tyrosines that in turn lead to the activation of the AKT- and MEK1/2-ERK1/2-pathways in and at the base of the cilium, and thus to ciliary resorption and cell cycle entrance (figure 4C). In contrast, PDGFRβ is not targeted to the membrane of the very short primary cilia in orpk mutant mouse embryonic fibroblasts (MEFs) supporting the conclusion that the primary cilium exclusively regulates PDGFRαα activation and function (Christensen et al., 2008; Schneider et al., 2005).

1.2.2) Cilia in mechanosensing

Kidney epithelia cells have one immotile cilium per cell (primary cilium) pointing into the tubular lumen. Defects in renal primary cilia contribute to the pathogenesis of polycystic kidney disease (PKD) (Pazour et al., 2000) due to the inability of these cilia to sense extracellular fluid flow (Liu et al., 2005; Praetorius and Spring, 2003). Cilia on renal cells bend under the urine flow resulting in an increased Ca^{2+} influx (Masyuk et al., 2006; Praetorius and Spring, 2001). Membrane potential measurements revealed that the ciliary concentration of Ca^{2+} is approximately five times higher than in the cytoplasm (Delling et al., 2013), leading to the activation of Ca^{2+}-signaling cascades (DeCaen et al., 2013) (figure 5). It has been shown that the heterodimer polycystin-1 (PC1)/polycystin-2 (PC2), in mammals encoded by the genes *Pkd-1* and *-2*, locate to the ciliary membrane (Delmas et al., 2002; Hanaoka et al., 2000; Mochizuki et al., 1996; Pazour et al., 2002; Stayner and Zhou, 2001; Yoder et al., 2002) and are responsible for the mechanotransduction pathway of cilia (DeCaen et al., 2013). PC2 functions as a Ca^{2+} channel (Koulen et al., 2002; Vassilev et al., 2001), whereas PC1 is a flow-sensor, activating G-protein-coupled signaling pathways, which in turn activate Ca^{2+} and K^+ channels (Delmas et al., 2002). Mutations in the genes *Pkd-1* and *-2* lead to renal cyst formation followed by renal failure in mice (Lu et al., 1997; Wu et al., 1998), the main phenotype of PKD. Cultured renal epithelial cells from transgenic mice, lacking PC1 are able to form cilia but no increased Ca^{2+} influx in response to fluid flow could be detected (Nauli et al., 2003). Furthermore, in PKD patients a mutation in PC2 was found to result in impaired sensitivity to changes of the intracellular Ca^{2+} concentration (Vassilev et al., 2001). These findings led to the conclusion that PKD may result from the loss of a regulated intracellular Ca^{2+} release signaling mechanism.

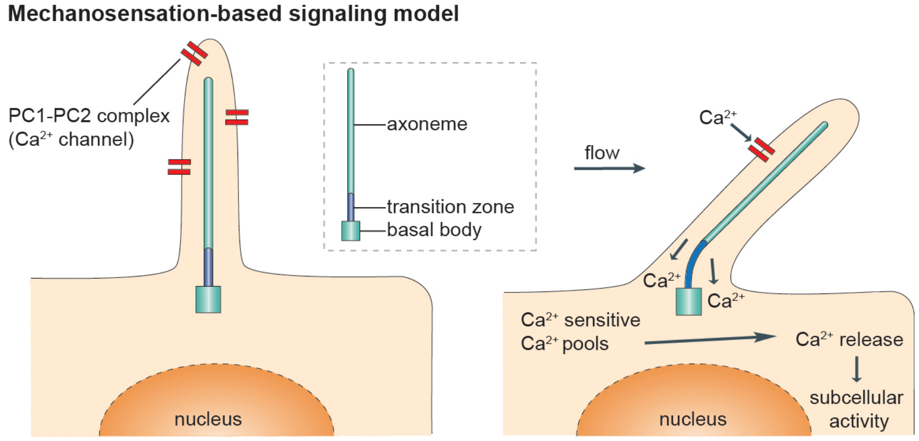

Figure 5: Mechanosensation-based signaling model: Flow-induced ciliary bending is pivotal for sensing the Ca^{2+}*influx into cilia via the PC1-PC2 complex, leading to the activation of the Ca*$^{2+}$*- signaling cascade (adapted from (Fliegauf et al., 2007)).*

1.2.3) Cilia in olfaction and photoreception

Olfactory sensory neurons end in dendritic knobs, the origin of clusters of olfactory cilia (Berbari et al., 2009) (figure 6B). Once the odorants contact the epithelium they act as ligands for olfactory G-protein-coupled receptors (GPCRs) in the ciliary membrane. Activation of these GPCRs triggers downstream events leading to the sensation of smell (McEwen et al., 2008). Defective cilia unable to respond to an odorant lead to loss of smell also known as anosmia (Badano et al., 2006; Kulaga et al., 2004).

Rod and cone photoreceptor cells are highly polarized sensory neurons (figure 6A). They consist of the inner segment, where protein synthesis and maturation occurs and the outer segment, full of membrane discs containing GPCRs like opsin and rhodopsin that sense the incoming light. The ‘connecting cilium’, an immotile cilium with a 9+0 axoneme, bridges inner and outer segments (Berbari et al., 2009; Besharse and Horst, 1990). Due to the high turnover rate of the outer segment (~2000 opsin molecules per minute) it was speculated that an efficient mechanism exists that ensures the delivery of components to the outer segment (Besharse and Horst, 1990). This has been proven by mutational analysis in mice, leading to severe retinal degeneration (Marszalek et al., 2000; Pazour, 2002) a cause for retinis pigmentosa (RP) (Badano et al., 2006).

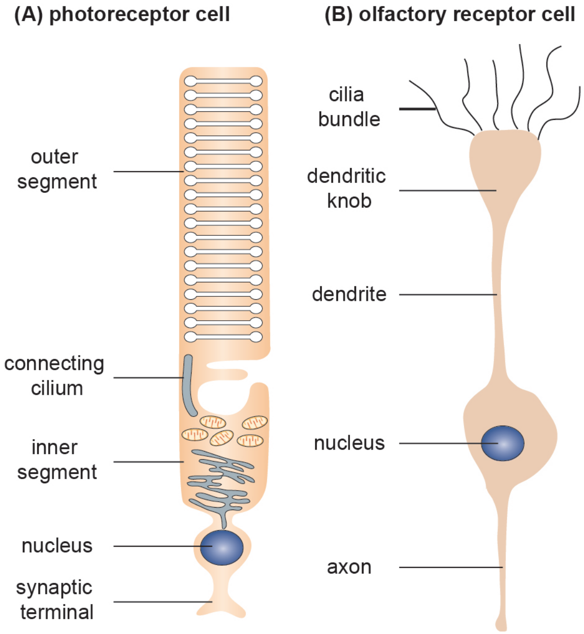

Figure 6: Cartoon representation of a photoreceptor and olfactory cell. (A) In the photoreceptor cell the inner and outer segments are linked through the 'connecting cilium' (adapted from (Fliegauf et al., 2007)). (B) Multiple cilia originate from the dendritic knob of an olfactory receptor cell.

All together, cilia have been shown to play important roles in signaling and sensory reception and can therefore be thought of as the antennae of the cell (Berbari et al., 2009; Christensen et al., 2008; Fliegauf et al., 2007; Gerdes and Katsanis, 2008; Goetz and Anderson, 2010; Singla and Reiter, 2006).

1.2.4) Cilia in motility

The motility of cilia is a result of the presents of various dynein arms facing the ciliary axoneme as described in section 1.1. Comparison of the bending pattern of wild type or mutant (either lacking IDA or ODA components) *Chlamydomonas reinhardtii* flagella indicated different functions for IDAs and ODAs (Brokaw and Kamiya, 1987). IDAs are thought to be responsible for the size and shape of the waveform by which the ciliary axoneme bends (Brokaw and Kamiya, 1987; Porter and Sale, 2000). On the other hand, the power and beat frequency of ciliary bending seems to be controlled by ODAs (Brokaw and Kamiya, 1987).

Beating of motile cilia facing the fallopian tubes in the female reproductive tract are absolutely necessary to move the zygote from the ovary to the uterus. Otherwise ectopic pregnancy or subfertility can occur (Lyons et al., 2006). The tail of the male sperm cell is also a motile cilium, thus male infertility is mostly linked with impaired sperm motility (Fliegauf et al., 2007; Munro et al., 1994). This phenotype is often seen in primary ciliary dyskinesia (PCD) a well-known ciliopathy normally combined with defects in nodal (see section 1.2.1) and respiratory cilia. The motile cilia on respiratory epithelial cells are indispensable for mucociliary clearance of the airways (Duchateau et al., 1985; Storm van's Gravesande and Omran, 2005). Furthermore, ependymal cells lining the ventricles of the brain also contain motile cilia to create the laminar flow of the cerebrospinal fluid (ependymal flow). Lack of this ependymal flow causes amongst others hydrocephalus formation in the early brain development (Banizs et al., 2005; Ibañez-Tallon et al., 2004).

1.3) Intraflagellar transport

How do cells construct and maintain the cilium organelle? Given that cilia are devoid of ribosomes and that axonomal components are assembled and turned over at the ciliary tip (Johnson and Rosenbaum, 1992; Marshall and Rosenbaum, 2001; Pazour et al., 2005), cilia rely on an active transport system for assembly and maintenance. Intraflagellar transport (IFT) was characterized in 1993 in the biflagellate algea *Chlamydomonas reinhardtii* (*Cr*) using differential interference contrast (DIC) microscopy visualizing particles moving bidirectional inside the cilium (Kozminski et al., 1993). Longitudinal sections of paralyzed *Chlamydomonas* flagella analyzed using electron microscopy showed granule-like particles (IFT particles), localized between the outer doublet MTs and the ciliary membrane arranged in long linear arrays (later referred to as IFT-trains (Pigino et al., 2009)) (figure 7). Quantification of the movement of the IFT-trains revealed a slower (2 µm/sec) anterograde transport (from the base to the ciliary tip) compared to a faster (3.5 µm/sec) retrograde transport (from the ciliary tip to the base) (Kozminski et al., 1993). Further analysis elucidated two types of IFT-trains. Long, narrow trains (~700 nm) that seem to be used in anterograde transport compared to short, more compact trains (~250 nm) that are likely responsible for retrograde transport (Pigino et al., 2009). Another study suggested a correlation between the state or length of the cilium and the IFT-trains unrelated to the direction of IFT (Engel et al., 2009). Therefore, further studies are necessary to shed light on the physiological role of different IFT-train types. The most detailed insight into the structure of IFT-trains so far is a 3D electron tomography reconstruction (Pigino et al., 2009), clearly showing two lanes of repeating building blocks. The authors suggested that one such building block might contain the IFT particle, motor proteins and cargo destined for cilia (figure 7).

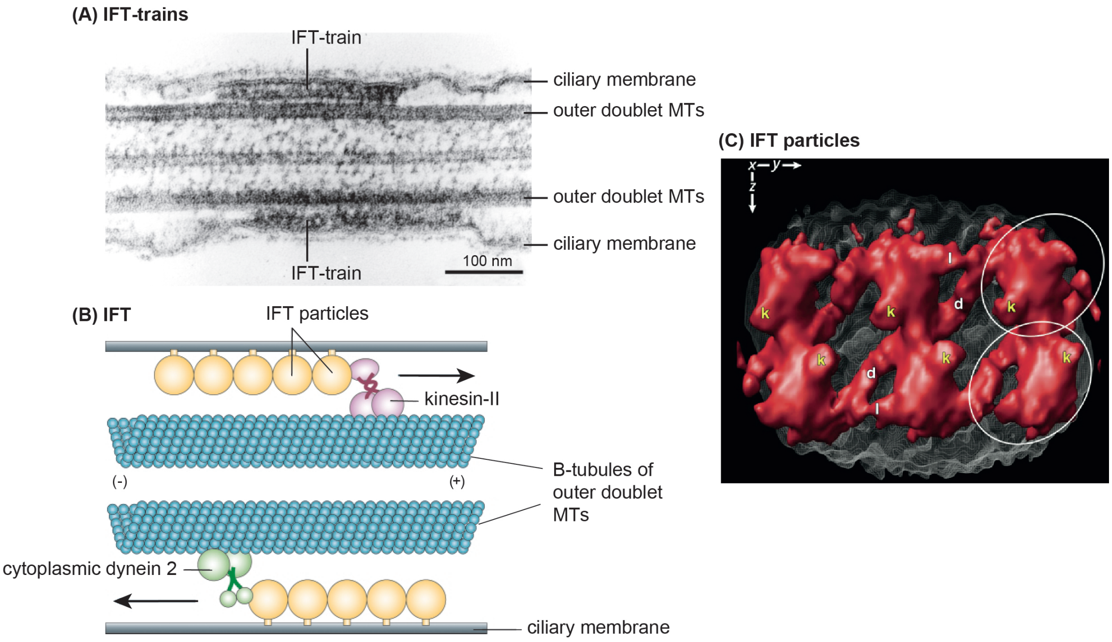

Figure 7: (A) Electron micrograph of a paralyzed Chlamydomonas flagellum. The IFT-trains are visualized as electron dense material between the ciliary membrane and the outer doublet MTs (adapted from (Kozminski et al., 1995)). (B) Schematic representation of the IFT machinery. IFT particles are transported to the tip of the cilium via the motor protein kinesin-II (anterograde IFT). Retrograde IFT, back to the base of the cilium, is powered by cytoplasmic dynein 2 (adapted from (Rosenbaum and Witman, 2002)). (C) 3D electron tomography reconstruction showing IFT particles arranged in two rows. Distinct links (l longitudinal, d diagonal to the axis of IFT-trains) connect the adjacent IFT particles (white ovals). Interactions between the IFT particle and the outer doublet MTs are indicated with k, presumably the motor protein (adapted from (Pigino et al., 2009)).

The first biochemical analysis of IFT particle proteins was carried out performing sucrose density gradient centrifugation of material isolated from *Chlamydomonas reinhardtii* flagella (Cole et al., 1998; Piperno and Mead, 1997). The 14 identified IFT proteins co-sediment at ~16S. Varying the ionic strength separates the proteins into two subcomplexes, named IFT-A and IFT-B. The IFT-B complex can be further trimmed down to a salt stable 'IFT-B core' and loosely attached 'peripheral' IFT-B proteins (Lucker et al., 2005). Over the last years more members of the IFT complex and their homologues in various organisms were discovered (table 1).

The motors responsible for IFT have also been identified. Switching a temperature sensitive *Chlamydomonas reinhardtti fla10* (gene for kinesin-II motor subunit) mutant to the restrictive temperature results in shrinking of cilia, termination of IFT and loss of IFT proteins from the cilium (Cole et al., 1998; Kozminski et al., 1995). This led to the conclusion that hetero-trimeric kinesin-II drives anterograde transport. The same phenotype of stumpy cilia or even loss of cilia is observed in IFT-B mutants (see section 1.4.2) (Brazelton et al., 2001; Pazour et al., 2000) indicating that IFT-B proteins are important for anterograde IFT. In contrast, deletion of the gene encoding dynein heavy chain isoform DHC1b results in short, non-motile cilia with bulky tips filled with granule-like particles. In these mutants anterograde IFT could be detected but retrograde IFT was completely stopped (Pazour et al., 1999; Porter et al., 1999; Signor et al., 1999). Mutational analysis of IFT-A proteins also revealed short cilia with accumulated IFT-B proteins at the tip (see section 1.4.1.2) (Absalon et al., 2008; Efimenko et al., 2006; Piperno et al., 1998), linking cytoplasmic dynein 2 (previously called cytoplasmic dynein 1b) and IFT-A proteins to retrograde IFT.

Taken together, IFT is a conserved mechanism, important for the assembly and maintenance of different kind of cilia in various organisms, ranging from (1) motile cilia in *Chlamydomonas reinhardtii* (Kozminski et al., 1995; Pazour et al., 1999; 2000), sea urchin (Morris and Scholey, 1997) and *Tetrahymena thermophila* (Brown et al., 1999) to (2) ciliated sensory neurons in *C.elegans* (Cole et al., 1998; Haycraft et al., 2001; Perkins et al., 1986; Qin et al., 2001) and (3) nodal cilia (Murcia et al., 2000), kidney primary cilia (Pazour et al., 2000) and rod outer segments in mice (Pazour, 2002).

Chlamydomonas reinhardtii	*Caenorhabditis elegans*	*Drosophila melanogaster*	*Trypanosoma brucei*	*mammals*	*Danio rerio*
IFT-A core					
IFT144, FAP66 (A9XPA7)	DYF-2 (G5ECZ4)	OSEG6 (A1ZBM3)	PIFTF6 (Q387M5)	IFT144, WDR19 (Q8NEZ3)	WDR19 (E7FGG5)
IFT140 (A8J4D9)	CHE-11 (P90757)	OSEG3 (Q9VPR0)	IFT140 (Q388F5)	IFT140 WDTC2 (Q96RY7)	IFT140 (F1R740)
IFT122 (H9CTG6)	DAF10 (G5EFW7)	OSEG1 (Q9VSJ6, Q8T9D3)	IFT122 (Q38B65)	IFT122, SPG, WDR10, WDR140 (Q9HBG6)	IFT122 (Q6NYH1)
IFT-A peripheral					
IFT139 (A9XPA6)	TTC21 (Q20255)	not identified	putative IFT139 (Q38EI1)	THM1, TTC21B (Q7Z4L5)	?
IFT121, FAP118 (A8JFR3)	IFTA-1 (Q18859)	OSEG4 (Q9W097)	PIFTD4 (Q57ZX9)	WDR35 (Q9P2L0)	WDR35 (B7ZD88)
IFT43, MOT41 (A8HYP5)	not identified	CG5780 (Q9VK67)	putative IFT43 (Q586Q5)	IFT43, C14orf179 (Q96FT9)	IFT43 (E7F555)
IFT-B core					
IFT88 (Q9FPW0)	OSM-5 (G5ED37)	NOMPB (Q9V9R6, Q7KRS6)	IFT88 (Q386Y0)	IFT88, Polaris, TTC10 (Q13099)	IFT88 (Q6RUQ9)
IFT81 (Q68RJ5)	IFT81 (A8DYR7)	not identified	putative IFT81 (Q38BY1)	IFT81, CDV-1R (Q8WYA0)	IFT81 (Q61VW2)
IFT74/72/71 (Q6RCE1)	IFT74 (Q18106)	not identified	putative IFT74 (Q57WF2)	IFT74, CCDC2, CMG-1 (Q96LB3)	Zgc:92052 (Q6DHU7)
IFT70, FAP259 (A8ITN7)	DYF-1 (Q8I7G4)	CG5142, DYF-1 (Q9VK41)	PIFTB2 (Q580S6)	TTC30A/B (Q8N4P2)	Fleer (A7YE96)
IFT52, BLD1 (Q946G4)	OSM-6 (G5EDF6)	CG9595, OSM-6 (G5EDF6)	IFT52 (Q388B0)	IFT52, NGD5, C20orf9 (Q9Y366)	IFT52 (Q5PRA7)
IFT46, FAP32 (A2T2X4)	DYF-6 (Q1KYP5, G5EF67, G5EDH6)	CG15161 (Q9VJ72)	putative IFT46 (Q583M4)	IFT46, C11orf2, C11orf60 (Q9NQC8)	IFT46 (A7MBP4)
IFT27, FAP156 (A8HN58)	not identified	not identified	putative IFT27 (Q580S0)	IFT27, RabL4, RAYL (Q9BW83)	IFT27, RabL4 (Q5PR92)
IFT25, FAP232 (B8LIX8)	not identified	not identified	putative IFT25 (Q382K6)	IFT25, C1orf41, HSP16.2, HSPB11 (Q9y547)	HSPB11 (A5JV83)
IFT22, FAP9 (A8HME3)	IFTA-2 (Q9XUC2)	not identified	IFT22, RabL5 (Q381A3)	IFT22, RabL5 (Q9H7X7)	IFT22, RabL5 (Q567Y6)
IFT-B peripheral					
IFT172, FLA11 (Q5DM57)	OSM-1 (Q22830)	OSM-1 (Q22830)	IFT172 (Q38CC3)	IFT172, SLB (Q9UG01)	SLB (Q5DV81)
IFT80 (A8IXE2)	CHE-2 (G5EGF0)	OSEG5 (Q9VII8)	IFT80 (Q388A9)	IFT80, WDR56, (Q9P2H3)	IFT80 (F1QXI6)
IFT57/55 (Q2XQY7)	CHE-13 (Q93833)	CG8853, IFT57 (Q9VQS5)	IFT57 (Q389K8)	IFT57, DERP8, ESRRBL1, HIPPI (Q9NWB7)	IFT57 (Q6IVW0)
IFT56, DYF-13 (A8JA42)	DYF-13 (Q95QT8)	CG4525 (Q9VF41)	PIFTC3 (Q57ZL2)	IFT56, TTC26, HOP (Q8BS45)*	Ttc26 (Q5PR66)
IFT54, FAP116 (A8JBY2)	DYF-11 (Q17595)	?	DYF-11 (Q38CJ3)	IFT54, MIP-T3, TRAF3IP1 (Q8TDR0)	Elipsa (B2BWH3)
IFT38, FAP22 (A8J6F1)	DYF-3 (Q6I6D4)	CG17599 (Q9VR64)	PIFTA1 (Q57WZ2)	Cluap1 (Q96AJ1)	Qilin (Q7ZVC2)
IFT20 (Q8LLV9)	IFT20 (Q8T52)	CG30441 (A1Z6F0)	IFT20 (Q584X2)	IFT20 (Q8IY31)	IFT20 (B2GRJ4)

Table 1: All IFT proteins known to date as well as their identified homologs in various organisms (Absalon et. al., 2008; Cole and Snell, 2009; Follit et. al., 2009, van Dam et al. 2013). www.uniprot.org was used to complete the list. Uniprot identifiers are listed in brackets. Note: Uniprot numbers for mammals correspond to the *Homo sapiens* protein, apart from one *Mus musculus* homolog*.

1.4) Structure and function of individual IFT proteins

The IFT proteins organize into a ~1.5 MDa complex that is thought to transport ciliary cargo within cilia. Therefore, it is not surprising that bioinformatics analysis predicts many domains in IFT proteins that mediate protein-protein interactions, like coiled coil, Tetratricopeptide repeats (TPRs) and tryptophan-aspartic acid (WD) 40-repeats (β-propellers) (figures 8 and 10).

The 6 IFT-A and 16 IFT-B proteins identified so far are discussed separately in the next sections. In addition, the IFT-B proteins are further divided into subgroups according to their predicted domain architecture. A short introduction will describe each protein and its possible role in IFT and ciliogenesis based on the available literature.

1.4.1) IFT-A complex

1.4.1.1) Domain architecture of IFT-A proteins

The IFT-A complex consists of six members, namely IFT144, IFT140, IFT139, IFT122, IFT121 and IFT43 that can be isolated from *Chlamydomonas reinhardtii* as a stable complex (Piperno and Mead, 1997). To date, little is known about direct protein-protein interactions within the IFT-A complex. A reason for this lack of information might be the large size of these proteins, leading to difficulties to produce recombinantly expressed proteins. The only direct interaction known so far could be observed between IFT121 and IFT43 using yeast-2-hybrid assays and co-purification trials (Behal et al., 2012). Furthermore, after knocking down IFT139 and IFT121 in retinal pigment epithelium (RPE) cells, a stable 'IFT-A core' complex still co-immunoprecipitates consisting of IFT144, IFT140 and IFT122 (Mukhopadhyay et al., 2010) (figure 8B).

Secondary structure predictions using the algorithms PSIPRED (Jones, 1999), TPRpred and REP revealed similar domain architecture for IFT144, IFT140, IFT122 and IFT121 (Taschner et al., 2012) (figure 8A). All four proteins are predicted to consist of N-terminal WD40-repeats followed by α-helical solenoid TPRs spanning till the C-terminus of the proteins. This domain architecture is similar to components of coat protein I (COPI)- and clathrin-coated vesicles, pointing to a common ancestry of these proteins (Devos et al., 2004; Jékely and Arendt, 2006; van Dam et al., 2013). For IFT139 only TPRs are predicted. For IFT43, the smallest protein in this complex, no domains apart from a short coiled coil region could be determined. None of the IFT-A proteins contain a predicted domain with enzymatic activity. Due to that the secondary structure predictions revealed only domains involved in protein-protein interactions, it is very likely hat the IFT-A complex serves as a structural platform within the IFT complex.

(A) Domain architecture of IFT-A proteins

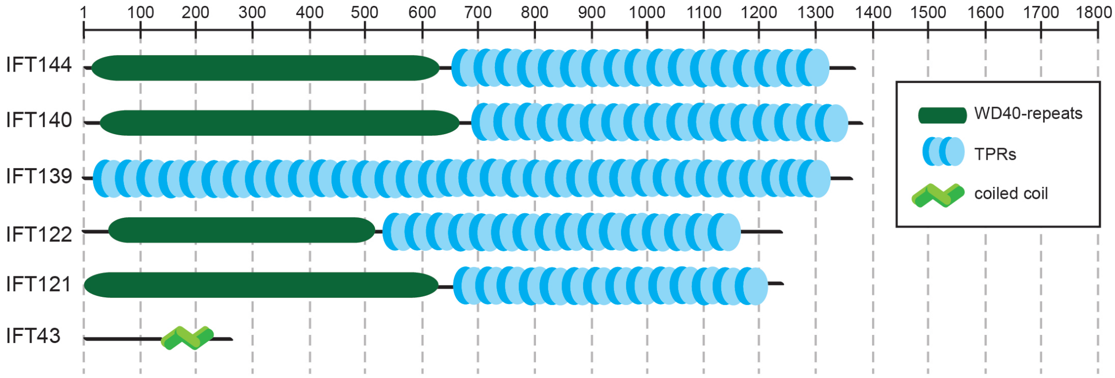

(B) IFT-A complex

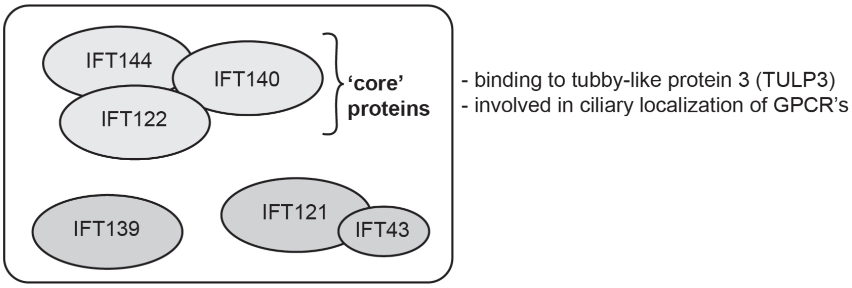

Figure 8: (A) Domain architecture of Chlamydomonas reinhardtii IFT-A proteins. (B) Preliminary interaction map of the IFT-A complex. Possible functions of the 'IFT-A core' are also depicted.

1.4.1.2) Function of IFT-A proteins

The 'IFT-A core' directly interacts with tubby-like protein 3 (TULP3), a member of the poorly understood tubby-like protein family, which seems to play a role in neuronal development and function. Furthermore, siRNA mediated depletion of either one of the 'IFT-A core' proteins or TULP3 in serum starved RPE cells inhibited the ciliary localization of a certain subset of GPCRs important for Shh signaling (Mukhopadhyay et al., 2010). This indicates that TULP3 serves as an adaptor between the IFT-A complex and cargo proteins destined for cilia. This is also in line with observations in IFT122 or IFT144 deficient mice that show, apart from various developmental defects, impaired Shh signaling (Cortellino et al., 2009; Liem et al., 2012; Qin et al., 2011). In contrast, mutations in THM1, the human ortholog of IFT139, lead to over-activation of Shh signaling (Goetz and Anderson, 2010; Tran et al., 2008). These findings clearly expose a correlation between IFT-A proteins and the Shh signaling pathway.

In general, a common phenotype seen for IFT-A proteins are bulky cilia with accumulated IFT-B proteins at the ciliary tip, linking retrograde IFT to the IFT-A complex. These phenomena have been observed for example in *dyf-2* (IFT144) mutants in *C.elegans* (Efimenko et al., 2006), mutations in the rempA locus (IFT140) in *Drosophila* (Lee et al., 2008a), mutations in THM1/TTC21B (IFT139) in mammals (Tran et al., 2008), depleting IFT122 in *Tetrahymena thermophila* (Tsao and Gorovsky, 2008), IFT122 deficient mice (Qin et al., 2011), RNAi knock down of PIFTD4 (IFT121) or PIFTF6 (IFT144) in *Trypanosoma brucei* (Absalon et al., 2008) and mutations in IFTA-1 (IFT121) in *C. elegans* (Blacque et al., 2006). Due to this conserved phenotype amongst different species it is not surprising that a set of human diseases, like Sensenbrenner syndrome and Jeune asphyxiating thoracic dystrophy (JATD), can be linked to mutations in certain IFT-A proteins (Arts et al., 2011; Bredrup et al., 2011; Gilissen et al., 2010).

1.4.2) IFT-B complex

So far 16 members of the IFT-B complex have been identified (Cole et al., 1998; Fan et al., 2010; Follit et al., 2009; Ishikawa et al., 2014; Lechtreck et al., 2009b; Lucker et al., 2005; Omori et al., 2008). Within the IFT-B complex, nine proteins organize in a salt stable ‘IFT-B core’, namely IFT88/81/74/70/52/46/27/25/22 (Taschner et al., 2014). In addition, IFT56 could also be an ‘IFT-B core’ member through its recently suggested direct interaction with IFT46 (Swiderski et al., 2014). The other six IFT-B proteins (IFT172, IFT80, IFT57, IFT54, IFT38 and IFT20) are considered as ‘peripheral’ proteins (Cole et al., 1998; Follit et al., 2009; Lucker et al., 2005) (figure 9).

Deletion of one of the IFT-B proteins in *Chlamydomonas reinhardtii* lead to stumpy cilia or even loss of cilia (Brazelton et al., 2001; Pazour et al., 2000), indicating their involvement in anterograde IFT. Furthermore, mutations in or depletion of certain IFT-B proteins in mice is embryonic lethal (Botilde et al., 2013; Houde et al., 2006; Huangfu et al., 2003; Murcia et al., 2000; Pasek et al., 2012), due to the loss of cilia thus confirming the importance of cilia during development (see section 1.2.1).

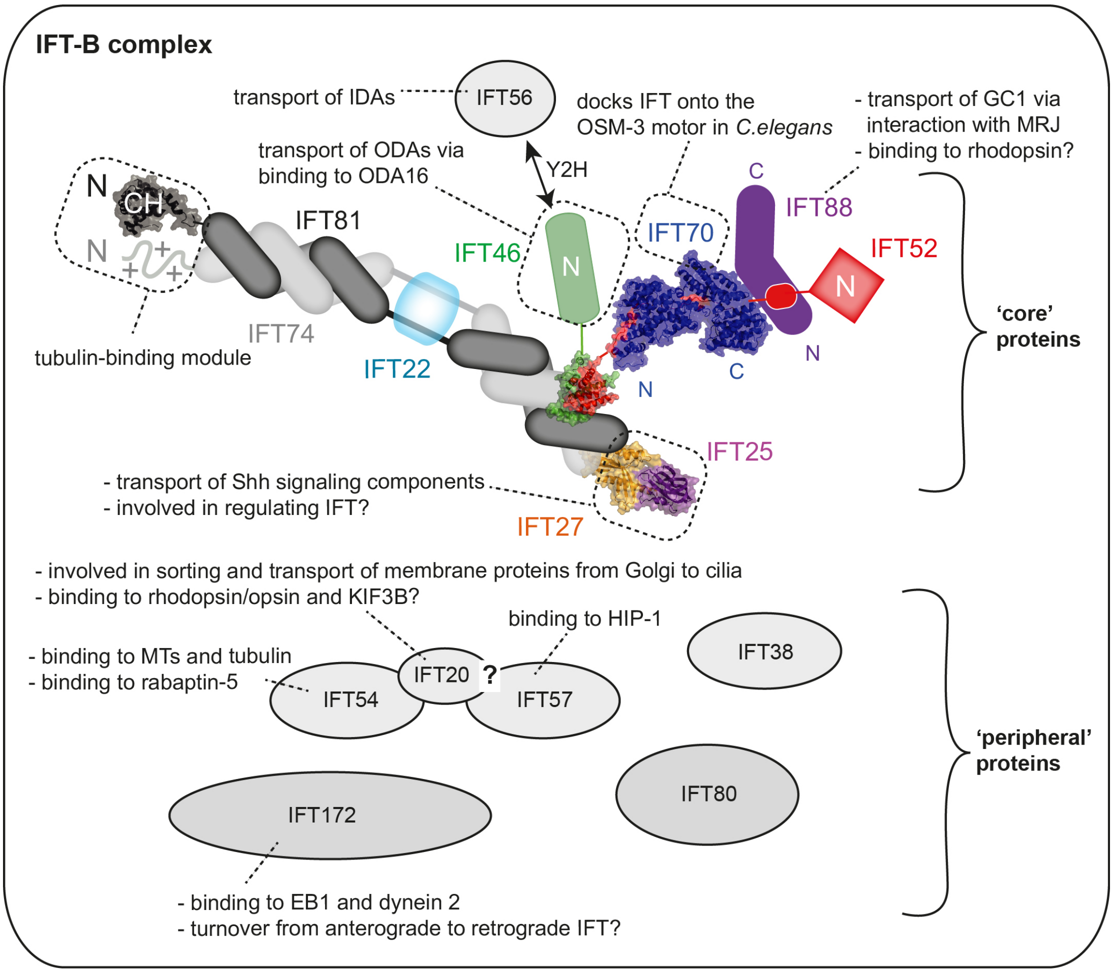

Figure 9: Preliminary interaction map of the IFT-B complex including the available crystal structures (adapted from (Taschner et al., 2014)). The possible functions of individual IFT-B proteins are listed as well. Y2H: yeast-2-hybrid assay.

The IFT-B proteins are predicted to be composed of mainly protein-protein interaction domains (Taschner et al., 2012) mediating the interactions between different IFT-B proteins (Baker et al., 2003; Bhogaraju et al., 2013a; Fan et al., 2010; Follit et al., 2009; Lucker et al., 2010; Omori et al., 2008; Taschner et al., 2011; 2014). Additional domains are predicted in several IFT-B proteins that are not necessary for IFT-B complex formation (Taschner et al., 2011; 2012) (figure 10A).

These domains could mediate the interaction to other binding partners such as motor proteins or ciliary cargo (Bhogaraju et al., 2013b).

Detailed structural information is available for a subset of IFT-B protein domains/regions and subcomplexes (figure 10B).

1.4.2.1) IFT-B proteins IFT27, IFT25 and IFT22

IFT22 and IFT27 show sequence similarity to Rab-like small GTPases (Bhogaraju et al., 2011; Qin et al., 2007; Schafer et al., 2006). Small GTPases are known to cycle between a GDP-bound inactive and a GTP-bound active state, a process that is highly regulated by guanine nucleotide exchange factors (GEFs) and GTPase-activating proteins (GAPs) (Bos et al., 2007; Cherfils and Zeghouf, 2013; Vetter and Wittinghofer, 2001). The nucleotide-binding pocket of GTPases is composed of the highly conserved G1 to 5 motifs. The main effector-, GEF- and GAP-binding sites of GTPases are the switch I and II regions. Binding of GEFs lead to conformational changes in the switch regions and the G1 motif (phosphate-binding loop), resulting in release of GDP and loading with GTP. GTP-loaded GTPases bind to downstream effectors in various pathways to regulate many different cell processes. The hydrolysis of GTP is facilitated by GAPs, leading to inactivation of the GTPase. Rab GTPases are typically involved in intracellular membrane trafficking and thus the 'IFT-B core' complex proteins IFT22 and IFT27 (Taschner et al., 2014) are suggested to play a role in regulating IFT (Qin et al., 2007). In contrast to other GTPases, IFT22 and IFT27 do not contain the prenylation motif typically located at the C-terminus of Rab GTPases, which allows them to associate directly with membranes (Adhiambo et al., 2009; Qin et al., 2007; Schafer et al., 2006). Furthermore, IFT22 is an atypical GTPase, lacking the G4 GTPase motif necessary for specificity for guanine over adenine nucleotides (Adhiambo et al., 2009; Schafer et al., 2006).

IFT22 (RabL5 in mammals, *Trypanosoma brucei*; IFTA-2 in *C.elegans*) has been shown to undergo IFT (Adhiambo et al., 2009; Schafer et al., 2006). Mutations in IFT22 resulted in normal cilia assembly and maintenance but in an increased life span of these worms (Schafer et al., 2006). This would indicate a role for IFT22 in regulating specific cilia signaling activities rather than a role in ciliogenesis. In contrast, RNAi mediated knock down of IFT22 in *Trypanosoma brucei* leads to short cilia with accumulated IFT particles at the ciliary tip, a phenotype typically seen when retrograde IFT is defective (Adhiambo et al., 2009). This raises the question if IFT22 has diverse functions in different species.

The crystal structures of *Chlamydomonas reinhardtii* IFT25ΔC/27 complex (Bhogaraju et al., 2011) and human IFT25 (Ramelot et al., 2009) have been determined (figure 10). IFT25 adopts a jelly-roll fold and coordinates a Ca^{2+} ion. The overall structure shows a relationship to sialidases, although the galactose-binding site of sialidases is not conserved in IFT25 (Bhogaraju et al., 2011). The specific function of IFT25 is not known. Furthermore, IFT27 is indeed a GTPase and displays very low intrinsic GTPase activity (Bhogaraju et al., 2011) but so far no effectors could be identified. The fact that IFT25 and IFT27 directly interact with each other (Bhogaraju et al., 2011; Follit et al., 2009; Rual et al., 2005; Wang et al., 2009) and that in mutant mice lacking IFT25, no IFT27 can be detected anymore (Keady et al., 2012), suggest that IFT25 is necessary to stabilize IFT27. The mutant mice showed normal cilia structure but Shh signaling was impaired implicating a role for IFT25/27 in mammalian Shh pathway (Eguether et al., 2014; Keady et al., 2012) rather than in ciliogenesis. Furthermore, both proteins are absent in *C.elegans* and *Drosophila* (Follit et al., 2009; Lechtreck et al., 2009b; Wang et al., 2009), suggesting that they are dispensable for ciliogenesis. A direct interaction between IFT27 and the nucleotide-free state of Arl6, an Arf-like GTPase, has been recently reported (Liew et al., 2014). Arl6 is a member of the BBSome complex, also undergoing IFT and the main player in Bardet-Biedl syndrome (BBS) (Blacque et al., 2004; Nachury et al., 2007). Mutations in the BBSome components prevent the delivery of specific receptors to the cilium (Berbari et al., 2008b) and cause abnormal accumulation of several signaling proteins (Lechtreck et al., 2009a), like the Shh proteins Ptch-1 and Smo (Eguether et al., 2014), within the cilium. All together, the observed data lead to the suggestion that GTP hydrolysis by IFT27 leads to disengagement of IFT25/27 from the rest of the IFT complex. In turn IFT25/27 binds to Arl6 and promotes exit of the BBSome (and its associated cargo) from cilia (Liew et al., 2014).

1.4.2.2) IFT-B proteins IFT88, IFT70 and TTC26 (IFT56)

Bioinformatics studies indicated high content of TPRs for IFT88, IFT70 and TTC26 (Taschner et al., 2012). The recently published crystal structure of *Cr*IFT70/52 revealed that IFT70 adopts a TPR superhelical structure that wraps around IFT52

(Taschner et al., 2014) (figure 10). This is in line with the insolubility of IFT70 in the absence of IFT52 and the stability of the IFT70/52 complex in high-salt conditions (unpublished data from Dr. Michael Taschner). Moreover, the interaction mode of the complex is antiparallel due to the binding of the N-terminal part of IFT70 to the C-terminal part of the IFT52 construct (Taschner et al., 2014). In addition, previous publications reported the formation of an IFT70/46 heterodimeric (Fan et al., 2010) and an IFT88/52/46 heterotrimeric (Lucker et al., 2010) subcomplex. Further interactions studies with recombinant proteins in *Chlamydomonas reinhardtii* revealed that IFT88/70/52/46 forms a stable subcomplex within the 'IFT-B core' (Taschner et al., 2011). Furthermore, in *Cr*IFT88 mutants the 'IFT-B core' is assembled but the 'peripheral' IFT-B proteins seem not properly attached to the 'IFT-B core' (Richey and Qin, 2012). In addition, yeast-2-hybrid assays and *in vitro* pull down experiments could show a direct interaction between IFT88 and MRJ (a member of the Dnaj family of co-chaperones in the Hsp70/Hsc70 system (Chuang et al., 2002)) that in turn binds to guanylyl cyclase 1 (GC1), leading to the assumption that MRJ may serve as an adaptor for the transport of GC1 (Bhowmick et al., 2009). The same authors also reported an association of IFT88 with rhodopsin via co-immunoprecipitation.

TTC26 (hereafter referred to as IFT56, according to the standard MW-based nomenclature of IFT proteins in *Chlamydomonas reinhardtti* (Cole et al., 1998; Rosenbaum and Witman, 2002)) was identified in various studies ranging from genomic search approaches in *C.elegans* cilia (Blacque et al., 2005; Efimenko et al., 2005) to proteomic analysis of primary cilia from mouse kidney cells (Ishikawa et al., 2012). It has been shown that IFT56 (DYF-13 in *C.elegans*; PIFTC3 in *Trypanosoma brucei*) undergoes IFT (Blacque et al., 2005; Ishikawa et al., 2014) and is absolutely required for ciliogenesis in *Trypanosoma brucei* (Absalon et al., 2008). Furthermore, tandem affinity purification and sucrose density gradient analysis revealed IFT56 as part of the IFT-B complex in *C.elegans* (Ishikawa et al., 2014) and yeast-2-hybrid assays identified an interaction between IFT56 and IFT46 (Swiderski et al., 2014). Interestingly, *Cr*IFT56 mutants are able to assembly short cilia but show impaired motility. Proteomic and biochemical analysis indicated a reduced set of certain IDAs (a, f and g) in *oda1dyf13* mutants (lacking ODAs and IFT56). Therefore, IFT56 seems to play an important role in transporting IDAs into cilia (Ishikawa et al., 2014). Furthermore, in *C.elegans* IFT56 might function together with IFT70 (DYF-1) in docking and activation of the homodimeric OSM-3 kinesin-II motor onto the IFT-B complex (Ou et al., 2005a; 2007) although a direct interaction could not be observed yet.

Mutations in fleer, the zebrafish homolog of IFT70, lead to defects in the structure of cilia combined with reduced tubulin glutamylation and glycylation (Pathak et al., 2011; 2007). This could imply a role for IFT70 in transporting tubulin or tubulin-modifying enzymes into cilia but the exact molecular basis for this phenomenon is not understood yet.

A breakthrough in cilia research was the discovery that IFT88 is homologous to the mouse protein polaris (encoded by the gene Tg737) (Pazour et al., 2000). Hypomorphic mutations in the Tg737 gene (*orpk* mice) lead to the assembly of stumpy cilia but the mice died shortly after birth due to the occurrence of PKD (Moyer et al., 1994; Pazour et al., 2000) (see section 1.2.2). Furthermore, Tg737$^{-/-}$ mice (*flexo/polaris* mice) die at embryonic stages, showing defective Shh and loss of nodal cilia, which are important for correct left-right-axis determination during embryogenesis (Huangfu et al., 2003; Murcia et al., 2000) (see section 1.2.1). *Cr*IFT88 mutants lost their ability to assembly cilia, leading to a bald phenotype (Pazour et al., 2000), pointing to an important function of IFT88 in *Chlamydomonas reinhardtii* ciliogenesis as well. In *C.elegans* and *Drosophila*, the orthologs of IFT88 are absolutely required for the formation of cilia on the dendritic tips of sensory neurons (Han et al., 2003; Haycraft et al., 2001).

1.4.2.3) IFT-B proteins IFT52 and IFT46

For IFT52 and IFT46 only α-helical regions at the very C-terminus are predicted, as well as a GIFT [for GldG, intraflagellar transport (IFT)] domain at the N-terminus of IFT52 (Taschner et al., 2012). The GIFT domain is suggested to bind to oligosaccharides (Beatson and Ponting, 2004) but this function could not be verified so far (Taschner et al., 2011). As already mentioned above, interactions studies with recombinant proteins in *Chlamydomonas reinhardtii* revealed that IFT88/70/52/46 forms a stable subcomplex within the 'IFT-B core' (Taschner et al., 2011). Notably, the middle and C-terminal part of IFT52 directly interacts with the second 'IFT-B core' subcomplex IFT81/74/27/25 (Taschner et al., 2011). The recently published crystal structures of *Cr*IFT70/52 and *Tt*52/46 (Taschner et al., 2014) strikingly show that IFT52 and IFT46 are key factors for IFT-B complex stability (figure 10). The heterodimer *Tt*IFT52/46 consists of α -helices tightly packed against each other. Therefore, it is unlikely that one of the proteins alone can constitute a domain with a stable conformation on its own. Due to the solved crystal structure and pull down experiments with recombinantly expressed proteins it was concluded that a stable IFT52/46 complex is necessary to assembly the entire 'IFT-B core' (Taschner et al., 2014). This was already assumed earlier due to reduced numbers of IFT-B particles in *Cr*IFT46 mutants (Hou et al., 2007; Richey and Qin, 2012) and the complete loss of cilia in *Cr*IFT52 mutants (Brazelton et al., 2001; Deane et al., 2001) most likely due to the inability to assemble the IFT-B complex (Richey and Qin, 2012).

In the *Chlamydomonas reinhardtti* suppressor strain $\mathrm{Sup}_{\mathrm{ift46}}1$ (a C-terminal fragment of IFT46 is still expressed), an unstable IFT-B complex is still formed (Richey and Qin, 2012) but ODAs were not detectable within cilia (Hou et al., 2007). Furthermore, yeast-2-hybrid and pull down assays revealed a direct interaction between IFT46 and ODA16 (Ahmed et al., 2008). Therefore, it is thought that ODA16 serves as an adaptor protein coupling the IFT machinery to ODAs to transport them into cilia (Ahmed et al., 2008; Hou et al., 2007).

1.4.2.4) IFT-B proteins IFT81, IFT74, IFT57, IFT54, FAP22 (IFT38) and IFT20

The six proteins IFT81, IFT74, IFT57, IFT54, FAP22 and IFT20 are predicted to contain coiled coil structures (Taschner et al., 2012), likely to mediate protein-protein interactions. It has been shown that IFT81 and IFT74 directly interact with each other via their coiled coil regions and also form a stable subcomplex with IFT27/25 within the 'IFT-B core' (Lucker et al., 2005; Taschner et al., 2011). Furthermore, IFT81 is able to interact with itself and IFT74 in yeast-2-hybrid assays, leading to the assumption of an $\mathrm{IFT}(81)_2/(74)_2$ heterotetramer (Lucker et al., 2005). However, reconstitution of the 'IFT-B core' nonamer IFT88/81/74/70/52/46/27/25/22 by using recombinantly expressed proteins indicates only one copy of each protein (Bhogaraju et al., 2013a; Taschner et al., 2014). Interaction partners of FAP22 (hereafter referred to as IFT38 (Nachury, 2014), following the standard MW-based nomenclature of IFT proteins in *Clamydomonas reinhardtti* (Cole et al., 1998; Rosenbaum and Witman, 2002)) are unknown so far. An interaction of IFT20 and IFT54 could be observed by immunoprecipitation (Follit et al., 2009) and yeast-2-hybrid assay (Omori et al., 2008). Co-immunoprecipitation and yeast-2-hybrid assays (Baker et al., 2003; Krock and Perkins, 2008) also indicate an interaction between IFT20 and IFT57. However, Lucker and colleagues could not confirm the interaction between IFT20 and IFT57 by performing yeast-2-hybrid assay and co-expression (Lucker et al., 2010). Therefore, the IFT20/57 interaction is still controversial. This is also the case for the reported interaction between IFT20 and KIF3B, a subunit of the anterograde heterotrimeric kinesin-II IFT motor, observed in co-immunoprecipitations and yeast-2-hybrid assays (Baker et al., 2003), because later pull down studies could not validate this interaction (Follit et al., 2006). Additionally, Keady and colleagues identified an interaction between IFT20 and rhodopsin/opsin leading to the notion that IFT20 may directly bind certain ciliary cargos (Keady et al., 2011). In line with this, deletion of IFT20 in cone photoreceptor cells leads to accumulation of rhodopsin/opsin at the Golgi complex (Keady et al., 2011). Additional studies are necessary to shed more light on IFT20 and its binding partners identified so far to elucidate the exact role of IFT20 within the IFT process.

One hint about the role of IFT20 came from the discovery that IFT20 is not only found around the basal body of cilia and within cilia like other IFT proteins but is also present at the Golgi (Cole et al., 1998; Deane et al., 2001; Follit et al., 2006; 2009). IFT20 is located at the Golgi complex (Follit et al., 2006; 2009) by interaction with the golgin GMAP210 (Follit et al., 2008). This finding led to the assumption that IFT20 may serve as a key player linking membrane protein maturation at the Golgi to IFT. The reported interactions of IFT20 with IFT54 (see above) indicate that IFT54 forms a bridge between Golgi-IFT20 and the IFT-B complex. This assumption is supported by the unique property of IFT54 in displacing IFT20 from the Golgi complex (Follit et al., 2009). RNAi induced strong depletion of IFT20 in RPE cells blocks cilia assembly, whereas moderate depletion in NRK epithelial cells leads to a reduced amount of PKD-2 (Follit et al., 2006), a Ca^{2+} channel located in the ciliary membrane and main player in PKD (Pazour et al., 2002; Vassilev et al., 2001) (see section 1.2.2). Furthermore, in GMAP210 deficient mouse embryonic kidney cells, IFT20 is not localized to the Golgi complex anymore and cilia are shorter, displaying reduced amounts of PKD-2 (Follit et al., 2008). These findings indicate that IFT20 and GMAP210 function together in the transport of membrane proteins from the Golgi to the base of the cilium.

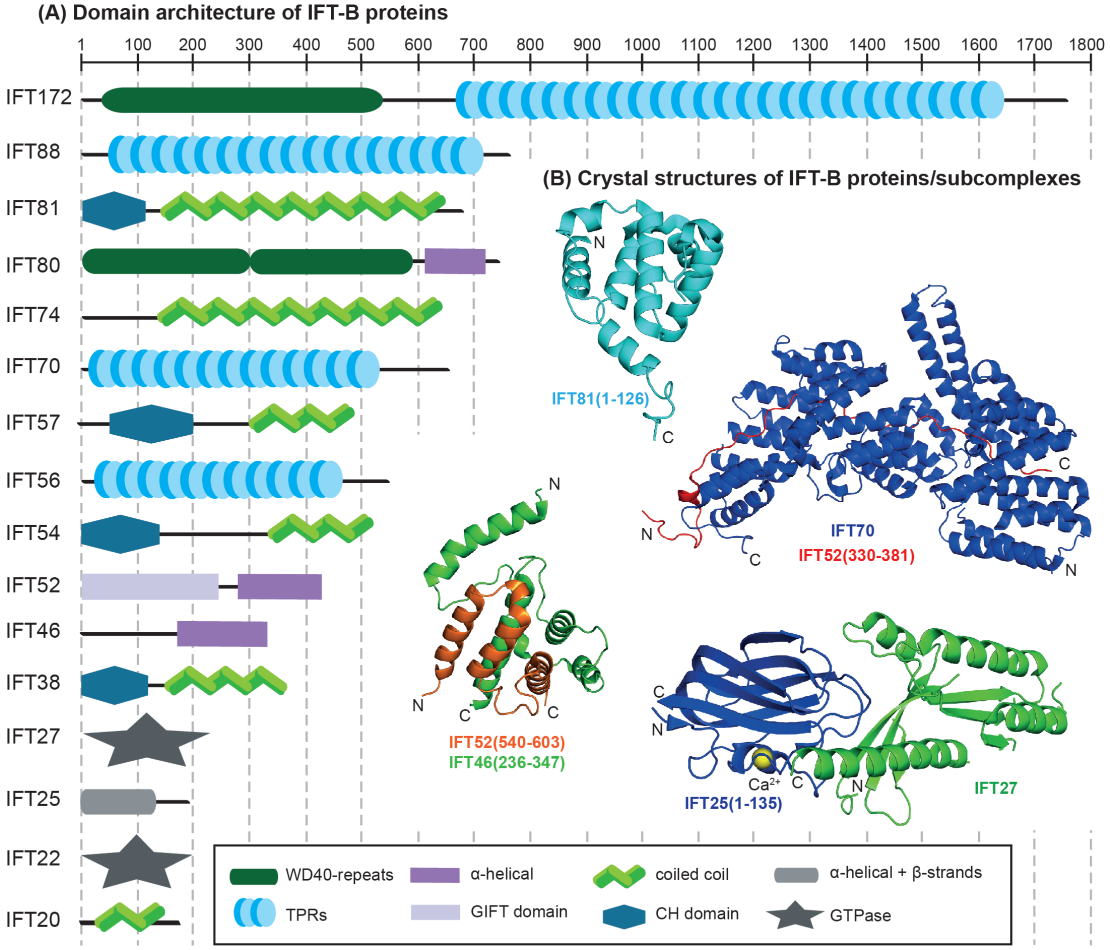

Figure 10: (A) Domain architecture of the Chlamydononas reinhardtii IFT-B proteins known to date. (B) Available crystal structures of different parts of the IFT-B complex (pdb ID is indicated in brackets): CrIFT25$_{1\text{-}135}$/27 complex (2YC2, 2YC4) (Bhogaraju et al., 2011), CrIFT81$_{1\text{-}126}$ (4LVP, 4LVR) (Bhogaraju et al., 2013a), CrIFT70/52$_{330\text{-}381}$ complex (4UZY), TtIFT52$_{540\text{-}603}$/46$_{236\text{-}347}$ complex (4UZZ) (Taschner et al., 2014).

IFT54 (DYF-11 in *C.elegans*) undergoes IFT presumably as part of the IFT-B complex (Kunitomo and Iino, 2008; Omori et al., 2008). Furthermore, exploring different deletion mutants of IFT54 in *C.elegans* revealed that the C-terminal coiled coil region is sufficient for proper localization and ciliogenesis (Kunitomo and Iino, 2008). Knock out of IFT54 in mice is embryonic lethal (Berbari et al., 2011), pointing to an important function of IFT54 during development. Morpholino knock down of IFT54 (elipsa in zebrafish) causes phenotypes typical for ciliary defects (Omori et al., 2008). The same authors reported a direct interaction between IFT54 and rabaptin-5, which in turn binds to Rab8. This small GTPase is thought to be involved in transport of vesicles to the cilium and fusion of these vesicles with the plasma membrane at the base of the cilium (Moritz et al., 2001; Nachury et al., 2007), indicating that IFT54 serves as a bridge to IFT.

In *C.elegans* IFT57 (CHE-13) undergoes IFT while the *che-13* mutants show defects in ciliogenesis (Haycraft et al., 2003; Perkins et al., 1986). Furthermore, IFT57 is a homolog of HIPPI in mammals, which in turn binds to Huntington-interacting protein 1 (HIP-1), a protein that might be relevant for the pathogenesis of Huntington's disease (Gervais et al., 2002). HIPPI deficient mice die at embryonic stages with detectable defects in nodal cilia, left-right patterning and Shh signaling (Houde et al., 2006), but the molecular mechanisms of IFT57 still have to be explored.

IFT38 (also known as FAP22 (*Clamydomonas reinhardtii*), DYF-3 (*C.elegans*), Qilin (zebrafish), Cluap1 (mammals), PIFTA1 (*Trypanosoma brucei*)) can be pulled down from zebrafish lysate with other IFT-B proteins using TAP-IFT54-GFP (Omori et al., 2008). Furthermore, IFT38 undergoes IFT in *C.elegans* (Ou et al., 2005b) and time-lapse fluorescence microscopy revealed a total loss of IFT in IFT38 deficient worms (Ou et al., 2005b). RNAi mediated knockdown of IFT38 in *Trypanosoma brucei* revealed its importance for proper ciliogenesis (Absalon et al., 2008). Furthermore, proteomic analysis of isolated *Trypanosoma brucei* flagella identified amongst several IFT proteins, tubulin, radial spokes, ODAs and IDAs also IFT38 (Subota et al., 2014). In mammals, Cluap1 is mainly localized at the base and tip of cilia whereas *Cluap1*$^{-/-}$ mice have no ciliated node cells, show repressed Shh signaling and die at embryonic stages (Botilde et al., 2013; Pasek et al., 2012). These findings led to the hypothesis that IFT38 is involved in ciliogenesis as part of the IFT-B complex but the exact function of IFT38 remains elusive.

Bioinformatics analysis predicted an α-helical domain in the N-terminal region of IFT81, IFT57, IFT54 (Taschner et al., 2012) and IFT38 (Schou et al., 2014). Using the HHPred algorithm (Soding et al., 2005), the domain showed similarity to Calponin Homology (CH) domains (IFT81: $E=2.2 \times 10^{-2}$, IFT54: $E=2 \times 10^{-57}$, IFT57: $E=7$, IFT38: $E=0.034$). Determining the high-resolution structure of the N-terminal domain of IFT81 indeed revealed a CH domain fold (Bhogaraju et al., 2013a) (figure 10). The CH domain is often found in MT and/or actin binding proteins, like the MT-plus-end-tracking protein EB1 (Hayashi and Ikura, 2003), Ndc80 that is involved in kinetochore-MT attachment during cell division (Ciferri et al., 2008) and actinin-4, important for cytoskeleton scaffolding and organization (Lee et al., 2008b). In line with this structure prediction, Ling and colleagues could show that the N-terminal part of the human orthologue of IFT54 (MIP-T3/TRAF3IP1) interacts with MTs in a MT-cosedimentation assay (Ling and Goeddel, 2000). Further experiments indicated this region of MIP-T3 also binds to tubulin (Ling and Goeddel, 2000). Additionally, overexpressing MIP-T3 in HEK293 cells followed by LC-MS/MS analysis identified amongst others tubulin and actin as binding partners of MIP-T3 (Guo et al., 2010). Taken together, these findings may indicate a role for the N-terminal domain of IFT54 in tubulin transport to construct the cilium. If the putative CH domains in IFT57 and IFT38 also function as MT and/or actin binding domains still have to be elucidated. In contrast, the CH domain in IFT81 has already been shown to serve together with IFT74 as a tubulin-binding module. Whereas the CH domain in IFT81 binds selectively to the globular domain of tubulin, IFT74 provides a positively charged stretch of residues attaching to the negatively charged E-hooks of tubulin to strengthen the binding (Bhogaraju et al., 2013a).

1.4.2.5) IFT-B proteins IFT172 and IFT80

IFT172 is the largest member of the IFT-B proteins. It has similar domain architecture to IFT-A proteins (see section 1.4.1); WD40-repeats at the N-terminal region followed by α-helical TPRs (Taschner et al., 2012) pointing to a relationship with components of COPI- and clathrin-coated vesicles (Devos et al., 2004; Jékely and Arendt, 2006; van Dam et al., 2013). The other IFT protein with two predicted WD40 β-propellers at the very N-terminus followed by a α-helical solenoid tail is IFT80 (Taschner et al., 2012).

In zebrafish, IFT172 was identified (amongst IFT81, IFT57 and IFT38) in a mutagenesis screen as a cause of PKD, a well-known cilium-related disease (Sun et al., 2004). Co-immunoprecipitation and GST-pull down experiments revealed an interaction of IFT172 with EB1, a MT-plus-end-tracking protein, at the ciliary tip (Pedersen et al., 2003; 2005). This interaction is also observed independently of other IFT proteins pointing to a possible role of IFT172 and EB1 in remodeling the IFT particle between anterograde and retrograde transport at the ciliary tip (Pedersen et al., 2005). This hypothesis is strengthened by the finding in *Chlamydomonas reinhardtti* that *fla11* (encodes IFT172) mutants at the restrictive temperature show an accumulation of IFT particles at the ciliary tip, pointing to an involvement of IFT172 in retrograde transport (Iomini et al., 2001). A similar phenotype has also been observed in *Tetrahymena thermophila* (Tsao and Gorovsky, 2008). Co-immunoprecipitations in *Chlamydomonas reinhardtii* revealed an interaction between IFT172 and cytoplasmic dynein 2 independent of IFT (Pedersen et al., 2006). Furthermore, IFT172 is required for the entry of the retrograde motor dynein 2 into the ciliary compartment (Pedersen et al., 2006; Williamson et al., 2012). Mutations in mouse IFT172 (*wimple*) are embryonic lethal, showing characteristic phenotypes of defective Shh signaling (Huangfu et al., 2003).

Knocking out IFT80 in *Tetrahymena thermophila* or *C.elegans* leads to defects in ciliogenesis (Beales et al., 2007; Fujiwara et al., 1999; Perkins et al., 1986). Furthermore, mutations in IFT80 cause JATD (see section 1.4.1.2), a severe human disease resulting in infancy death (Beales et al., 2007). This is in line with observations in IFT80 deficient zebrafish, demonstrating phenotypes like cystic kidneys and photoreceptor degeneration, typical for JATD (Beales et al., 2007; Hudak et al., 2010). Mice with a hypomorphic mutation in IFT80 show a high percentage of embryonic lethality pointing to an important function of IFT80 during development, whereas the postnatal survivors did not show any discernable phenotype. MEF cells established from these mice revealed an impaired activation of Shh signaling but had no defects in cilia assembly (Rix et al., 2011). A possible reason could be that the IFT80 level necessary for ciliogenesis is masked by the hypomorphic expression in this cell line. It is therefore very likely that a knock out of IFT80 will show a total loss of ciliation and complete embryonic lethality like other IFT proteins (see above IFT172, IFT88) (Rix et al., 2011).

Taken together, almost all of the IFT-B proteins consist of multiple domains. Most of these domains mediate protein-protein interactions within the IFT-B complex. Furthermore, it has been extensively shown that IFT is absolutely required for the assembly and maintenance of cilia in various organisms. But the exact mechanism of how IFT proteins recognize and bind ciliary cargo is largely unknown. Therefore, further biochemical and structural studies are required to gain more insights into the functions of the individual domains in the IFT proteins and therefore in the IFT process.

1.5) Transport of proteins to the cilium

Compared with other trafficking routes the knowledge of the transport to the cilium is still in its infancy. As already mentioned in section 1.3 cilia are devoid of ribosomes, thus all proteins destined for cilia have to be transported to the cilium. Membrane proteins such as ion channels and signaling receptors destined for the ciliary membrane have to be synthesized in the endoplasmic reticulum and processed in the Golgi complex. After maturation, the proteins undergo vesicle-mediated transport to the base of the cilium where the vesicles fuse with the ciliary membrane (Nachury et al., 2010). Coat formation is a conserved mechanism in cells to ensure sorting and transport of proteins from a donor to an acceptor membrane (Dacks and Field, 2007). Small GTPases of the Rab and ADP-ribosylation factor (Arf) family are known to play important roles in intracellular membrane trafficking (Gillingham and Munro, 2007; Leroux, 2007).

Vesicle budding at the trans Golgi network (TGN) is mediated through ciliary targeting complexes, comprised of the small GTPases Rab11 and Arf4, the Arf GAP ASAP1, the Rab11/Arf effector FIP3 (Rab11 family-interacting protein 3) and Rabin8, the GEF for Rab8 and effector of Rab11 (Knodler et al., 2010; Mazelova et al., 2009; Sung and Leroux, 2013; Wang et al., 2012). Respectively, at the TGN, Arf4 directly binds the ciliary targeting motif (CTM) VxPx of rhodopsin (Sung et al., 1994; Tam et al., 2000) and thus ensures the correct sorting of rhodopsin to vesicles destined for cilia (Deretic et al., 2005). After recruitment of FIP3, which binds simultaneously to Rab11 and Arfs (Shiba et al., 2006), and ASAP1 that directly interacts with Rab11 and FIP3 (Inoue et al., 2008; Mazelova et al., 2009) vesicle budding is initiated (Mazelova et al., 2009). Whereat the exact chronology of protein recruitment as well as the interactions between the proteins are not completely understood yet. The budding process is further supported by the BAR (Bin/amphiphysin/Rvs) domain at the N-terminus of ASAP1 which induces membrane curvature (Nie et al., 2006; Peter et al., 2004). Furthermore, GTP-loaded Rab11 interacts with Rabin8 and stimulates its GEF activity towards Rab8 that in turn promotes docking and fusion of the vesicles with the plasma membrane at the base of the cilium (Knodler et al., 2010; Moritz et al., 2001; Nachury et al., 2007; Westlake et al., 2011). Reaching the ciliary compartment, the membrane proteins are transported with the IFT machinery to their destined position. In line with this, Rab8 interacts with BBS proteins (Nachury et al., 2007) and binds rabaptin-5, which in turn interacts with IFT54 at the basal body (Omori et al., 2008), thus probably linking vesicular to intraciliary trafficking.

Furthermore, it has been shown that the BBSome complex undergoes IFT and it was therefore proposed to serve as an adaptor between the IFT complex and IFT cargo (Blacque et al., 2004; Lechtreck et al., 2009a; Nachury et al., 2007). In line with this, the BBSome as well as the IFT-A complex are crucial for the transport of several membrane proteins into and/or out of the cilium (Berbari et al., 2008b; Liem et al., 2012; Mukhopadhyay et al., 2010). In addition, due to the predicted similar domain architecture of several IFT-A and BBSome proteins to components of COPI- and clathrin-coated vesicles (Devos et al., 2004; Jékely and Arendt, 2006; van Dam et al., 2013), it is assumed that the IFT-A and BBSome complexes either polymerize into flat coats to cluster membrane proteins or they bud of cargo-containing vesicles that fuse with the ciliary membrane (Nachury et al., 2010). One possibility could be the recognition of selective CTMs probably via the predicted WD40-repeats in several IFT-A and BBSome proteins, a property known from clathrin-mediated transport (Haar et al., 2000). Jin and colleagues indeed could demonstrate that the BBSome assembles in a coat and directly recognizes the CTM of somatostatin receptor 3 (Sstr3) that is then transported to the ciliary membrane (Jin et al., 2010). The CTM of Sstr3 ((F/Y/W)/R motif) is conserved in several ciliary GPCRs including rhodopsin, serotonin receptor 6 (Htr6) and the olfactory receptor proteins ODR-10 and STR-1 (Brailov et al., 2000; Corbit et al., 2005; Dwyer et al., 2001; Händel et al., 1999). Deletion of the (F/Y/W)/R motif in *C. elegans* ORD-10 and STR-1 resulted in trapped proteins in the cell body (Dwyer et al., 2001). The same CTM was also identified in mammalian Smo. Mutation of this motif prevents ciliary location and activity of Smo in zebrafish embryos and cultured cells (Corbit et al., 2005). However, carefully examination of the high-resolution structure of rhodopsin (Palczewski et al., 2000) reveals that the FR motif (Phe^{313} Arg^{314}) is buried in the hydrophobic core of the short amphipatic helix VIII and thus probably necessary for proper protein folding. Therefore, the question arises if the dislocation of GPCRs after mutating the (F/Y/W)/R motif is rather a cause of structural impairments of the proteins than in ciliary targeting.

Further localization experiments with different fragment of Sstr3 and Htr6 revealed that the third intracellular loop of these GPCRs is sufficient for ciliary localization.

Sequence comparison of this region of Sstr3 and Htr6 with all known human GPCRs identified a consensus sequence of Ax(S/A)xQ. Mutation of the conserved alanine or glutamine in this motif resulted in mislocalization of Sstr3 and Htr6 (Berbari et al., 2008a).

The CTMs mentioned above have been identified only in a few membrane proteins located in the ciliary membrane. Due to the high abundance of proteins in the ciliary membrane, targeting of these proteins to the ciliary compartment seems to be more complex. Either additional, yet unidentified CTMs are present in ciliary proteins or different recognition methods exist to target membrane proteins to the ciliary compartment.

Even less is known about the ciliary transport of soluble proteins like tubulin and radial spoke proteins, after their synthesis at free polysomes. Elegant work in *Chlamydomonas reinhardtii*, combining biochemical characterization of vesicles containing ciliary cargo and *in situ* localization of ciliary proteins on these vesicles by using gold labeling and electron microscopy revealed new insights into this topic (Wood and Rosenbaum, 2014). The authors were able to detect amongst others the membrane protein PKD-2 (see section 1.2.2) as well as radial spoke proteins, IFT46 and tubulin at the outside surface of vesicles destined for cilia and proposed a model in which the cell couples the transport of axonemal and membrane components to the ciliary compartment. This is in line with previous studies reporting an association of IFT proteins (IFT140, IFT88, IFT57, IFT52 and IFT20) with cytoplasmic vesicles in photoreceptor cells and retinal neurons of mice (Sedmak and Wolfrum, 2010; 2011).

Furthermore, it has been shown that tubulin directly binds to the IFT complex (Bhogaraju et al., 2013a). In addition, there is evidence that radial spokes, ODAs and motor proteins also serve as IFT cargo (Hou et al., 2007; Johnson and Rosenbaum, 1992; Qin et al., 2004; Scholey, 2012). In the C-terminal tail of the homodimeric anterograde IFT motor KIF-17 the KRKK motif was identified as a CTM (Dishinger et al., 2010; Scholey, 2008). Furthermore, KIF-17 interacts with the nuclear import protein importin-β2 pointing to a relationship to nuclear localization signals. Gradients of importin-β2 and the small GTPase Ran are crucial for the entry of KIF-17 into the ciliary compartment and therefore play important roles in ciliogenesis (Dishinger et al., 2010; Fan et al., 2011).

Taken together, all the findings mentioned above indicate an involvement of IFT proteins not only in cilia assembly and maintenance but also in cell trafficking processes although a direct link between the IFT machinery and CTMs of ciliary proteins have not been identified so far. It is plausible that ciliary cargo may compete via their CTMs at more generic binding sites. In contrast, high abundant proteins in cilia, like tubulin, dynein arms and radial spokes most likely have dedicated binding sites on the IFT complex (like the CH domain in IFT81 (Bhogaraju et al., 2013a)) to ensure efficient delivery to the tip of growing cilia. Future research is required for a more complete understanding of the direct interactions between the IFT complex and ciliary cargo.

1.6) Aim of the thesis

To date a lot of information is available concerning the process of IFT in various model organisms, like *Chlamydomonas reinhardtii*, *C.elegans* and mouse. But mutational analysis or knock out of the IFT proteins *in vivo* often resulted in common phenotypes, making it impossible to assign specific functions of individual IFT proteins. Therefore, it is essential to put more effort in the characterization of the molecular mechanisms underlying the IFT process. One strategy is the determination of high-resolution structures of IFT proteins. One advantage of high-resolution structures is the possibility to determine the exact boundaries of domains or specific mutations in protein-protein interfaces or possible cargo/adaptor binding sites. Introducing point mutations or deleting entire domains *in vitro* will give more detailed insights into the IFT complex organization as well as the entire IFT process. To date, only few direct interactions have been reported between IFT proteins and ciliary cargoes: IFT81/74-tubulin (Bhogaraju et al., 2013a), IFT88-MRJ (Bhowmick et al., 2009) and IFT46-ODA16 (Ahmed et al., 2008).

The study described in this thesis aimed at understanding the role of the IFT-B proteins IFT57, IFT54, IFT38 and IFT20 within the IFT process. Therefore, the expression and purification protocols of the four IFT proteins had to be established. Furthermore, the predicted CH domains in IFT57, IFT54 and IFT38 were characterized using a combination of biochemical and biophysical approaches. In addition, the high-resolution structure of the CH domain of IFT54 was obtained.

2) Results

2.1) Chapter I

‘Molecular Basis of Tubulin Transport Within the Cilium by IFT74 and IFT81’

ensuring that multiple genes have precisely timed transcription starts and sufficient levels of activation (*21*).

The ancestral roles of the mammalian pluripotency control factors Pou5f1 and Sox2 during the early development of nonmammalian vertebrates have long been a mystery (*28*). Our results show that the composition of post-MBT Pou5f1 and Sox2 binding sites, co-occupancy with Nanog, their chromatin state, and Pol II binding are similar in zebrafish embryos and mammalian ES cells (fig. S13 and supplementary text). Thus, the ancestral function of the pluripotency factors is zygotic gene activation and developmental timing control in the early vertebrate embryo. In a sense, it is a first major reprogramming event from transcriptionally silent cleavage-stage cells to pluripotent post-MBT blastomeres. In this context, Pou5f1 and Sox2 contribute to all main embryonic regulatory pathways. Considered together with the orthology of target gene sets, the zygotic priming-activation-timing mechanism may have evolved to control the cell pluripotency state in mammalian development.

References and Notes

1. W. Tadros, H. D. Lipshitz, *Development* **136**, 3033–3042 (2009).
2. A. J. Giraldez *et al.*, *Science* **312**, 75–79 (2006).
3. H. L. Liang *et al.*, *Nature* **456**, 400–403 (2008).
4. J. R. ten Bosch, J. A. Benavides, T. W. Cline, *Development* **133**, 1967–1977 (2006).
5. R. Satija, R. K. Bradley, *Genome Res.* **22**, 656–665 (2012).
6. C. Y. Nien *et al.*, *PLoS Genet.* **7**, e1002339 (2011).
7. E. Z. Kvon, G. Stampfel, J. O. Yáñez-Cuna, B. J. Dickson, A. Stark, *Genes Dev.* **26**, 908–913 (2012).
8. M. M. Harrison, X. Y. Li, T. Kaplan, M. R. Botchan, M. B. Eisen, *PLoS Genet.* **7**, e1002266 (2011).
9. D. A. Kane, C. B. Kimmel, *Development* **119**, 447–456 (1993).
10. C. Xu *et al.*, *Dev. Cell* **22**, 625–638 (2012).
11. H.-G. Belting *et al.*, *Development* **128**, 4165–4176 (2001).
12. Y. Okuda *et al.*, *Dev. Dyn.* **235**, 811–825 (2006).
13. Y. Okuda, E. Ogura, H. Kondoh, Y. Kamachi, *PLoS Genet.* **6**, e1000936 (2010).
14. X. Chen *et al.*, *Cell* **133**, 1106–1117 (2008).
15. J. Kim, J. Chu, X. Shen, J. Wang, S. H. Orkin, *Cell* **132**, 1049–1061 (2008).
16. Y. H. Loh *et al.*, *Nat. Genet.* **38**, 431–440 (2006).
17. K. Lunde, H. G. Belting, W. Driever, *Curr. Biol.* **14**, 48–55 (2004).
18. G. Reim, M. Brand, *Development* **133**, 2757–2770 (2006).
19. G. Reim, T. Mizoguchi, D. Y. Stainier, Y. Kikuchi, M. Brand, *Dev. Cell* **6**, 91–101 (2004).
20. H. G. Belting *et al.*, *Dev. Biol.* **356**, 323–336 (2011).
21. D. Onichtchouk *et al.*, *Mol. Syst. Biol.* **6**, 354 (2010).
22. I. Papatsenko, M. Levine, D. Papatsenko, *Bioinformatics* **26**, 2731–2736 (2010).
23. H. Aanes *et al.*, *Genome Res.* **21**, 1328–1338 (2011).
24. M. Lagha, J. P. Bothma, M. Levine, *Trends Genet.* **28**, 409–416 (2012).
25. L. C. Lindeman *et al.*, *Dev. Cell* **21**, 993–1004 (2011).
26. R. H. Morley *et al.*, *Proc. Natl. Acad. Sci. U.S.A.* **106**, 3829–3834 (2009).
27. Z. Liu *et al.*, *J. Biol. Chem.* **286**, 28520–28532 (2011).
28. B. Fernandez-Tresguerres *et al.*, *Proc. Natl. Acad. Sci. U.S.A.* **107**, 19955–19960 (2010).
29. C. Y. McLean *et al.*, *Nat. Biotechnol.* **28**, 495–501 (2010).

Acknowledgments: We thank S. Shvartsman for scientific discussion; S. Arnold, G. Pyrowolakis, V. Taylor, A. Fuchs, S. Eckerle, and M. Fernandes for comments; B. Wendik and J. Paddeken for participating in initial stages of this work; Y. Kamachi for Sox3/19a/19b antibody; L. Yampolsky for help with statistics; and S. Götter for fish care. Supported by Deutsche Forschungsgemeinschaft grants DFG-EXC294 and DFG-SFB592 (W.D. and D.O.) and Bundesministerium für Bildung und Forschung grant BMBF-0313921FRISYS (W.D.). Microarray and ChIP-Seq data GEO (www.ncbi.nlm.nih.gov/geo) accession numbers: CHIP-seq data, GSE39780; microarray data, GSE41107, GSE17655, and GSE17656.

Supplementary Materials
www.sciencemag.org/cgi/content/full/science.1242527/DC1
Materials and Methods
Supplementary Text
Figs. S1 to S13
Tables S1 to S10
References (*30*–*56*)

28 June 2013; accepted 31 July 2013

10.1126/science.1242527

Molecular Basis of Tubulin Transport Within the Cilium by IFT74 and IFT81

Sagar Bhogaraju,[1] Lukas Cajanek,[2] Cécile Fort,[3] Thierry Blisnick,[3] Kristina Weber,[1] Michael Taschner,[1] Naoko Mizuno,[1] Stefan Lamla,[4]* Philippe Bastin,[3] Erich A. Nigg,[2] Esben Lorentzen[1]†

Intraflagellar transport (IFT) of ciliary precursors such as tubulin from the cytoplasm to the ciliary tip is involved in the construction of the cilium, a hairlike organelle found on most eukaryotic cells. However, the molecular mechanisms of IFT are poorly understood. Here, we found that the two core IFT proteins IFT74 and IFT81 form a tubulin-binding module and mapped the interaction to a calponin homology domain of IFT81 and a highly basic domain in IFT74. Knockdown of IFT81 and rescue experiments with point mutants showed that tubulin binding by IFT81 was required for ciliogenesis in human cells.

Cilia are microtubule-based organelles that function in motility, sensory reception, and signaling (*1*). Ciliary dysfunction results in numerous diseases and disorders commonly known as ciliopathies. Intraflagellar transport (IFT) is involved in cilium formation (*2*, *3*) but also functions in other cellular processes, such as the recycling of T cell receptors at the immune synapse (*4*). IFT relies on kinesin-2 and IFT-dynein molecular motors moving along the microtubule-based axoneme of cilia (*5*–*7*) and on the IFT complex, which contains at least 20 different protein subunits. Although ~600 proteins are known to reside in the cilium (*8*), we know very little about how they are recognized as ciliary cargo by the IFT machinery (*9*–*11*).

To identify potential cargo-binding sites on the IFT complex, we carried out bioinformatical and biochemical screening and identified conserved domains that were not required for IFT complex formation. We reasoned that such domains could protrude from the IFT particle-core structure and would thus be in a prime position for cargo recognition. The two IFT core proteins IFT74 and IFT81 were found to possess N-terminal domains (IFT74N and IFT81N) that were not required for IFT complex formation or stability (fig. S1). Whereas IFT81N is highly conserved in sequence and predicted to be a folded domain, IFT74N was likely to be disordered and was highly basic with an isoelectric point (pI) > 12 (fig. S2). To characterize the properties of IFT74N and IFT81N, we purified recombinant *Homo sapiens* (Hs) IFT81N, *Chlamydomonas reinhardtii* (Cr) IFT81N, and a truncated HsIFT74/81 heterodimeric complex (fig. S3) (IFT74N alone degraded rapidly and could not be purified) and determined the crystal structure of CrIFT81N (Fig. 1, A to C; fig. S4, A to D; and table S1). The crystal structure revealed that IFT81N adopts the fold of a calponin homology (CH) domain with unexpected structural similarity to the kinetochore complex component NDC80 with microtubule (MT)–binding properties (*12*). Given that the cilium consists of a MT-based axoneme, IFT of large quantities of tubulin is required for cilium formation (*13*). We thus tested the tubulin-binding properties of HsIFT81N using affinity pull-downs (Fig. 1D and fig. S4E) and microscale thermophoresis (MST) with unpolymerized bovine αβ-tubulin (Fig. 1, E and F). HsIFT81N bound tubulin with a dissociation constant (K_d) of 16 μM via a highly conserved, positively charged surface patch, which was enhanced 18-fold by IFT74N (Fig. 1G and fig. S3). Because this result was unexpected, we also carried out MT sedimentation assays and electron microscopy (EM) to visualize IFT81 or IFT74/81 bound to MT (fig. S5). The IFT74/81 complex,

---

[1] Department of Structural Cell Biology, Max Planck Institute of Biochemistry, Am Klopferspitz 18, D-82152 Martinsried, Germany. [2] Biozentrum, University of Basel, Klingelbergstrasse 50/70, CH-4056 Basel, Switzerland. [3] Trypanosome Cell Biology Unit, Institut Pasteur and CNRS URA2581, 25 Rue du Docteur Roux, 75015 Paris, France. [4] Department of Cell Biology, Max Planck Institute of Biochemistry, Am Klopferspitz 18, D-82152 Martinsried, Germany.

*Present address: Anni-Albers-Straße 11, D-80807 München, Germany.

†Corresponding author. E-mail: lorentze@biochem.mpg.de

but not IFT81N, at low μM concentration cosedimented with MT during ultracentrifugation (fig. S5, D and E) and decorated MT (fig. S5F). Thus, the tubulin-binding module is formed by the IFT74/81 complex rather than by IFT81N alone.

To dissect the binding mode in the IFT74/81:αβ-tubulin complex, samples were prepared from MT and unpolymerized αβ-tubulin lacking the highly acidic C-terminal tails, often referred to as E-hooks (*12*) (fig. S5A). αβ-tubulin lacking E-hooks had similar affinity for IFT81N as intact tubulin (fig. S5, B and C), which suggested that IFT81N recognizes the globular domain of αβ-tubulin with no substantial interaction with the E-hooks. IFT74/81 displayed robust MT binding in sedimentation assays, which was, however, reduced to background levels in the absence of the β-tubulin E-hook (fig. S5E). Thus, IFT81N appears to bind the globular domain of tubulin to provide specificity, and IFT74N recognizes the β-tubulin tail to increase affinity (Fig. 1H).

To examine the role of tubulin binding by IFT74/81 in a cellular system, we transiently expressed Flag-HsIFT81 or Flag-HsIFT81ΔN in human RPE-1 cells and induced formation of primary cilia either by treatment with 0.5 μM cytochalasin D (Fig. 2) (*14*) or serum starvation (fig. S6, A and D). In these experiments, centrioles were visualized by staining for CAP350 and cilia by staining for the small guanosine triphosphatase Arl13b or acetylated tubulin. We detected both Flag-HsIFT81 and Flag-HsIFT81ΔN at the tip of the primary cilium and, to a minor extent, also along the axoneme (fig. S6A), suggesting that IFT81N is not required for the transport of IFT81 within the primary cilium. Remarkably, however, the expression of Flag-HsIFT81ΔN had a strong negative impact on the extent of ciliogenesis (fig. S6, B to D), suggesting that excess IFT81ΔN caused a dominant-negative effect, presumably through formation of IFT complexes unable to bind tubulin.

To further investigate the function of the tubulin-binding domain of IFT81 in ciliogenesis, we carried out small interfering RNA (siRNA)–rescue experiments. siRNA-mediated depletion of IFT81 (fig. S6E) strongly reduced the percentage of ciliated cells (Fig. 2), which could be rescued by coexpression of an siRNA-resistant full-length IFT81, as expected. In contrast, none of the IFT81 mutants deficient in tubulin binding in vitro (HsIFT81mut^1 and HsIFT81mut^2) compensated fully for the depletion of endogenous IFT81. Whereas expression of the deletion mutant (HsIFT81ΔN) or the mutant with reduced tubulin-binding ability (HsIFT81mut^1) resulted in partial rescue, expression of HsIFT81mut^2, in which the entire tubulin-binding patch was mutated, completely failed to rescue the siRNA-mediated knockdown of IFT81 (Fig. 2B). Thus, the entire negative effect on cilium formation by IFT81 depletion was recapitulated with a specific tubulin-binding–deficient mutant.

The fact that IFT81ΔN formed stable IFT core complexes (fig. S1) suggested that the ciliogenesis phenotype was because of reduced tubulin binding and not a general failure of IFT. To rule out whether mutation of the IFT81N CH domain resulted in general IFT deficiency, we turned to the unicellular protozoan parasite *Trypanosoma brucei*, where IFT has been well studied (*15*), and tested the effect of IFT81N CH-domain disruption on IFT. Yellow fluorescent protein (YFP)–tagged but otherwise normal IFT81 or mutant IFT81 (IFT81$_{\text{I46D,L47D}}$, Dm) where the CH domain was unfolded (fig. S7A) were expressed at wild-type levels. One of the two *IFT81* alleles was replaced with either YFP::IFT81 or YFP::IFT81Dm, leaving one WT *IFT81* allele unaltered (fig. S7B). Both the localization and the IFT speed of IFT81 and IFT81Dm were similar to that observed for other IFT proteins as judged by live-cell imaging and kymographic analysis (Fig. 3 and movies S1 and 2) (*15*). Thus, IFT81N is not required for IFT complex assembly or normal IFT in vivo, which corroborates that the ciliogenesis phenotype observed upon IFT81N CH-domain mutation (Fig. 2) was indeed because of tubulin-binding deficiency.

Axonemal precursors such as tubulin are added to the tip of the cilium in a length-dependent man-

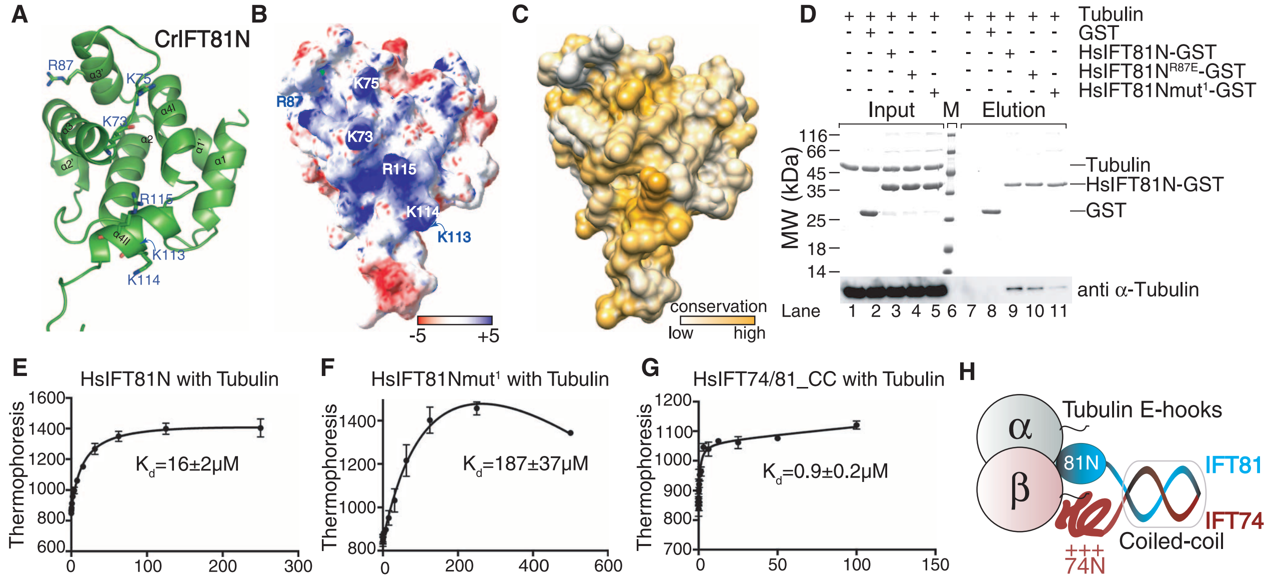

Fig. 1. IFT81 and IFT74 form a tubulin-binding module. (**A**) Cartoon representation of the crystal structure of CrIFT81N domain, with conserved lysines and arginines implicated in tubulin binding shown as sticks. (**B**) Electrostatic surface potential of IFT81N displaying the positively charged patch with the residues labeled according to the HsIFT81 sequence. (**C**) Surface conservation of IFT81N demonstrates that the basic patch is well conserved among different species (also see fig. S2). (**D**) Tubulin binding evaluated by glutathione (GSH) affinity pull-down of bovine αβ-tubulin using glutathione *S*-transferase (GST)–HsIFT81N. Whereas tubulin does not bind the GSH beads and is not pulled down by GST alone, a substantial portion is pulled down by GST-HsIFT81N, demonstrating binding. Whereas the single-point mutation R87E does not strongly impair binding, the K73K75/EE double mutant (mut^1) results in reduced amounts of pulled-down tubulin, indicating reduced binding. (**E**) Quantification of tubulin binding to untagged HsIFT81N by microscale thermophoresis reveals a K_d of 16 μM. (**F**) The HsIFT81N mut^1 has drastically reduced binding with a K_d of 187 μM, showing that the basic patch is required for tubulin binding. (**G**) Microscale thermophoresis titration of tubulin with truncated HsIFT7481 complex reveals a K_d of 0.9 μM. The curves in (E), (F), and (G) are calculated for three independent experiments, and the error bars represent the mean ± SD. (**H**) The experiments shown in (D) to (G), along with the data in fig. S5, suggest a model in which IFT81N recognizes the globular domain of tubulin, providing specificity, and IFT74N binds the acidic tail of β-tubulin, providing increased affinity.

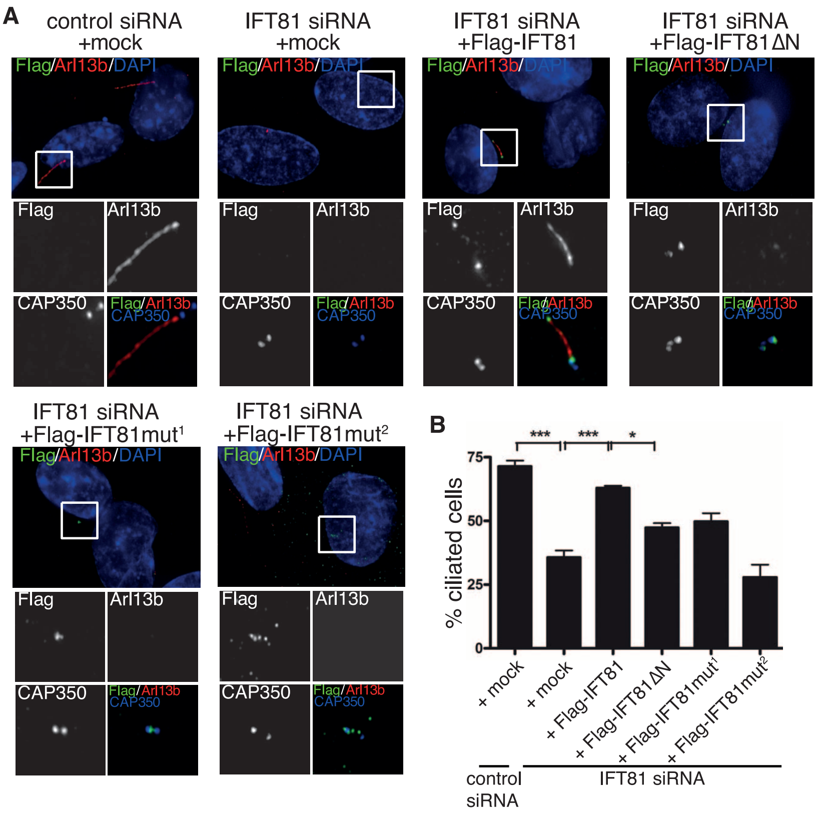

Fig. 2. Tubulin binding by IFT81 is required for ciliogenesis in human cells. (**A**) Transient expression of Flag-IFT81, but not the tubulin-binding–deficient IFT81 mutants (in green), rescues the ciliogenesis defect after IFT81 siRNA knockdown. Primary cilia formation was induced by 0.5 μM cytochalasin D and detected by antibody to Arl13b (in red). CAP350 (in blue, inset images only) was used to visualize centrosomes. Mut^1 and Mut^2 are K73K75/EE and K73K75K113K114R115/EEEEE tubulin-binding mutants, respectively. Scale bar, 5 μm. (**B**) Quantification of the rescue experiment shown in (A). *n* = 3 independent experiments; statistical analyses by one-way analysis of variance.

ner (*16*, *17*). The removal of tubulin from the axonemal tip, on the other hand, appears to be constant, with no dependence on cilium length (*17*, *18*). These observations inspired the balance-point model, in which the length of a mature cilium is the result of equal delivery and removal rates for axonemal precursors (*17*, *19*). Furthermore, the concentration of tubulin in the cytoplasm influences ciliogenesis and cilium length in mammalian cells (*20*). Based on the measured affinity between IFT74/81 and tubulin (K_d = 0.9 μM) (Fig. 1G), we calculated the fraction of IFT complexes bound to αβ-tubulin as a function of tubulin concentration (Fig. 4A). Because the cellular tubulin concentration is estimated to be in the low μM range (*21*) and tubulin expression is induced at the onset of ciliogenesis (*22*), the IFT74/81:tubulin affinity is optimal for regulating cilium length via tubulin transport (Fig. 4B). The prediction is thus that most IFT complexes are loaded with tubulin during early stages of ciliogenesis, whereas lower occupancies are found during steady-state cilium length (Fig. 4), which agrees well with previously obtained data demonstrating that tubulin transport in full-length cilia yields only faint traces on kymographs, likely due to low tubulin occupancy on IFT complexes (*13*). During cilium growth, both anterograde IFT complex concentration and tubulin binding are negatively correlated with cilia length, resulting in a decreasing assembly rate as the cilium approaches steady-state length.

Here, we have shown that the two core IFT proteins IFT74 and IFT81 form a tubulin-binding module required for ciliogenesis, which suggests a role of IFT74/81 in the transport of tubulin within cilia. The fact that the high-affinity binding of tubulin occurs only for the IFT74/81 complex and

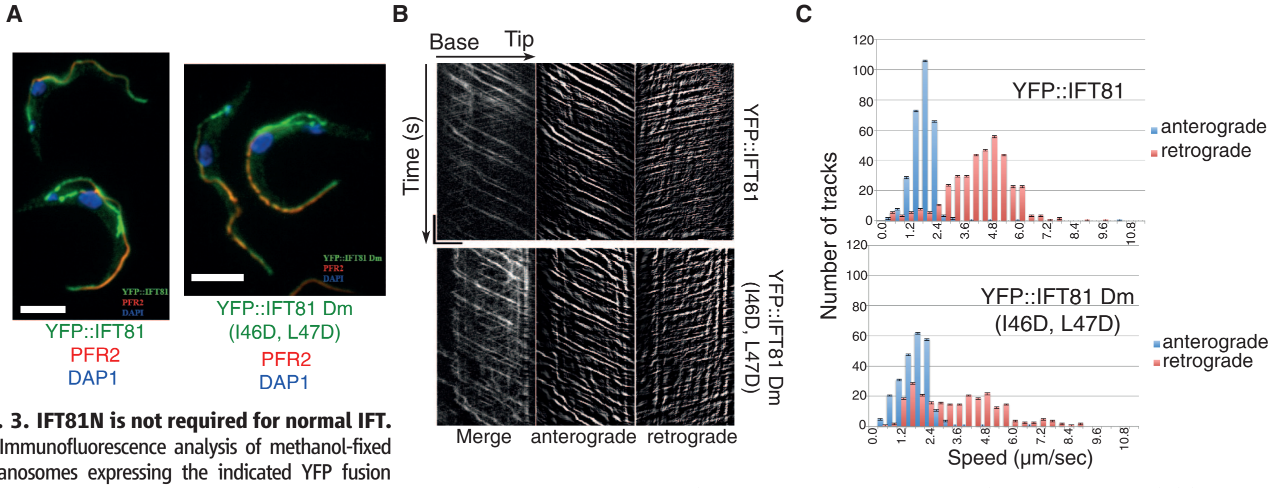

Fig. 3. IFT81N is not required for normal IFT. (**A**) Immunofluorescence analysis of methanol-fixed trypanosomes expressing the indicated YFP fusion proteins from the endogenous locus stained with an antibody to green fluorescent protein (GFP) (green) and with the antibody to PFR2 L8C4 to visualize the flagellum (red). The left panel corresponds to a control strain expressing YFP::IFT81 and the right panel to the mutant YFP::IFT81Dm, where the IFT81N CH domain is unfolded. Scale bar, 5 μm. (**B**) Kymograph generation and separation of anterograde and retrograde traces. Kymographs were extracted from videos of cells expressing YFP::IFT81 (movie S1) or YFP::IFT81Dm (movie S2). Panels show the complete kymograph, anterograde events, and retrograde events (from left to right). The *x* axis corresponds to the length of the flagellum (horizontal scale bar, 5 μm) and the *y* axis to the elapsed time (vertical scale bar, 5 s). (**C**) Quantitation of the kymograph analysis shown in (B). Anterograde (blue) and retrograde velocity (red) distribution of IFT particles are calculated from cells expressing YFP::IFT81 and YFP::IFT81Dm. The kymographic analysis reveals robust anterograde trafficking with a speed of 1.75 ± 0.55 μm/s for YFP::IFT81 (*n* = 294 tracks from 15 cells) and 1.68 ± 0.72 μm s^{-1} for YFP::IFT81Dm (*n* = 244 tracks from 15 cells). These values are in line with those reported for anterograde movement of GFP-IFT52 (*15*). Curiously, retrograde transport was slowed down in the case of YFP::IFT81Dm, where a second population of relatively slow trains was detected.

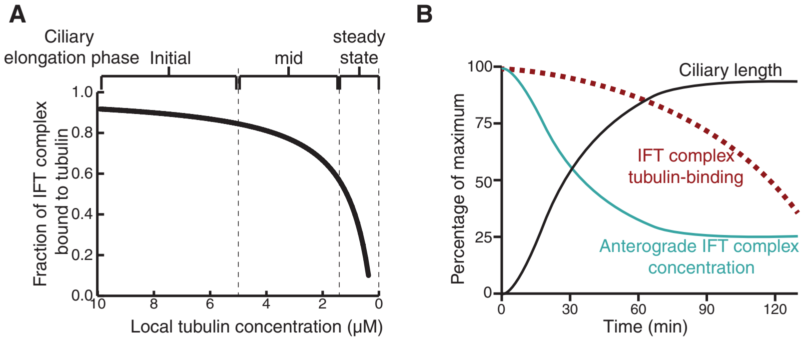

Fig. 4. Model for tubulin transport and ciliary length control. (**A**) Fraction of IFT complex bound to tubulin at varying tubulin concentrations is plotted using the equation $O_{IFT} = [Tub]/\{K_d + [Tub]\}$. O_{IFT} is the fraction of IFT bound to tubulin, K_d is the binding constant that is experimentally determined in this study as 0.9 μM, and [Tub] is the local concentration of free tubulin at the base of the cilium. (**B**) From the point of initiation of flagellar regeneration, the relationship between the ciliary length, the concentration of anterograde IFT particles, and O_{IFT} is plotted.

not for IFT81 alone could help ensure that tubulin cargo only binds in the context of properly assembled IFT complexes. Because tubulin constitutes the backbone of all cilia, it makes sense that the tubulin has a dedicated cargo-binding site on the IFT core complex (*23*). We hypothesize that, although abundant ciliary cargo proteins such as tubulin may undergo IFT via dedicated transport modules, less abundant ciliary proteins are likely to compete for generic cargo-binding sites on the IFT complex.

References and Notes

1. H. Ishikawa, W. F. Marshall, *Nat. Rev. Mol. Cell Biol.* **12**, 222–234 (2011).
2. K. G. Kozminski, K. A. Johnson, P. Forscher, J. L. Rosenbaum, *Proc. Natl. Acad. Sci. U.S.A.* **90**, 5519–5523 (1993).
3. J. L. Rosenbaum, G. B. Witman, *Nat. Rev. Mol. Cell Biol.* **3**, 813–825 (2002).
4. F. Finetti *et al.*, *Nat. Cell Biol.* **11**, 1332–1339 (2009).
5. K. G. Kozminski, P. L. Beech, J. L. Rosenbaum, *J. Cell Biol.* **131**, 1517–1527 (1995).
6. D. G. Cole *et al.*, *J. Cell Biol.* **141**, 993–1008 (1998).
7. G. J. Pazour, B. L. Dickert, G. B. Witman, *J. Cell Biol.* **144**, 473–481 (1999).
8. G. J. Pazour, N. Agrin, J. Leszyk, G. B. Witman, *J. Cell Biol.* **170**, 103–113 (2005).
9. H. Qin, D. R. Diener, S. Geimer, D. G. Cole, J. L. Rosenbaum, *J. Cell Biol.* **164**, 255–266 (2004).
10. Y. Hou *et al.*, *J. Cell Biol.* **176**, 653–665 (2007).
11. G. Piperno, K. Mead, *Proc. Natl. Acad. Sci. U.S.A.* **94**, 4457–4462 (1997).
12. C. Ciferri *et al.*, *Cell* **133**, 427–439 (2008).
13. L. Hao *et al.*, *Nat. Cell Biol.* **13**, 790–798 (2011).
14. J. Kim *et al.*, *Nature* **464**, 1048–1051 (2010).
15. J. Buisson *et al.*, *J. Cell Sci.* **126**, 327–338 (2013).
16. K. A. Johnson, J. L. Rosenbaum, *J. Cell Biol.* **119**, 1605–1611 (1992).
17. W. F. Marshall, J. L. Rosenbaum, *J. Cell Biol.* **155**, 405–414 (2001).
18. L. Song, W. L. Dentler, *J. Biol. Chem.* **276**, 29754–29763 (2001).
19. W. F. Marshall, H. Qin, M. Rodrigo Brenni, J. L. Rosenbaum, *Mol. Biol. Cell* **16**, 270–278 (2005).
20. N. Sharma, Z. A. Kosan, J. E. Stallworth, N. F. Berbari, B. K. Yoder, *Mol. Biol. Cell* **22**, 806–816 (2011).
21. G. Hiller, K. Weber, *Cell* **14**, 795–804 (1978).
22. R. E. Stephens, *Dev. Biol.* **61**, 311–329 (1977).
23. B. F. Lucker *et al.*, *J. Biol. Chem.* **280**, 27688–27696 (2005).

Acknowledgments: We thank the staff at SLS for help with x-ray diffraction data collection; the crystallization facility of the Max Planck Institute of Biochemistry (Munich) for access to crystallization screening; the staff at Biozentrum Imaging Core Facility for assistance; C. Basquin for static light-scattering experiments; C. Jung for help with microscale thermophoresis; and S. Chakrabarti, A. Cook, and B. D. Engel for carefully reading and correcting the manuscript. B. D. Engel is additionally acknowledged for assistance with Fig. 4 and for many valuable discussions concerning ciliary length control. We thank the Plateforme d'Imagerie Dynamique for providing access to their equipment and Jean-Yves Tinevez for technical advice. We acknowledge M. Morawetz and M. Stiegler for technical assistance with molecular biology. This work was funded by an Emmy Noether grant (DGF; LO1627/1-1), the European Research Council (ERC grant 310343), and the European Molecular Biology Organization Young Investigator program. Work at the Institut Pasteur was funded by Agence Nationale de la Recherche grant ANR-11-BSV8-016. C.F. is funded by a fellowship from the Ministère de l'Enseignement et de la Recherche (ED387). E.A.N. acknowledges support from the University of Basel and the Swiss National Science Foundation (31003A_132428/1). M.T. is the recipient of an Erwin Schroedinger stipend granted by the Austrian Science Fund J3148-B12, S.B was supported by the International Max Planck Research School for Molecular and Cellular Life Sciences (IMPRS), and L.C. was supported by the FEBS long-term fellowship. The authors declare that they have no conflict of interest. The data presented in this paper are tabulated in the main paper and the supplementary materials. Structural coordinates have been deposited at the Protein DataBank, accession nos. 4LVP and 4LVR.

Supplementary Materials

www.sciencemag.org/cgi/content/full/341/6149/1009/DC1
Materials and Methods
Supplementary Text
Figs. S1 to S8
Table S1
References (*24*–*47*)

24 May 2013; accepted 1 August 2013
10.1126/science.1240985

Crystal Structure of MraY, an Essential Membrane Enzyme for Bacterial Cell Wall Synthesis

Ben C. Chung,[1] Jinshi Zhao,[1]* Robert A. Gillespie,[1]* Do-Yeon Kwon,[2] Ziqiang Guan,[1] Jiyong Hong,[2,3] Pei Zhou,[1,2] Seok-Yong Lee[1]†

MraY (phospho-MurNAc-pentapeptide translocase) is an integral membrane enzyme that catalyzes an essential step of bacterial cell wall biosynthesis: the transfer of the peptidoglycan precursor phospho-MurNAc-pentapeptide to the lipid carrier undecaprenyl phosphate. MraY has long been considered a promising target for the development of antibiotics, but the lack of a structure has hindered mechanistic understanding of this critical enzyme and the enzyme superfamily in general. The superfamily includes enzymes involved in bacterial lipopolysaccharide/teichoic acid formation and eukaryotic N-linked glycosylation, modifications that are central in many biological processes. We present the crystal structure of MraY from *Aquifex aeolicus* ($MraY_{AA}$) at 3.3 Å resolution, which allows us to visualize the overall architecture, locate Mg^{2+} within the active site, and provide a structural basis of catalysis for this class of enzyme.

Bacteria maintain their cell shapes at different osmotic pressures by using the mesh-like layers of the cell wall to surround and stabilize the membrane. The cell wall of both Gram-negative and Gram-positive bacteria is composed of peptidoglycan, a cross-linked polymer of carbohydrates and amino acids. Because biosynthesis of peptidoglycan is a critical process for bacteria, it has been a major target for antibiotics (*1*, *2*). Peptidoglycan biosynthesis involves three main stages. First, the peptidoglycan precursor UDP-*N*-acetylmuramoyl (MurNAc)–pentapeptide (L-Ala-γ-D-Glu-diaminopimelic acid/L-Lys-D-Ala-D-Ala) is synthesized in the cytosol. Second, this hydrophilic precursor is attached to a carrier lipid, and the lipid-linked precursor is flipped across the membrane to the periplasm.Third, peptidoglycan precursors are polymerized to form the cell wall.

MraY, or phospho-MurNAc-pentapeptide translocase, is an integral membrane protein responsible for the second stage of peptidoglycan

---

[1]Department of Biochemistry, Duke University Medical Center, 2 Genome Ct, Durham, NC 27710, USA. [2]Department of Chemistry, Duke University, Durham, NC 27708, USA. [3]Department of Pharmacology and Cancer Biology, Duke University Medical Center, Durham, NC 27710, USA.

*These authors contributed equally to this work.
†Corresponding author. E-mail: sylee@biochem.duke.edu

www.sciencemag.org/cgi/content/341/6149/1009/DC1

Supplementary Materials for

Molecular Basis of Tubulin Transport Within the Cilium by IFT74 and IFT81

Sagar Bhogaraju, Lukas Cajanek, Cécile Fort, Thierry Blisnick,
Kristina Weber, Michael Taschner, Naoko Mizuno, Stefan Lamla,
Philippe Bastin, Erich A. Nigg, Esben Lorentzen*

*Corresponding author. E-mail: lorentze@biochem.mpg.de

Published 30 August 2013, *Science* **341**, 1009 (2013)
DOI: 10.1126/science.1240985

This PDF file includes:

- Materials and Methods
- Supplementary Text
- Figs. S1 to S8
- Table S1
- References

Other Supplementary Material for this manuscript includes the following:
(available at www.sciencemag.org/cgi/content/full/341/6149/1009/DC1)

- Movies S1 and S2

Materials and Methods

Purification and reconstitution of IFT-B complexes

For purification of the *C.reinhardtii* IFT81ΔN/74ΔN/His$_6$-27/25ΔC complex, insect cells (HighFive, Invitrogen) were infected with baculovirus expressing the complex and grown for 72hours. Extract preparation was carried out as described previously (*24*), and the complex purified using a combination of Ni-NTA, ion-exchange (monoQ column) and size exclusion chromatography. Purification of the IFT70/IFT52/IFT46 complex from *E.coli* was performed as described previously (*24*). Reconstitution of the heptameric IFT81ΔN/74ΔN/70/52/46/His$_6$-27/25ΔC complex was achieved by mixing equimolar amounts of the IFT81ΔN/74ΔN/His$_6$-27/25ΔC complex and the IFT70/52/46 complex, followed by Superose6 size exclusion chromatography after an incubation at 4°C for 3hours.

Protein purification and crystallization

His tagged CrIFT81 (residues 1-126) was expressed in *E.coli* BL21 (DE3) GOLD pLysS strain and lysed by sonication in a buffer containing 50mM Tris pH 7.5, 150mM NaCl and 10% glycerol. The protein was purified by Ni-NTA affinity chromatography followed by TEV cleavage to remove the His tag and size exclusion chromatography in a buffer of 10mM HEPES pH 7.5, 150mM NaCl using a superdex 75 or 200 column. CrIFT81N was concentrated to 20mg/ml and crystallized by vapor diffusion. Crystals of CrIFT81N appeared in 0.8M $(NH_4)_2SO_4$, 0.1 M Tris pH 8.0 precipitant condition (Figure S3C). HsIFT81N was purified using the same procedure. Point mutants of HsIFT81N were made using the Quikchange site directed mutagenesis protocol from Agilent Technologies® and all the mutants were expressed and purified like the WT protein. The

IFT81/74_CC complex was produced by co-expression of His_6-HsIFT81 (residues 1-215) and His_6-HsIFT74 (residues 1-272) in the *E.coli* strain BL21 (DE3) GOLD pLysS. Cells were lysed and the proteins were purified using the same procedure as described above.

X-ray diffraction data collection and structure determination

Crystals of CrIFT81N were flash cooled in liquid nitrogen in mother liquor supplemented with 25% glycerol as a cryoprotectant. Diffraction data were collected at the Swiss light source (SLS, Villigen, Switzerland) and processed with the XDS package (*25*). Single wavelength anomalous dispersion X-ray diffraction data were collected from tantalum bromide (Ta_6Br_{12}) soaked and experimental phases calculated using the PHENIX package (*26*). The program BUCCANEER (*27*) was used to automatically build ~80% of the CrIFT81N structure. The model was completed by iterative cycles of manual model building in the program COOT (*28*) and refinement in PHENIX. The obtained structure from the Ta_6Br_{12} soak was then used as a search model for molecular replacement with native data.

MT co-sedimentation assays

99% pure bovine brain tubulin was obtained from Cytoskeleton® and MT were polymerized according to the manufacturers instructions. For co-sedimentation experiments, 3µM of MTs were pre-incubated with 3µM of protein (HsIFT81N or HsIFT74/81_CC) at room temperature for 30min in BRB80 buffer (80mM Pipes-KOH pH 6.8, 1mM EGTA, 2mM $MgCl_2$) supplemented with 20µM taxol to a final reaction volume of 50µL. This reaction mixture was pipetted onto 100µL of cushion buffer (50%

glycerol, 80mM Pipes-KOH pH 6.8, 2mM $MgCl_2$, 1mM EGTA) supplemented with 20µM taxol. The resulting solution was centrifuged at 40.000rpm for 30min in a Beckmann TLA100 rotor. Supernatants and pellets were analyzed using SDS-PAGE followed by coomassie staining.

Electron microscopy

Taxol-stabilized MTs at a concentration of 5µM were mixed with 1.5µM of GST-HsIFT81N or HsIFT74/81_CC in 50 µL of BRB80 buffer. The mixture was incubated for 30 BRB80min at room temperature and 5µL of this reaction mix were placed onto a glow discharged EM grid followed by 2-3 rounds of washing with BRB80 buffer. The sample was stained using 1% Uranyl acetate solution. Images were collected using a FEI-CM200 microscope operating at 160kV at 38,000X magnification corresponding to a pixel size of 2.78Å.

Tubulin co-precipitation assays

3µM of tubulin and 10µM of GST tagged proteins were mixed in 100µL of BRB80 buffer and incubated on ice for 30min. The reaction mixture was then added to 15µL of pre-blocked GSH beads and incubated on a shaker for 1hour at 4°C. The beads were washed extensively with the BRB80 buffer and the proteins bound to GSH beads were eluted with 30mM glutathione and analyzed by SDS-PAGE.

Microscale thermophoresis (MST)

Bovine tubulin was labeled on lysine side-chains using the Cy3 protein labeling kit from Jena Bioscience according to the manufacturers instructions. The average number of lysines labeled per αβ-tubulin dimer was estimated to be 3.6. 200nM of labeled tubulin was titrated with 0.03-2000µM of HsIFT81N or HsIFT81Nmut1 in a total volume of 20µL and 10-16 thermophoresis measurements recorded. Each sample was incubated at room temperature for 10min before measurement. For the HsIFT81/74_CC complex, a lower concentration of 0.003-200µM was used. Thermophoresis measurements were carried out using the NanoTemper Monolith NT.115 instrument (NanoTemper Technologies GmbH) using 50% LED and 65% laser power with the laser on for 40sec followed by an off period of 10sec. The resulting raw data were analysed using the NanoTemper software to obtain binding curves and Kds were calculated using Prism (GraphPad Software).

Subitlisin treatment of tubulin/microtubules

8µM of preformed and taxol stabilized MTs were mixed with 1.25µM of subtilisin in BRB80 buffer containing 20µM taxol in a total volume of 50µL. This reaction mixture was incubated at 30°C for 30min and the proteolysis stopped by adding 1mM PMSF. Proteolysed MTs were spun at 40.000rpm for 30min in a Beckmann TLA100 rotor and the pellet re-dissolved in BRB80 buffer supplemented with 20µM taxol. For the subtilisin treatment of soluble tubulin, 25µM of tubulin were mixed with 1.25µM of subtilisin in a total volume of 120µL of BRB80 buffer. The solution was divided into two equal halves, which were incubated at 30°C for 30min or 120min, respectively, followed by inactivation of the protease by the addition of 1mM PMSF. Untreated and subtilisin treated tubulin were purified using size exclusion chromatography (superdex 200 column) as shown in Fig. S5A.

Cell culture and transfections

The RPE-1 and U2OS cells were cultured as previously described (*29*). For transient gene expression, cells were transfected with TransIT-LT1 (Mirus) according manufacturers instructions with pcDNA3.1-IFT81 full length (F.L.) and pcDNA3.1-IFT81ΔN (human IFT81 sequences). For the rescue experiments, RNAi resistant plasmid was generated by making silent mutations in the siRNA spanning regions of *IFT81* gene and subsequent cloning of this construct into the pcDNA5.1 vector. This RNAi resistant pcDNA5.1-IFT81 F.L. plasmid was further used to generate rescue plasmids with point and deletion mutations (mut^1, mut^2 and ΔN). For rescue experiments, RPE-1 cells were first transfected with control (GL2) or IFT81 siRNA (target sequence: GGATATCAGTGCAATGGAA and CAGCTCATTAAGAGAGTTGAA, each at 50μM) using Oligofectamine (Invitrogen) according manufacturers recommendations. Cells were subsequently nucleofected with pcDNA5.1-IFT81 (F.L., mut1, mut2 or ΔN) rescue plasmids using Amaxa 4D-Nucleofector (Lonza) and the DS137 program, 48h after the siRNA transfection. Following the plasmid transfection, the formation of primary cilia in RPE-1 cells was induced either by 0.5μM Cytochalasin D (Sigma) or by changing into serum-free media for 24h.

Immunofluorescence microscopy

Cells grown on coverslips were washed with PBS and fixed in methanol (-20°C/5min). In case of the detection of acetylated tubulin, cells were cold treated (+4°C/30min) prior the methanol fixation. Blocking, incubation with primary and secondary antibodies, and washing were done as described before (*29*). The following primary and secondary antibodies were used: mouse anti-acetylated tubulin (6-11B-1, Sigma), rabbit anti-Arl13b (17711, Proteintech), mouse anti-Flag (M2, Sigma), rabbit anti-Flag (F7425, Sigma), rat anti-IFT81, goat anti-CAP350 (*30*), rabbit anti-Cep135 (*31*) (both Alexa 647-labeled), rabbit anti-Cep152 (*32*) (Alexa 555-labeled), Alexa 488 anti-mouse, Alexa 488 anti-rabbit, Alexa 555 anti-mouse, Alexa 555 anti-rabbit (all from Invitrogen), and Cy2 anti-rat (Jackson Immuno Research). Direct labeling of primary antibodies was done with the Alexa-antibody labeling kit (Invitrogen). Coverslips were mounted on slides using Glycergel (Dako). Wide-field imaging was performed on a DeltaVision system (Applied Precision) with a 60x/1.2 or 100x/1.4 Apo plan oil immersion objective. Image stacks were taken with a z-distance of 0.2µm, deconvolved (conservative ratio, 3-5 cycles) and projected as maximal intensity image using SoftWoRX (Applied Precision). For cell counts, at least 50 transfected cells per condition and experiment were analyzed for the presence/absence of primary cilia.

Statistical analyses

Statistical analyses (Students t-test, one-way ANOVA with Bonferronis multiple comparison test) were performed using Prism. $p<0.05$ was considered as statistically significant difference (*), p<0.01 (**), p<0.001 (***). Results are presented as mean plus standard error of the mean (SEM).

Generation of trypanosome expressing YFP::IFT81 cell lines

All cells used for this work were derived from *T. brucei* strain 427 (procyclic stage) and were cultured in SDM79 medium supplemented with hemin and 10% foetal calf serum. Cell lines expressing unaltered or mutated YFP::IFT81 were obtained after endogenous tagging. The first 500 nucleotides of the *IFT81* gene (Gene DB number Tb927.10.2640) were chemically synthesized (GeneCust, Luxembourg) and cloned in frame with the *YFP* gene within the HindIII and ApaI sites of the p2675 vector (*33*). The construct was linearized within the *IFT81* sequence with the enzyme XcmI and nucleofected (*34*) in wild-type trypanosomes, leading to integration by homologous recombination in the endogenous locus and to expression of the full length coding sequence of IFT81 fused to YFP. Expression of an IFT81-YFP fusion protein of the correct size was confirmed by western blotting with an anti-GFP antibody (Roche) that cross-reacts with YFP. The IFT81 I46D, L47D double-mutant (YFP::IFT81Dm) was generated from the p2675IFT81 plasmid using the Quikchange site directed mutagenesis protocol from Agilent Technologies®. The construct was linearized and transfected, leading to similar expression levels of YFP::IFT81Dm as for unaltered YFT-IFT81 described above.

Life microscopy analysis of trypanosome cells

Trypanosomes were taken from cultures grown at 1.10^7 cells/mL and the expression of YFP::IFT81 or YFP::IFT81DM was observed in live cells using a spinning disk

UltraView Vox microscope equipped with an oil immersion objective (magnification x100 with a 1.4 numerical aperture). Images were acquired using the Volocity software (Perkin Elmer) with an EMCCD camera (ImagEM X2, Hamamatsu) operating in streaming mode. Images were captured with an exposure time of 100ms during 30secs. Images were analysed using the Volocity software and Image J and kymographs were extracted using Quia (*15*).

Supplementary Text

Model for ciliary length control (Fig. 4 and S8)

Intraflagellar transport is known to play a direct role in ciliary length control as partial inhibition of IFT in a *C.reinhardtii* mutant resulted in shorter flagella (*17*). Similarly, partial depletion of the IFT pool results in the formation of shorter flagella in trypanosomes (35). To assess whether the modulation of tubulin transport is another plausible mechanism for controlling cilium length, we used the measured affinity (K_d=0.9μM) to calculate the fraction of IFT complexes bound to αβ-tubulin as a function of tubulin concentration (Fig. 4A). According to this calculation, 90% of IFT complexes have tubulin bound when the cellular concentration of free tubulin is 8μM, whereas only 10% of IFT complexes have tubulin bound at a tubulin concentration of 0.1μM. As the cellular tubulin concentration is estimated to be in the low μM range (*21*), the affinity to IFT74/81 is thus optimal for such a regulatory mechanism. Tubulin is concentrated at the transition zone fibres emanating from the basal body (*36*), a location where IFT protein also concentrate (*37*). Furthermore, tubulin expression is induced at the onset of ciliogenesis followed by a gradual decrease in tubulin concentration during cilium growth (22, *38-41*). This implies that the tubulin-loading of IFT74/81 is maximal during the early stages of ciliogenesis and may decrease as the cilium elongates and the concentration of free tubulin in the cytoplasm is reduced (Fig. 4B and S8). As a result, less tubulin is delivered to the tip of the cilium as it continues to grow. Combined with modulating IFT, this mechanism could provide an additional important control of cilium length.

Further regulation of the IFT of axonemal precursors is likely to occur via post-translational modifications that modulate affinity to the IFT machinery. Tubulin itself is known to undergo a large number of modifications (*42*), primarily in the acidic C-terminal tail recognized by IFT74, and modifications in this region could thus change binding properties. Recently, the induction of arginine methylation, which is known to affect protein-protein interactions (*43*), was shown to occur during cilia resorption. The methylation pattern was punctate along the length of the cilium, reminiscent of IFT protein staining, indicating that one or more IFT proteins could be methylated (*44*, *45*). Indeed, a protein post-translational modification database (PhosphoSitePlus®) search reveals that human IFT74 is methylated at R51 (*46*). This residue is part of the basic IFT74 N-terminus required for the high affinity tubulin binding by IFT74/81. Methylation of R51 may thus interfere with the function of IFT74 by neutralizing the critical positive charge required for binding to tubulin E-hooks and hence may compromise tubulin transport by the IFT complex. Methylation of IFT81/74 arginines to reduce the affinity for tubulin might thus be a regulatory pathway that is especially active during ciliary resorption, although further studies are required to elucidate its importance.

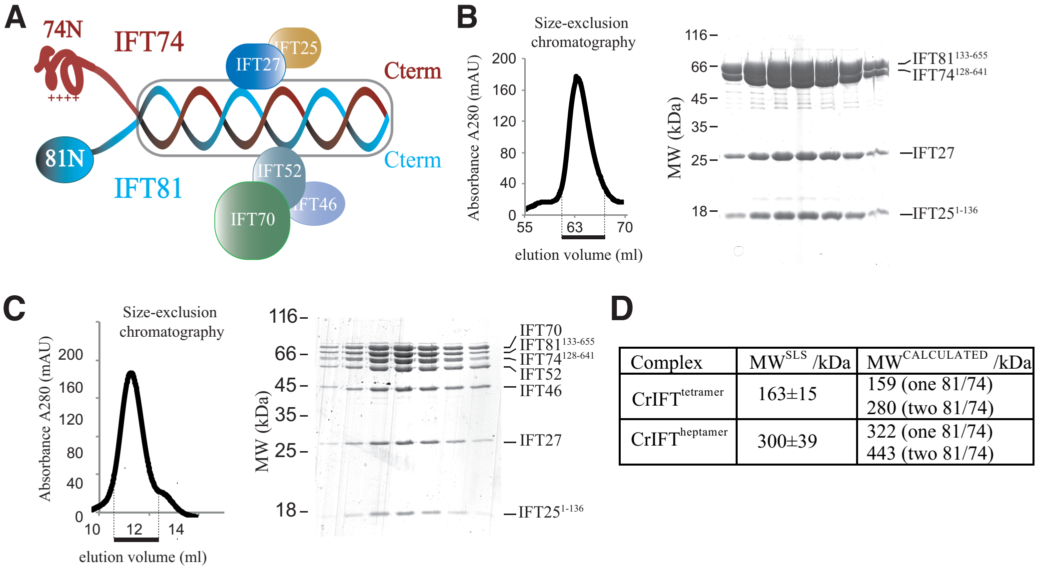

Complex	MW^{SLS} /kDa	MW^{CALCULATED} /kDa
CrIFT^{tetramer}	163±15	159 (one 81/74) 280 (two 81/74)
CrIFT^{heptamer}	300±39	322 (one 81/74) 443 (two 81/74)

Fig. S1.

(A) Schematics of the IFT-B core complex (not to scale) illustrate that both the IFT25/27 and the IFT46/52/70 sub-complexes associate with the coiled coil regions of IFT74/81. **(B)** Chromatogram from size exclusion purification (left) and associated coomassie-stained SDS-PAGE gel of the indicated peak fraction (right) for purified *C.reinhardtii* IFT25ΔC/27/74ΔN/81ΔN complex lacking the N-terminal regions of IFT74 and IFT81. **(C)** Purification of a heptameric IFT-B core complex obtained by mixing the tetramer shown in (**B**) with a trimeric IFT46/52/70 complex followed by purification using size exclusion chromatography. The results show that IFT74N and IFT81N are dispensable for IFT core complex formation. **(D)** Comparision of the experimentally determined molecular weights with the theoritical molecular weights of CrIFT^{tetramer} (IFT74ΔN, IFT81ΔN, IFT25ΔC and IFT27) and crIFT^{heptamer} (IFT74ΔN, IFT81ΔN, IFT25ΔC, IFT27, IFT70, IFT52 and IFT46). Analysis shows that the molecular weights obtained by static light scattering (SLS) comply with a single copy of both IFT74 and IFT81 in the IFT complex.

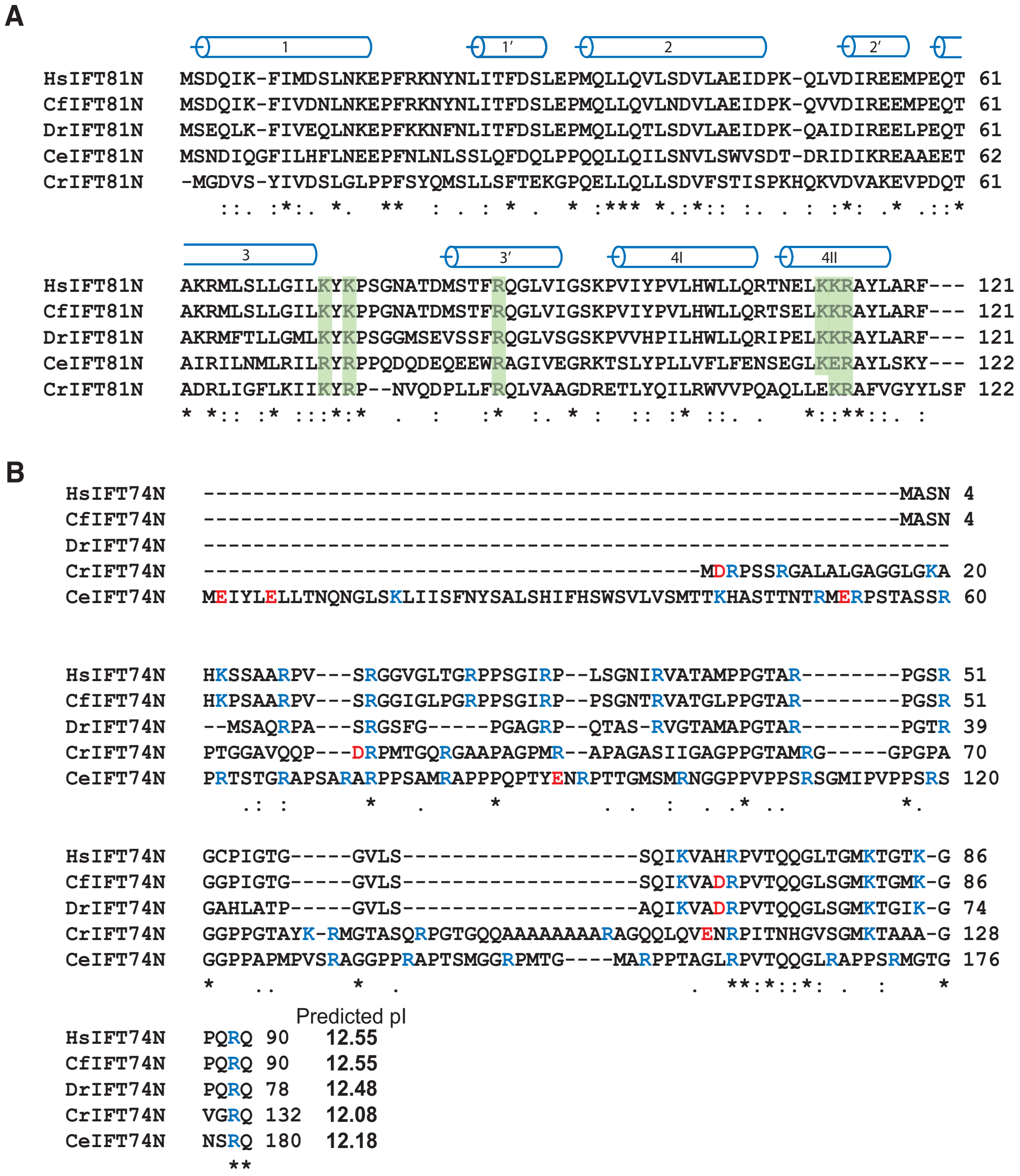

```
HsIFT81N   MSDQIK-FIMDSLNKEPFRKNYNLITFDSLEPMQLLQVLSDVLAEIDPK-QLVDIREEMPEQT 61
CfIFT81N   MSDQIK-FIVDNLNKEPFRKNYNLITFDSLEPMQLLQVLNDVLAEIDPK-QVVDIREEMPEQT 61
DrIFT81N   MSEQLK-FIVEQLNKEPFKKNFNLITFDSLEPMQLLQTLSDVLAEIDPK-QAIDIREELPEQT 61
CeIFT81N   MSNDIQGFILHFLNEEPFNLNLSSLQFDQLPPQQLLQILSNVLSWVSDT-DRIDIKREAAEET 62
CrIFT81N   -MGDVS-YIVDSLGLPPFSYQMSLLSFTEKGPQELLQLLSDVFSTISPKHQKVDVAKEVPDQT 61
              ::. :*:. *.  **  : . : * .  * :*** *.:*:: :. . : :*: .* .::*

HsIFT81N   AKRMLSLLGILKYKPSGNATDMSTFRQGLVIGSKPVIYPVLHWLLQRTNELKKRAYLARF--- 121
CfIFT81N   AKRMLSLLGILKYKPPGNATDMSTFRQGLVIGSKPVIYPVLHWLLQRTSELKKRAYLARF--- 121
DrIFT81N   AKRMFTLLGMLKYKPSGGMSEVSSFRQGLVSGSKPVVHPILHWLLQRIPELKKRAYLARF--- 121
CeIFT81N   AIRILNMLRILRYRPPQDQDEQEEWRAGIVEGRKTSLYPLLVFLFENSEGLKERAYLSKY--- 122
CrIFT81N   ADRLIGFLKIIKYRP--NVQDPLLFRQLVAAGDRETLYQILRWVVPQAQLLEKRAFVGYYLSF 122
           * *:: :* :::*:*  .  :   :*  :. * :  :: :* ::. .   *::**::. :
```

```
HsIFT74N   --------------------------------------------------------MASN 4
CfIFT74N   --------------------------------------------------------MASN 4
DrIFT74N   ------------------------------------------------------------
CrIFT74N   ----------------------------------------MDRPSSRGALALGAGGLGKA 20
CeIFT74N   MEIYLELLTNQNGLSKLIISFNYSALSHIFHSWSVLVSMTTKHASTTNTRMERPSTASSR 60


HsIFT74N   HKSSAARPV---SRGGVGLTGRPPSGIRP--LSGNIRVATAMPPGTAR--------PGSR 51
CfIFT74N   HKPSAARPV---SRGGIGLPGRPPSGIRP--PSGNTRVATGLPPGTAR--------PGSR 51
DrIFT74N   --MSAQRPA---SRGSFG-----PGAGRP--QTAS-RVGTAMAPGTAR--------PGTR 39
CrIFT74N   PTGGAVQQP---DRPMTGQRGAAPAGPMR--APAGASIIGAGPPGTAMRG-----GPGPA 70
CeIFT74N   PRTSTGRAPSARARPPSAMRAPPPQPTYENRPTTGMSMRNGGPPVPPSRSGMIPVPPSRS 120
              .: :      *   .     *        . .  :  . .* ..         *.

HsIFT74N   GCPIGTG-----GVLS-------------------SQIKVAHRPVTQQGLTGMKTGTK-G 86
CfIFT74N   GGPIGTG-----GVLS-------------------SQIKVADRPVTQQGLSGMKTGMK-G 86
DrIFT74N   GAHLATP-----GVLS-------------------AQIKVADRPVTQQGLSGMKTGIK-G 74
CrIFT74N   GGPPGTAYK-RMGTASQRPGTGQQAAAAAAAARAGQQLQVENRPITNHGVSGMKTAAA-G 128
CeIFT74N   GGPPAPMPVSRAGGPPRAPTSMGGRPMTG----MARPPTAGLRPVTQQGLRAPPSRMGTG 176
           *   ..      *  .                       .  **:*::*: .  :    *

                          Predicted pI
HsIFT74N   PQRQ 90      12.55
CfIFT74N   PQRQ 90      12.55
DrIFT74N   PQRQ 78      12.48
CrIFT74N   VGRQ 132     12.08
CeIFT74N   NSRQ 180     12.18
             **
```

Fig. S2

(A) Sequence alignment of the N-termini of IFT81 proteins from diverse ciliated organisms. Secondary structure elements derived from the CrIFT81N structure are indicated at the top and the conservation of residues are shown at the bottom of the alignment. Functional tubulin binding residues are colored green. **(B)** Sequence alignment of the N-terminal region preceding the predicted coiled-coil domain of IFT74 from different organisms. Conservation is indicated below the sequence. Positively- and negatively-charged residues are shown in blue and red, respectively. The theoretical pIs calculated using the program ProtParam (http://web.expasy.org/protparam/) are indicated.

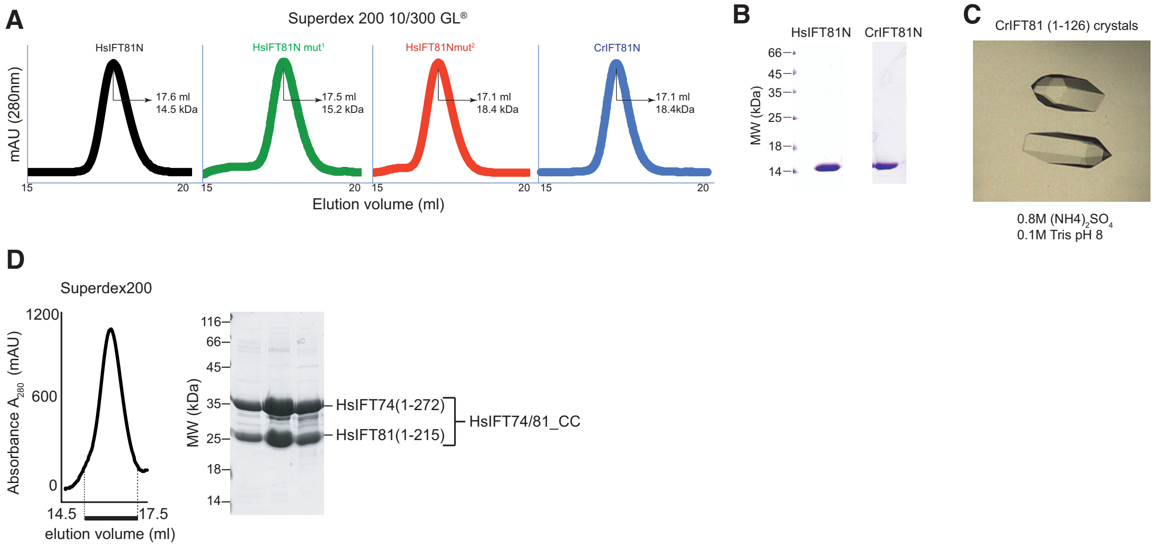

Fig. S3

(A) Size exclusion profiles of IFT81N wild-type and mutant proteins demonstrating that all mutant proteins elute similarly to the wild-type protein and are thus likely to be properly folded. **(B)** Coomassie stained SDS-PAGE gels of purified HsIFT81N and CrIFT81N. **(C)** Hexagonal crystals of CrIFT81N grown by vapor diffusion. **(D)** Purification of truncated HsIFT74/81 complex (HsIFT7481_CC) by size exclusion chromatography. HsIFT7481_CC contains all of the N-terminal domains and a sufficient portion of the coiled-coil domains to form a stable complex.

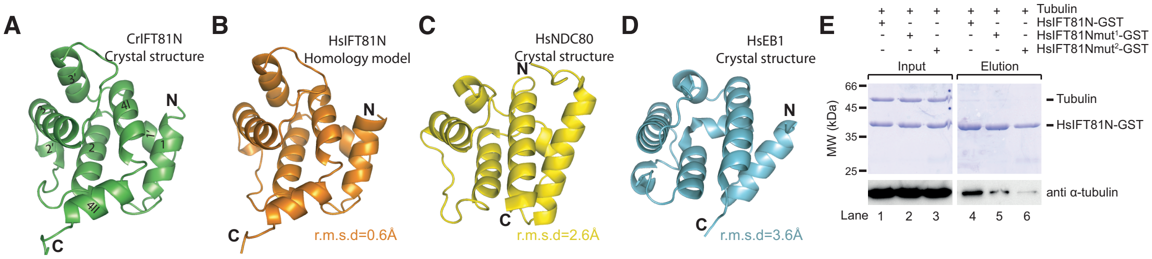

Fig. S4
(A) 2.3Å resolution crystal structure of CrIFT81N shown as a cartoon representation. The termini and α-helices of the domain are labelled. **(B)** Homology model of HsIFT81N based on the crystal structure of CrIFT81N displayed in the same orientation as in panel (A). **(C, D)** Crystal structures of the CH-domains of the MT-binding proteins NDC80 and EB1 after superpositioning onto the CrIFT81N structure shown in **(A)**. **(E)** αβ-tubulin pull-down with wildtype and mutant GST-HsIFT81N proteins. (Top) Coomassie-stained SDS gel of input and eluted proteins. (Bottom) Western-blot using anti α-tubulin antibody to visualize tubulin pulled-down by GST-HsIFT81N. Mutation of conserved basic residues of IFT81N reduces the amount of pulled-down tubulin.

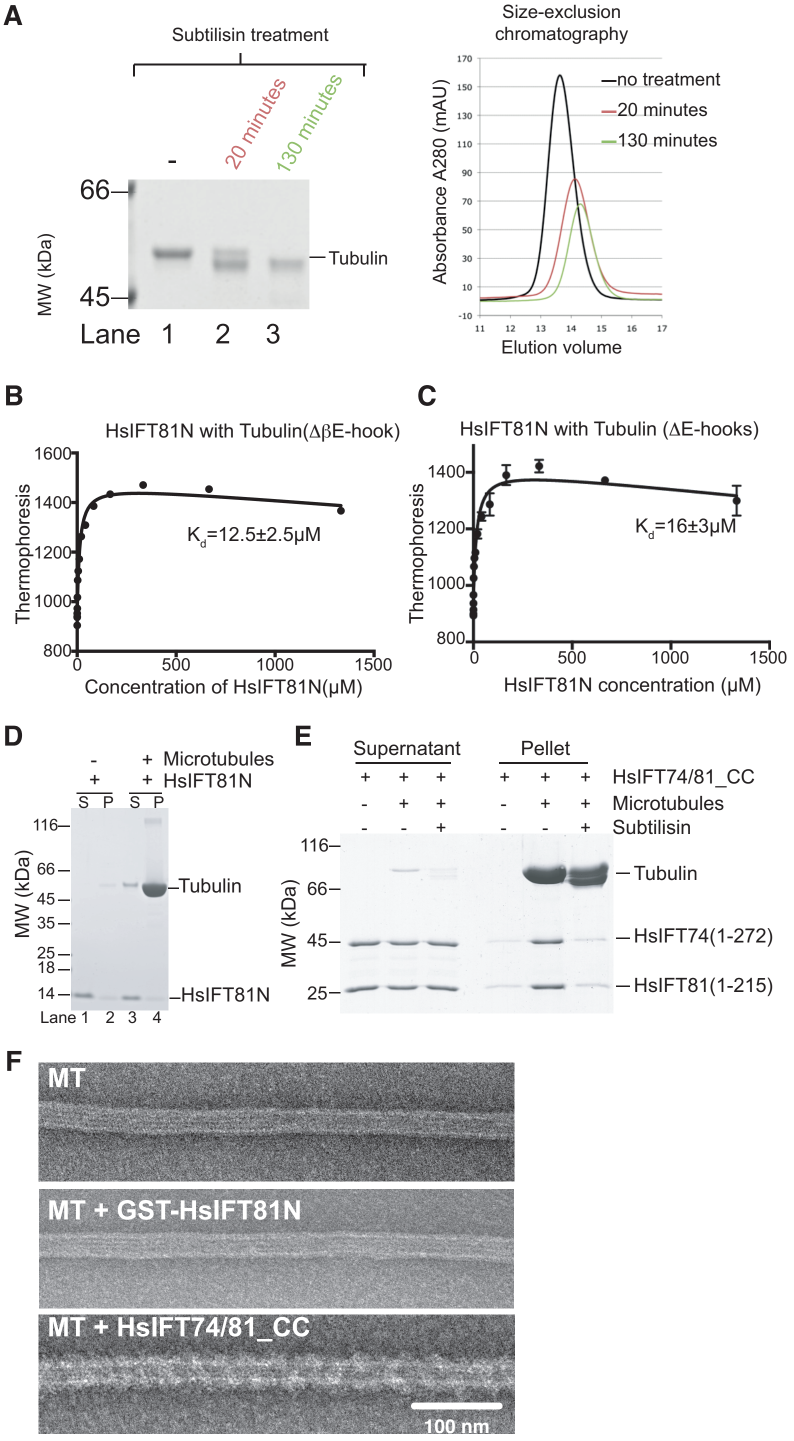

Fig. S5

(A) (left) Coomassie-stained SDS-PAGE gel of subtilisin-protease treated αβ-tubulin to remove the E-hook of β-tubulin (after 20 min) or both α- and β-tubulin (after 130 min). (right) size-exclusion chromatography of proteolysed tubulin **(B)** Microscale thermophoresis titration of αβ-tubulin lacking the C-terminal tail of β-tubulin (tubulin ΔβE-hook) with HsIFT81N (panel (A), 20 min treatment) showing a similar affinity as for intact αβ-tubulin. **(C)** Microscale thermophoresis titration of αβ-tubulin lacking both the acidic C-terminal tails with HsIFT81N gives a Kd of 16μM. Panels (B) and (C) demonstrate that IFT81N does not required the tubulin E-hooks for interaction. **(D)** MT-sedimentation assay with HsIFT81N and subsequent SDS-PAGE analysis of the supernatant (S) and the pellet (P) reveal only background levels of HsIFT81N co-sedimenting with MT. **(E)** MT-sedimentation experiments where intact αβ-tubulin or tubulin lacking the C-terminal tail of β-tubulin is co-sedimented with the HsIFT74/81_CC complex demonstrates that the high-affinity interaction mediated by IFT74N requires the C-terminal tail of β-tubulin. The concentration of tubulin and HsIFT81N used in the experiments in panels (D) and (E) was 5μM. **(F)** Negative stain EM of taxol stabilized MT incubated with HsIFT81N or HsIFT74/81_CC complex. HsIFT74/81_CC but not HsIFT81N decorates MT. The concentration of tubulin was 1μM and that of IFT81N and HsIFT74/81_CC was 1.5μM.

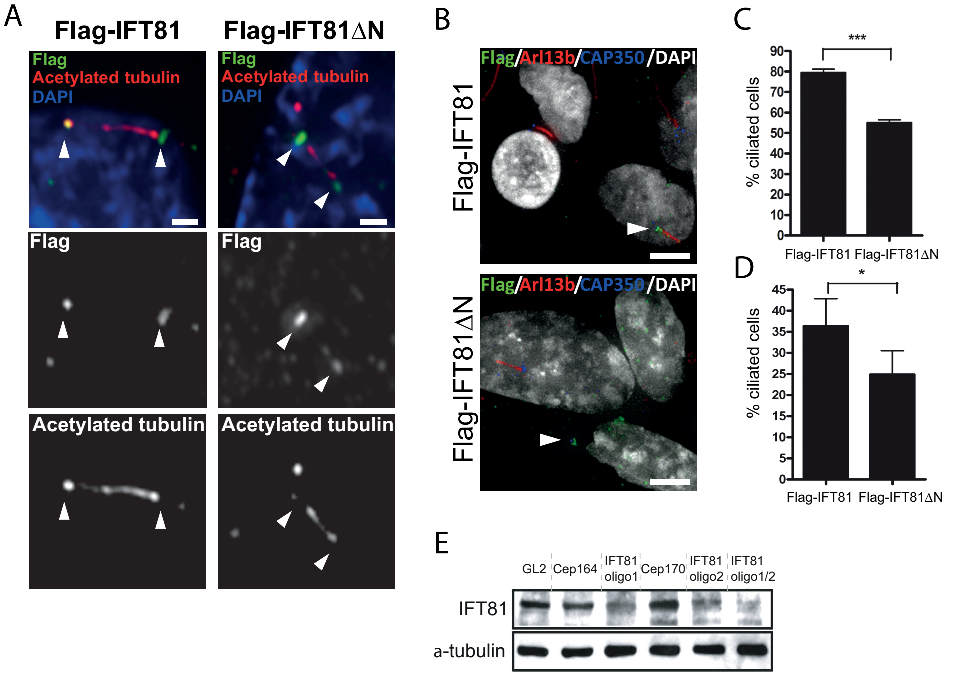

Fig. S6

(A) Both Flag-IFT81 and Flag-IFT81ΔN (in green) are detected at the basal body and the tip of the primary cilium (induced by serum starvation) in RPE1 cells (see the arrowheads). Acetylated tubulin immuno-staining (in red) was used to visualize primary cilia. Scale bar, 1 µm. **(B)** Transient expression of Flag-IFT81ΔN, but not Flag-IFT81 (in green) impairs formation of primary cilia induced by 24h treatment with 0.5µM cytochalasin D in RPE1 cells. Primary cilia were detected by Arl13b immuno-staining (in red), CAP350 (in blue) was used to visualize centrosomes. Arrowheads show Flag positive cells. Scale bar, 5 µm. **(C)** Quantification of the effects of Flag-IFT81 and Flag-IFT81ΔN expression on the presence of primary cilia induced by 0.5µM cytochalasin D. n=3, $p<0.001$(***) by Student's t-test. **(D)** Quantification of the effects of Flag-IFT81 and Flag-IFT81ΔN expression on the presence of primary cilia induced 24h serum starvation. n=4, $p<0.05$(*) by Student's t-test. **(E)** IFT81 siRNA knockdown efficiency was probed by testing the levels of IFT81 protein with anti-IFT81. Transfection of either IFT81 oligo1 or IFT81 oligo2 reduced the protein levels. Combination of oligo1 and oligo2 had the maximum effect on the IFT81 protein levels and hence it was used in the siRNA rescue experiments shown in Fig. 2. Various control RNAi (GL2, Cep164 & Cep170) did not affect IFT81 levels. Levels of α-tubulin in each lane are indicated as a loading control.

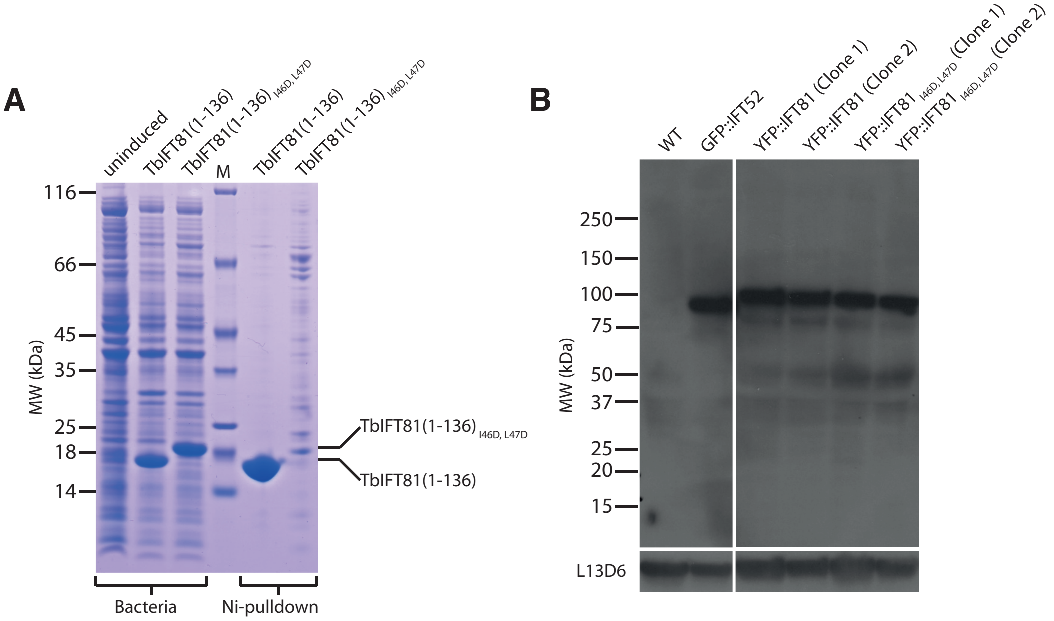

Fig. S7

(A) Expression and Ni-NTA pulldown of His tagged WT and I46D, L47D (Dm) structure-based mutant of *Tryponosma brucei* (Tb) IFT81(1-136). Both proteins are highly expressed as seen from the lanes labeled ‘Bacteria’. The ‘Ni-pulldown’ lanes show that while the WT construct is highly soluble, the mutant solubility is severely compromised indicating that this double mutation disrupts the fold of the N-terminal domain of TbIFT81. **(B)** Western blotting analysis of total protein samples from the Tb cells expressing normal and the mutant (Dm) version of IFT81. 50µg of total protein for each lane are separated on a 4-15% SDS-PAGE and probed with the anti-GFP marker to detect the fusion proteins GFP-IFT52 (*47*), YFP::IFT81 or YFP::IFT81(I46D, L47D). The blot was reprobed with L13D6 to detect paraflagellar rod (PFR) proteins as loading control.

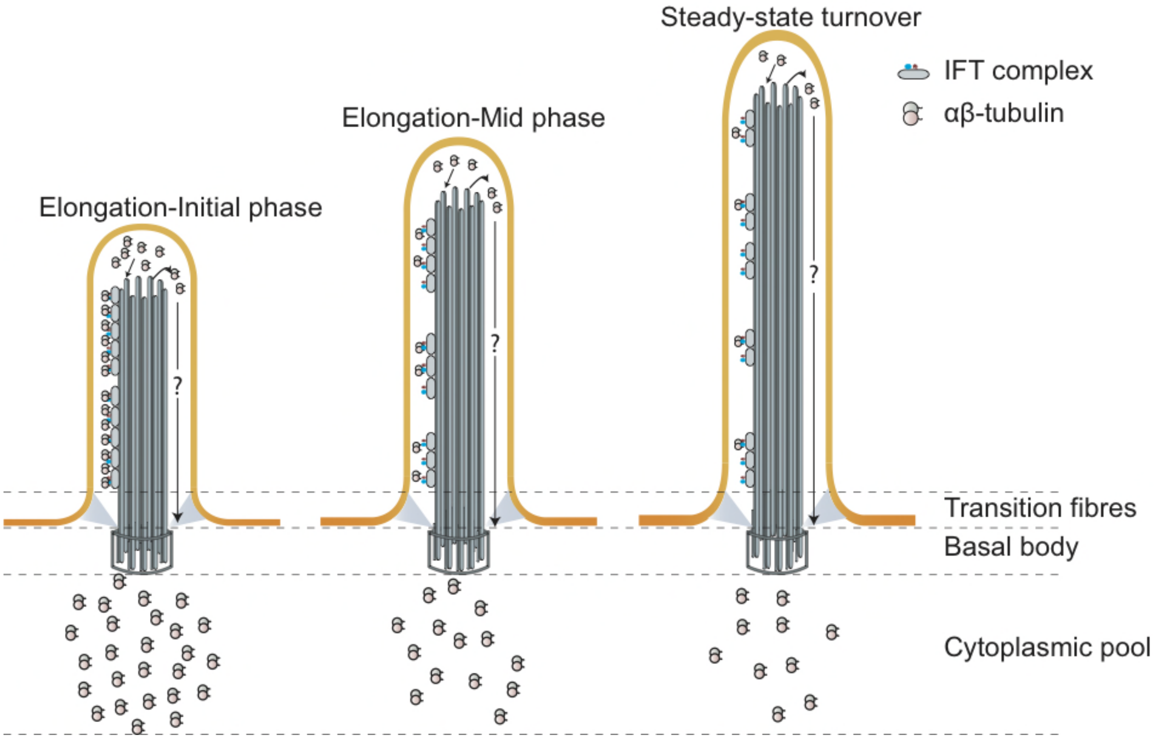

Fig. S8

Model for ciliary length control: 3 representative phases of cilia growth are shown. Each phase is characterized by a varying fraction of IFT complexes bound to tubulin. O_{IFT} is highest in the initial elongation phase and gradually decreases as the cilia approaches its steady state length.

Table S1. Data collection and refinement statistics

	Cr81N_Native	Cr81N_Ta_6Br_{12}
Data collection and scaling		
Wavelength (Å)	0.9793	1.2545
Resolution range (Å)	38 - 2.5 (2.6 - 2.5)	38 - 2.3 (2.4 - 2.3)
Space group	P 6_4 2 2	P 6_4 2 2
Unit cell (Å)	75.1, 75.1, 93.4	76.1 76.1, 94.1
Unique reflections	5727 (869)	13616 (2177)
Multiplicity	12.0 (12.0)	20.1 (20.0)
Completeness (%)	99.5 (96.9)	99.8 (98.1)
Mean I/sigma(I)	21.9 (3.0)	49.2 (12.4)
R-sym	0.05 (0.64)	0.03 (0.20)
Refinement		
Number of reflections	5162	13116
Protein residues	120	124
Number of atoms		
Protein	948	981
Ligands (Ta)	NA	4
Water	0	21
R-work	0.2522 (0.3448)	0.2141 (0.2736)
R-free	0.2854 (0.3657)	0.2391 (0.3218)
Ramachandran favoured (%)	95.6	96.6
Ramachandran outliers (%)	0	0
RMS(bonds)	0.009	0.009
RMS(angles)	1.37	1.30
Average B-factors		
Protein	98.7	57.1
Solvent	NA	57.2

Statistics for the highest-resolution shell are shown in parentheses.

Movie S1 and S2

Movies of WT and Dm mutant IFT81 YFP tagged trypanosome cell lines, respectively.

References

1. H. Ishikawa, W. F. Marshall, Ciliogenesis: Building the cell's antenna. *Nat. Rev. Mol. Cell Biol.* **12**, 222–234 (2011). doi:10.1038/nrm3085 Medline

2. K. G. Kozminski, K. A. Johnson, P. Forscher, J. L. Rosenbaum, A motility in the eukaryotic flagellum unrelated to flagellar beating. *Proc. Natl. Acad. Sci. U.S.A.* **90**, 5519–5523 (1993). doi:10.1073/pnas.90.12.5519 Medline

3. J. L. Rosenbaum, G. B. Witman, Intraflagellar transport. *Nat. Rev. Mol. Cell Biol.* **3**, 813–825 (2002). doi:10.1038/nrm952 Medline

4. F. Finetti, S. R. Paccani, M. G. Riparbelli, E. Giacomello, G. Perinetti, G. J. Pazour, J. L. Rosenbaum, C. T. Baldari, Intraflagellar transport is required for polarized recycling of the TCR/CD3 complex to the immune synapse. *Nat. Cell Biol.* **11**, 1332–1339 (2009). doi:10.1038/ncb1977 Medline

5. K. G. Kozminski, P. L. Beech, J. L. Rosenbaum, The *Chlamydomonas* kinesin-like protein FLA10 is involved in motility associated with the flagellar membrane. *J. Cell Biol.* **131**, 1517–1527 (1995). doi:10.1083/jcb.131.6.1517 Medline

6. D. G. Cole, D. R. Diener, A. L. Himelblau, P. L. Beech, J. C. Fuster, J. L. Rosenbaum, *Chlamydomonas* kinesin-II-dependent intraflagellar transport (IFT): IFT particles contain proteins required for ciliary assembly in *Caenorhabditis elegans* sensory neurons. *J. Cell Biol.* **141**, 993–1008 (1998). doi:10.1083/jcb.141.4.993 Medline

7. G. J. Pazour, B. L. Dickert, G. B. Witman, The DHC1b (DHC2) isoform of cytoplasmic dynein is required for flagellar assembly. *J. Cell Biol.* **144**, 473–481 (1999). doi:10.1083/jcb.144.3.473 Medline

8. G. J. Pazour, N. Agrin, J. Leszyk, G. B. Witman, Proteomic analysis of a eukaryotic cilium. *J. Cell Biol.* **170**, 103–113 (2005). doi:10.1083/jcb.200504008 Medline

9. H. Qin, D. R. Diener, S. Geimer, D. G. Cole, J. L. Rosenbaum, Intraflagellar transport (IFT) cargo: IFT transports flagellar precursors to the tip and turnover products to the cell body. *J. Cell Biol.* **164**, 255–266 (2004). doi:10.1083/jcb.200308132 Medline

10. Y. Hou, H. Qin, J. A. Follit, G. J. Pazour, J. L. Rosenbaum, G. B. Witman, Functional analysis of an individual IFT protein: IFT46 is required for transport of outer dynein arms into flagella. *J. Cell Biol.* **176**, 653–665 (2007). doi:10.1083/jcb.200608041 Medline

11. G. Piperno, K. Mead, Transport of a novel complex in the cytoplasmic matrix of *Chlamydomonas* flagella. *Proc. Natl. Acad. Sci. U.S.A.* **94**, 4457–4462 (1997). doi:10.1073/pnas.94.9.4457 Medline

12. C. Ciferri, S. Pasqualato, E. Screpanti, G. Varetti, S. Santaguida, G. Dos Reis, A. Maiolica, J. Polka, J. G. De Luca, P. De Wulf, M. Salek, J. Rappsilber, C. A. Moores, E. D. Salmon, A. Musacchio, Implications for kinetochore-microtubule attachment from the structure of an engineered Ndc80 complex. *Cell* **133**, 427–439 (2008). doi:10.1016/j.cell.2008.03.020 Medline

13. L. Hao, M. Thein, I. Brust-Mascher, G. Civelekoglu-Scholey, Y. Lu, S. Acar, B. Prevo, S. Shaham, J. M. Scholey, Intraflagellar transport delivers tubulin isotypes to sensory cilium

middle and distal segments. *Nat. Cell Biol.* **13**, 790–798 (2011). doi:10.1038/ncb2268 Medline

14. J. Kim, J. E. Lee, S. Heynen-Genel, E. Suyama, K. Ono, K. Lee, T. Ideker, P. Aza-Blanc, J. G. Gleeson, Functional genomic screen for modulators of ciliogenesis and cilium length. *Nature* **464**, 1048–1051 (2010). doi:10.1038/nature08895 Medline
15. J. Buisson, N. Chenouard, T. Lagache, T. Blisnick, J. C. Olivo-Marin, P. Bastin, Intraflagellar transport proteins cycle between the flagellum and its base. *J. Cell Sci.* **126**, 327–338 (2013). doi:10.1242/jcs.117069 Medline
16. K. A. Johnson, J. L. Rosenbaum, Polarity of flagellar assembly in *Chlamydomonas*. *J. Cell Biol.* **119**, 1605–1611 (1992). doi:10.1083/jcb.119.6.1605 Medline
17. W. F. Marshall, J. L. Rosenbaum, Intraflagellar transport balances continuous turnover of outer doublet microtubules: Implications for flagellar length control. *J. Cell Biol.* **155**, 405–414 (2001). doi:10.1083/jcb.200106141 Medline
18. L. Song, W. L. Dentler, Flagellar protein dynamics in *Chlamydomonas*. *J. Biol. Chem.* **276**, 29754–29763 (2001). doi:10.1074/jbc.M103184200 Medline
19. W. F. Marshall, H. Qin, M. Rodrigo Brenni, J. L. Rosenbaum, Flagellar length control system: testing a simple model based on intraflagellar transport and turnover. *Mol. Biol. Cell* **16**, 270–278 (2005). doi:10.1091/mbc.E04-07-0586 Medline
20. N. Sharma, Z. A. Kosan, J. E. Stallworth, N. F. Berbari, B. K. Yoder, Soluble levels of cytosolic tubulin regulate ciliary length control. *Mol. Biol. Cell* **22**, 806–816 (2011). doi:10.1091/mbc.E10-03-0269 Medline
21. G. Hiller, K. Weber, Radioimmunoassay for tubulin: A quantitative comparison of the tubulin content of different established tissue culture cells and tissues. *Cell* **14**, 795–804 (1978). doi:10.1016/0092-8674(78)90335-5 Medline
22. R. E. Stephens, Differential protein synthesis and utilization during cilia formation in sea urchin embryos. *Dev. Biol.* **61**, 311–329 (1977). doi:10.1016/0012-1606(77)90301-3 Medline
23. B. F. Lucker, R. H. Behal, H. Qin, L. C. Siron, W. D. Taggart, J. L. Rosenbaum, D. G. Cole, Characterization of the intraflagellar transport complex B core: Direct interaction of the IFT81 and IFT74/72 subunits. *J. Biol. Chem.* **280**, 27688–27696 (2005). doi:10.1074/jbc.M505062200 Medline
24. M. Taschner, S. Bhogaraju, M. Vetter, M. Morawetz, E. Lorentzen, Biochemical mapping of interactions within the intraflagellar transport (IFT) B core complex: IFT52 binds directly to four other IFT-B subunits. *J. Biol. Chem.* **286**, 26344–26352 (2011). doi:10.1074/jbc.M111.254920 Medline
25. W. Kabsch, XDS. *Acta Crystallogr.* **66**, 125–132 (2010). doi:10.1107/S0907444909047337
26. P. D. Adams *et al.*, PHENIX: A comprehensive Python-based system for macromolecular structure solution. *Acta Crystallogr.* **D66**, 213–221 (2010). doi:10.1107/S0907444909052925

27. K. Cowtan, The Buccaneer software for automated model building. *Acta Crystallogr.* **D62**, 1002–1011 (2006). doi:10.1107/S0907444906022116

28. P. Emsley, B. Lohkamp, W. G. Scott, K. Cowtan, Features and development of Coot. *Acta Crystallogr.* **D66**, 486–501 (2010). doi:10.1107/S0907444910007493

29. T. I. Schmidt, J. Kleylein-Sohn, J. Westendorf, M. Le Clech, S. B. Lavoie, Y. D. Stierhof, E. A. Nigg, Control of centriole length by CPAP and CP110. *Curr. Biol.* **19**, 1005–1011 (2009). doi:10.1016/j.cub.2009.05.016 Medline

30. X. Yan, R. Habedanck, E. A. Nigg, A complex of two centrosomal proteins, CAP350 and FOP, cooperates with EB1 in microtubule anchoring. *Mol. Biol. Cell* **17**, 634–644 (2006). doi:10.1091/mbc.E05-08-0810 Medline

31. J. Kleylein-Sohn, J. Westendorf, M. Le Clech, R. Habedanck, Y. D. Stierhof, E. A. Nigg, Plk4-induced centriole biogenesis in human cells. *Dev. Cell* **13**, 190–202 (2007). doi:10.1016/j.devcel.2007.07.002 Medline

32. K. F. Sonnen, L. Schermelleh, H. Leonhardt, E. A. Nigg, 3D-structured illumination microscopy provides novel insight into architecture of human centrosomes. *Biol. Open* **1**, 965–976 (2012). doi:10.1242/bio.20122337 Medline

33. S. Kelly, J. Reed, S. Kramer, L. Ellis, H. Webb, J. Sunter, J. Salje, N. Marinsek, K. Gull, B. Wickstead, M. Carrington, Functional genomics in *Trypanosoma brucei*: A collection of vectors for the expression of tagged proteins from endogenous and ectopic gene loci. *Mol. Biochem. Parasitol.* **154**, 103–109 (2007). doi:10.1016/j.molbiopara.2007.03.012 Medline

34. G. Burkard, C. M. Fragoso, I. Roditi, Highly efficient stable transformation of bloodstream forms of Trypanosoma brucei. *Mol. Biochem. Parasitol.* **153**, 220–223 (2007). doi:10.1016/j.molbiopara.2007.02.008 Medline

35. L. Kohl, D. Robinson, P. Bastin, Novel roles for the flagellum in cell morphogenesis and cytokinesis of trypanosomes. *EMBO J.* **22**, 5336–5346 (2003). doi:10.1093/emboj/cdg518 Medline

36. A. Stephan, S. Vaughan, M. K. Shaw, K. Gull, P. G. McKean, An essential quality control mechanism at the eukaryotic basal body prior to intraflagellar transport. *Traffic* **8**, 1323–1330 (2007). doi:10.1111/j.1600-0854.2007.00611.x Medline

37. J. A. Deane, D. G. Cole, E. S. Seeley, D. R. Diener, J. L. Rosenbaum, Localization of intraflagellar transport protein IFT52 identifies basal body transitional fibers as the docking site for IFT particles. *Curr. Biol.* **11**, 1586–1590 (2001). doi:10.1016/S0960-9822(01)00484-5 Medline

38. S. D. Guttman, M. A. Gorovsky, Cilia regeneration in starved tetrahymena: An inducible system for studying gene expression and organelle biogenesis. *Cell* **17**, 307–317 (1979). doi:10.1016/0092-8674(79)90156-9 Medline

39. D. P. Weeks, P. S. Collis, Induction of microtubule protein synthesis in *Chlamydomonas reinhardi* during flagellar regeneration. *Cell* **9**, 15–27 (1976). doi:10.1016/0092-8674(76)90048-9 Medline

40. C. D. Silflow, J. L. Rosenbaum, Multiple alpha- and beta-tubulin genes in *Chlamydomonas* and regulation of tubulin mRNA levels after deflagellation. *Cell* **24**, 81–88 (1981). doi:10.1016/0092-8674(81)90503-1 Medline

41. V. Stolc, M. P. Samanta, W. Tongprasit, W. F. Marshall, Genome-wide transcriptional analysis of flagellar regeneration in *Chlamydomonas reinhardtii* identifies orthologs of ciliary disease genes. *Proc. Natl. Acad. Sci. U.S.A.* **102**, 3703–3707 (2005). doi:10.1073/pnas.0408358102 Medline

42. C. Janke, J. C. Bulinski, Post-translational regulation of the microtubule cytoskeleton: mechanisms and functions. *Nat. Rev. Mol. Cell Biol.* **12**, 773–786 (2011). doi:10.1038/nrm3227 Medline

43. M. T. Bedford, S. G. Clarke, Protein arginine methylation in mammals: Who, what, and why. *Mol. Cell* **33**, 1–13 (2009). doi:10.1016/j.molcel.2008.12.013 Medline

44. M. J. Schneider, M. Ulland, R. D. Sloboda, A protein methylation pathway in *Chlamydomonas* flagella is active during flagellar resorption. *Mol. Biol. Cell* **19**, 4319–4327 (2008). doi:10.1091/mbc.E08-05-0470 Medline

45. R. D. Sloboda, L. Howard, Protein methylation in full length *Chlamydomonas* flagella. *Cell Motil. Cytoskeleton* **66**, 650–660 (2009). doi:10.1002/cm.20387 Medline

46. P. V. Hornbeck, J. M. Kornhauser, S. Tkachev, B. Zhang, E. Skrzypek, B. Murray, V. Latham, M. Sullivan, PhosphoSitePlus: A comprehensive resource for investigating the structure and function of experimentally determined post-translational modifications in man and mouse. *Nucleic Acids Res.* **40**, (D1), D261–D270 (2012). doi:10.1093/nar/gkr1122 Medline

47. S. Absalon, T. Blisnick, L. Kohl, G. Toutirais, G. Doré, D. Julkowska, A. Tavenet, P. Bastin, Intraflagellar transport and functional analysis of genes required for flagellum formation in trypanosomes. *Mol. Biol. Cell* **19**, 929–944 (2008). doi:10.1091/mbc.E07-08-0749 Medline

2.2) Chapter II

‘The CH domain of IFT54 binds tubulin whereas the CH domains of IFT38 and IFT57 interact with IFT80 and IFT172, respectively’

The CH domain of IFT54 binds tubulin whereas the CH domains of IFT38 and IFT57 interact with IFT80 and IFT172, respectively

Kristina Weber, Michael Taschner, Marc Stiegler and Esben Lorentzen*

Department of Structural Cell Biology, Max-Planck-Institute of Biochemistry, Am Klopferspitz 18, D-82152 Martinsried, Germany

E-mail: lorentze@biochem.mpg.de
* Corresponding author
Phone: + 49 (89) 8578 – 3479
Fax: + 49(89) 8578 – 3605

Keywords: cilia; intraflagellar transport; IFT172; IFT80; IFT57; IFT54; IFT38; IFT20; Cluap1; tubulin, Calponin Homology domain, CH domain

Abbreviations: CC: coiled coil, CH: Calponin Homology domain, IFT: intraflagellar transport, MT: microtubule

Abstract

The Intraflagellar transport (IFT) system is needed to form and maintain the cilium, an important organelle that functions in motility, sensory reception and signaling on many different cell types. Recently it has been shown that the Calponin Homology (CH) domain of IFT81 together with the positively charged N-terminal patch of IFT74 serves as tubulin-binding module, linking tubulin transport within cilia to IFT. Three additional CH domains are predicted in IFT38, IFT54 and IFT57. Here, we show that IFT20/54 and IFT38/57 can be expressed and purified in two stable subcomplexes. Furthermore, we solved the high-resolution crystal structure of the IFT54 CH domain and show that this domain mediates tubulin binding within the IFT20/54 complex. In contrast, the CH domains of IFT38/57 lost their ability to bind tubulin and instead mediate interactions with IFT80 and IFT172 within the IFT-B complex.

Introduction

Cilia are microtubule (MT)-based appendages protruding from the surface of many different cell types (Fliegauf et al., 2007). To build and maintain a functional cilium a specialized intraflagellar transport (IFT) is in place (Kozminski et al., 1993). The IFT complex consists of 22 proteins that can be divided into two subcomplexes, IFT-A and IFT-B (Cole et al., 1998; Fan et al., 2010; Follit et al., 2009; Ishikawa et al., 2014; Lechtreck et al., 2009; Lucker et al., 2005; Omori et al., 2008; Piperno and Mead, 1997). Nine of the IFT-B proteins have been shown to form a stable 'IFT-B core' consisting of IFT88/81/74/70/52/46/27/25/22 (Taschner et al., 2014). Yeast-2-hybrid assays further indicate an interaction between IFT56 and IFT46, pointing to IFT56 as a member of the 'IFT-B core' (Swiderski et al., 2014). The remaining six IFT-B proteins (IFT172, IFT80, IFT57, IFT54, IFT38, IFT20) are considered as 'peripheral' proteins (Cole et al., 1998; Follit et al., 2009; Lucker et al., 2005; Nachury, 2014).

Ciliary cargo is transported via IFT and the motor protein heterotrimeric kinesin II from the basal body region to the tip of the cilium (anterograde IFT) (Cole et al., 1998; Craft et al., 2015; Hao et al., 2011; Kozminski et al., 1995; Qin et al., 2004). At the ciliary tip, exchange of the cargo and remodeling of the IFT complex takes place and dynein 2 transports the IFT complex and recycling products back to the cell body (retrograde IFT) (Marshall and Rosenbaum, 2001; Pazour et al., 1999; Porter et al., 1999; Qin et al., 2004; Signor et al., 1999). Given that >600 different proteins function inside the cilium and in the ciliary membrane (Pazour et al., 2005) only little is known about cargo interaction sites within the IFT complex.

Recently, Bhogaraju and colleagues could show that the 'IFT-B core' proteins IFT81/74 provide a tubulin-binding module (Bhogaraju et al., 2013). The N-terminal part of IFT81 adopts a Calponin Homology (CH) domain fold and selectively binds to the globular domain of tubulin whereas the positively charged N-terminus of IFT74 strengthens the binding via interaction with the negatively charged E-hooks of β-tubulin. Quantification of the binding revealed a K_d of 0.9 µM. Furthermore, in *Chlamydomonas reinhardtii* it has been shown that the frequency of GFP-tubulin moved by anterograde IFT in growing cilia is elevated (18.3 ± 6.9 particles/min) compared to steady-state cilia (~0.3 particles/min) (Craft et al., 2015). Given that the entry rate of IFT-trains does not correlate with the length of cilia (Craft et al., 2015; Dentler, 2005; Engel et al., 2009), Craft and colleagues proposed a model in which growing cilia induce a signal resulting in an increased load of tubulin onto IFT particles and thus to an elevated tubulin concentration within cilia (Craft et al., 2015).

The ciliary axoneme has a MT-based backbone. Therefore, the main building block to assemble a cilium is tubulin. Thus, the question arises if one tubulin-binding module within IFT is sufficient to assemble a cilium. Calculations done, taken into account the growing rate of the cilium (Rosenbaum et al., 1969), the frequency of IFT particle entrance into a cilium (Dentler, 2005; Engel et al., 2009; Mueller et al., 2005) and the length of IFT-trains (Pigino et al., 2009), led to the hypothesis of more than one tubulin-binding module within the IFT machinery to achieve the transport rate of tubulin necessary to assemble functional cilia (Bhogaraju et al., 2014). Bioinformatics analysis using the HHPred algorithm (Soding et al., 2005) predicted three additional CH domains in the N-terminal part of IFT38, IFT54 and IFT57 (Schou et al., 2014; Taschner et al., 2012). Therefore, these three proteins are possible candidates for additional tubulin-binding sites within the IFT process.

To understand the interplay between different IFT-B proteins as well as to identify further possible cargo interaction sites we focused in this study on IFT20, IFT38, IFT54 and IFT57 due to the similar domain architecture of the latter three. Here we show that IFT57 directly interacts with IFT38, as part of the IFT-B complex. In addition, we solved the high-resolution structure of the N-terminal CH domain of IFT54 and could verify their tubulin-binding ability indicating another cargo-binding site within the IFT complex. Furthermore, we observed that the predicted CH domains of IFT38 and IFT57 lost their tubulin-binding ability and instead mediate the binding to IFT80 and IFT172.

Results

Purification of the IFT54/20 complex

An interaction between IFT20 and IFT54 was reported based on immunoprecipitation (Follit et al., 2009) and yeast-2-hybrid assays (Omori et al., 2008). To obtain a stable IFT20/54 subcomplex for detailed biochemical studies, *Chlamydomonas reinhardtii* IFT20 and IFT54 were recombinantly expressed in insect cells. Whereas IFT20 could be purified in isolation, IFT54 was prone to degradation during the purification procedure. Thus, co-expression was carried out, resulting in a dimeric IFT54/20 complex (Fig. 1B). Mass spec analysis identified the proteins as full-length.

In order to test whether the C-terminal coiled coil (CC) regions are sufficient to mediate complex formation, truncated *C. reinhardtii* (*Cr*) and *M. musculus* (*Mm*) versions harboring the CC region of IFT20 (*Cr*IFT20$_{1\text{-}125}$, *Mm*IFT20) and IFT54 (*Cr*IFT54$_{346\text{-}510}$, *Mm*IFT54$_{462\text{-}625}$) were designed, expressed in *E.coli* and purified. Size exclusion chromatography (SEC) resulted in a single peak that shifted to higher MW compared to the single proteins, showing that indeed the CC regions are sufficient to form the dimeric complex (Fig. 1C, S1A). Secondary structure predictions revealed an additional α-helical CH domain at the very N-terminus of IFT54. The CH domain was cloned (*Cr*IFT54$_{1\text{-}134}$, *Mm*IFT54$_{1\text{-}133}$), purified and tested for their ability to bind IFT20. The SEC elution profiles resulted in two peaks, showing that the CH domain in IFT54 is not able to interact with IFT20. In agreement with previously published results (Follit et al., 2009; Omori et al., 2008), this demonstrates that *C. reinhardtii* and *M. musculus* IFT20 interacts with IFT54 via the CC region and not the CH domain (Fig. 1D, S1B).

Furthermore, a direct interaction between IFT20 and IFT57 was reported (Baker et al., 2003; Krock and Perkins, 2008) although it was not confirmed in a later study (Lucker et al., 2010). To assess if IFT20, IFT54 and IFT57 can form a trimeric complex, pull down experiments using the purified CC regions of IFT20, IFT54 and IFT57 (*Cr*IFT20$_{1\text{-}125}$, *Cr*IFT54$_{346\text{-}510}$, *Cr*IFT57$_{301\text{-}469}$) were performed. The obtained results clearly demonstrated that GST-tagged IFT57CC does not interact with IFT20CC/54CC (Fig. 1E).

IFT38 interacts directly with IFT57

IFT38 (also known as FAP22 (*C. reinhardtti*), DYF-3 (*C.elegans*), Cluap1 (mammals), Qilin (*D.rerio*) and PIFTA1 (*T. brucei*)) has been shown to undergo IFT (Ou et al., 2005) and is required for ciliogenesis in *Trypanosoma bruceii* (Absalon et al., 2008). Furthermore, IFT38 can be pulled down amongst other IFT-B proteins from zebrafish lysate using TAP-IFT54-GFP (Omori et al., 2008), pointing to IFT38 as a member of the IFT-B complex.

Both, IFT38 and IFT57 harbor C-terminal CC regions, known to mediate protein-protein interactions. Therefore, it was tested whether these two proteins form a complex. Single expression of *Cr*IFT38 in insect cells resulted in insoluble protein. *Cr*IFT57 was soluble but tended to aggregate during the purification procedure. Co-expression of IFT38 and IFT57 resulted in a soluble complex, eluting in a single peak in SEC (Fig. 2A). In order to confirm the formation of an IFT38/57 complex, analytical ultracentrifugation (AUC) was performed. AUC resulted in one peak with a MW of 81 kDa, which corresponds to the predicted molecular weight of a heterodimeric IFT38/57 complex ($MW_{calculated}$ = 93 kDa) (Fig. 2B).

In summary, we could confirm the direct interaction between IFT20/54 as previously reported (Follit et al., 2009; Omori et al., 2008). Additionally, we identified a new direct interaction between IFT38 and IFT57 demonstrating that IFT38 is indeed a member of the IFT-B complex.

IFT20/54 but not IFT38/57 binds tubulin via the N-terminal CH domain

The Calponin Homology (CH) domain is well known from various tubulin/MT- or actin-binding proteins, like the MT-plus-end tracking protein EB1 (Hayashi and Ikura, 2003), Ndc80 that plays important roles in kinetochore-MT attachment during cell division (Ciferri et al., 2008) and actinin4, involved in the scaffolding and organization of the cytoskeleton (Lee et al., 2008). In order to test if the predicted CH domains in IFT38, IFT54 and IFT57 also function in MT/tubulin-binding, pull down experiments were carried out using recombinantly purified *Cr*IFT20/54 and *Cr*IFT38/57. Surprisingly, IFT20/54 but not IFT38/57 was able to pull down tubulin (Fig. 3A). Quantification of the binding between tubulin and *Cr*IFT20/54 was achieved by performing microscale thermophoresis (MST) measurements, where fluorescently labeled tubulin was titrated with untagged *Cr*IFT20/54 and revealed a binding constant (K_d) of 3 µM (Fig. 3B). To further narrow down the tubulin-binding region of IFT54, the N-terminal CH domain of IFT54 was also tested for its tubulin binding ability. Previous studies already showed that the N-terminal part of IFT54 is able to interact with tubulin (Ling and Goeddel, 2000). By pull down experiments, we mapped the tubulin-binding region of IFT54 to the CH domain in IFT54 (*Cr*$IFT54_{1-134}$, *Mm*$IFT54_{1-133}$) (Fig. 3C). In order to reveal the IFT54 CH domain binding site on tubulin, we further tested if the globular domain of tubulin is sufficient for binding to IFT54, like in IFT81 (Bhogaraju et al., 2013) or whether the E-hooks of tubulin are crucial for the binding to IFT54. Therefore, tubulin was treated with the protease subtilisin for 20 min to cut off the C-terminal tail of β-tubulin or for 130 min to also remove the C-terminal tail of α-tubulin. Subtilisin-treated tubulin was then used in pull down experiments. The CH domain of *M. musculus* IFT54 was still able to bind to tubulin regardless of the presents of E-hooks, indicating that the IFT54 CH domain binds to the globular domain of tubulin (Fig. 3D).

IFT20/54 also binds to MTs

In order to verify the MT-binding ability of IFT20/54, MT-sedimentation assays were performed. Adding MTs to *Cr*IFT20/54 resulted in pelleting of IFT20/54 thus confirming the interaction between IFT20/54 and MTs (Fig. 4A). MTs are built from polymerized αβ-tubulin heterodimers. In the previous section we could show that the CH domain of IFT54 binds to tubulin, therefore it was tested if the CH domain is also sufficient to mediate the binding to MTs. Surprisingly, the CH domain of IFT54 alone is either not able to bind to MTs (*C. reinhardtti*, Fig. 4B) or binds MTs only very weakly (*M. musculus*, data not shown). But as already reported from Bhogaraju and colleagues the CH domain in IFT81 is sufficient to bind MTs but the positively charged N-terminus of IFT74 increases the binding affinity (Bhogaraju et al., 2013). A closer look at the unstructured region between the CH domain and the CC region of IFT54 revealed a slightly positive charge at pH 7.5 with an isoelectric point (pI) of 9.32. Therefore, longer constructs of *C. reinhardtii* and *M. musculus* IFT54 were designed, including the CH domain followed by different lengths of the unstructured region (*Cr*IFT54$_{1\text{-}187}$, *Cr*IFT54$_{1\text{-}227}$, *Cr*IFT54$_{1\text{-}346}$, *Mm*IFT54$_{1\text{-}190}$, *Mm*IFT54$_{1\text{-}257}$). The longest *Cr*IFT54 constructs spans till the predicted start of the CC region. All longer constructs tested in the MT-sedimentation assay were able to bind to MTs (*C. reinhardtti*, data not shown; *M. musculus*, Fig. 4C). This finding suggests that parts of the positively charged unstructured region in IFT54 contribute to MT-binding.

Taken together, IFT20/54 but not IFT38/57 is able to bind to tubulin/MTs. Within IFT54 itself, the CH domain together with the slightly positive charged patch adjacent to the CH domain mediates the binding to tubulin/MTs.

Crystal structure of the IFT54 CH domain

Crystallization trials were performed with the N-terminal CH domain of IFT54 (*Cr*IFT54$_{1\text{-}134}$, *Mm*IFT54$_{1\text{-}133}$) to further elucidate the MT/tubulin-binding ability of IFT54. Crystals were obtained for the *C. reinhardtii* and *M. musculus* IFT54 CH domain (Fig. S2). Native crystals diffracted to 1.9Å (*Cr*IFT54$_{1\text{-}134}$) and 1.6Å (*Mm*IFT54$_{1\text{-}133}$). A SAD dataset of Selenomethionine substituted *Cr*IFT54$_{1\text{-}134}$ crystals was also collected at the Se peak wavelength at the Swiss Light Source (Villigen, Switzerland). The final model of *Cr*IFT54$_{1\text{-}134}$ (R-free: 0.244 and R-work: 0.2087) was used as a molecular replacement model to solve the structure of *Mm*IFT54$_{1\text{-}133}$ (R-free: 0.2161 and R-work: 0.1905) (table S1, Fig. 5A and B). The solved structure shows a bundle of five α-helices adopting the fold of a CH domain. Overlying the *C. reinhardtii* and *M. musculus* IFT54 CH domain gave a very high accordance, as expected from the sequence alignments (Fig. 6A) with a root-mean-square deviation (RMSD) of 0.750 Å (665 to 665 atoms). In contrast, superimposing the CH domains of IFT54 and IFT81 revealed a slightly different arrangement (RMSD: 3.3) (Fig. 5C).

A conserved patch of the IFT54 CH domain mediates the binding to tubulin

Electrostatic surface potential analysis showed a positively charged patch at one side of the IFT54 CH domain, which is evolutionarily conserved (Fig. 6C and D). It is very likely that this patch mediates the binding to MTs/tubulin due to possible electrostatic interactions with the negatively charged E-hooks of tubulin. Although we could show that the globular domain of tubulin is sufficient to mediate the binding between tubulin and the CH domain of IFT54 (Fig. 3D), the electrostatic interactions could still contribute to the binding. In order to address if the positively charged patch of the IFT54 CH domain is indeed the site of interaction with tubulin, tubulin-binding mutants of the *M. musculus* IFT54 CH domain were designed (Fig. 6B). Five single mutations and one triple mutation were cloned, expressed in E.coli cells and purified (Fig. S3). Tubulin pull down experiments were carried out with all six mutants. Surprisingly, all five single mutants either located in the positively charged patch (R18E, K25E, K29E, R33E) or next to the patch (R94) were able to bind to tubulin. The triple mutant (K64E K66E K69E) located at the edge of the positively charged patch completely abolished tubulin binding (Fig. 6E and F). This demonstrates that positively charged surface residues of the IFT54 CH domain mediate tubulin binding.

The CH domains of IFT38 and IFT57 directly interact with IFT80 and IFT172

The IFT20/54 complex binds tubulin via the CH domain in IFT54 (see previous sections). But we could not detect any interaction between IFT38/57 and tubulin (Fig. 3A). In order to verify if IFT20/54 and IFT38/57 interact with the 'IFT-B core', we performed *in vitro* pull down assays with recombinantly expressed proteins but could not observe any binding (data not shown). Therefore, we put our attention on the remaining IFT-B proteins.

Full length *Cr*IFT172 was expressed in insect cells but it was not soluble during the purification procedure. Therefore, we focused on a truncated version of IFT172. IFT172ΔC (IFT172$_{1\text{-}968}$) and full length IFT80 were expressed in insect cells and purified (Fig S4). SEC analysis revealed that IFT172ΔC and IFT80 do not form a complex (data not shown). In affinity pull down assays using a mixture of recombinantly purified IFT172ΔC/IFT80 and the CH domains of IFT38 (*Cr*IFT38$_{1\text{-}133}$) and IFT57 (*Cr*IFT57$_{1\text{-}234}$) we could observe that the CH domain in IFT38 selectively pulls down IFT80 whereas the CH domain in IFT57 interacts with IFT172ΔC. The CC regions of IFT38 (*Cr*IFT38$_{126\text{-}325}$) and IFT57 (*Cr*IFT57$_{301\text{-}469}$) do not contribute to complex formation. Taken together, the predicted CH domains in IFT38 and IFT57 lost their ability to bind tubulin but instead mediate the interaction to the IFT-B proteins IFT172 and IFT80.

Discussion

We could confirm the reported interaction between IFT20 and IFT54 (Follit et al., 2009; Omori et al., 2008) with recombinantly purified proteins. An interaction between IFT20 and IFT57, as reported previously (Baker et al., 2003; Krock and Perkins, 2008) is rather unlikely taking the results presented here into account. Moreover, a strong direct interaction between IFT38 and IFT57 could be shown, pointing to IFT38 as a new member of the IFT-B complex.

Furthermore we were able to confirm the tubulin/MT-binding ability of IFT54 reported by Ling and colleagues (Ling and Goeddel, 2000). Structural determination of the predicted α-helical domain at the N-terminus of IFT54 clearly showed that the domain adopts a CH domain fold. We could obtain tubulin binding for the *C. reinhardtti* and *M. musculus* IFT54 CH domain as well as for the *Cr*IFT20/54 full-length complex but surprisingly not for the *Cr*IFT38/57 complex, although the predicted α-helical domains in IFT38 and IFT57 are classified as CH domains (Schou et al., 2014; Taschner et al., 2012).

Regarding the tubulin/MT binding of IFT54, we could clearly show that indeed the CH domain mediates the interaction to tubulin because a triple mutant (*Mm*IFT54$_{\text{K64E K66E K69E}}$) abolished tubulin binding. Even though both *C. reinhardtti* and *M. musculus* IFT54 CH domains are able to bind tubulin, differences occur in their binding ability to MTs. Whereas in *M. musculus* the CH domain of IFT54 is sufficient to obtain MT binding, in *C. reinhardtii* the presence of the slightly positive patch adjacent to the CH domain clearly supports MT binding.

For the binding of IFT81/74 to tubulin a K_d of 0.9 µM was measured (Bhogaraju et al., 2013). In this study we determined a slightly higher K_d (3 µM) for the binding of IFT20/54 to tubulin. An explanation for the differences in the obtained affinities of IFT81/74 and IFT20/54 to tubulin could be the model presented by Craft et al., (Craft et al., 2015). They proposed that the load of tubulin on IFT-trains increases in a growing cilium, therefore we hypothesize that the tubulin-binding sites of both IFT81/74 and IFT20/54 are occupied by tubulin. In contrast, in a steady-state cilium only the IFT81/74 module with a higher affinity to tubulin is loaded with tubulin.

Taken together, we could confirm the prediction of additional tubulin-binding modules apart from IFT81/74 (Bhogaraju et al., 2013) within the IFT complex (Bhogaraju et al., 2014). The IFT20/54 complex serves as a second tubulin-binding module via its CH domain in IFT54. If further binding sites for tubulin/MTs exist in the IFT machinery still has to be elucidated. In contrast, the predicted CH domains in IFT38 and IFT57 lost their tubulin-binding ability and mediate the binding to the IFT-B proteins IFT80 and IFT172.

Material and Methods

Cloning, expression and purification of recombinant proteins from E.coli

Truncations of *Cr*IFT57, *Cr*/*Mm*IFT54, *Cr*IFT38 and *Cr*/*Mm*IFT20 either containing the N-terminal CH domain or the C-terminal CC region were cloned into bacterial pEC vectors with cleavable GST- or hexahistidine (HIS)-tags as described previously (Taschner et al., 2014) and expressed in the E.coli BL21 (DE3) Gold pLysS strain. E.coli cells were lysed by sonication in 50 mM Tris*HCL pH 7.5, 150 mM NaCl, 5 mM β-mercaptoethanol and 10% glycerol. The lysates were cleared by centrifugation (Beckman Coulter® Avanti® J-26XPI, 25000 rpm) and passed over a Ni^{2+}-NTA column (affinity chromatography, GE Healthcare). After affinity-tag cleavage using tobacco etch virus (TEV) protease, anion exchange chromatography (MonoQ, GE healthcare) and size exclusion chromatography (SEC) (HiLoad75, GE healthcare) in 10 mM HEPES pH 7.5, 150 mM NaCl and 1 mM DTT was performed. All samples were analyzed using SDS-PAGE.

Cloning, expression and purification of recombinant proteins from insect cells

For heterodimeric *Cr*IFT54/20 and *Cr*IFT38/57 complex purification as well as *Cr*IFT172ΔC and *Cr*IFT80, the proteins were cloned either untagged or with TEV-cleavable HIS-tag into pFL vectors. After producing viral particles as previously described (Taschner et al., 2014), the proteins/protein complexes were expressed by infection of HighFive insect cells (Invitrogen). The cells were homogenized using a Dounce Homogenizer in a 20 mM HEPES pH 7.5 buffer containing 250 mM sucrose, 5 mM β-mercaptoethanol, 10 mM KCl, 1.5 mM $MgCl_2$ and protease inhibitor cocktail (Roche) and then purified in large-scale as described above.

Affinity pull down experiments

Tubulin pull down experiments were carried out using a final concentration of 4 µM tubulin (Cytoskeleton #TL238) mixed with 7 µM HIS-tagged protein/protein complex in a total volume of 100 µL 1xBRB80 (80 mM PIPES-KOH, 1 mM $MgCl_2$, 1 mM EGTA, pH 6.8) buffer supplemented with 20 mM imidazole. After 30 min of pre-incubation, the protein solution was incubated with BSA-blocked Ni^{2+}-NTA beads. After extensive washing the proteins were eluted from the beads using 1xBRB80 buffer supplemented with 500 mM Imidazole. Pull downs were analyzed using SDS PAGE followed by Western Blot. The nitrocellulose membrane was pre-blocked for 30 min in 5% milk/PBST before the 1st antibody (anti-alpha tubulin (mouse), Sigma-Aldrich T9026) was added for at least one hour. After three washes in PBST the 2nd antibody (anti-mouse IgG-HRP (goat), Enzo BML-SA204-0100) was added to the membrane for 45 min, followed by three washes in PBST. The Amersham™ ECL™ Prime Western Blotting Detection Reagent from GE Healthcare and an ImageQuant LAS4000 device (GE Healthcare) was used to detect the signal.

Pull down experiments to determine the interaction between different proteins or complexes, were also performed. Therefore 60 µg of purified GST- or HIS-tagged protein/protein complex was mixed with an excess of purified HIS-tagged or untagged protein in a total volume of 150 µL buffer (10 mM HEPES pH 7.5, 100 mM NaCl, 10% glycerol, 1 mM DTT, 10 mM Imidazole), pre-incubated for 30 min at 4°C, and then incubated on BSA-blocked GSH- or Ni^{2+}-NTA-beads. Extensively washing with buffer was followed by an elution step using the same buffer supplemented either with 30 mM reduced glutathione (GSH-beads) or with 500 mM Imidazole (Ni^{2+}-NTA beads). All pull downs were analyzed using SDS-PAGE.

Analytical ultracentrifugation (AUC)

Sedimentation velocity experiments were performed on an Optima XL-I analytical ultracentrifuge (Beckman Inc., Palo Alto, Ca, U.S.A.) using an An-60 Ti rotor and double-sector epon centerpieces. The *Cr*IFT38/57 complex (0.56 mg/mL) was in a 10 mM HEPES (pH 7.5) buffer containing 100 mM NaCl, 10% glycerol and 2 mM TCep. Buffer density and viscosity was measured using a DMA 5000 densitometer and an AMVn viscosimeter, respectively (both Anton Paar, Graz, Austria). Protein concentration distribution was monitored at 280 nm, at 54.000 rpm and 20°C. Time-derivative analysis was computed using the SEDFIT software package, version 12.1b (Schuck, 2000), resulting in a c(s) distribution and an estimate for the molecular weight Mf (from the sedimentation coefficient and the diffusion coefficient, as inferred from the broadening of the sedimentation boundary, assuming all observed species share the same frictional coefficient f/f0).

Microscale thermophoresis (MST)

The lysine side chains of bovine tubulin (Cytoskeleton #TL238) were fluorescently labeled using the Cy3 protein labeling kit from Jena Bioscience according to their protocol. 100 nM of fluorescently labeled tubulin were then titrated with purified *Cr*IFT20/54 (200 µM) in a total volume of 20 µL to carry out 16 data points. The measurements were recorded on a NanoTemper Monolith NT.115 device (NanoTemper Technologies GmbH) using the following settings: LED power 65% (green), MST power 50%, Laser on 40sec, Laser off 5sec. The raw data were then analyzed using the software from NanoTemper to visualize the binding curves and Prism (GraphPad Software) to calculate the K_ds.

Subtilisin treatment of tubulin

Bovine tubulin (Cytoskeleton #TL238) was incubated at 30°C with 1.25 µM of the protease subtilisin. Incubation time was either 20 min to cut off the C-terminal tail of β-tubulin or 130 min to remove also the C-terminal tail of α-tubulin. 1 mM PMSF was added to stop the proteolysis. After ultracentrifugation in a Beckmann TLA100 rotor (68000 rpm, 30min, 35°C) the pellet was resuspended in 20 µL of 1xBRB80.

Subtilisin-treated tubulin was purified using size exclusion chromatography (SEC) (Superdex200, GE healthcare) (Bhogaraju et al., 2013) and then used for tubulin pull downs.

MT-cosedimentation assay

Lyophylized bovine tubulin (Cytoskeleton #TL238) was solved in 1xBRB80 buffer supplemented with 3 mM GTP according to the manufactures protocol and incubated for 45min at 37°C. 50 µM Taxole was added to stabilize the polymerization of tubulin. After a second incubation for 40min at 37°C, ultracentrifugation in a Beckmann TLA100 rotor (68000 rpm, 30min, 37°C) was performed and the pelleted MTs resuspended in 20 µL of 1xBRB80 supplemented with 20 µM Taxole.

2 µM of the polymerized MTs were mixed with 2 µM of protein/protein complex in a total volume of 50 µL 1xBRB80 buffer containing 5 mM DTT and 20 µM Taxole. After 20 min incubation at room temperature the reaction mix was pipetted on 100 µL Cushion buffer (1xBRB80, 50% glycerol, 20 µM Taxole). After ultracentrifugation in a Beckmann TLA100 rotor (48000 rpm, 20min, 25°C), a supernatant sample was taken, the pellet extensively washed with 1xBRB80, 20 µM Taxole buffer and then resuspended in 2x SDS loading dye. Supernatant and pellet samples were then analyzed by SDS-PAGE. Western Blot analysis was carried out as described above. The 1st antibody (anti-HIS-tag (Novagen 70796-3)) was used to detect the HIS-tagged protein/protein complex and as 2nd antibody anti-mouse IgG-HRP (goat) (Enzo BML-SA204-0100).

Crystallization of the IFT54 CH-domain

The CH domains of *C. reinhardtii* and *M. musculus* IFT54 were expressed and purified in large-scale amounts as described above. Furthermore, *Cr*IFT54CH was also expressed in E.coli BL21 (DE3) Gold pLysS strain growing in medium containing Selenomethionine (SeMet) and purified, to obtain the phases needed to solve the high-resolution structure. All crystals appeared using the sitting drop vapour diffusion method after mixing the protein solution at a ratio of 1:1 with the reservoir solution. *Cr*IFT54CH (~28 mg/mL) crystals were obtained at 18°C in 50 mM Tris*HCL pH 8.3 supplemented with 2% MPD, 80 mM ammonium sulfate, 30% PEG5000 and 5% glycerol. *Cr*IFT54CH SeMet (~24 mg/mL) crystals grew at 18°C in 50 mM Tris*HCL pH 8.3, 80 mM ammonium sulfate, 2% MPD, 26% PEG5000 and

7% glycerol. Crystals of *Mm*IFT54CH (~36 mg/mL) were obtained at 4°C in a solution containing 4% MPD, 0.2 M ammonium acetate, 32% PEG3350 and 50 mM MES pH 5.8.

Data collection and structure determination

Native *Cr*IFT54CH crystals diffracted X-rays to 1.9Å, *Mm*IFT54CH crystals to 1.6Å and *Cr*IFT54CH SeMet crystals to 2Å at the Swiss Light Source (Villigen, Switzerland). The final model of *Cr*IFT54CH was taken as a molecular replacement model to solve the structure of *Mm*IFT54CH. XDS was used to process the data, model building and refinement was performed with COOT and PHENIX.

References

Absalon, S., Blisnick, T., Kohl, L., Toutirais, G., Dore, G., Julkowska, D., Tavenet, A., and Bastin, P. (2008). Intraflagellar transport and functional analysis of genes required for flagellum formation in trypanosomes. Mol Biol Cell *19*, 929–944.

Baker, S., Freeman, K., Luby-Phelps, K., Pazour, G., and Besharse, J. (2003). IFT20 links kinesin II with a mammalian intraflagellar transport complex that is conserved in motile flagella and sensory cilia. J Biol Chem *278*, 34211–34218.

Bhogaraju, S., Cajanek, L., Fort, C., Blisnick, T., Weber, K., Taschner, M., Mizuno, N., Lamla, S., Bastin, P., Nigg, E.A., et al. (2013). Molecular Basis of Tubulin Transport Within the Cilium by IFT74 and IFT81. Science *341*, 1009–1012.

Bhogaraju, S., Weber, K., Engel, B.D., Lechtreck, K.-F., and Lorentzen, E. (2014). Getting tubulin to the tip of the cilium: One IFT train, many different tubulin cargo-binding sites? Bioessays *36*, 463–467.

Ciferri, C., Pasqualato, S., Screpanti, E., Varetti, G., Santaguida, S., Reis, Dos, G., Maiolica, A., Polka, J., De Luca, J., De Wulf, P., et al. (2008). Implications for kinetochore-microtubule attachment from the structure of an engineered Ndc80 complex. Cell *133*, 427–439.

Cole, D., Diener, D., Himelblau, A., Beech, P., Fuster, J., and Rosenbaum, J. (1998). Chlamydomonas kinesin-II-dependent intraflagellar transport (IFT): IFT particles contain proteins required for ciliary assembly in Caenorhabditis elegans sensory neurons. J Cell Biol *141*, 993–1008.

Craft, J.M., Harris, J.A., Hyman, S., Kner, P., and Lechtreck, K.F. (2015). Tubulin transport by IFT is upregulated during ciliary growth by a cilium-autonomous mechanism. The Journal of Cell Biology *208*, 223–237.

Dentler, W. (2005). Intraflagellar transport (IFT) during assembly and disassembly of Chlamydomonas flagella. J Cell Biol *170*, 649–659.

Engel, B.D., Ludington, W.B., and Marshall, W.F. (2009). Intraflagellar transport particle size scales inversely with flagellar length: revisiting the balance-point length control model. J Cell Biol *187*, 81–89.

Fan, Z.-C., Behal, R.H., Geimer, S., Wang, Z., Williamson, S.M., Zhang, H., Cole, D.G., and Qin, H. (2010). Chlamydomonas IFT70/CrDYF-1 is a core component of IFT particle complex B and is required for flagellar assembly. Mol Biol Cell *21*, 2696–2706.

Fliegauf, M., Benzing, T., and Omran, H. (2007). When cilia go bad: cilia defects and ciliopathies. Nat Rev Mol Cell Biol *8*, 880–893.

Follit, J., Xu, F., Keady, B., and Pazour, G. (2009). Characterization of mouse IFT complex B. Cell Motil Cytoskeleton *66*, 457–468.

Hao, L., Thein, M., Brust-Mascher, I., Civelekoglu-Scholey, G., Lu, Y., Acar, S., Prevo, B., Shaham, S., and Scholey, J. (2011). Intraflagellar transport delivers tubulin isotypes to sensory cilium middle and distal segments. Nat Cell Biol *13*, 790–798.

Hayashi, I., and Ikura, M. (2003). Crystal structure of the amino-terminal microtubule-binding domain of end-binding protein 1 (EB1). J Biol Chem *278*, 36430–36434.

Ishikawa, H., Ide, T., Yagi, T., Jiang, X., Hirono, M., Sasaki, H., Yanagisawa, H., Wemmer, K.A., Stainier, D.Y., Qin, H., et al. (2014). TTC26/DYF13 is an intraflagellar transport protein required for transport of motility-related proteins into flagella. Elife *3*, e01566.

Kozminski, K., Beech, P., and Rosenbaum, J. (1995). The Chlamydomonas kinesin-like protein FLA10 is involved in motility associated with the flagellar membrane. J Cell Biol *131*, 1517–1527.

Kozminski, K., Johnson, K., Forscher, P., and Rosenbaum, J. (1993). A motility in the eukaryotic flagellum unrelated to flagellar beating. Proc Natl Acad Sci U S A *90*, 5519–5523.

Krock, B., and Perkins, B. (2008). The intraflagellar transport protein IFT57 is required for cilia maintenance and regulates IFT-particle-kinesin-II dissociation in vertebrate photoreceptors. J Cell Sci *121*, 1907–1915.

Lechtreck, K.-F., Luro, S., Awata, J., and Witman, G.B. (2009). HA-tagging of putative flagellar proteins in Chlamydomonas reinhardtii identifies a novel protein of intraflagellar transport complex B. Cell Motil Cytoskeleton *66*, 469–482.

Lee, S., Weins, A., Hayes, D., Pollak, M., and Dominguez, R. (2008). Crystal structure of the actin-binding domain of alpha-actinin-4 Lys255Glu mutant implicated in focal segmental glomerulosclerosis. J Mol Biol *376*, 317–324.

Ling, L., and Goeddel, D. (2000). MIP-T3, a novel protein linking tumor necrosis factor receptor-associated factor 3 to the microtubule network. J Biol Chem *275*, 23852–23860.

Lucker, B., Behal, R., Qin, H., Siron, L., Taggart, W., Rosenbaum, J., and Cole, D. (2005). Characterization of the intraflagellar transport complex B core: direct interaction of the IFT81 and IFT74/72 subunits. J Biol Chem *280*, 27688–27696.

Lucker, B., Miller, M., Dziedzic, S., Blackmarr, P., and Cole, D. (2010). Direct interactions of intraflagellar transport complex B proteins IFT88, IFT52, and IFT46. J Biol Chem *285*, 21508–21518.

Marshall, W.F., and Rosenbaum, J.L. (2001). Intraflagellar transport balances continuous turnover of outer doublet microtubules: implications for flagellar length control. J Cell Biol *155*, 405–414.

Mueller, J., Perrone, C.A., Bower, R., Cole, D.G., and Porter, M.E. (2005). The FLA3 KAP subunit is required for localization of kinesin-2 to the site of flagellar assembly and processive anterograde intraflagellar transport. Mol Biol Cell *16*, 1341–1354.

Nachury, M.V. (2014). How do cilia organize signalling cascades? Philos. Trans. R. Soc. Lond., B, Biol. Sci. *369*.

Omori, Y., Zhao, C., Saras, A., Mukhopadhyay, S., Kim, W., Furukawa, T., Sengupta, P., Veraksa, A., and Malicki, J. (2008). Elipsa is an early determinant of ciliogenesis that links the IFT particle to membrane-associated small GTPase Rab8. Nat Cell Biol *10*, 437–444.

Ou, G., Qin, H., Rosenbaum, J., and Scholey, J. (2005). The PKD protein qilin undergoes intraflagellar transport. Curr Biol *15*, R410–R411.

Pazour, G.J., Dickert, B.L., and Witman, G.B. (1999). The DHC1b (DHC2) isoform of cytoplasmic dynein is required for flagellar assembly. J Cell Biol *144*, 473–481.

Pazour, G., Agrin, N., Leszyk, J., and Witman, G. (2005). Proteomic analysis of a eukaryotic cilium. J Cell Biol *170*, 103–113.

Pigino, G., Geimer, S., Lanzavecchia, S., Paccagnini, E., Cantele, F., Diener, D., Rosenbaum, J., and Lupetti, P. (2009). Electron-tomographic analysis of intraflagellar transport particle trains in situ. J Cell Biol *187*, 135–148.

Piperno, G., and Mead, K. (1997). Transport of a novel complex in the cytoplasmic matrix of Chlamydomonas flagella. Proc Natl Acad Sci USA *94*, 4457–4462.

Porter, M.E., Bower, R., Knott, J.A., Byrd, P., and Dentler, W. (1999). Cytoplasmic dynein heavy chain 1b is required for flagellar assembly in Chlamydomonas. Mol Biol Cell *10*, 693–712.

Qin, H., Diener, D., Geimer, S., Cole, D., and Rosenbaum, J. (2004). Intraflagellar transport (IFT) cargo: IFT transports flagellar precursors to the tip and turnover products to the cell body. J Cell Biol *164*, 255–266.

Rosenbaum, J.L., Moulder, J.E., and Ringo, D.L. (1969). Flagellar elongation and shortening in Chlamydomonas. The use of cycloheximide and colchicine to study the synthesis and assembly of flagellar proteins. J Cell Biol *41*, 600–619.

Schou, K.B., Andersen, J.S., and Pedersen, L.B. (2014). A divergent calponin homology (NN-CH) domain defines a novel family: implications for evolution of ciliary IFT complex B proteins. Bioinformatics *30*, 899–902.

Schuck, P. (2000). Size-distribution analysis of macromolecules by sedimentation velocity ultracentrifugation and lamm equation modeling. Biophys J *78*, 1606–1619.

Signor, D., Wedaman, K.P., Orozco, J.T., Dwyer, N.D., Bargmann, C.I., Rose, L.S., and Scholey, J.M. (1999). Role of a class DHC1b dynein in retrograde transport of IFT motors and IFT raft particles along cilia, but not dendrites, in chemosensory neurons of living Caenorhabditis elegans. J Cell Biol *147*, 519–530.

Soding, J., Biegert, A., and Lupas, A.N. (2005). The HHpred interactive server for protein homology detection and structure prediction. Nucleic Acids Research *33*, W244–W248.

Swiderski, R.E., Nakano, Y., Mullins, R.F., Seo, S., and Bánfi, B. (2014). A mutation in the mouse ttc26 gene leads to impaired hedgehog signaling. PLoS Genet *10*, e1004689.

Taschner, M., Bhogaraju, S., and Lorentzen, E. (2012). Architecture and function of IFT complex proteins in ciliogenesis. Differentiation *83*, S12–S22.

Taschner, M., Kotsis, F., Braeuer, P., Kuehn, E.W., and Lorentzen, E. (2014). Crystal structures of IFT70/52 and IFT52/46 provide insight into intraflagellar transport B core complex assembly. The Journal of Cell Biology *207*, 269–282.

Acknowledgements

We thank the crystallization facility of the Max Planck Institute of Biochemistry (MPIB, Munich) for access to crystallization screening, the staff from the Swiss Light Source (Villigen, Switzerland) for their help in collecting the X-ray diffraction data, Elisabeth Weyher-Stingl and Dr. Stephan Uebel (MPIB core facility) for mass spec analysis and AUC measurements. Furthermore, we acknowledge Michaela Schaper and Marc Stiegler for technical assistance with molecular cloning and Michaela Rhode and Elfriede Eppinger for help with the insect cell culture. We also thank Gregory Pazour for providing plasmids of mouse IFT proteins.

Author contributions

K.W. carried out and performed almost all the experiments. M.T. purified and performed the interaction test of the IFT38 and IFT57 CH domains with IFT80 and

IFT172. M.S. performed the interaction test with the CC regions of IFT20, IFT54 and IFT57. E.L. supervised all experiments. K.W. and E.L. wrote the paper.

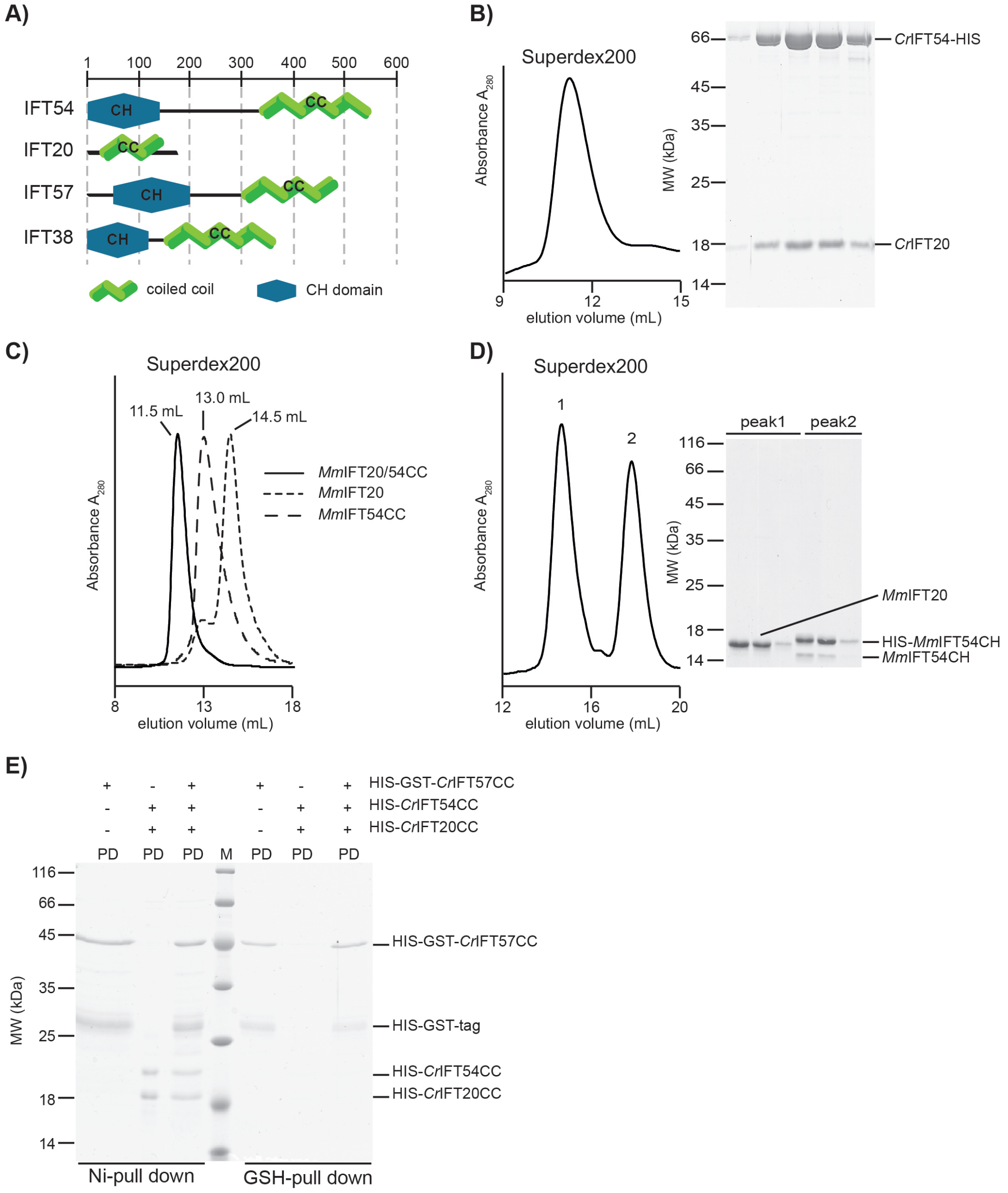

Fig. 1: IFT20 and IFT54 form a dimeric complex. (A) Predicted domain architecture of *C. reinhardtii* IFT20, IFT38, IFT54 and IFT57. **(B)** Size exclusion chromatography (SEC) profile of a *Cr*IFT20/54 purification and corresponding SDS-PAGE of the elution peak showing that both proteins elute in one peak, pointing to the formation of a dimeric complex. **(C)** SEC profiles of *Mm*IFT20, *Mm*IFT54CC and *Mm*IFT20/54CC showing that the *Mm*IFT20/54CC peak is shifted to higher MW. This demonstrates that the coiled coil (CC) region of *Mm*IFT54 is sufficient to interact with *Mm*IFT20. **(D)** The predicted α -helical Calponin Homology (CH) domain at the N-terminus of *Mm*IFT54 is not necessary for complex formation with *Mm*IFT20, indicated by two distinct peaks in the SEC elution profile. **(E)** Ni^{2+}-NTA and glutathione (GSH) affinity pull downs using the CC regions of *Cr*IFT20, *Cr*IFT54 and *Cr*IFT57. The CC regions of *Cr*IFT20 and *Cr*IFT54 form a complex that cannot

pull downed by the CC region of *Cr*IFT57, indicating that IFT20, IFT54 and IFT57 do not form a trimeric complex.

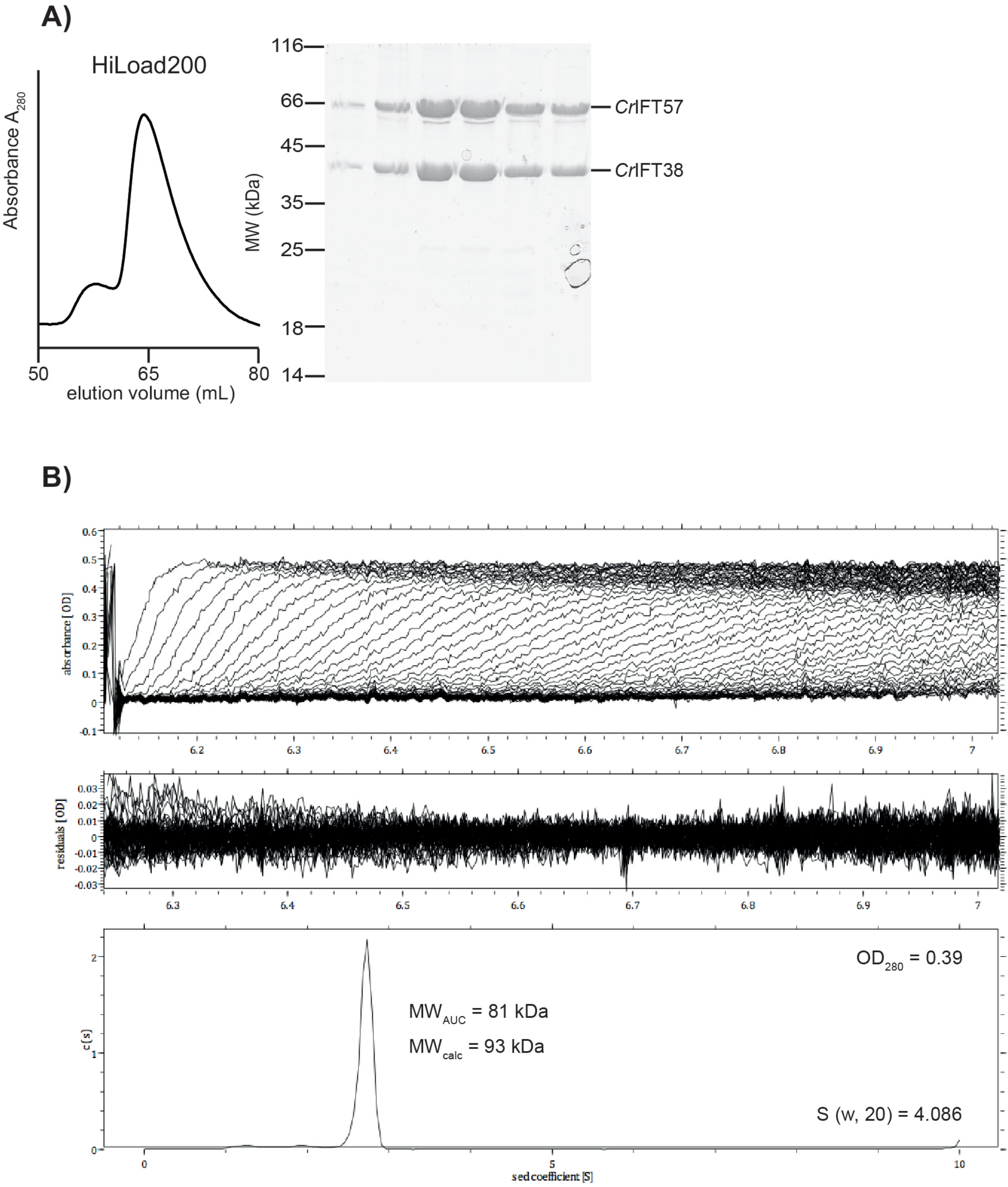

Fig. 2: IFT38 directly interacts with IFT57. (A) *Cr*IFT38 and *Cr*IFT57 elute in one peak in SEC, pointing to a direct interaction of the two proteins. The SDS-PAGE of the peak fractions indicates the formation of an IFT38/57 complex in stoichiometric amounts. **(B)** Analytical ultracentrifugation (AUC) of the dimeric complex HIS-*Cr*IFT38/HIS-*Cr*IFT57. To obtain a better clarity only every 5th scan is depicted. The calculated MW of *Cr*IFT38/57 is 93 kDa. In AUC, only one main peak was determined (MW_{AUC} = 81 kDa), pointing to an IFT38/57 complex.

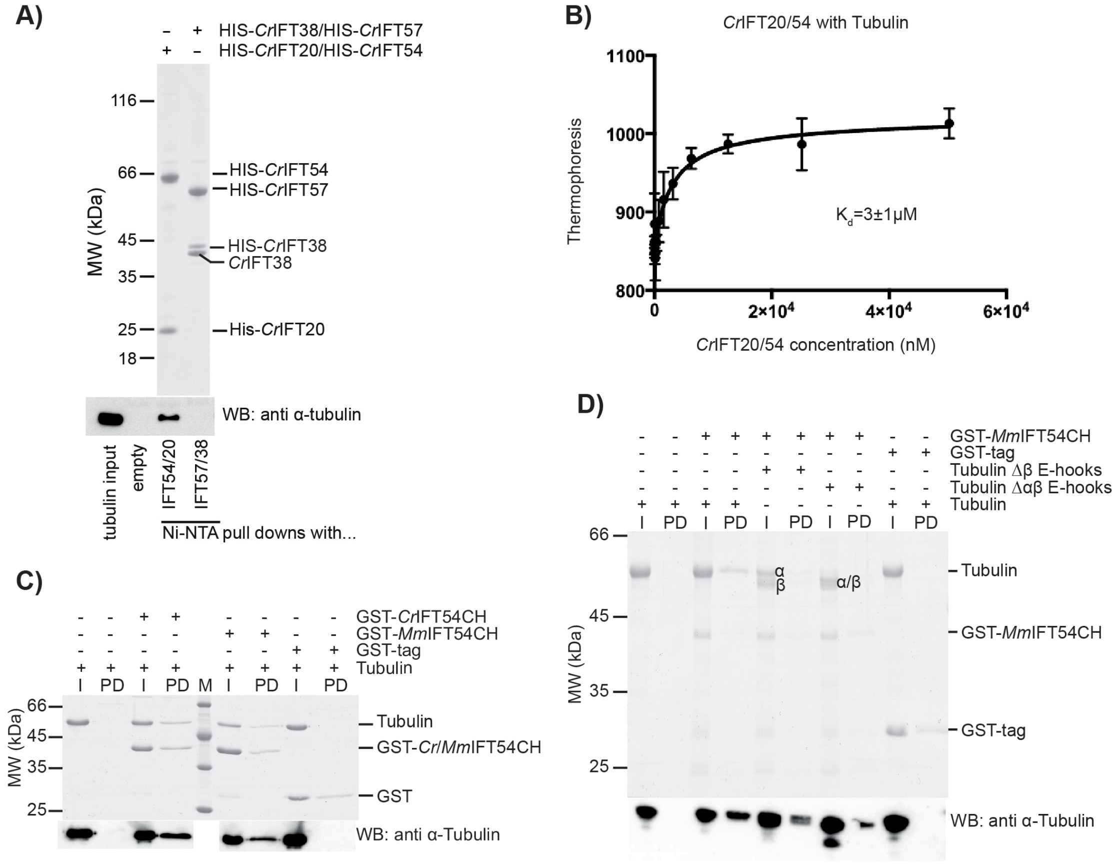

Fig. 3: IFT20/54 but not IFT38/57 binds tubulin. **(A)** Ni^{2+}-NTA affinity pull down using bovine αβ-tubulin and both dimers *Cr*IFT20/54 and *Cr*IFT38/57. Only the IFT20/54 complex pulls down tubulin. **(B)** Quantification of the binding affinity between bovine αβ-tubulin and untagged *Cr*IFT20/54 using microscale thermophoresis (MST) revealed a K_d of 3 μM. The curve was calculated for five independent measurements. The error bars represent the mean ± SD. **(C)** Glutathione (GSH) affinity pull down experiments using bovine αβ-tubulin and glutathione S-transferase (GST)-*Mm/Cr*IFT54 CH domain. The GST-tag does not pull down tubulin. The IFT54 CH domain is sufficient to pull down tubulin. **(D)** Bovine αβ-tubulin was treated with the protease subtilisin to remove the E-hooks of β-tubulin (20 min) or α- and β-tubulin (130 min). GSH affinity pull downs of subtilisin-treated tubulin and *Mm*IFT54CH indicate that the CH domain in IFT54 binds to the globular domain of tubulin.

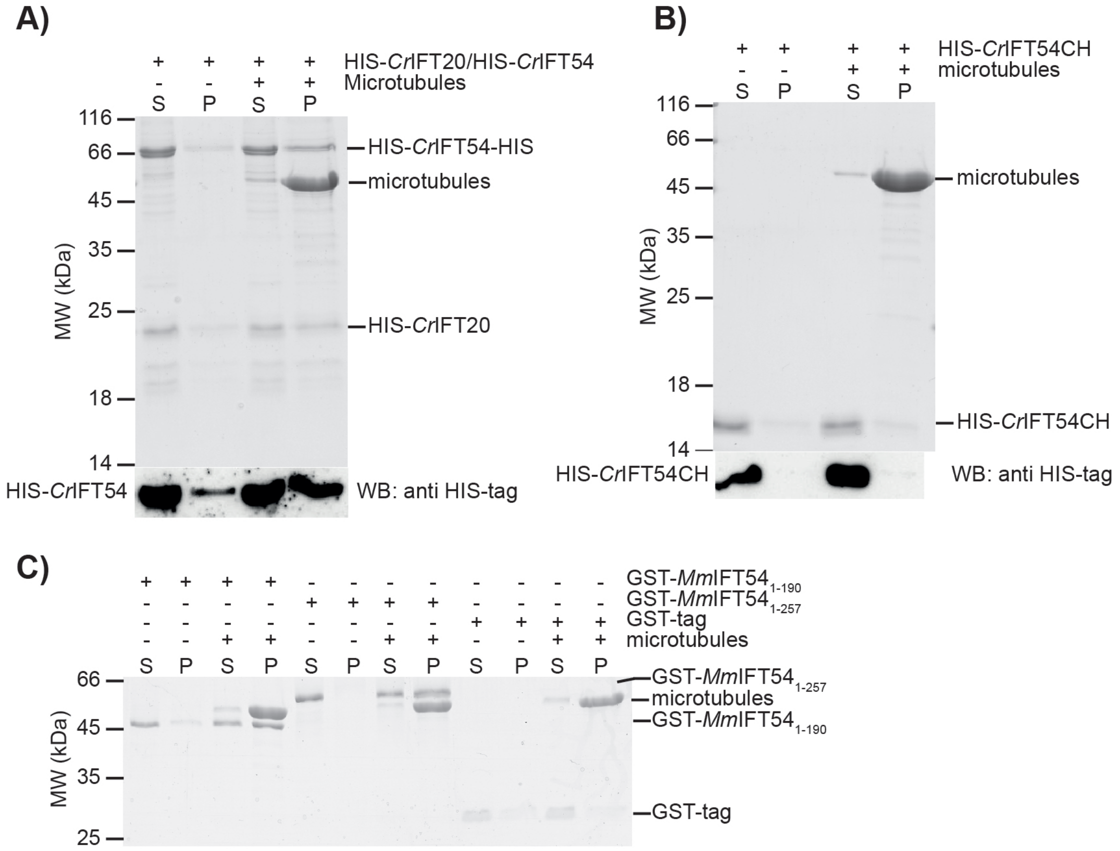

Fig. 4: IFT20/54 also binds to MTs. (A) MT-cosedimentation assay, using polymerized bovine αβ-tubulin and *Cr*IFT20/54 Adding MTs to *Cr*IFT20/54 resulted in an increased amount of pelleted *Cr*IFT20/54. **(B)** The CH domain of *Cr*IFT54 alone does not bind to MTs in MT-cosedimentation assays. **(C)** MT-cosedimentation assays of N-terminal constructs of GST-*Mm*IFT54 (comprising the CH domain and parts of the positively charged unstructured middle region) and MTs revealed pelleting of both IFT54 constructs. The GST-tag does not pellet with MTs. Additional residues adjacent to the CH domain seem to contribute to MT binding.

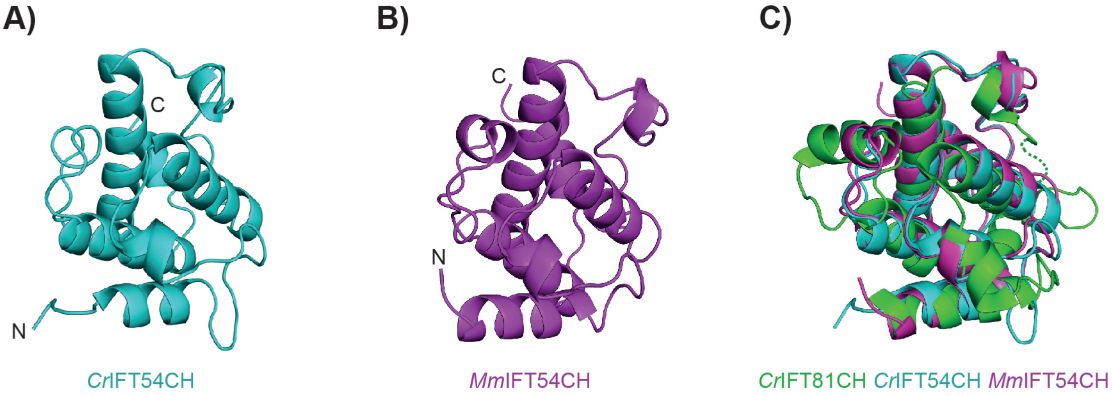

Fig. 5: High-resolution structure of the IFT54 CH domain. (A/B) Cartoon representation of the IFT54 CH domain of *C. reinhardtii* (residues 1-134) in cyan (A) and *M. musculus* (residues 1-133) in purple (B). **(C)** Superimposition of the CH domains in *Cr*/*Mm*IFT54 and *Cr*IFT81 (pdb: 4VLP) indicate slight differences for the CH domain in IFT81 and IFT54.

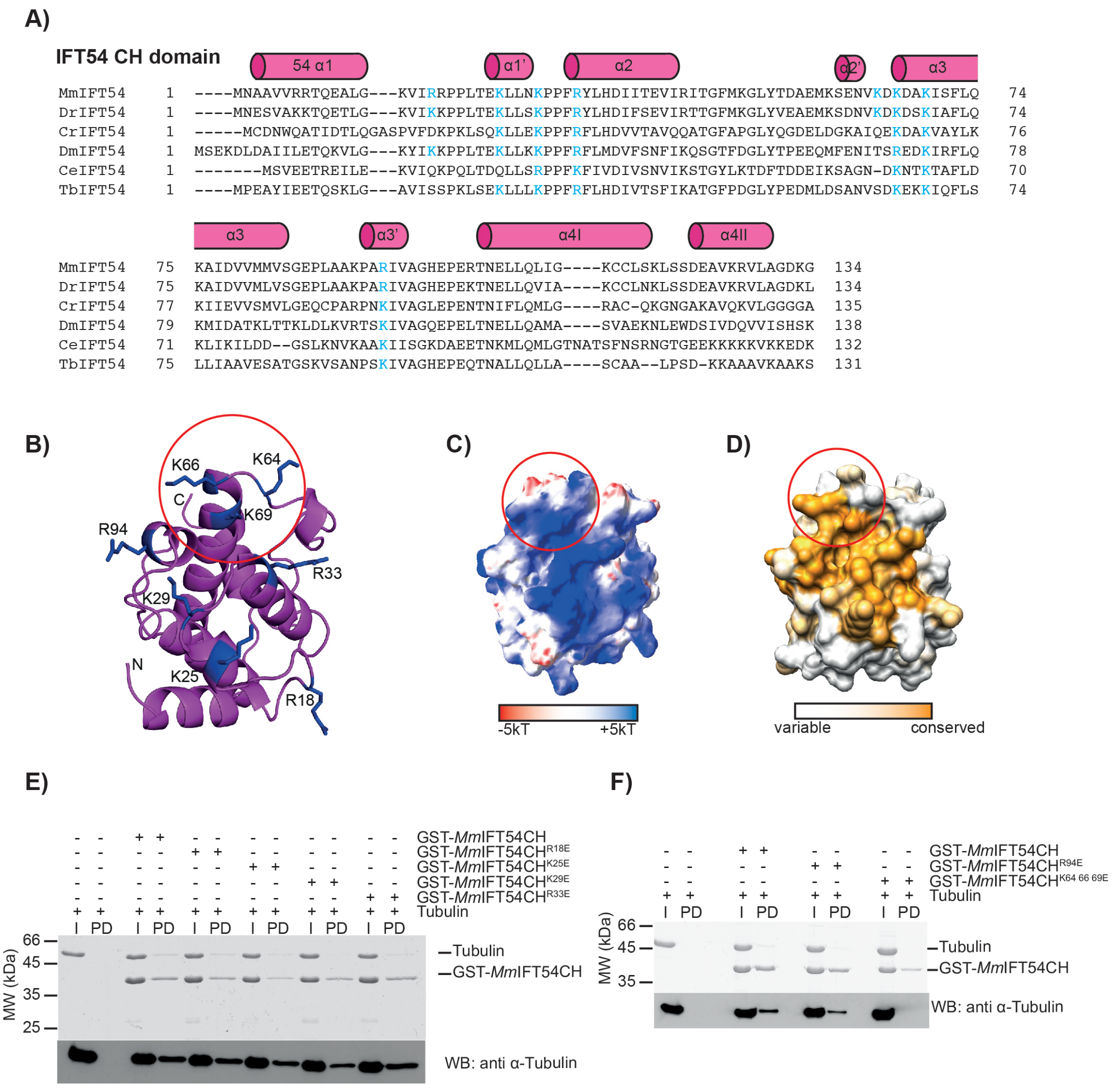

Fig. 6: The CH domain in IFT54 is a tubulin-binding module. (A) Sequence alignment of the N-terminal CH domain of IFT54 in different species. The secondary structure for IFT54 is displayed above the sequence. The positively charged arginines and lysines that are highly conserved and could play a role in tubulin binding are marked in cyan. *Mus musculus* (*Mm*), *Danio rerio* (*Dr*), *Chlamydomonas reinhardtii* (*Cr*), *Drosophila melanogaster* (*Dm*), *Caenorhabditis elegans* (*Ce*), *Trypanosoma bruceii* (*Tb*) **(B)** Cartoon representation of the crystal structure of *Mm*IFT54 CH domain. The residues probably implicated in tubulin binding are presented as blue sticks (single mutants). The residues of the designed *Mm*IFT54 triple mutant are indicated with a red circle. **(C)** Electrostatic surface potential of IFT54 indicates a positively charged patch. The amino acids mutated in the triple mutant are lying at the edge of this patch (red circle). **(D)** The conversation scores demonstrates that the positively charged patch at the surface of IFT54 is highly conserved throughout different species, as well as the position of the mutated residues in the triple mutant (red circle). **(E/F)** GSH affinity pull down experiments using bovine αβ-tubulin and *Mm*IFT54. Tubulin alone does not bind to GSH beads. Wild type *Mm*IFT54 as well as the single mutants of *Mm*IFT54 (R18E, K25E, K29E, R33E, R94E) pull down tubulin. In contrast, the triple mutant of *Mm*IFT54 (K64E K66E K69E) fully abolishes tubulin binding.

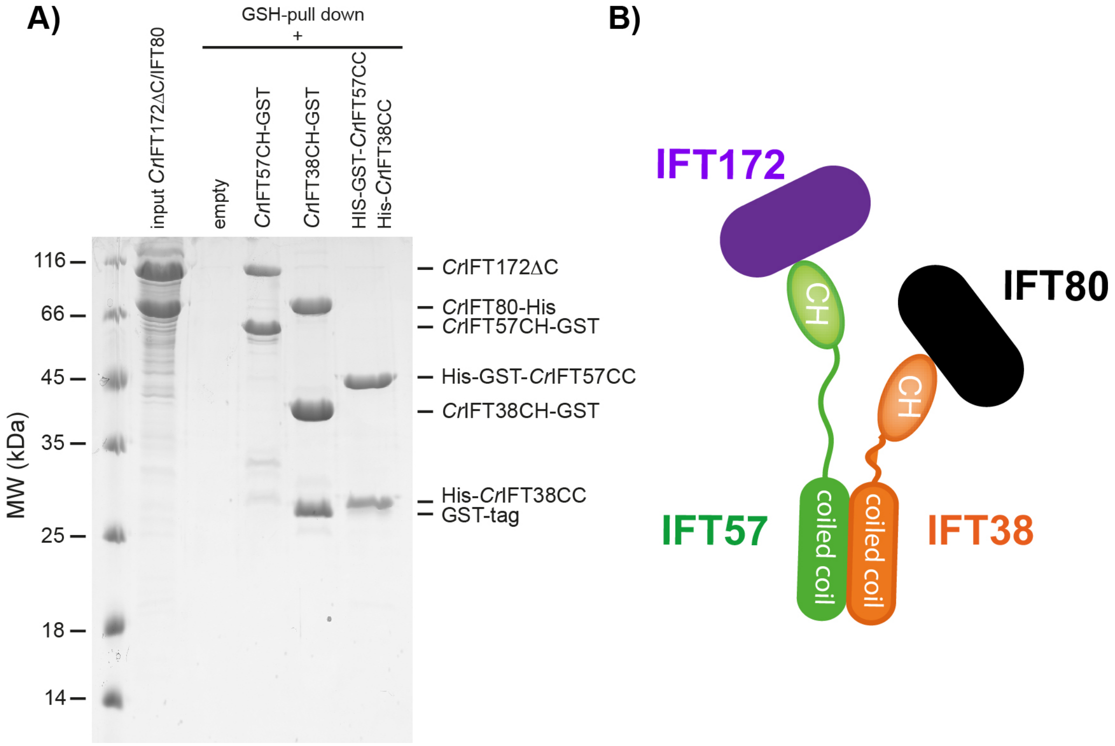

Fig. 7: The CH domains in IFT38 and IFT57 directly interact with IFT172 and IFT80 (A) GSH affinity pull down assays using a mixture of *Cr*IFT172ΔC/IFT80 as input and either CC- or CH-constructs of *Cr*IFT38 and *Cr*IFT57. The CH domain of IFT57 specifically pulls down IFT172ΔC, whereas the CH domain of IFT38 binds to IFT80. None of the CC regions of IFT38 or IFT57 is able to pull down IFT172ΔC or IFT80. **(B)** Preliminary interaction model of the interaction between the four IFT-B proteins IFT172, IFT80, IFT57 and IFT38.

Supplemental information

Table S1: Summary of data collection and refinement statistics

	*Cr*IFT54CH SeMet	*Cr*IFT54CH native	*Mm*IFT54CH native
Data collection and scaling	anomalous signal from Se to ~2Å		
Wavelength (Å)	0.979140	1.0	1.0
Resolution range (Å)	37.2 - 1.60 (1.66 - 1.60)	36.365 - 1.88 (1.99 - 1.88)	36.47 - 1.59 (1.69 - 1.59)
Space group	F222	F222	P1
Unit cell (Å)	a = 57.83, b = 145.90, c = 148.80, α = β = γ = 90.0	a = 57.66, b = 145.82, c = 147.87, α = β = γ = 90.0	a = 38.00 , b = 59.80, c = 61.50, α = 108.50, β = 105.40, γ = 90.30
Total reflections	556754 (86179)	117060 (14884)	176087 (26494)
Unique reflections	80222 (12779)	25144 (3712)	60996 (9267)
Multiplicity	6.9 (6.7)	4.7 (4.0)	2.9 (2.9)
Completeness (%)	99.7 (98.4)	98.2 (90.9)	93.9 (88.4)
Mean I/sigma(I)	15.14 (2.53)	11.16 (1.73)	10.45 (1.59)
R-merge	0.113 (0.563)	0.173 (0.937)	0.146 (0.969)
CC½	N/A	0.997 (0.683)	0.998 (0.552)
Refinement			
Number of reflections	41577	25133	60975
Protein residues	265	265	528
Number of atoms	4613	2231	4515
Protein (non solvent)	2079	2054	4084
Water (solvent)	376	177	431
R-work	0.1844 (0.2334)	0.2087 (0.2825)	0.1905 (0.2854)
R-free	0.2137 (0.2578)	0.2440 (0.3152)	0.2161 (0.3239)
Ramachandran favoured (%)		99.63	98.88
Ramachandran outliers (%)		0.0	0.0
RMS bonds (Å)	0.010	0.011	0.007
RMS angles (Å)	1.187	1.260	1.005
Average B-factors	15.31	23.45	19.49

Statistics for the highest-resolution shell are shown in parentheses.

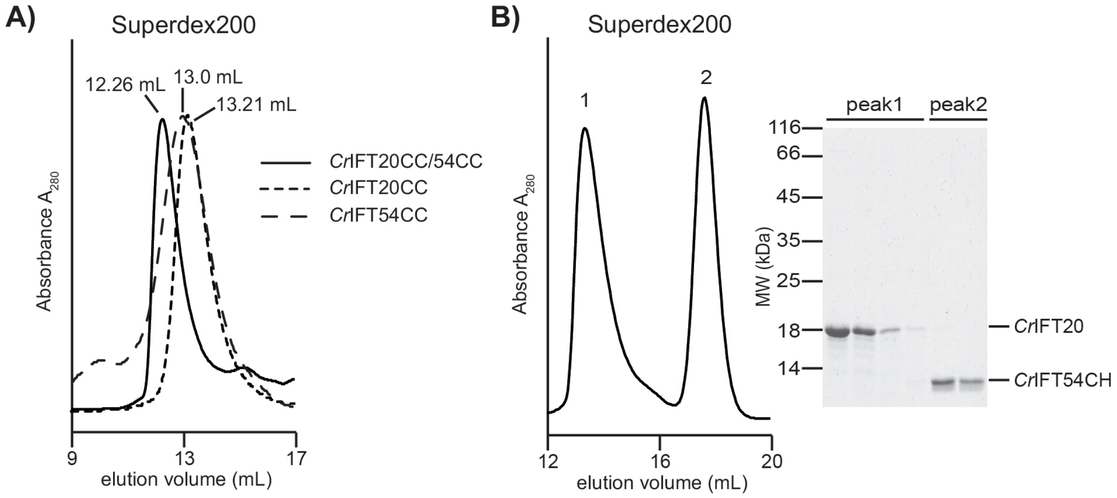

Fig S1: Complex formation between IFT20 and IFT54 is mediated via the CC domains. (A) SEC profiles of the *Cr*IFT20CC, *Cr*IFT54CC and *Cr*IFT20CC/54CC elution peaks showing that the *Cr*IFT20CC/54CC peak is shifted to higher MW. This demonstrates that CC regions of *Cr*IFT20 and *Cr*IFT54 are sufficient for complex formation. **(B)** The predicted N-terminal α-helical CH domain of *Cr*IFT54 is not necessary for complex formation with *Cr*IFT20, indicated by two peaks in the SEC profile and the corresponding SDS-PAGE.

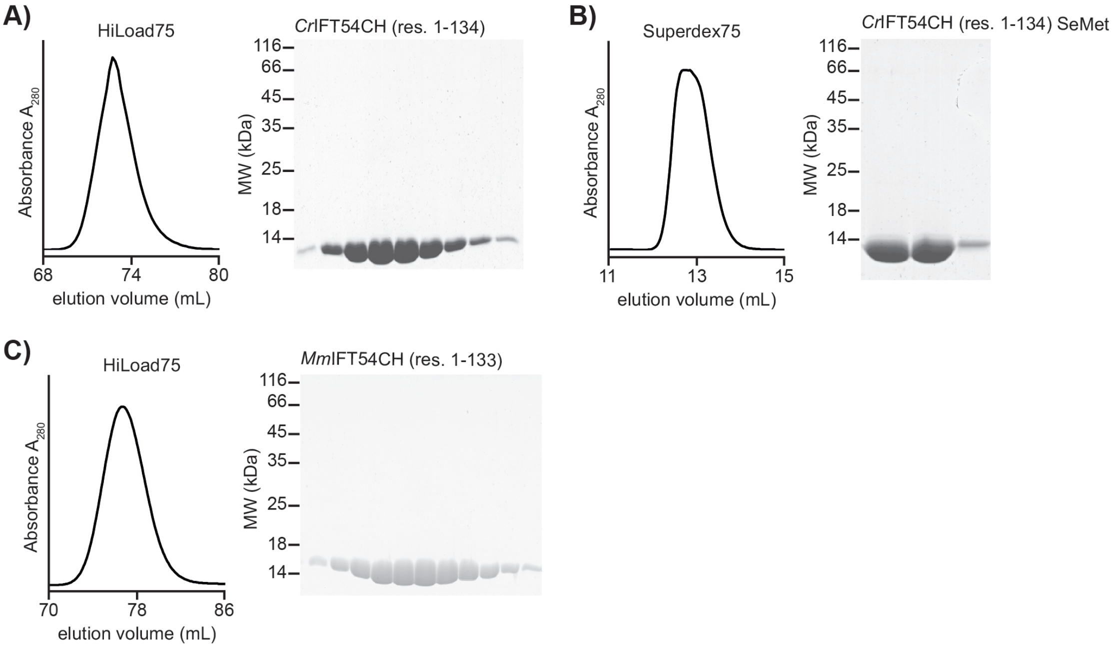

Fig. S2: Purification of the CH domain in IFT54. (A/B/C) SEC profiles and corresponding SDS-PAGE of the elution peaks are shown for *Cr*IFT54CH (residues 1-134) (A), *Cr*IFT54CH (residues 1-134) (all methionines substituted by selenomethionines (SeMet)) (B) and *Mm*IFT54CH (residues 1-133) (C).

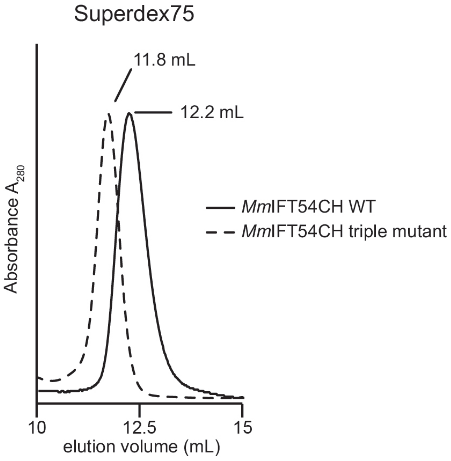

Fig. S3: Purification of *Mm*IFT54 CH domain wild type and triple mutant. Comparison of the SEC profiles of *Mm*IFT54 CH domain wild type ($MW_{theoretical}$ = 15.1 kDa) and triple mutant (K64E K66E K69E) ($MW_{theoretical}$ = 15.1 kDa) demonstrates that the triple mutant elutes similar to the wild type. This indicates that the triple mutant is properly formed.

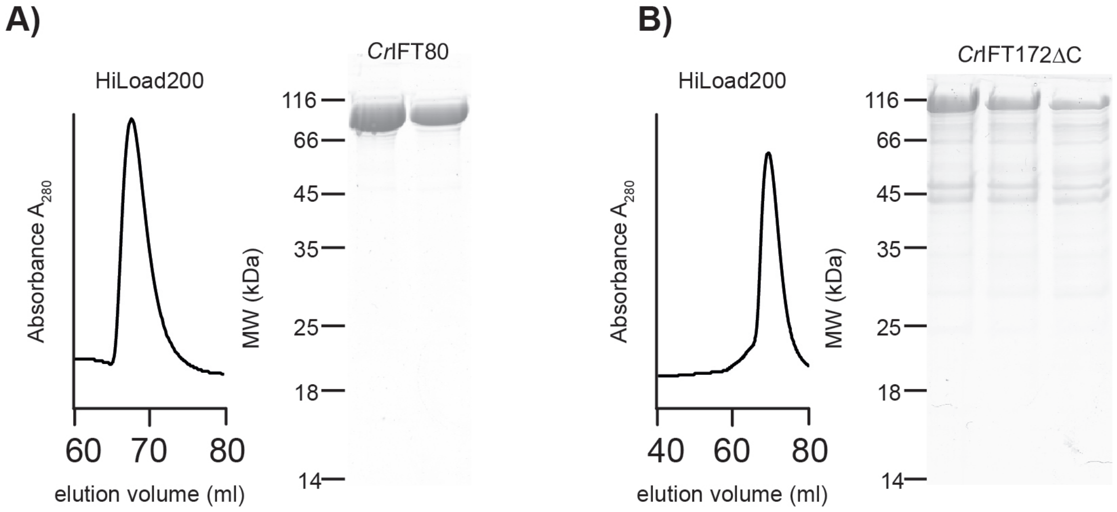

Fig. S4: Purification of IFT80 and IFT172ΔC. (A/B) SEC profiles and corresponding SDS-PAGE of the elution peaks are shown for *Cr*IFT80 (A) and *Cr*IFT172ΔC (residues 1-968) (B).

2.3) Chapter III

‘Hypomorphic mutations in TRAF3IP1/IFT54 reveal a new role for IFT proteins in microtubule stabilization’

Hypomorphic mutations in TRAF3IP1/IFT54 reveal a new role for IFT proteins in microtubule stabilization

Albane A. Bizet[1,2], Anita Becker-Heck[3], Rebecca Ryan[1,2], Kristina Weber[4], Emilie Filhol[1,2], Pauline Krug[1,2], Jan Halbritter[5], Marion Delous[1,2], Bolan Linghu[6], Edward J. Oakeley[3], Mohammed Zarhrate[2,7], Patrick Nitschké[2,8], Fabrizio Serluca[6], Marie-Christine Lasbennes[3], Fan Yang[6], Tewis Bouwmeester[3], Lucile Pinson[9], Elisabeth Cassuto[10], Philippe Dubot[11], Neveen A. Soliman Elshakhs[12], José A. Sahel[13], Rémi Salomon[1,2,14], Iain A. Drummond[15,16], Marie-Claire Gubler[1,2], Corinne Antignac[1,2,17], Salahdine Chibout[3], Joseph. D. Szustakowski[6], Friedhelm Hildebrandt[5], Esben Lorentzen[4], Andreas W. Sailer[3], Alexandre Benmerah[1,2*], Pierre Saint-Mezard[3*] and Sophie Saunier[1,2*]

[1]Inserm UMR-1163, Laboratory of Hereditary Kidney Diseases, Paris, France;

[2]Paris Descartes Sorbonne Paris Cité University, Imagine Institute, Paris, France;

[3]Novartis Institutes for Biomedical Research, Basel, Switzerland;

[4]Department of Structural Cell Biology, Max-Planck-Institute of Biochemistry, Martinsried, Germany;

[5]Division of Nephrology, Department of Medicine, Boston Children’s Hospital and Harvard Medical School, Boston, MA, USA;

[6]Novartis Institutes for Biomedical Research, Cambridge, MA, USA;

[7]Inserm UMR-1163, Genomic Core Facility, Paris, France;

[8]Paris Descartes Sorbonne Paris Cité University, Bioinformatics Core Facility, Paris, France;

[9]Pediatric department, Arnaud de Villeneuve University Health Center, Montpellier, France;

[10]Nephrology department, L'Archet II Hospital, Nice University Health Center, France;

[11]Hemodialysis-Nephrology department, William Morey Hospital, Chalon-sur-Saône, France;

[12] Department of Pediatrics, Center of Pediatric Nephrology and Transplantation, Cairo University; Egyptian Group for Orphan Renal Diseases, Cairo, Egypt;

[13]INSERM U968; CNRS UMR 7210; Sorbonne Universités, Université Pierre et Marie Curie, UMR S968; Centre Hospitalier National d'Ophtalmologie des Quinze-Vingts, INSERM, Direction de l'Hospitalisation et de l'Organisation des Soins, Centre d'Investigation Clinique 1423, Paris, France;

[14]Assistance Publique - Hôpitaux de Paris, Pediatric Nephrologic department, Necker-Enfants Malades Hospital, Paris, France;

[15]Nephrology Division, Massachusetts General Hospital, Charlestown, MA, USA;

[16]Department of Genetics, Harvard Medical School, Boston, MA, USA;

[17]Assistance Publique-Hôpitaux de Paris, Department of Genetics, Necker-Enfants Malades Hospital, Paris, France.

Correspondence should be addressed to: P.S-M. (pierre.saint-mezard@novartis.com) and S.S. (sophie.saunier@inserm.fr)

* Co-senior authors

Introductory paragraph:

Ciliopathies are a large group of clinically and genetically heterogeneous disorders caused by defects in primary cilia[1]. We identified mutations in *TRAF3IP1* (TNF Receptor-Associated Factor Interacting Protein 1) in 8 patients from 5 families with nephrophthisis (NPH) and retinal degeneration, the two most common manifestations of ciliopathies. *TRAF3IP1* encodes IFT54, a subunit of the IFT-B complex required for ciliogenesis. The identified hypomorphic mutations result in mild ciliary defects in patients but also reveal an unexpected role of IFT54 as a negative regulator of microtubule stability via MAP4 (Microtubule-Associated-Protein 4). Microtubule defects are associated with altered epithelialization/polarity in renal cells and with pronephric cysts and microphthalmia in zebrafish embryos. Our findings highlight the regulation of cytoplasmic microtubule dynamics as a role of the IFT54 protein, beyond the cilium, contributing to the development of NPH-related ciliopathies.

Main text :

NPH is an autosomal recessive renal ciliopathy characterized by massive interstitial fibrosis, tubular basement membrane thickening and cyst formation, leading to end-stage renal disease (ESRD) during childhood[2]. To date, NPH-causing mutations have been identified in more than 20 genes (*NPHP1-19*)[3-5], accounting for about 50% of all cases presenting with NPH[6].

Linkage analysis combined with whole exome sequencing in parallel to targeted exome sequencing ("ciliome")[3,7,8] conducted in 1,427 individuals with NPH revealed mutations in *TRAF3IP1* in 8 individuals from 5 unrelated families (**Table 1).** Three families carried three different homozygous missense mutations, whereas in one family, the affected individual NPH683-21 was compound heterozygous for a missense and a stop codon mutation (**Table 1 and Supplementary Fig. 1 a-c**). Lastly, we identified a homozygous mutation in individual NPH1110-22, that creates a new donor splice site after exon 13, leading to a premature stop codon with consecutively increased mRNA decay (**Supplementary Fig. 1 d-g**). All of these patients presented with tubulo-interstitial nephritis characteristic of NPH (leading to ESRD between 3 and 16 years). Extra-renal manifestations included mild to severe retinitis pigmentosa (RP) consistent with Senior-Løken Syndrome (**Table 1, Fig. 1a-d and Supplementary Fig. 2**). In addition, four patients presented with liver defects, six with skeletal anomalies (polydactyly, microdactyly, pelvic defects) and four with obesity (**Table 1 and Fig. 1e**), phenotypes also commonly associated with mutations in *IFT* genes[8-10]. We thus propose *NPHP20* as an alias for *TRAF3IP1*.

The IFT complex is required for ciliogenesis and is composed of two complexes, IFT-A and IFT-B, involved in retrograde and anterograde transport respectively[11]. *TRAF3IP1* encodes IFT54, which forms a peripheral IFT-B sub-complex with IFT20[12] and is important for the entry of assembled IFT particles and their cargos into cilia[13]. Inactivation of *Traf3ip1* is embryonic lethal and causes characteristic ciliopathies phenotypes, including neural developmental defects, polydactyly and microphthalmia in mice[14], and curved body axis, pronephric cysts and retinal degeneration in the *elipsa* zebrafish mutant[15,16]. Although the organ involvement seen in affected individuals is consistent with loss-of-function animal models, the milder phenotypes observed suggest the identified mutations are hypomorphic.

IFT54 binds to IFT20 via its C-terminal coiled-coil (CC) domain[17] (**Fig. 1f**). In contrast to the two truncating alleles, none of the missense mutations, including the C-terminal p.M520R, had any impact on IFT20 binding, indicating that the IFT54-IFT20 IFTB subcomplex is preserved in most patients (**Supplementary Fig. 3**). Interestingly, the N-terminal p.I17S and p.V125M/A substitutions are predicted to disrupt two hydrophobic pockets of the N-terminal calponin-homology (CH) domain of IFT54, which was previously known to be involved in tubulin binding[18] (**Fig. 1g**). Consistently, introduction of the p.I17S or p.V125A/M mutations in the isolated CH-domain (1-133), generated insoluble (likely unfolded) recombinant proteins (**Supplementary Fig. 4a-d**). Moreover, circular dichroism and calorimetry experiments, using full-length IFT54 in complex with IFT20 (**Supplementary Fig. 4e**), indicated that the CH domain of the IFT54 mutants is not accurately folded at 37°C (**Fig. 1h**). Altogether, these data indicate that the N-terminal mutations likely affect tubulin binding and stability of IFT54 *in vivo*.

To confirm the pathogenicity of the identified *TRAF3IP1* mutations, we injected WT and mutated RNA in both *elipsa* mutant and *traf3ip1* morphant zebrafish embryos. While injection of WT RNA resulted in a partial rescue of the mutant phenotypes, injection of mutated RNA constructs mimicking the human mutations could not rescue the curved body axis, glomerular cysts, dilated pronephric tubules, oval eye shape and loss of photoreceptors, and even led to an exacerbation of the eye phenotype (**Fig. 2a-c' and Supplementary Fig. 5a-c**). This further proves that mutations in *TRAF3IP1* are causal for NPH and retinal degeneration.

IFT54 is an anterograde IFT that localizes at the base (transition zone and basal body) and at the tip of cilia in control cells (fibroblasts and IMCD3 cells, **Fig. 3a-b' and Supplementary Fig. 6a-c**). Remarkably, IFT54 was absent from the transition zone and from the tip of cilia in fibroblasts from affected individuals as well as in mIMCD3 knock-down

(KD) cells expressing IFT54 mutants (**Fig. 3a-b', Supplementary Figs. 6c and 7a**), indicating that the mutations impair entry of IFT54 into the ciliary compartment. Therefore, we assessed the effects of *TRAF3IP1* mutations on ciliogenesis in patients' fibroblasts. While there was no difference in the percentage of ciliated cells, cilia were significantly longer (**Fig. 3c-c"**). Consistently, ciliogenesis defects in *Traf3ip1*-depleted zebrafish embryos and mIMCD3-KD cells were partially rescued by re-expression of IFT54-mutants, except p.R155* (**Supplementary Figs. 5d and 6d**). This suggests that the observed phenotype in patients as well as in zebrafish may not be caused by ciliogenesis defects *per se*.

The cilia formed in patients' fibroblasts presented no obvious change in the localization of key ciliary proteins (IFT46, IFT140, FBF1, Inversin, Anks6 and Smoothened; **Supplementary Fig. 7b-g**), suggesting no general defect in ciliary composition and trafficking. However, adenylyl cyclase III (ACIII) was strongly decreased (**Fig. 3d-d'**). Consequently, translocation of PKA catalytic subunits from the cilia base to the cytoplasm was impaired upon forskolin treatment, an AC activator (**Fig. 3e-e'**). Our results therefore link IFT54 to regulation of the cAMP/PKA pathway and provide a rationale for the obesity observed in these patients, as previously reported in ACIII deficient mice[19].

The mild cilia structural defects associated with hypomorphic mutations of *TRAF3IP1* seem insufficient to account for the large phenotypic spectrum of the patients, suggesting additional function(s) for IFT54. Indeed, among several previously identified candidate partners of IFT54[18], we found that the interaction of IFT54 with MAP4 was severely impaired by the N-terminal mutations p.I17S, p.V125A and p.V125M (**Fig. 4a**). MAP4 is the major MAP in non-neuronal cells[20] that stabilizes microtubules[21] and is a negative regulator of ciliary length[22]. Ciliary MAP4 staining was drastically reduced in patients' fibroblasts (**Fig. 4b-b'**), which might explain the observed increased cilia length in mutant fibroblasts and suggests that MAP4 may be an IFT54 cargo for ciliary import.

In addition to its ciliary localization, IFT54 can be found along cytoplasmic microtubules[23,24], and N-terminal mutations effectively impaired this localization (**Supplementary Fig. 8**). Unexpectedly, MAP4 staining was strongly increased along cytoplasmic microtubules in mutant cells, which correlated with enhanced protein expression, but without changes in mRNA levels (**Fig. 4c-c' and Supplementary Fig. 9a-d**). These results suggest that IFT54 negatively regulates MAP4 expression and its recruitment to microtubules, which in turn is expected to result in their stabilization[21]. Consistently, acetylation of α-tubulin, a modification occurring on stable microtubules[25], was enhanced in mutant cells as well as in patients' kidney tubules (**Fig. 4d and Supplementary Fig. 9d-e**), a yet unexplained observation in several ciliopathy models[14,26,27]. The increased stability of microtubules was confirmed by the presence of abnormally cold-resistant MAP4-positive microtubules in mutant cells (**Fig. 4e and Supplementary Fig. 9f**). In addition, EB1 staining at the plus-tips of microtubules[28] was drastically reduced (**Fig. 4f**) indicating a less dynamic microtubule network. This result was confirmed *in vivo* using EB3-GFP as a reporter of plus-tip dynamics, as *elipsa* mutant embryos showed slower rates of microtubule polymerization compared to heterozygous control siblings (**Fig. 4g-g'**). Altogether, these data emphasize a novel role for IFT54 as a negative regulator of microtubule stability through MAP4. Remarkably, MAP4 loss-of-function mutations have been reported in patients with Seckel syndrome [29], featuring microcephaly and dwarfism. We demonstrate here that *TRAF3IP1* hypomorphic mutations conversely cause increased expression of MAP4 and result in NPH, retinal degeneration and hepatic fibrosis. Therefore, fine regulation of MAP4 appears to be essential for proper tissue homeostasis.

Microtubule network architecture is crucial for epithelial integrity[28,30], hence we investigated the impact of *TRAF3IP1* mutations on epithelialization. The microtubule network appeared disorganized in polarized *Traf3ip1*-KD mIMCD3 cells, and was restored by re-expression of IFT54-WT but not by IFT54-mutants (**Supplementary Fig. 10a**). The reformation of tight junctions and cell polarity were assessed following Ca^{2+} switch and trans-epithelial resistance (TER) measurement (**Fig. 5a-d**). *Traf3ip1*-KD cells presented a decreased TER and reduced E-cadherin and β-catenin localization at cell junctions, both of which were partially rescued by re-expression of WT and the p.V125M mutant but not by the p.R155* or p.M520R mutants (**Fig. 5a-b and Supplementary Fig. 10b**). These results suggest that some IFT54 mutant proteins may perturb the establishment of cell junction during epithelialization, as we previously reported for NPHP1 and NPHP4[31]. In addition, *Traf3ip1*-KD cells and cells re-expressing IFT54-mutant proteins appeared flatter than controls and displayed decreased expression of the apical marker Gp135 (**Fig. 5a, c-d**). In 3D culture, mIMCD3 control cells formed single lumen spheres, whereas *Traf3ip1*-KD cells formed abnormal structures with small lumens filled with dividing cells and/or surrounding misarranged nuclei, with dramatically altered expression of the tight junction component ZO1 (**Fig. 5e-e'**). Normal lumen formation and ZO1 localization were restored by re-expression of IFT54-WT but not by IFT54 mutant proteins (**Fig. 5e-e'**). These results demonstrate that in addition to its known role in ciliogenesis, IFT54 plays a key function in the early steps of epithelial morphogenesis, a process independent of cilia[32].

In summary, we identified mutations of *TRAF3IP1* as a cause of NPH associated with retinal degeneration. Detailed analyses of *TRAF3IP1* pathogenic mutations have unveiled a cilia-independent role for this IFT protein in cytoplasmic microtubule stabilization. In addition to IFT54, other NPHPs and IFT proteins have been reported to localize along the cytoplasmic microtubule network[27,33,34], suggesting a shared extra-ciliary function. Here we show that IFT54 acts as a negative regulator of MAP4, likely by preventing its association with microtubules either by directly competing with MAP4 and/or by inducing MAP4 phosphorylation by PKA[35] or other MAP4 regulating kinases[21]. Mutations of IFT54 in turn result in the stabilization of MAP4 on microtubules and therefore increased MAP4 expression. We propose that altered cytoplasmic microtubule dynamics and cell polarity defects constitute an understudied disease mechanism, which may contribute significantly to the tubulo-interstitial lesions observed in NPH, retinal degeneration or hepatic fibrosis, all common progressive features of "ciliopathies".

Acknowledgements:

We are grateful to the patients and their families for their participation. We thank J. Malicki for providing us with the *elipsa* zebrafish, G. Pazour, J. Nelson, L. Pederson and R. Köster for giving us the Flag-*Mm*IFT54, GFP-MAP4 and EB3-GFP constructs, respectively. We greatly acknowledge M. Garfa-Traoré and N. Goudin (Necker cell imaging facility) for providing expert knowledge on confocal microscopy, E. Weyher-Stingl (core facility, MPI of Biochemistry) for assistance with the CD measurements, H. Voshol for support in mass spectrometry and J. Duca for help in molecular modeling, C. Bole-Feysot, O. Alibeu, S. Pruvost and M. Parisot (Imagine Genomic plateform) and the Necker Bioinformatic facility. We thank S. Berissi (Histology facility), G. Pivert (Pathology department, Necker hospital), O. Pellé (Cell sorting facility), S. Laurent and N. Dörner (Cellular Biology, NIBR), for their excellent technical assistance. The authors are grateful to the following scientists for their support: L. Klickstein, M. Labow, M. Schebesta, and K. Johnson for providing intellectual input at various stages of the project.

This work was supported by grants from the "Agence Nationale de la Recherche" (ANR) to S.S. (20100BLAN112202) and investments for the future program-ANR-10-IAHY-01 to S.S., the Fondation pour la Recherche Médicale (DEQ20130326532 to SS and RR) and (DEA20120624188 to P.K.). This research was supported by a grant from the NIH to F.H. (DK068306). F.H. is an Investigator of the Howard Hughes Medical Institute and Warren E. Grupe Professor of Pediatrics at the Harvard Medical School.

Author contributions: A.A.B. and A.B.H. performed cell biology and biochemical experiments with the help of M.C.L.. R.R. performed zebrafish studies with the help of F.S. and the input of I.A.D. and M.D.. K.W. carried out the purification and *in vitro* interaction studies under the supervision of E.L.. E.F., P.K., J.H., E.J.O., M.Z., P.N., F.H., B.L, Y.F., J.D.S. and S.S. performed mutational analysis. S.S., P.S-M., J.D.S., A.W.S., T.B., S.C., and C.A. initiated the project. H.V., L.P., E.C., P.D., N.A.S.E., J.A.S., R.S., C.A, M-C.G. recruited subjects and/or provided clinical information. A.A.B., A.B.H., R.R., K.W, E.L, A.W.S., A.B., P.S-M. and S.S. designed the experiments and wrote the manuscript (with input from J.H, F.H, C.A. and I.A.D).

Figure legends

Figure 1: Identification of *TRAF3IP1* mutations in patients with nephronophthisis and retinal degeneration. Periodic acid schiff (**a**), trichrome (**b**) and silver methenamine (**c**) staining on kidney sections from individual NPH302-23 (**a-b**) and NPH1110-22 (**c**) revealed massive interstitial fibrosis (arrow-heads) with cell infiltration, atrophic tubules with thickening of the basement membrane (arrows), as well as dilatation of proximal tubules (asterisks), characteristic of NPH. (**d**). Fundus photograph of individual NPH1110-22 showed characteristic aspects of RP, with pigmentary reorganization, papillary pallor and thin retinal vessels. (**e**). Left hand X-ray of individual NPH1110-22 showing short fingers (brachydactyly). (**f**) Organization of exons of *TRAF3IP1* cDNA (top panel) and functional domains of IFT54 protein with an N-terminal calponin homology (CH) domain involved in tubulin binding, an Arginine-rich motif and a C-terminal coiled-coil domain involved in IFT20 binding. Black bars indicate positions of the identified mutations. Family numbers are underlined. H, homozygous; h, heterozygous. (**g**) Crystal structure of the CH domain of *Mm*IFT54 showing that the I17 and V125 residues locate in conserved hydrophobic pockets (dotted line circles). The mutant residues S17 and M125 were introduced (red) to show their effects on these hydrophobic pockets. (**h**) Secondary structure determination and thermal unfolding using circular dichroism (CD) spectroscopy for WT as well as p.V126A and p.V126M mutants of *Cr*IFT54 in complex with *Cr*IFT20.

Figure 2: Patient mutations do not rescue the ciliopathy-associated phenotypes characteristic of *elipsa* mutants. (**a**) Lateral views of zebrafish larvae at 72 hpf of WT control, *elipsa* uninjected larvae and *elipsa* larvae injected with WT or mutant RNA constructs (p.R154* and p.V459R correspond to the human p.R155* and p.M520R mutations, respectively). Approximately 20% of V125M-injected *elipsa* larvae displayed an alternative stunted phenotype with pronephric cysts and eye defects, but lacking the characteristic body axis curvature. (**a'**) Phenotype distribution as determined by quantification of angle of body axis curvature ($n \geq 30$, 4 independent experiments). Scale bar, 0.5 mm. (**b**) Eye phenotypes (5 dpf) of WT control, *elipsa* uninjected larvae and *elipsa* larvae injected with WT/mutant RNA constructs, lateral views, anterior to the left. Scale bar, 0.1 mm. (**b'**) Surface area of the retina (mean +/- SD of n=10, 2 independent experiments, *P= 0.05, **P < 0.01, and *** P< 0.001, Dunnett's multiple-comparison test). (**c**) H&E staining of histological cross sections of *elipsa* mutant larvae injected with WT or mutant RNA constructs at 72 hpf. Gross cystic dilations of the glomerular region extending to the pronephric tubule are indicated by asterisks. (**c'**)

Percentage of pronephric cysts in *elipsa* mutant larvae as well as rescued larvae (n ≥ 30, 4 independent experiments).

Figure 3: Mutations in *TRAF3IP1* impair IFT54 ciliary trafficking and cilia-mediated signaling. (**a**) Ciliary distribution of IFT54 in serum-starved control and patients' fibroblasts stained for IFT54 (red), the axonemal marker acetylated α-tubulin (green) and the basal body marker γ-tubulin (blue). (**a'**) Percentage of cilia with IFT54 at the distal tip of cilia (arrows in (**a**), mean +/- SEM of n=4 experiments, ***P<0.001, Bonferronni's multiple-comparison test). (**b**) Distribution of IFT54 at the basal body in ciliated fibroblasts stained for IFT54 (red) and for γ-tubulin (blue) and centrin (green), markers of proximal and distal parts of centrioles, respectively. A schematic representation of the orientation of the two centrioles, with the localization of the distal (DAP) and subdistal (sDAP) appendages shown. Scale bars, 1μm. (**b'**) Intensity of IFT54 staining at the transition zone (TZ, mean +/- SEM of n=3 experiments, ***P<0.001, Dunn's post-hoc test). (**c**) Ciliogenesis was analyzed by immunofluorescence in fibroblasts stained for ARL13B (cilia, green). Scale bar, 10μm. (**c'**) Percentage of ciliated cells and (**c''**) cilia length (n>200 cells from 4 independent experiments; ns: not-significant, ***P<0.001, Dunn's post-hoc test). (**d**) ACIII (red), acetylated α-tubulin (green) and γ-tubulin (blue) stainings in serum-starved fibroblasts. Scale bar, 1μm. (**d'**) Intensity of ACIII within cilia (mean +/- SEM of n≥3 experiments, *P<0.05, Dunn's post-hoc test). (**e**) Fibroblasts were treated with 1μM forskolin, an activator of ACs, for 1hr and stained for ARL13B (green) and PKAc (red). Scale bar, 2μm. (**e'**) Percentage of cells with PKAc at the cilia base after forskolin treatment (mean +/- SEM of n=3 experiments, *** P<0.001, Dunnett's post-hoc test).

Figure 4: Mutations of *TRAF3IP1* lead to impaired interaction and increased recruitment of MAP4 to cytoplasmic microtubules causing microtubule stabilization. (**a**) Lysates from HEK293T cells co-expressing Flag-tagged WT or mutant forms of *Mm*IFT54 (p.K155*, p.I453R and p.M458Mfs3* correspond to the human mutations p.R155*, p.M520R and p.M525Mfs3*) and GFP-MAP4 were immunoprecipitated with an anti-GFP antibody. The co-immunoprecipitation of GFP-MAP4 and Flag-IFT54 constructs was followed by western-blot (WB) using GFP and Flag antibodies. (**b**) Serum-starved fibroblasts were fixed in PFA to visualize ciliary MAP4 (red; acetylated α-tubulin, green). Scale bar, 2μm. (**b'**) Intensity of ciliary MAP4 staining (mean +/- SEM of n=5 experiments, *P<0.05, ***P<0.001, Dunn's post-hoc test). (**c**) Expression of MAP4 and GAPDH in control and patients'

fibroblasts was analyzed by WB. (**c'**) Relative expression of MAP4 normalized to that of GAPDH (mean +/- SEM of n=5 experiments, *P<0.05, Dunn's post-hoc test). (**d**) Fibroblasts were stained for acetylated α-tubulin (green). Scale bar, 10µm. (**e**) Fibroblasts treated for 10 min on ice (to depolymerize the microtubules) were fixed with MeOH (to visualize MAP4 on microtubules) and stained for α-tubulin (green), γ-tubulin (light blue) and MAP4 (red). Scale bar, 10µm. (**f**) Fibroblasts were stained for α-tubulin (green) and the microtubule plus-tip associated protein EB1 (red). Scale bar, 2µm. (**g**). WT and *elipsa* embryos were injected with EB3-GFP to follow the dynamics of the growing ends of microtubules which were analyzed by time lapse confocal microscopy and Imaris tracking software. Pseudo colors were used to visualize the speed of EB3 comets (from blue (slow) to red (fast)). (**g'**) Track speed analysis of EB3-GFP comets in WT and *elipsa* embryos (n=6, mean +/- SD, *** P<0.001, *t*-test).

Figure 5: *TRAF3IP1* mutations lead to epithelialization and polarity defects. (**a**) mIMCD3 cells grown until confluence on filters were subjected to Ca^{2+}-free medium to disrupt the tight junctions. Six hours after Ca^{2+} addition, cells were analyzed by immunofluorescence using the apical marker Gp135 (red) and β-catenin (light blue) to stain the cell junctions. Scale bar, 10 µm. (**b**) Following Ca^{2+} switch, tight junction re-formation was assessed by measurement of trans-epithelial resistance (TER) at different time points (mean +/- SEM of n=5 independent experiments, two-way ANOVA; ns: not-significant, ***P<0.001 at 6hrs). (**c**) Height of mIMCD3 cells grown on filters measured as the distance from the base to the top of the cells (GFP staining, not shown; mean +/- SD of n≥20, from 3 independent experiments, ***P<0.001, Bonferonni's multiple-comparison test). (**d**). Expression of the apical marker Gp135 was analyzed by Western-blot with α-tubulin as a loading control. (**e**) mIMCD3 cells grown in matrigel 3D matrix to form spheroids were stained for ZO1 (tight junctions, red) and analyzed by confocal microscopy. Equatorial sections of representative spheres are shown for each cell line. Scale bars, 10µm. (**e'**) Percentage of abnormal spheroids (no/small lumen filled with cells) (mean +/- SD, n=80 spheroids from 2 independent experiments, *** P ≤ 0,001, ** P <0.002, Bonferonni's multiple-comparison test).

Materials and Methods:

Patients and families:

Written informed consent was obtained for all individuals enrolled in this study and approved by the Institutional Review boards at the University of Paris Descartes and at the University of Michigan.

Homozygosity mapping, whole exome (WES) and "ciliome" sequencing and mutation calling

Homozygosity mapping in the family NPH302 and A4336 was performed using 'Human Mapping 250k NspI' array and parametric logarithm of odds (LOD) scores were calculated with MERLIN software [36] for NPH302, and GENEHUNTER 2.1[37] / ALLEGRO[38] for A4336, assuming autosomal-recessive inheritance. In A4336, whole exome sequencing (WES) and variant burden analysis was performed as described previously [39]. In brief, genomic DNA was isolated from blood lymphocytes and subjected to exome capture using Agilent SureSelectTM human exome capture arrays (Life Technologies^{TM}) followed by next generation sequencing on the IlluminaTM sequencing platform. Illumina's processing software ELAND (CASAVA 1.8.2) was used to map reads to the human reference genome (build 19), and SAMtools37 was used to call single nucleotide variants and insertion/deletion at targeted bases. Variants with minor allele frequencies <1% in the Yale (1,972 European subjects), NHLBI GO Exome Sequencing Project (4,300 European and 2,202 African American subjects), dbSNP (version 135) or 1,000 Genomes (1,094 subjects of various ethnicities) databases were selected and annotated for impact on the encoded protein and for conservation of the reference base and amino acid among orthologs across phylogeny. Sequence reads were mapped to the human reference genome assembly (GRCh37/hg19) using CLC Genomics WorkbenchTM (version 4.7.2) software (CLC bio, Aarhus, Denmark). Mutation calling was performed by geneticists/cell biologists, who had knowledge of the clinical phenotypes and pedigree structure, as well as experience with homozygosity mapping and exome evaluation. In NPH302-23, WES and variant burden analysis was performed as described previously[40]. Ciliary exome targeted sequencing and bioinformatics filtering was conducted in NPH579-22, NPH638-21 and NPH1110-22, using a custom SureSelect capture kit (Agilent Technologies) targeting 4.5 Mb of 20,168 exons (1 221 ciliary candidate genes), including *TRAF3IP1*[7,41]. Briefly, Agilent SureSelect librairies were prepared from 3 µg of 300 genomic DNA samples sheared with a Covaris S2 Ultrasonicator according to manufacturer's instructions. The SOLiD molecular barcodes for traceable ID of samples were added at the end of the capture step. The Ovation Ultralow System (NuGEN Technologies) was used to prepare HiSeq2500 pre-capture barcoded libraries. The ciliome capture by hybridization was performed on a pool of 10 to 16 barcoded precapture libraries. Sequencing performed on SOLiD5500XL (Life Technologies) and HiSeq2500 (Illumina) was done on pools of barcoded ciliome librairies (64 barcoded ciliome libraries per SOLiD FlowChip and 16 ciliome libraries per lane of HiSeq FlowCell). Paired-end reads were generated (75+35 for SOLiD, 100+100 for HiSeq) and mapped on human genome reference (NCBI build37/hg19 version) using Burrows-Wheeler Aligner (Illumina) or mapread (SoliD). Downstream processing was carried out with the Genome Analysis Toolkit (GATK), SAMtools, and Picard Tools, following documented best practices (http://www.broadinstitute.org/gatk/guide/topic?name=best-practices). All variants were annotated using a software system developed by the Paris Descartes University Bioinformatics platform. The mean depth of coverage obtained was greater than 90x, and more than 89% of the exome was covered at least 15x. Different filters were applied to exclude all variants located in non-exonic regions, pseudogenes, UTRs or known polymorphic variants with a frequency above 1% i.e. present in databases such as dbSNP, 1000 genome projects and all variants identified by in-house exome sequencing (5150 exomes and 1020 ciliomes). The functional consequence of missense variants was predicted using SIFT (http://sift.jcvi.org/www/SIFT_enst_submit.html) and PolyPhen2 software (http://genetics.bwh.harvard.edu/pph2/). Sanger sequencing using the primers described in **Table S1** was performed to validate the NGS findings and the segregation of the mutation within all the families.

Cloning, expression, purification and pull down experiments of recombinant proteins

Truncations of *Mm*IFT54 containing the N-terminal CH-domain (either WT or point-mutations) were cloned into bacterial pEC vectors with cleavable GST- or hexahistidine-tags as described previously[42] and expressed in the *E.coli* BL21 (DE3) Gold pLysS strain. *E.coli* cells were lysed by sonication in 50mM Tris-HCL pH 7.5, 150mM NaCl, 5mM β-mercaptoethanol and 10% glycerol. The lysates were incubated with BSA-blocked Ni^{2+}-NTA or GSH-beads for 1h followed by 3 washes with lysis buffer. Bound material was eluted in lysis buffer supplemented with 500mM imidazole (Ni^{2+}-NTA beads) or 30mM reduced glutathione (GSH-beads). Large-scale purification of the MmIFT54 CH-domain included the additional steps (after affinity-tag cleavage using tobacco etch virus (TEV) protease) of anion exchange chromatography (MonoQ, GE healthcare) and size exclusion chromatography

(HiLoad75, GE healthcare) in 10mM HEPES pH 7.5, 150mM NaCl and 1mM DTT. All samples were analyzed using SDS-PAGE.

For heterodimeric IFT54/20 complex purification, full-length *Cr*IFT54 (WT or point-mutants) and *Cr*IFT20 were cloned either untagged or with TEV-cleavable HIS-tag into pFL vectors. After producing viral particles as previously described[42], IFT20/54 (WT or V126A/M) were expressed by infection of HighFive insect cells (Invitrogen). The cells were homogenized using a Dounce Homogenizer in a 20mM HEPES pH 7.5 buffer containing 250mM sucrose, 5mM β-mercaptoethanol, 10mM KCl, 1.5mM $MgCl_2$ and protease inhibitor cocktail (Roche) and then purified in large-scale as described above.

Circular dichroism (CD) spectroscopy

Secondary structure content was analysed on a Jasco J-715 spectropolarimeter at 4°C using 0.1mg/mL of recombinant purified proteins in a 0.1-cm quartz cuvette. The measurements were performed in 10mM HEPES 7.5, 100mM NaCl, 10% glycerol and 5mM DTT. Data were obtained and processed using the Spectra Manager v2.06 software from Jasco. The measured curves were buffer corrected and secondary structure assignments were done using the CONTIN fitting method and SMP56 as the reference protein set. Melting curves were measured continuously from 10-90°C, with additional full spectra taken in 10°C steps. Data analysis was performed in Spectra Manager v2.06.

Zebrafish strains and morpholinos

Adult zebrafish were maintained at 28°C, in system water with a conductivity of 500 µS and a pH of 7. Embryos were cultured at 28°C in embryo medium with 0.1% w/v methylene blue. The *elipsa tp49d* mutant, which encodes a premature stop codon at position 195, (previously described) was obtained as a gift from J. Malicki. Heterozygous sibling embryos were used as controls for all experiments using the *elipsa* mutant line. An anti-sense morpholino targeting *traf3ip1* (previously published[16]) was used for all knockdown experiments. Wild-type Tü:AB fish were used for all morpholino experiments.

To rescue the *elipsa*/*traf3ip1* knockdown phenotype, full length zebrafish *ift54* coding sequence was amplified by RT-PCR. Site-directed mutagenesis was then used to introduce mutations at the desired locations. The resulting products were then cloned into the pGEM-Teasy vector and constructs were linearized and transcribed using the SP6/T7 mMessage mMachine kit (Ambion). Approximately 100 pg of mRNA was injected into embryos at the 1-cell stage.

Effects of RNA injections (WT and mutated RNAs) were evaluated based on severity of body curvature, analysis of pronephric cilia, presence or absence of pronephric cysts and surface area of the retina. Body curvature was quantified by measuring the internal angle of each larva using ImageJ software. Larvae were classified as follows: severe (0-60°), moderate (60-90°), mild (90-120°) and normal (over 120°). Live embryos and larvae were photographed using a Leica M165FC microscope and camera. For histological analysis, larvae were fixed in 4% paraformaldehyde (PFA), embedded in paraffin and sectioned at 5 µm. Sections were stained with haemotoxylin & eosin and photographed with a Nikon DXM1200F camera and an Olympus BX41 microscope.

Plasmids, cell culture and establishment of stable cell lines

*Mm*Flag-*Ift54* construct was a gift from G. Pazour[17]. Human cDNA of *TRAF3IP1* (Invitrogen) was cloned into the pcDNA-DEST40 N vector. The mutations were created using the QuickChange site-directed mutagenesis kit according to the manufacturers protocol (Stratagene). For gene silencing of *TRAF3IP1*, the shRNA sequences described in **Table S1** were cloned into the lentiviral pLKO.1 vector that contained a cassette conferring puromycin resistance. mIMCD3 were transduced with non-targeted (shNTC) or *Traf3ip1*-specific shRNA sequences and selected by adding puromycin (2µg/ml) to the culture medium (DMEM/F12(1:1) with GlutaMaxI medium containing 10% FBS, 100 U/ml penicillin and 100 mg/ml streptomycin). For rescue experiments, shNTC and sh*Traf3ip1*(shRNA #461) mIMCD3 cells were transfected with pDEST40-GFP-*TRAF3IP1*-WT or mutant plasmids using Amaxa Cell Line Nucleofector (Solution V, program O17)[43], sorted by FACS and selected with 0.35 mg/ml G418 (Life Technologies). Fibroblasts were obtained from skin biopsies of patients and cultured in Optimem supplemented with 10% FBS, 100 U/ml penicillin and 100 mg/ml streptomycin (all from Life Technologies). Ciliogenesis was induced by starving the cells in serum-free Optimem for 24hrs. 293T cells were cultured in DMEM supplemented with 10% FBS, 100 U/ml penicillin and 100 mg/ml streptomycin.

Antibodies

The used antibodies are: acetylated α-tubulin (6-11-B-1) and α-tubulin (T5168) from Sigma; EB1 (610534) and anti-PKAc (610980) from BD biosciences; EB2 (K52), acetylated α-tubulin (ab24610) and α-tubulin (ab18251) from Abcam; IFT54 (HPA037858, Atlas Antibodies); ZO1 (61-7300, Life Technologies); ARL13B (17711-1-AP, Proteintech); Gp135 (AF1556, R&D); γ-tubulin (DQ-19, Sigma); γ-tubulin (C-20), MAP4 (H-300and G-10) and

ACIII (C-20) from Santa Cruz. Highly cross adsorbed secondary antibodies (Alexa Fluor 488, Alexa Fluor 546, AlexaFluor 555, AlexaFluor 532 and Alexa Fluor 647) were obtained from Molecular Probes (Life Technologies).

Immunofluorescence and image analysis

Zebrafish embryos at 48 hpf were fixed overnight at 4°C in 4% PFA, washed in PBS and incubated in PBS-Triton-4% BSA for 1 hour at 4°C prior to antibody incubation. Alternatively, fibroblasts and mIMCD3 cells were fixed in 4% PFA, permeabilized with 0.2% Triton-X 100 or fixed in ice-cold Methanol for 5min and incubated with 1% skim milk or 1% BSA, 0.1% Tween20 prior to incubation with primary (1 to 3 hours at room temperature or overnight at 4°C) and secondary (30 minutes at room temperature) antibodies. Appropriate controls were performed omitting the primary antibodies. DNA was stained with Dapi or Hoechst (except for STED imaging). Confocal images were taken on either Zeiss LSM 700 or LEICA SP8 microscopes. Images were analyzed with ImageJ. Alternatively, super resolution images were acquired using a LEICA SP8 gSTED micrococoscope, equipped with a 660nm laser that quenches the fluorescence outside the centre of the focus. Images were then deconvoluted using Huygens software. Ciliogenesis analyses were performed on a CV7000 confocal microscope from YOKOGAWA with 40X long distance. Z-stacks were acquired with identical acquisition settings (gain, offset, laser power) and all measurements of fluorescence intensity were performed on maximum intensity projection, calculated with the Yokogawa software. For all cilia numerical values (frequency, length), we developed one specific pipeline using CellProfiler software[44]. In brief, nuclei were detected as primary objects using Otsu Adaptive two-class thresholding. For cilia length, a mask was constructed by applying MoG global thresholding on ARL13B staining, followed by measurement of the major axis length. Cilia frequency was calculated by dividing cilia and nuclei counts. All data points are performed in duplicate with 4 fields acquired per well, and an average of 300 cells/field. Cell profiler pipeline was run using the Linux cluster interface JENKINS. Spheroids were directly analysed using the ZEN 2011 software (Zeiss).

Calcium switch assay and TER measurement

mIMCD3 cells grown on 65mm Transwell filters for 7 days were subjected to Ca^{2+} switch as described in Straight *et al.*[45]. TER was determined using a Millicell-ERS volt–ohm meter (Millipore) immediately after the addition of normal growth medium and at the indicated time points. 6hrs after Ca^{2+} switch, cells were fixed with 4% PFA and processed as described above.

Spheroid Assay

3D spheroid cell culture was performed using 5% Matrigel (BD) in chamber slides (Lab-TEK). 10,000 cells were plated per chamber and spheroids were grown at 37°C/5% CO_2 for 5 days. Spheroids were fixed with 1% PFA, further stained and analysed as described in "immunofluorescence analysis".

Protein extraction and western blotting

Cells were extracted in 50mM Tris-HCl, 150mM NaCl, 0.5% sodium deoxycholate, 2mM EDTA, 1% Triton X-100 and 0.1% sodium dodecyl sulfate. Protein dosage was then performed using the BCA protein assay kit (ThermoScientific). 30-50µg of proteins were loaded on 8% or 10% acrylamide gels, blotted on PVDF membrane (Millipore) and the membrane was incubated using the indicated antibodies. Western blots were then analyzed with Bioprofil software.

qPCR

Total cellular mRNA was isolated using Qiagen Extraction Kit and treated with DNase I. 1µg of total RNA was reverse-transcribed using Superscript II (Life Technologies). Relative expression levels of the *TRAF3IP1* or *MAP4* mRNAs were determined by real-time PCR using either Absolute SYBR Green ROX Mix (ABgene) or TaqMan Gene Expression Assay (Applied Biosystems) with specific primers (**Table S1**). *HhTRAF3IP1, HhMAP4, MmTraf3ip1* (Mm01285632_m1, Life Technologies) expression performed in triplicate was normalized to *HhGAPDH* or *MmTbp* (Mm00446971_m1, Life Technologies) mRNA expression. Data were analyzed with the $2^{-\Delta\Delta Ct}$ method [31].

Co-Immunoprecipitation

HEK 293T cells were co-transfected with Flag-tagged *Mm*IFT54 constructs and GFP-IFT20 (kindly given by G. Pazour) or GFP-MAP4 (gift from J. Nelson) using the calcium phosphate method. 48 hrs post-transfection, cells were lysed in 50mM Tris-HCl pH 7.5, 150 mM NaCl, 0.5% Triton and lysates were first incubated with rabbit or mouse isotypic control antibodies and G-protein beads for 1hr at 4°C. Pre-cleared lysates (containing 1mg of proteins) were then incubated with rabbit anti-Flag (Sigma) or mouse monoclonal anti-GFP antibodies (Roche) coupled to G-protein beads for 3 hrs at 4°C. Beads were then washed three times with increasing amounts of NaCl (600nM; 300nM and 150nM NaCl in 50mM Tris-HCl pH 7.5), resuspended in 2X sample buffer and boiled for 5 min. Western blot analyses were conducted as described above.

Microtubule tracking

EB3-GFP plasmid (obtained from R. Köster) was linearized and reverse-transcribed using the SP6 mMessage mMachine kit (Ambion). *Elipsa* embryos were then injected with 50 pg of EB3-GFP RNA at the 1-cell stage, and photographed at 60 hpf. Time-lapse confocal microscopy images were recorded over a period of 5 minutes, and the resulting sequences were analysed using Imaris software to quantify the microtubule dynamics *in vivo*.

Statistical analyses

Results are presented as means of $n \geq 2$ independent experiments ± standard error/deviation. Statistical analyses were performed with the GraphPad Prism software by using ANOVA followed by Bonferonni's or Dunnett's multiple-comparisons test versus a control group (post-hoc) or by using Kruskal-Wallis test followed by Dunn's multiple-comparisons post-hoc test. $p<0.05$ was considered statistically significant.

References

1. Baker, K. & Beales, P.L. Making sense of cilia in disease: the human ciliopathies. *Am J Med Genet C Semin Med Genet* **151C**, 281-95 (2009).
2. Salomon, R., Saunier, S. & Niaudet, P. Nephronophthisis. *Pediatr Nephrol* **24**, 2333-44 (2009).
3. Perrault, I. *et al.* Mainzer-Saldino syndrome is a ciliopathy caused by IFT140 mutations. *Am J Hum Genet* **90**, 864-70 (2012).
4. Schueler, M. *et al.* DCDC2 Mutations Cause a Renal-Hepatic Ciliopathy by Disrupting Wnt Signaling. *The American Journal of Human Genetics* **96**, 81-92 (2015).
5. Wolf, M.T.F. Nephronophthisis and related syndromes. *Current Opinion in Pediatrics* **Publish Ahead of Print**(9000).
6. Delous, M., Gaudé, H.M. & Saunier, S. Genetic bases and pathogenic mechanisms of nephronophthisis. *Drug Discovery Today: Disease Mechanisms* **10**, e143-e151 (2013).
7. Failler, M. *et al.* Mutations of CEP83 Cause Infantile Nephronophthisis and Intellectual Disability. *American Journal of Human Genetics* **94**, 905-914 (2014).
8. Halbritter, J. *et al.* Defects in the IFT-B component IFT172 cause Jeune and Mainzer-Saldino syndromes in humans. *Am J Hum Genet* **93**, 915-25 (2013).
9. Bredrup, C. *et al.* Ciliopathies with Skeletal Anomalies and Renal Insufficiency due to Mutations in the IFT-A Gene WDR19. *American Journal of Human Genetics* **89**, 634-643 (2011).
10. Davis, E.E. *et al.* TTC21B contributes both causal and modifying alleles across the ciliopathy spectrum. *Nat Genet* **43**, 189-196 (2011).
11. Ishikawa, H. & Marshall, W.F. Ciliogenesis: building the cell's antenna. *Nat Rev Mol Cell Biol* **12**, 222-234 (2011).
12. Taschner, M., Bhogaraju, S. & Lorentzen, E. Architecture and function of IFT complex proteins in ciliogenesis. *Differentiation* **83**, S12-S22 (2012).
13. Wei, Q. *et al.* Transition fibre protein FBF1 is required for the ciliary entry of assembled intraflagellar transport complexes. *Nat Commun* **4**, 2750 (2013).
14. Berbari, N.F. *et al.* Mutations in Traf3ip1 reveal defects in ciliogenesis, embryonic development, and altered cell size regulation. *Dev Biol* **360**, 66-76 (2011).
15. Doerre, G. & Malicki, J. Genetic analysis of photoreceptor cell development in the zebrafish retina. *Mechanisms of Development* **110**, 125-138 (2002).
16. Omori, Y. *et al.* elipsa is an early determinant of ciliogenesis that links the IFT particle to membrane-associated small GTPase Rab8. *Nat Cell Biol* **10**, 437-444 (2008).
17. Follit, J.A., Xu, F., Keady, B.T. & Pazour, G.J. Characterization of mouse IFT complex B. *Cell Motility and the Cytoskeleton* **66**, 457-468 (2009).
18. Guo, C.W. *et al.* Proteomic analysis reveals novel binding partners of MIP-T3 in human cells. *Proteomics* **10**, 2337-47 (2010).
19. Wang, Z. *et al.* Adult Type 3 Adenylyl Cyclase–Deficient Mice Are Obese. *PLoS ONE* **4**, e6979 (2009).
20. Kremer, B.E., Haystead, T. & Macara, I.G. Mammalian Septins Regulate Microtubule Stability through Interaction with the Microtubule-binding Protein MAP4. *Molecular Biology of the Cell* **16**, 4648-4659 (2005).
21. Ebneth, A., Drewes, G., Mandelkow, E. & Mandelkow, E. Phosphorylation of MAP2c and MAP4 by MARK kinases leads to the destabilization of microtubules in cells. *Cell Motil Cytoskeleton.* **44**, 209-24 (1999).
22. Ghossoub, R. *et al.* Septins 2, 7 and 9 and MAP4 colocalize along the axoneme in the primary cilium and control ciliary length *J Cell Sci* **126**, 2583-2594 (2013).
23. Ling, L. & Goeddel, D.V. MIP-T3, a novel protein linking tumor necrosis factor receptor-associated factor 3 to the microtubule network. *J Biol Chem* **275**, 23852-60 (2000).

24. Morris, J.A., Kandpal, G., Ma, L. & Austin, C.P. DISC1 (Disrupted-In-Schizophrenia 1) is a centrosome-associated protein that interacts with MAP1A, MIPT3, ATF4/5 and NUDEL: regulation and loss of interaction with mutation. *Human Molecular Genetics* **12**, 1591-1608 (2003).
25. Piperno, G., LeDizet, M. & Chang, X.J. Microtubules containing acetylated alpha-tubulin in mammalian cells in culture. *The Journal of Cell Biology* **104**, 289-302 (1987).
26. Berbari, N.F. *et al.* Microtubule modifications and stability are altered by cilia perturbation and in cystic kidney disease. *Cytoskeleton (Hoboken)* **70**, 24-31 (2013).
27. Huynh Cong, E. *et al.* A Homozygous Missense Mutation in the Ciliary Gene TTC21B Causes Familial FSGS *JASN* (2014).
28. Goldspink, D.A. *et al.* The microtubule end-binding protein EB2 is a central regulator of microtubule reorganisation in apico-basal epithelial differentiation. *J Cell Sci* **126**, 4000-14 (2013).
29. Zahnleiter, D. *et al.* MAP4-Dependent Regulation of Microtubule Formation Affects Centrosome, Cilia, and Golgi Architecture as a Central Mechanism in Growth Regulation. *Human Mutation*, n/a-n/a (2014).
30. Cohen, D., Brennwald, P.J., Rodriguez-Boulan, E. & Müsch, A. Mammalian PAR-1 determines epithelial lumen polarity by organizing the microtubule cytoskeleton. *The Journal of Cell Biology* **164**, 717-727 (2004).
31. Delous, M. *et al.* Nephrocystin-1 and nephrocystin-4 are required for epithelial morphogenesis and associate with PALS1/PATJ and Par6. *Hum Mol Genet* **18**, 4711-23 (2009).
32. Boehlke, C. *et al.* Kif3a Guides Microtubular Dynamics, Migration and Lumen Formation of MDCK Cells. *PLoS ONE* **8**, e62165 (2013).
33. Nürnberger, J. *et al.* The Invs Gene Encodes a Microtubule-Associated Protein. *Journal of the American Society of Nephrology* **15**, 1700-1710 (2004).
34. Mollet, G. *et al.* Characterization of the nephrocystin/nephrocystin-4 complex and subcellular localization of nephrocystin-4 to primary cilia and centrosomes. *Hum Mol Genet* **14**, 645-56 (2005).
35. Ou, Y. *et al.* Activation of cyclic AMP/PKA pathway inhibits bladder cancer cell invasion by targeting MAP4-dependent microtubule dynamics. *Urologic Oncology: Seminars and Original Investigations* **32**, 47.e21-47.e28 (2014).
36. Abecasis, G.R., Cherny, S.S., Cookson, W.O. & Cardon, L.R. Merlin-rapid analysis of dense genetic maps using sparse gene flow trees. *Nat Genet* **30**, 97-101 (2002).
37. Strauch, K. *et al.* Parametric and nonparametric multipoint linkage analysis with imprinting and two-locus-trait models: application to mite sensitization. *American Journal of Human Genetics* **66**, 1945-1957 (2000).
38. Gudbjartsson, D.F., Jonasson, K., Frigge, M.L. & Kong, A. Allegro, a new computer program for multipoint linkage analysis. *Nat Genet* **25**, 12-13 (2000).
39. Boyden, L.M. *et al.* Mutations in Kelch-like 3 and Cullin 3 cause hypertension and electrolyte abnormalities. *Nature* **482**, 98-102 (2012).
40. Boyer, O. *et al.* LMX1B Mutations Cause Hereditary FSGS without Extrarenal Involvement. *Journal of the American Society of Nephrology* **24**, 1216-1222 (2013).
41. Thomas, S. *et al.* TCTN3 Mutations Cause Mohr-Majewski Syndrome. *American Journal of Human Genetics* **91**, 372-378 (2012).
42. Taschner, M., Kotsis, F., Braeuer, P., Kuehn, E.W. & Lorentzen, E. Crystal structures of IFT70/52 and IFT52/46 provide insight into intraflagellar transport B core complex assembly. *The Journal of Cell Biology* **207**, 269-282 (2014).
43. Tammachote, R. *et al.* Ciliary and centrosomal defects associated with mutation and depletion of the Meckel syndrome genes MKS1 and MKS3. *Human Molecular Genetics* **18**, 3311-3323 (2009).
44. Kamentsky, L. *et al.* Improved structure, function and compatibility for CellProfiler: modular high-throughput image analysis software. *Bioinformatics* **27**, 1179-1180 (2011).

45. Straight, S.W. *et al.* Loss of PALS1 Expression Leads to Tight Junction and Polarity Defects. *Molecular Biology of the Cell* **15**, 1981-1990 (2004).

Family	Patient	Ethnic origin	Nucleotide alteration	Deduced protein change	Exon	AA sequence conservation	Parental consanguinity/segregation	PolyPhen2/ SIFT	Renal Disease (ESRD at age)	Extrarenal clinical features
NPH638	II-1	Senegal	c.374T>C (het) c.463C>T (het)	p.V125A p.R155*	4 4	*C. elegans* -	No CS Segregation: confirmed	0,799/0 -	NPH, ESRD at 7	HF, RP
NPH579	II-4	Portugal	c.1559T>G (hom)	p.M520R	13	*Orangutan*	probable CS	0,216/0,01	NPH, ESRD at age ND	obesity, bronchitis, mild occular defects, polydactyly
	II-2		c.1559T>G (hom)	p.M520R	13	*Orangutan*	probable CS	0,216/0,01	NPH, ESRD at 16	developmental delay, polydactyly, bronchitis, RP,obesity, hypogonadism
NPH1110	II-2	European	c.1575+6T>G (hom)	p.M525Mfs*3	13	-	CS	-	NPH, ESRD at 15	microdactyly, growth delay, RP, HF (liver transplantation 20 year-old)
NPH302	II-3	Marocco	c.373G>A (hom)	p.V125M	4	*C.elegans*	CS	1/0,01	NPH, ESRD at 6	nystagmus, RP with macular defect ambli opia, obesity, bone defects (pelvis)
	II-4		c.373G>A (hom)	p.V125M	4	*C.elegans*	CS	1/0,01	NPH, ESRD at 5	RP (onset 5 years), obesity, bone defects (pelvis)
	II-6		c.373G>A (hom)	p.V125M	4	*C.elegans*	CS	1/0,01	NPH, ESRD at 6 (small size kidneys)	hexadactyly, strabismus, RP, cholestasis
A4336	II-2	Egyptian	c.51T>G	p.I17S	1	*C. elegans*	CS	1/0	ESRD at 3	polydactyly, RP, Caroli disease, CT-head: bilateral basal ganglia calcifications

Table1: Clinical and pathological phenotypes of patients bearing mutations of *TRAF3IP1*. ESRD: end-stage renal disease; hom: homozygous; het: heterozygous; HF: hepatic fibrosis; NPH: nephronophthisis; RP: retinitis pigmentosa.

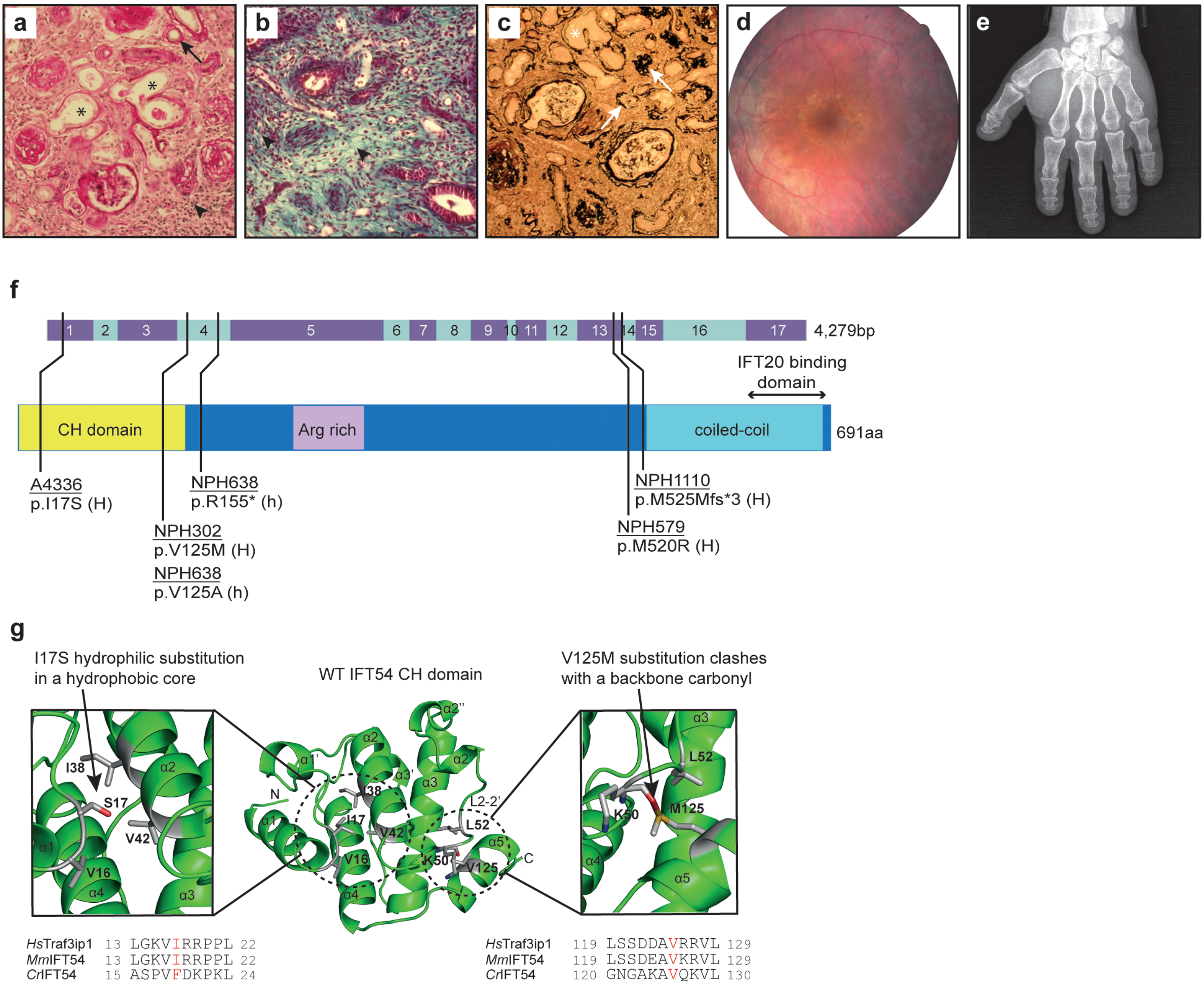

h

sample	Secondary structure determination α (%)	 β (%)	 Turn (%)	 Unstructured (%)	Thermal unfolding Melting temperature TM (°C) (± s.d.)
$CrIFT54_{WT}/CrIFT20$	46	9	16	29	51.15 ± 0.040
$CrIFT54_{V126A}/CrIFT20$	39	11	19	31	48.75 ± 0.061
$CrIFT54_{V126M}/CrIFT20$	35	16	18	31	48.15 ± 0.106
CrIFT20	71	1	6	22	41.62 ± 0.146

Figure 1

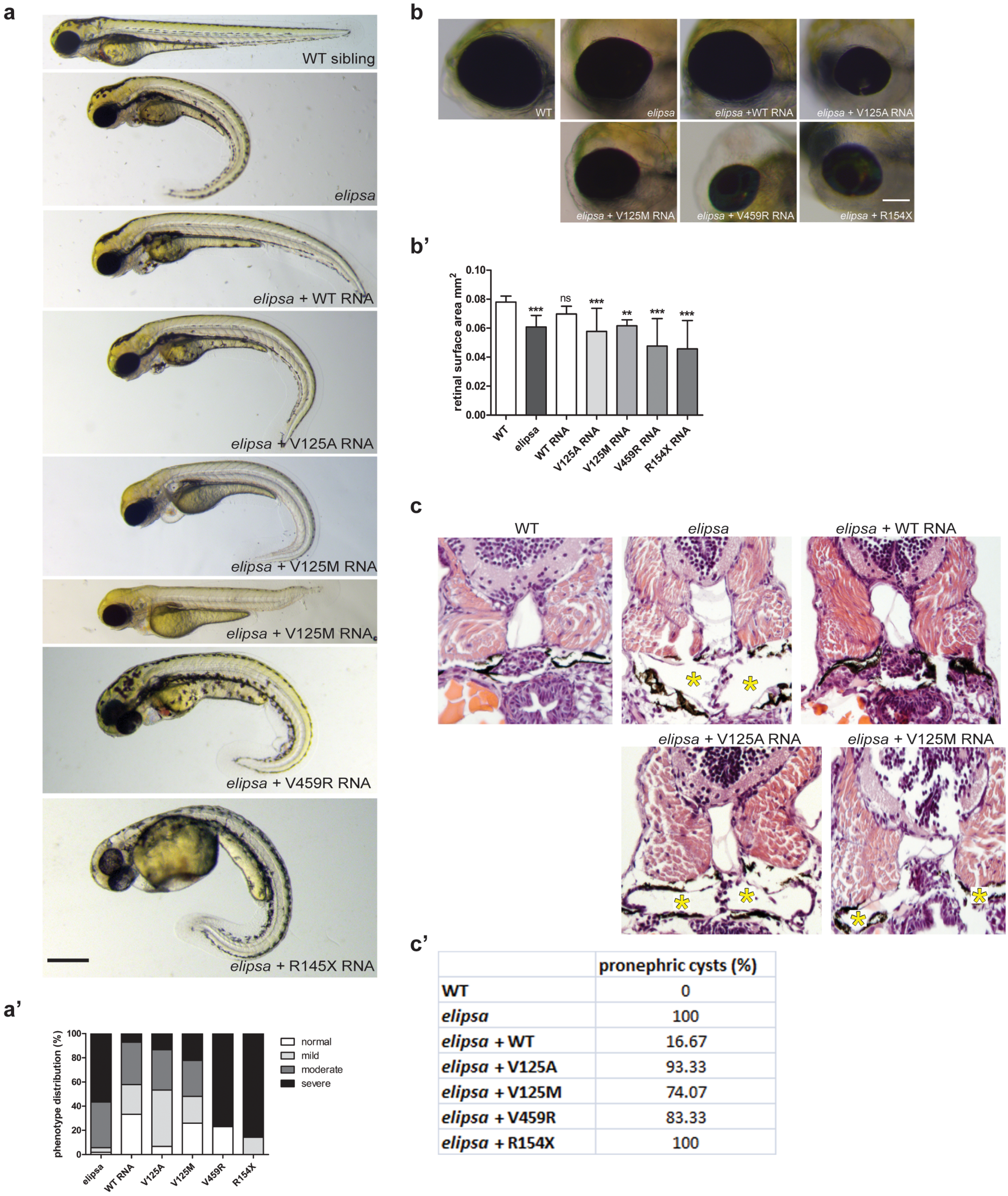

	pronephric cysts (%)
WT	0
elipsa	100
elipsa + WT	16.67
elipsa + V125A	93.33
elipsa + V125M	74.07
elipsa + V459R	83.33
elipsa + R154X	100

Figure 2

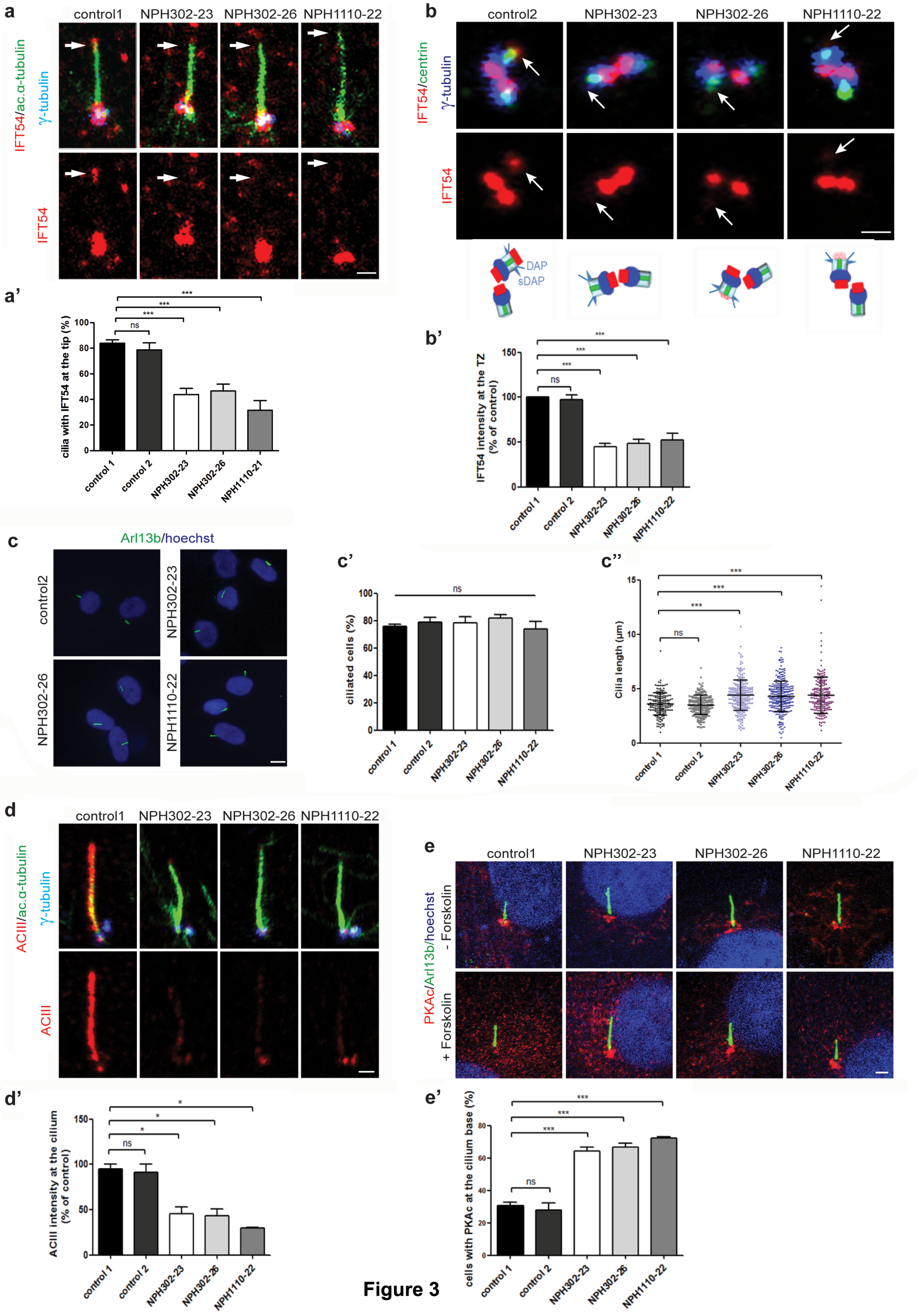
a
control1
NPH302-23
NPH302-26
NPH1110-22
IFT54/ac.α-tubulin
γ-tubulin
IFT54
a'
cilia with IFT54 at the tip (%)
0
20
40
60
80
100
ns
***
***
***
control 1
control 2
NPH302-23
NPH302-26
NPH1110-21
b
control2
NPH302-23
NPH302-26
NPH1110-22
IFT54/centrin
γ-tubulin
IFT54
DAP
sDAP
b'
IFT54 intensity at the TZ (% of control)
0
50
100
150
ns
***
***
***
control 1
control 2
NPH302-23
NPH302-26
NPH1110-22
c
Arl13b/hoechst
control2
NPH302-23
NPH302-26
NPH1110-22
c'
ciliated cells (%)
0
20
40
60
80
100
ns
control 1
control 2
NPH302-23
NPH302-26
NPH1110-22
c''
Cilia length (µm)
0
5
10
15
ns
***
***
***
control 1
control 2
NPH302-23
NPH302-26
NPH1110-22
d
control1
NPH302-23
NPH302-26
NPH1110-22
ACIII/ac.α-tubulin
γ-tubulin
ACIII
d'
ACIII intensity at the cilium (% of control)
0
50
100
150
ns
*
*
*
control 1
control 2
NPH302-23
NPH302-26
NPH1110-22
e
control1
NPH302-23
NPH302-26
NPH1110-22
PKAc/Arl13b/hoechst
- Forskolin
+ Forskolin
e'
cells with PKAc at the cilium base (%)
0
20
40
60
80
ns
***
***
***
control 1
control 2
NPH302-23
NPH302-26
NPH1110-22

Figure 3

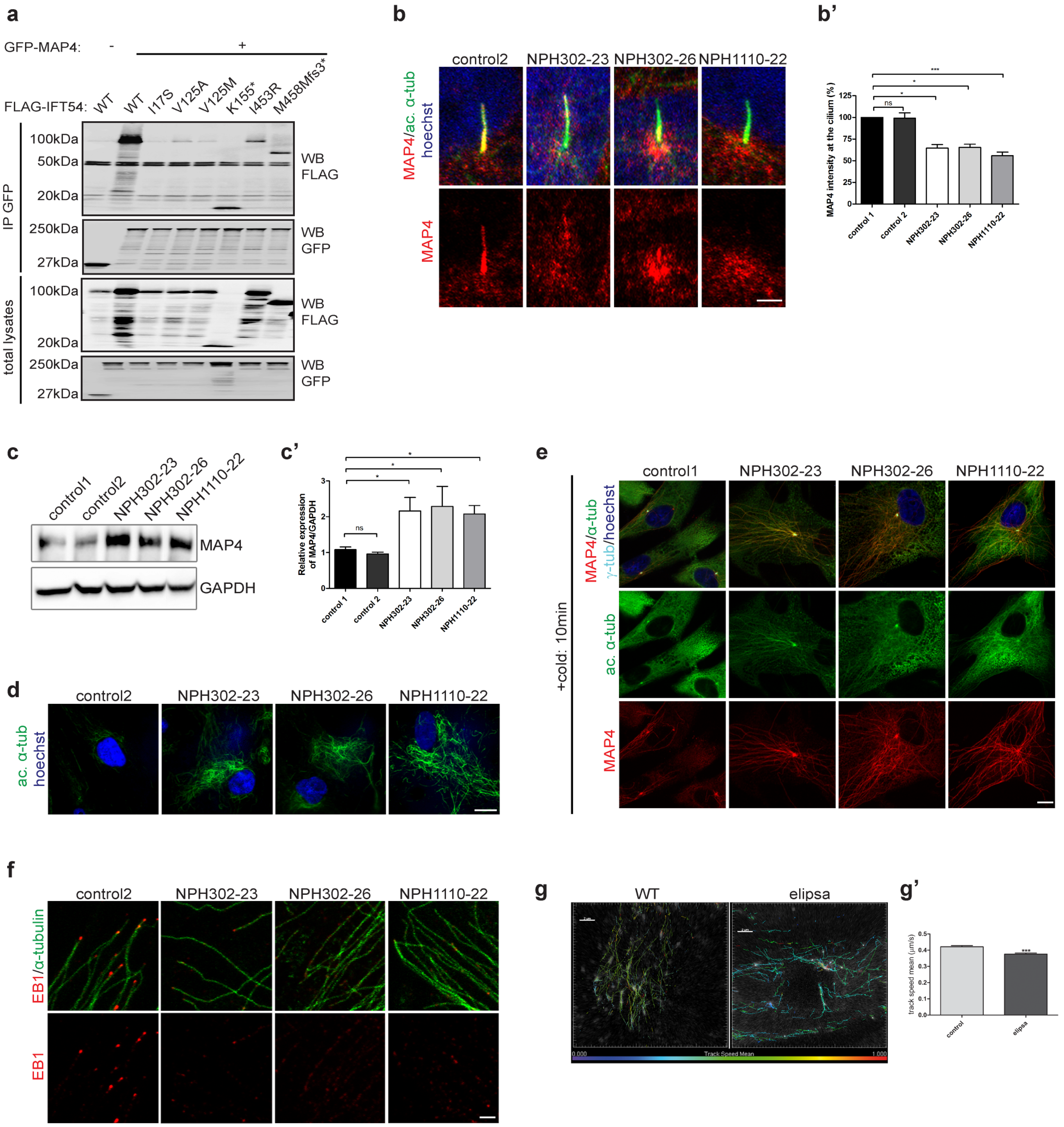
a
GFP-MAP4: - +
FLAG-IFT54: WT WT I17S V125A V125M K155* I453R M458Mfs3*
IP GFP
100kDa
50kDa
20kDa
WB FLAG
250kDa
27kDa
WB GFP
total lysates
100kDa
20kDa
WB FLAG
250kDa
27kDa
WB GFP
b
control2 NPH302-23 NPH302-26 NPH1110-22
MAP4/ac. α-tub hoechst
MAP4
b'
MAP4 intensity at the cilium (%)
0
25
50
75
100
125
ns
*
*
***
control 1
control 2
NPH302-23
NPH302-26
NPH1110-22
c
control1 control2 NPH302-23 NPH302-26 NPH1110-22
MAP4
GAPDH
c'
Relative expression of MAP4/GAPDH
0
1
2
3
ns
*
*
*
control 1
control 2
NPH302-23
NPH302-26
NPH1110-22
d
control2 NPH302-23 NPH302-26 NPH1110-22
ac. α-tub hoechst
e
+cold: 10min
control1 NPH302-23 NPH302-26 NPH1110-22
MAP4/α-tub γ-tub/hoechst
ac. α-tub
MAP4
f
control2 NPH302-23 NPH302-26 NPH1110-22
EB1/α-tubulin
EB1
g
WT
elipsa
2 µm
2 µm
0.000
Track Speed Mean
1.000
g'
track speed mean (µm/s)
0.0
0.1
0.2
0.3
0.4
0.5
***
control
elipsa

Figure 4

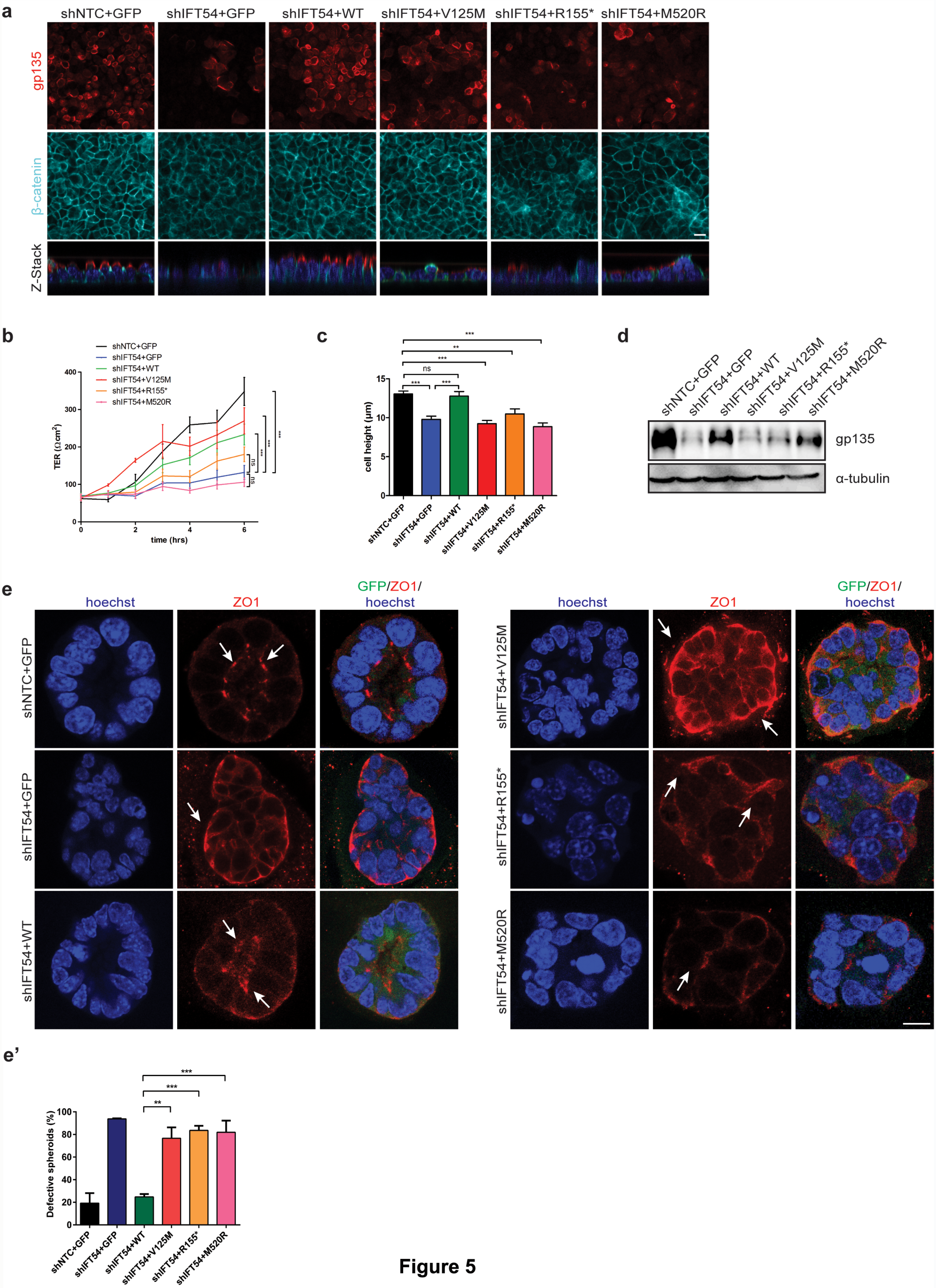
a
shNTC+GFP
shIFT54+GFP
shIFT54+WT
shIFT54+V125M
shIFT54+R155*
shIFT54+M520R
gp135
β-catenin
Z-Stack
b
shNTC+GFP
shIFT54+GFP
shIFT54+WT
shIFT54+V125M
shIFT54+R155*
shIFT54+M520R
TER (Ωcm²)
time (hrs)
0
100
200
300
400
0
2
4
6
ns
ns
***
***
***
c
cell height (μm)
0
5
10
15
***
**
***
ns
***
***
shNTC+GFP
shIFT54+GFP
shIFT54+WT
shIFT54+V125M
shIFT54+R155*
shIFT54+M520R
d
shNTC+GFP
shIFT54+GFP
shIFT54+WT
shIFT54+V125M
shIFT54+R155*
shIFT54+M520R
gp135
α-tubulin
e
hoechst
ZO1
GFP/ZO1/hoechst
shNTC+GFP
shIFT54+GFP
shIFT54+WT
shIFT54+V125M
shIFT54+R155*
shIFT54+M520R
e'
Defective spheroids (%)
0
20
40
60
80
100
***
***
**
shNTC+GFP
shIFT54+GFP
shIFT54+WT
shIFT54+V125M
shIFT54+R155*
shIFT54+M520R

Figure 5

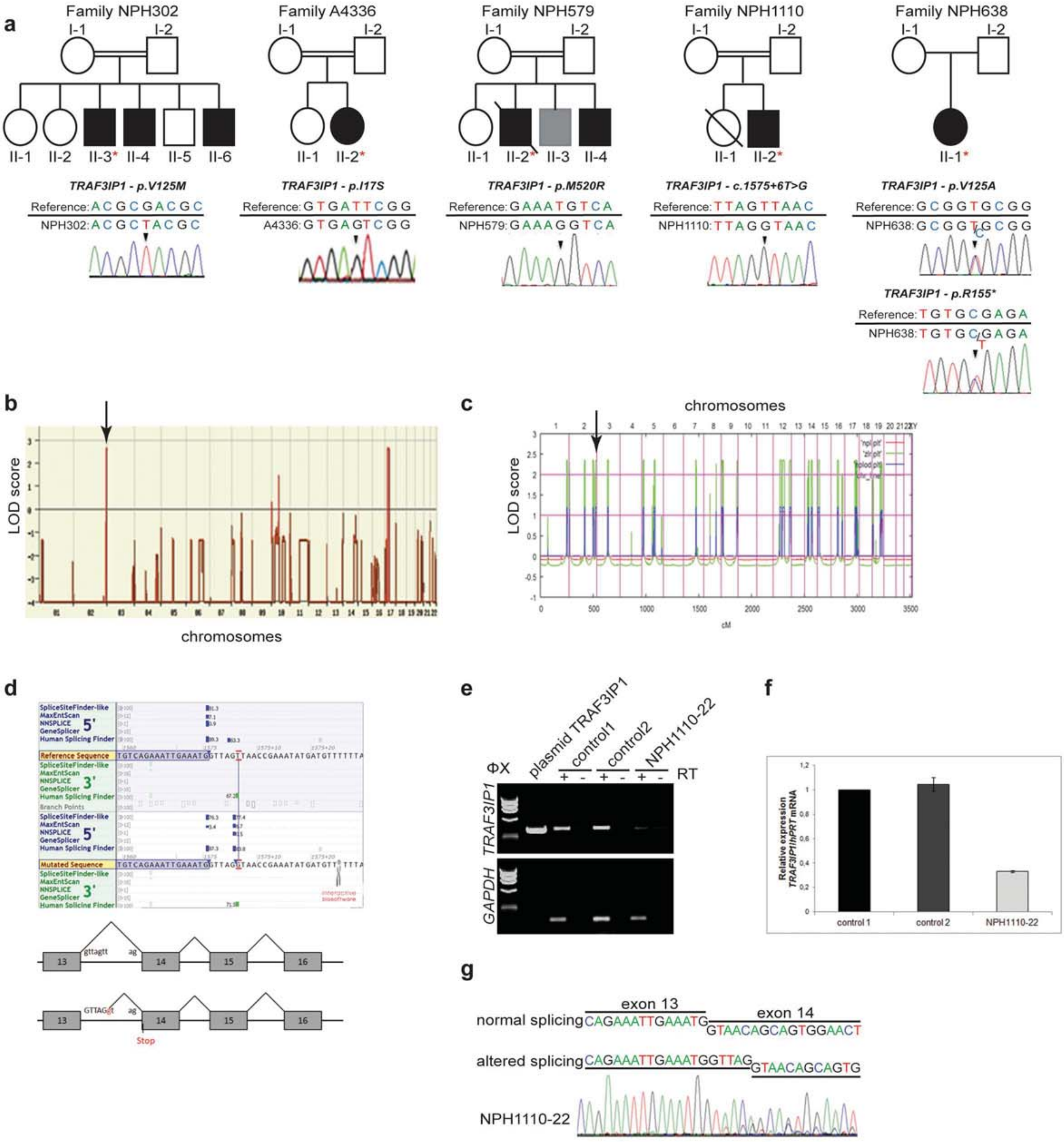

Supplementary Figure 1: Sequence and linkage analysis. (**a**) Pedigree of families with mutations in *TRAF3IP1*. WES or “ciliome” sequencing was performed on individuals indicated by a red asterisk. Below each pedigree, the sequence trace with identified mutated nucleotide is shown. (**b-c**) Linkage analysis of families NPH302 (**b**) and A4336 (**c**) revealed homozygous regions of 15MB and 211MB, respectively. A maximum logarithm of odds (LOD) scores of 2.6557 (**b**) and 2.4 (**c**) was obtained at the *TRAF3IP1* locus (arrow). (**d**) In individual NPH1110-22, the identified c.1575+6T>G mutation on intron 13 creates a new donor splice site with a higher score than the “normal” one leading to a preamture STOP codon (p.M525Mfs*3), according to Alamut prediction. (**e**) RT-PCR analysis of the *TRAF3IP1* transcript in patient NPH1110-22 fibroblasts harboring the c.1575+6T>G mutation and control individuals using primers located in exons 9 and 16 (**Table S1**). A single band of 509 bp was detected from controls and individual NPH1110-22 cDNAs. (**f**) q-PCR demonstrating decreased expression of *TRAF3IP1* mRNA in individual NPH1110-22 compared to controls. (**g**) Sanger sequencing of the NPH1110-22 RT-PCR product revealed that the c.1575+6T>G mutation leads to partial aberrant splicing: the normal splicing sequence is detected as well as the altered splicing product. Altogether, these results indicate that, in individual NPH1110-22, some WT mRNA remains while the aberrant spliced mRNA undergoes mRNA decay.

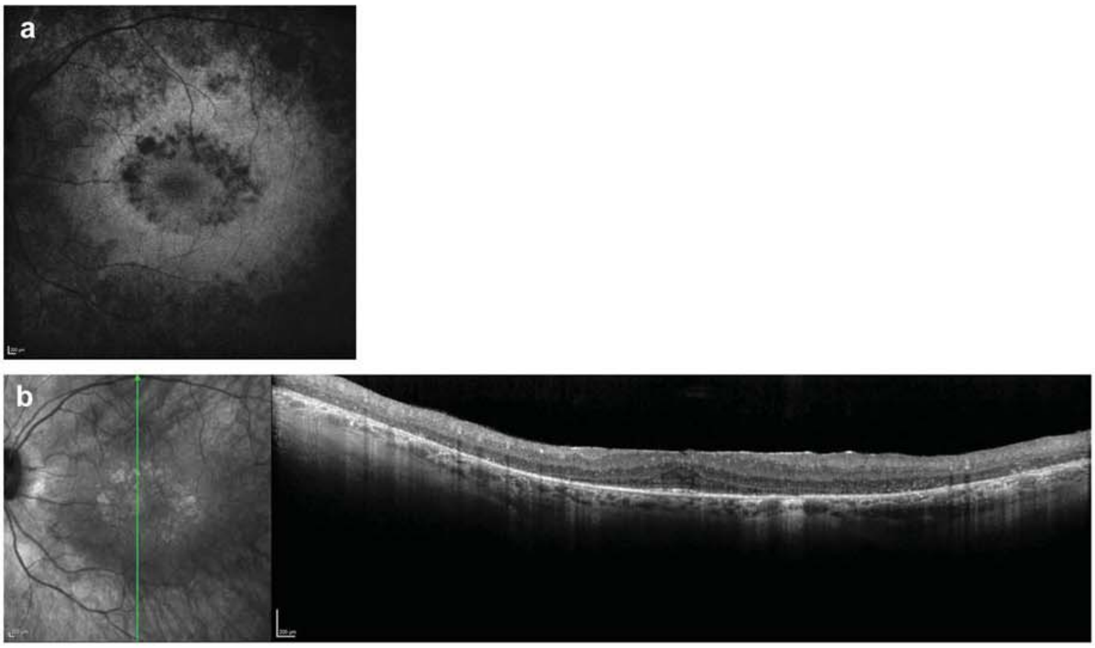

Supplementary Figure 2: Retinal defects in affected individual NPHP1110-22. (**a**) Autofluorescence of the fundus of individual NPH1110-22 showing diffuse peripheric hypo-autofluorescences and a relatively unaffected posterior pole of the retina, with nevertheless, a ring of perimacular hypo-autofluorescences surrounded by speckled hyper-autofluorescences. (**b**) Optical coherence tomography (OCT, NPH1110-22) showing retinal reduction marked by loss of the deep layers corresponding to photoreceptors. The fovea is erased due to traction exerted by the retinal membrane

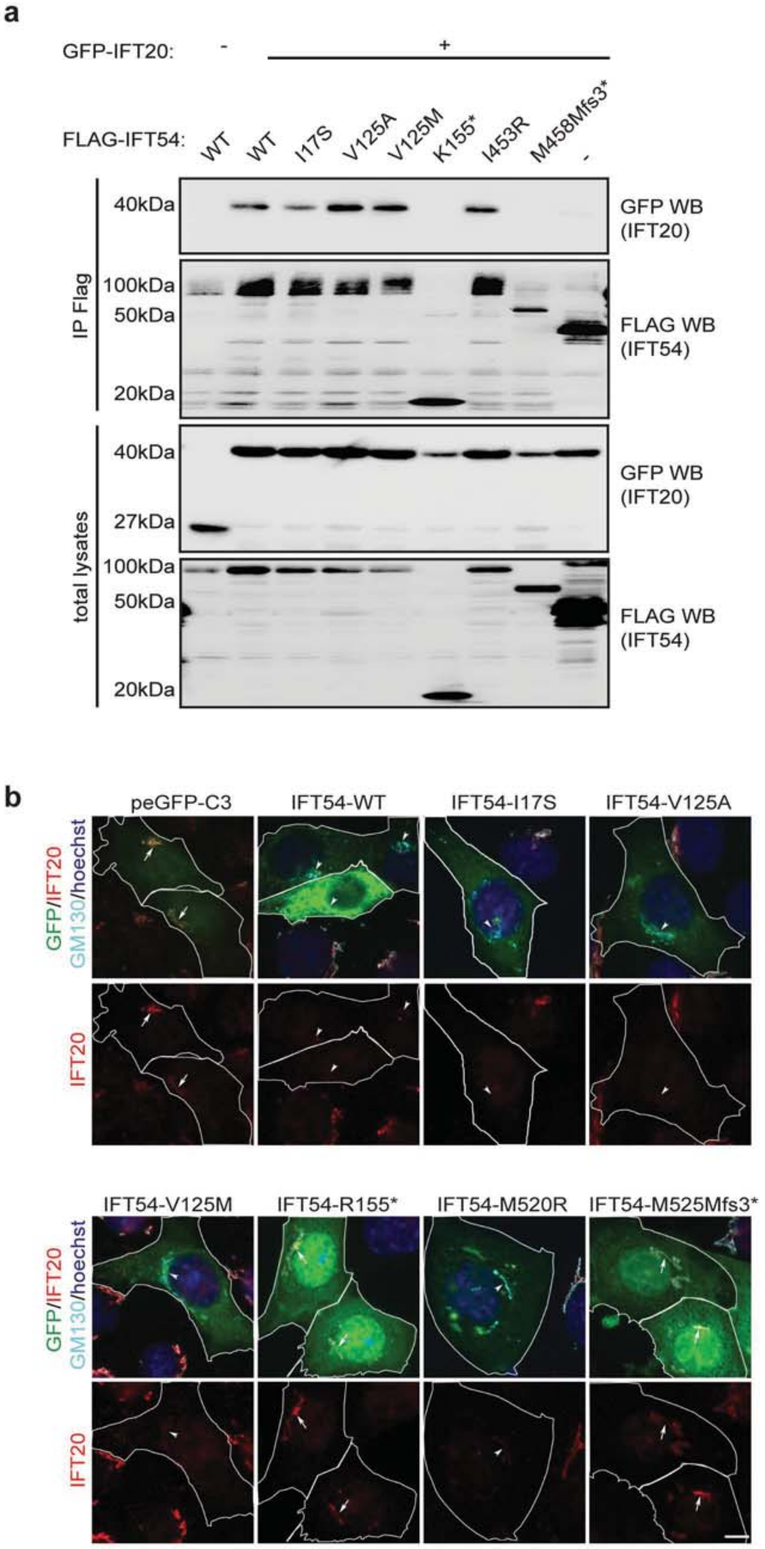

Supplementary Figure 3: Missense mutations of *TRAF3IP1* did not affect recruitment of IFT 20. (**a**) Lysates from HEK293T cells co-expressing Flag-tagged WT or mutant forms of *Mm*IFT54 (p.K155*, p.I453R and p.M458Mfs3* correspond to the human mutations p.R155*, p.M520R and p.M525Mfs3*) and GFP-IFT20 (as indicated) were immunoprecipitated (IP) with an anti-Flag antibody. The co-immunoprecipitation of GFP-IFT20 and Flag-IFT54 constructs was followed by Western-blot (WB) using GFP and Flag antibodies (as indicated). (**b**) Since overexpression of IFT54 has been reported to prevent IFT20 localization to the Golgi[13], we performed immunofluorescence analysis of endogenous IFT20 (red) and the Golgi marker GM130 (light blue) in mIMCD3 cells transfected with GFP-IFT54 (green) WT and mutant constructs. Transfected cells are delineated in white. Arrows and arrowheads highlight IFT20 positive and negative Golgi apparatus, respectively. Scale bars, 10µm.

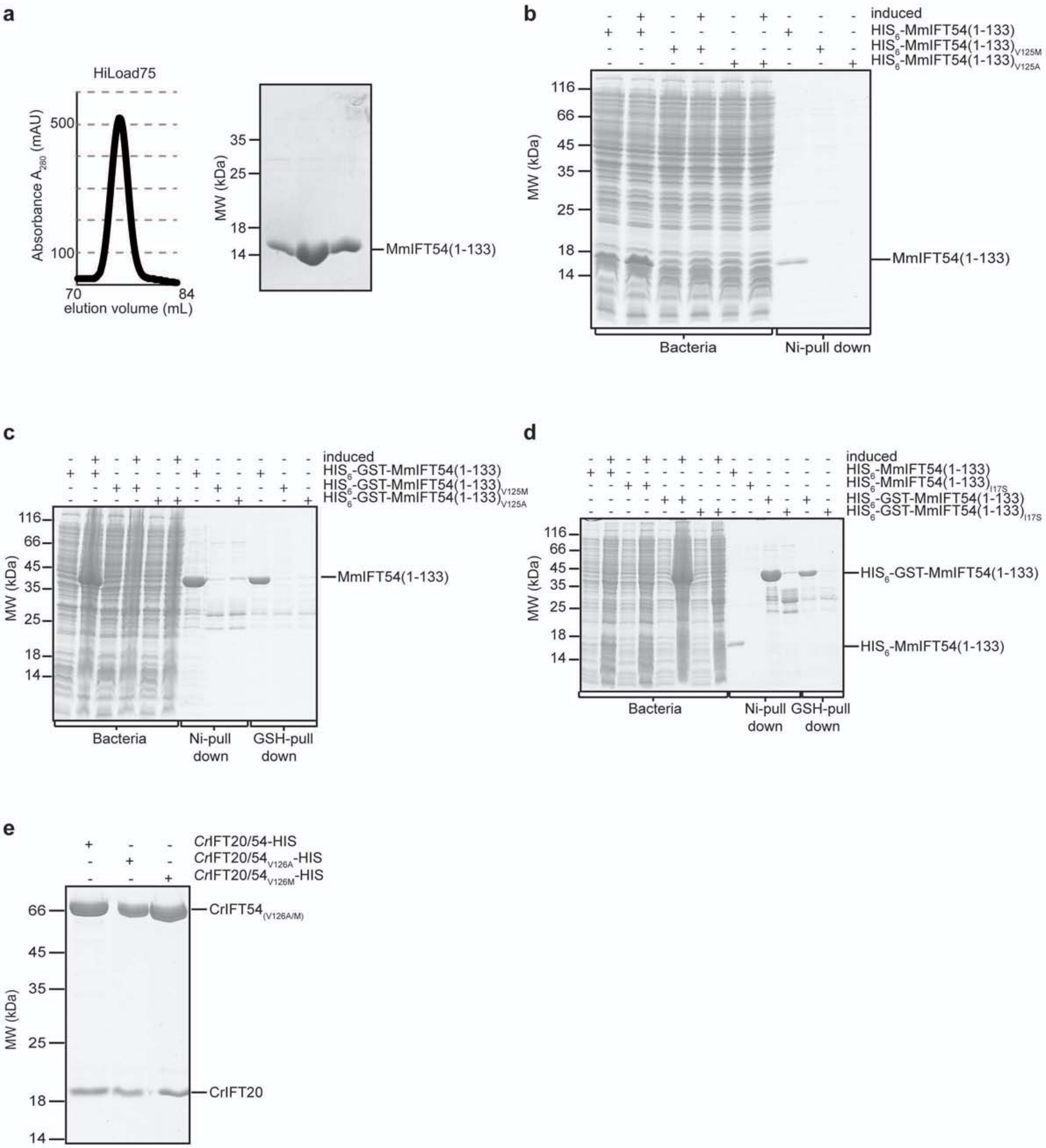

Supplementary Figure 4: Purification and pull down experiments of IFT54 and IFT20/54. (**a**) Size exclusion chromatography profile and Coomassie-stained SDS gel of purified *Mm*IFT54(1-133). (**b-d**) Expression tests in E. coli of WT and mutant *Mm*IFT54 N-terminal CH domains mutants p.V125M and p.V125A (**b and c**) or p.I17S (**d**) (Histidine (HIS) (**b**) and/or GST (**c and d**) tagged forms) induced by 500µM IPTG (Isopropyl-β-D-thiogalactopyranosid). (**e**) Coomassie stained SDS gel of histidine-tagged forms of *Chlamydomonas reinhardtii* (*Cr*) IFT54 WT, V126A and V126M mutants in complex with IFT20 after size exclusion chromatography.

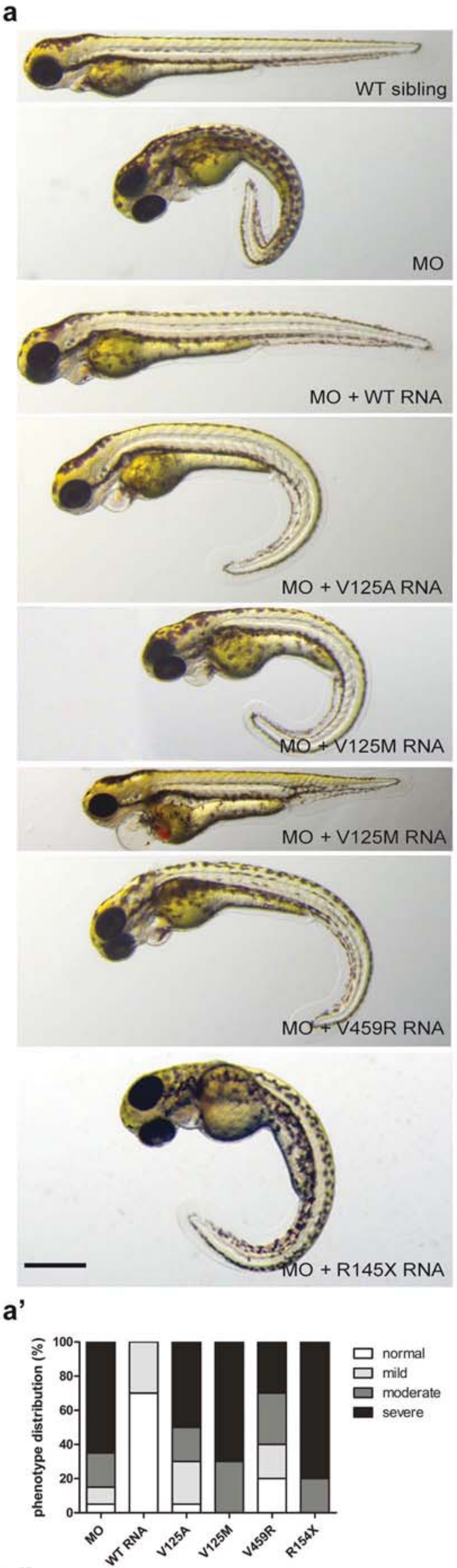

a''

	pronephric cysts (%)
MO	80
MO + WT	25
MO + V125A	84.21
MO + V125M	69.57
MO + V459R	84.62
MO + R154X	80.95

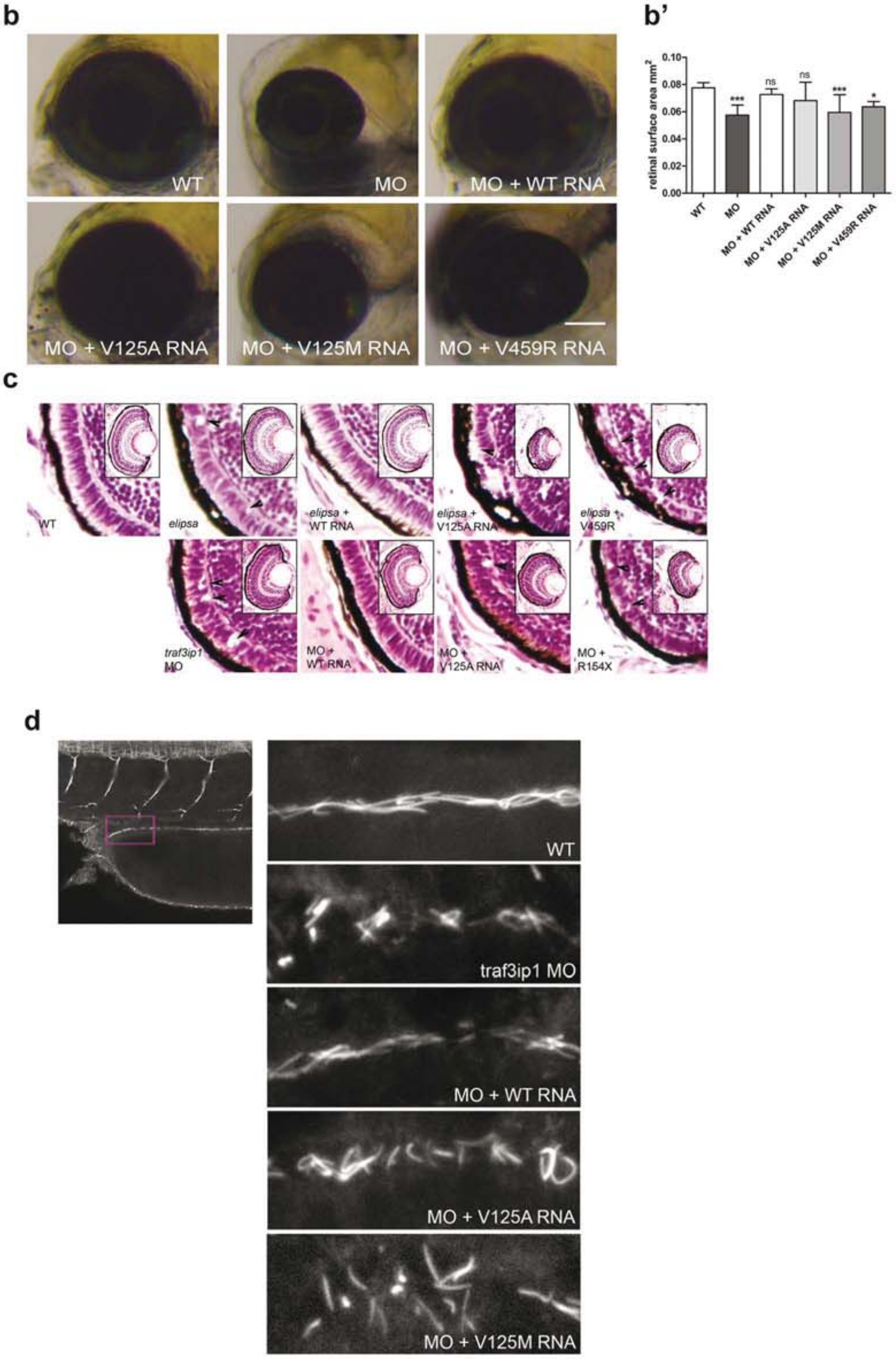

Supplementary Figure 5: Patient mutations do not rescue the kidney and retinal phenotypes characteristic of *traf3ip1* morphant larvae. (a) Body axis curvature phenotype of *traf3ip1* morphant larvae (72 hpf) and morphant larvae co-injected with WT and mutant *traf3ip1* RNA. Scale bar, 0.5 mm. (**a'**) Phenotype distribution as determined by quantification of angle of body axis curvature (n=20, 3 independent experiments). (**a''**) Percentage of pronephric cysts in morphant and rescued larvae (n ≥ 20, 3 independent experiments). (**b**) Eye phenotypes (5 dpf) of WT, *traf3ip1* morphant larvae, and larvae co-injected with *traf3ip1* morpholino and WT/mutant RNA constructs. Scale bar, 0.1 mm. (**b'**) Surface area of the retina (mean +/- SD of n=10 from 2 independent experiments, *P<0.05, **P< 0.01 and ***P< 0.001, Dunnett's multiple-comparison test) (**c**) H&E staining of histological cross sections through the eyes of *elipsa* mutant larvae and *traf3ip1* morphant larvae injected with WT or mutant RNA. Loss of photoreceptor cells is indicated by arrowheads. (**d**) Cilia in the pronephric duct (48 hpf) of indicated morphants were stained using an antibody for acetylated-α-tubulin (n=9, 3 independent experiments).

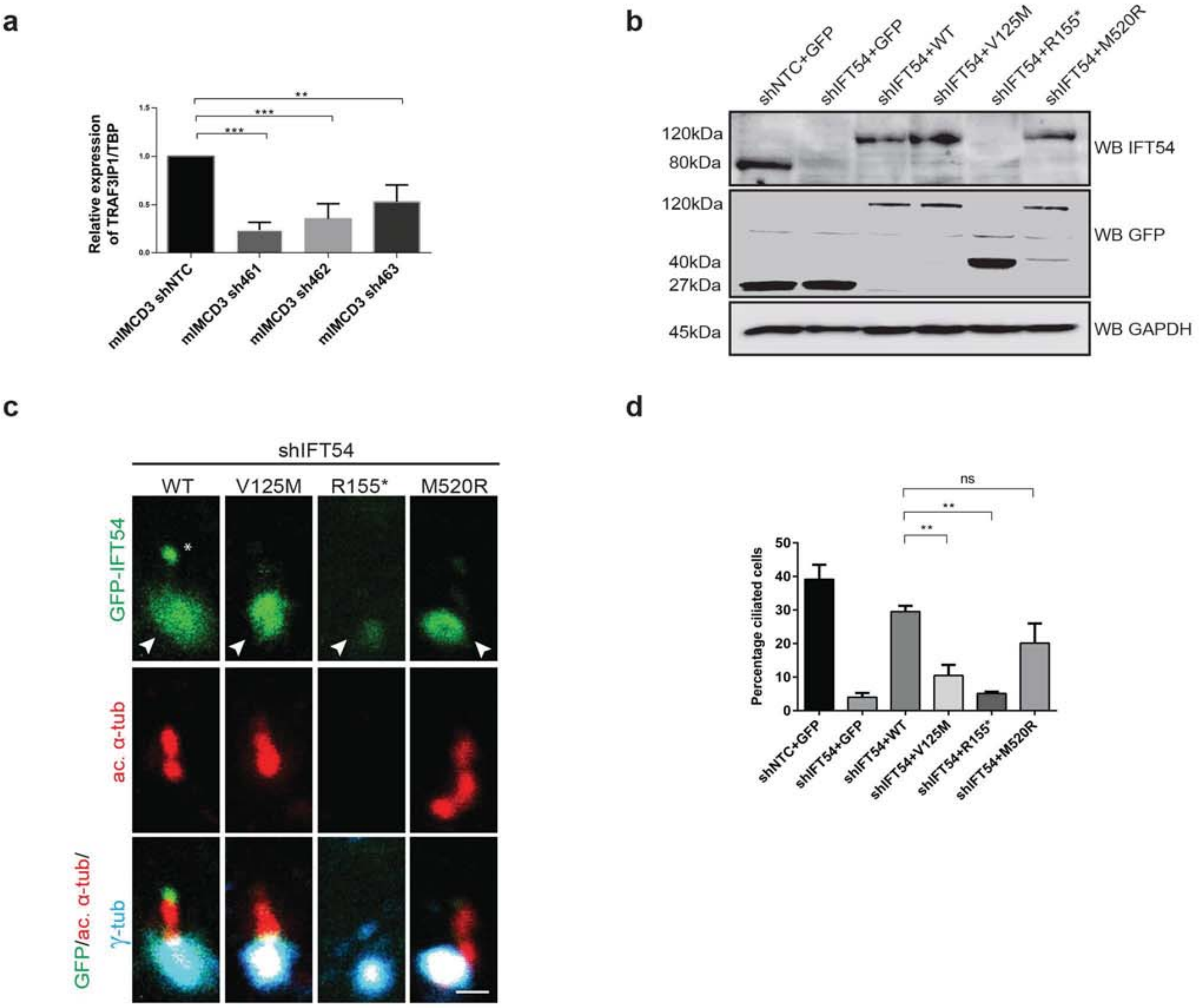

Supplementary Figure 6: Missense mutations partially rescue ciliogenesis defects in *Traf3ip1* knockdown (KD) mIMCD3 cells. (**a**) Relative expression of *Traf3ip1* in shRNA knockdown mIMCD3 clones was analysed by qRT-PCR and normalized to *Tbp* (mean +/- SD of n=3 experiments, **P<0.005, ***P<0.0007, Bonferonni's multiple-comparison test). (**b**) Expression of IFT54 (top), GFP-fusions (middle) and GAPDH (bottom) in *Traf3ip1* knockdown mIMCD3 (shIFT54) stably expressing GFP-tagged IFT54 WT or mutant proteins (green) was analyzed by western blot (WB). (**c**) *Traf3ip1* KD mIMCD3 (shIFT54) stably expressing GFP-tagged IFT54 WT or indicated mutant proteins were fixed and stained for acetylated α-tubulin (cilium, red) and α-tubulin (basal body, light blue). GFP stainings at the basal body region and the tip of cilia are indicated by arrowheads and asterisks, respectively. Scale bar, 1 µm. (**d**) Quantification of ciliated cells in *Traf3ip1* KD mIMCD3 (shIFT54) stably expressing GFP-tagged IFT54 WT or mutant proteins stained for ARL13B (n cells > 500, mean +/- SD of n=2 experiments, ns : not-significant, **P<0.006, Bonferonni's multiple-comparison test).

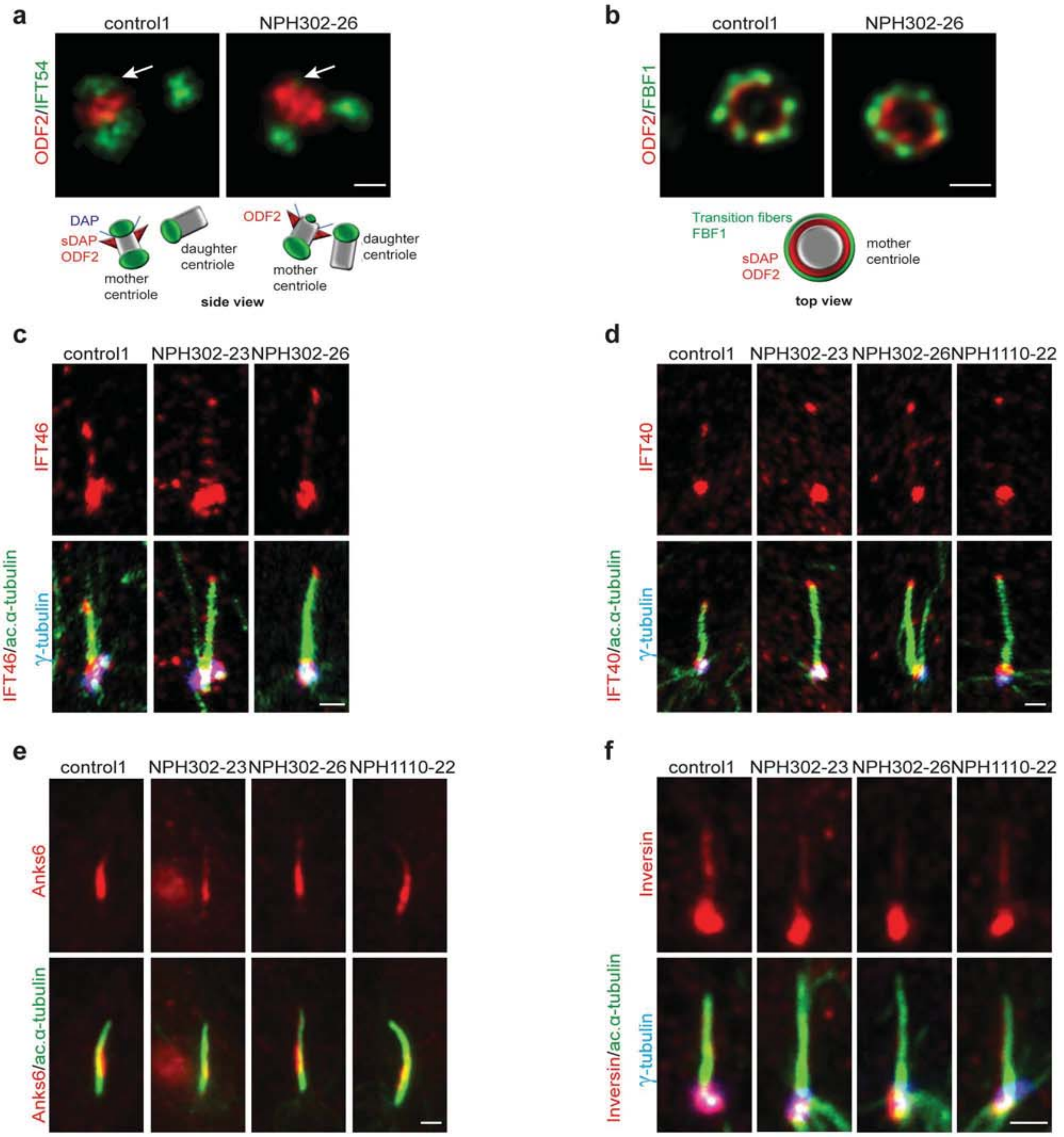

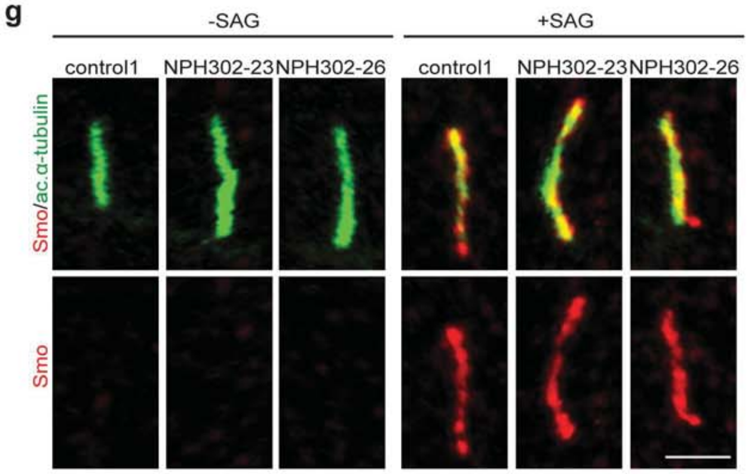

Supplementary Figure 7: Localization of ciliary proteins in fibroblasts from affected individuals. (**a**, **b**) Ciliated fibroblasts from control and the NPH302-26 affected individual were fixed and stained for ODF2 (red, subdistal appendages) and either IFT54 (green, (**a**)) or FBF1 (green, (**b**)) and analyzed by STED microscopy. A schematic representation of the orientation of the analyzed centrioles is shown (sDAPs, subdistal appendages; DAPs, distal appendages). Arrows in (**a**) indicate the pool of IFT54 present at the distal tip of the mother centriole corresponding to the transition zone. Scale bars, 0.25µm. (**c-f**) Ciliated fibroblasts from control and indicated affected individuals were stained for acetylated-α-tubulin (green, cilia) and α-tubulin (light blue, basal body) and either IFT46 (red, **c**), IFT40 (red, **d**), Anks6 (red, **e**) or Inversin (red, **f**). Scale bars, 1µm. (**g**) Ciliated fibroblasts from control and affected individuals treated (+) or not (-) with 100nM of the Hh agonist (SAG) for 24hrs were fixed and stained for acetylated-α–tubulin (green, cilia) and Smoothened (red). Scale bar, 1µm.

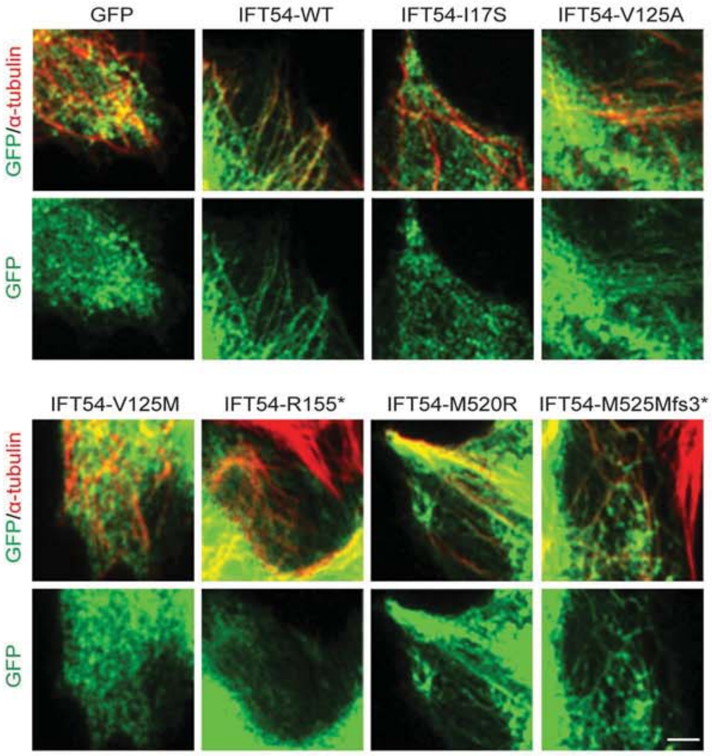

Supplementary Figure 8: *TRAF3IP1* mutations impair IFT54 localization along the cytoplasmic microtubules. RPE1 cells transfected with WT or mutant forms of GFP-IFT54 (green) were treated with 1μM taxol for 1hr to stabilize the microtubule network then fixed with MeOH and stained for α-tubulin (red). Scale bar, 2μm.

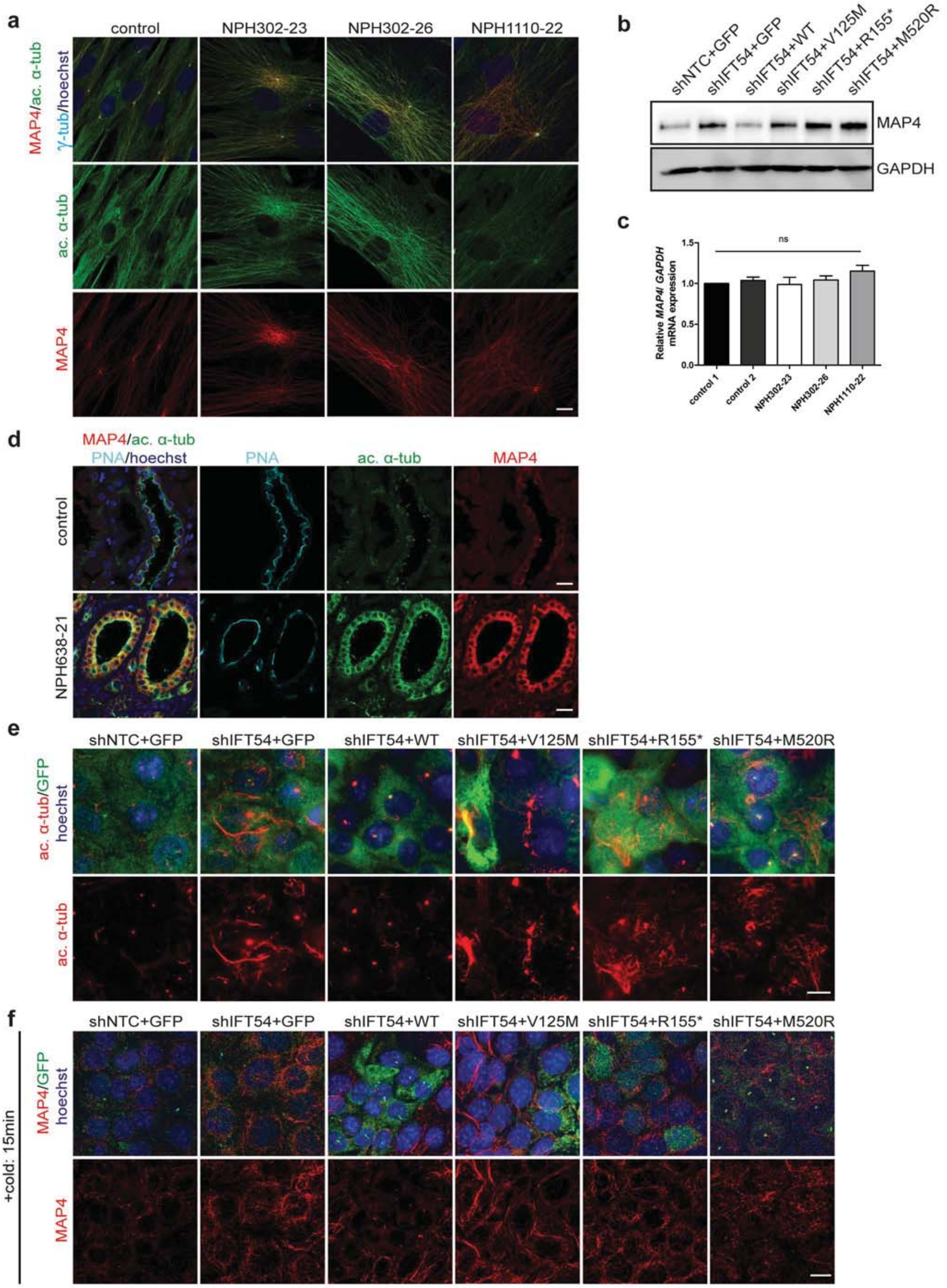

Supplementary Figure 9: *TRAF3IP1* mutations impair MAP4 localization and expression, resulting in increased microtubule stabilization. (**a**) Fibroblasts from control and affected individuals were fixed in MeOH and stained for α-tubulin (green, microtubules) and MAP4 (red). Scale bar, 10µm. (**b**) Expression of MAP4 and GAPDH (loading control) in control and *Traf3ip1*-KD mIMCD3 cells expressing GFP or GFP-IFT54 fusions were analyzed by Western blot. (**c**) Relative expression of *MAP4* to that of *GAPDH* was analyzed by qPCR in control and mutant fibroblasts. (**d**) Kidney biopsies from control and the NPH638-21 affected individual were stained for MAP4 (red), acetylated α-tubulin (green) and with peanut agglutinin (PNA, light blue, distal tubules). Scale bar, 20µm. (**e-f**) Control and *Traf3ip1*-KD mIMCD3 cells expressing either GFP or IFT54 GFP-fusions (green) were either fixed directly in MeOH and stained for acetylated α-tubulin (red, **e**), or treated 15 min on ice before MeOH fixation and stained for MAP4 (red, **f**). Scale bar, 10µm.

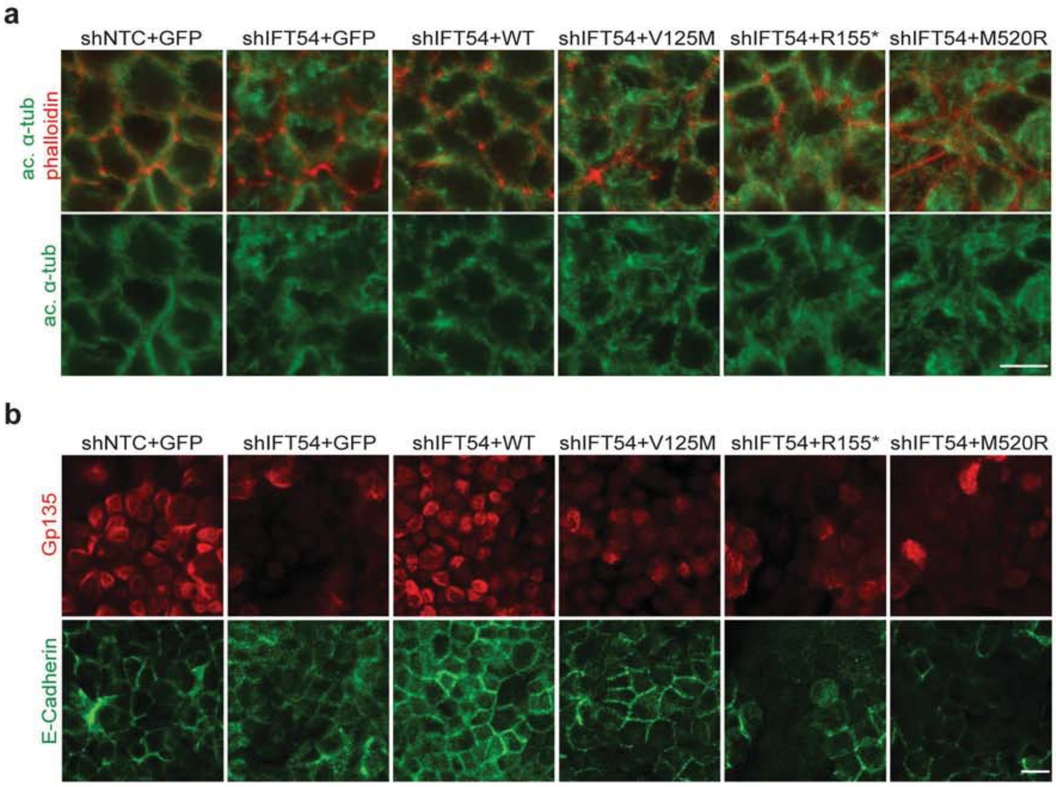

Supplementary Figure 10: *TRAF3IP1* mutations lead to defects in microtubule organization and epithelialization. (**a**) Control and *Traf3ip1*-KD mIMCD3 cells expressing either GFP or IFT54 GFP-fusions grown on filters were fixed and stained for α-tubulin (green, microtubules) and for actin using phalloidin (red). Confocal images corresponding to representative x,y mid-sections are shown. Scale bar, 10μm. (**b**) Control and *Traf3ip1*-KD mIMCD3 cells expressing either GFP or IFT54 GFP-fusions were grown on filters, fixed 6h after Ca^{2+} switch and stained with antibodies against E-Cadherin (green, cell junctions) and Gp135 (red, apical membrane marker). Scale bar, 10μm.

name	purpose	species	position on cDNA	exon	sequence
TRAF3IP1-1F	gene screening	human		1	GCACTGTGGGATGGAAACCG
TRAF3IP1-1R	gene screening	human		1	CAGAAGCAGCTCTGCCAGCAAT
TRAF3IP1-2F	gene screening	human		2	GTGGATGAGGCTGATGAGG
TRAF3IP1-2R	gene screening	human		2	CCAGTTGCCACAATGAGAAA
TRAF3IP1-3F	gene screening	human		3	TGTGGCAACTGGATGTCAT
TRAF3IP1-3R	gene screening	human		3	GGGTTCCCGACTTTCTACTG
TRAF3IP1-4F	gene screening	human		4	GGGTGGACGCTACTGTTA
TRAF3IP1-4R	gene screening	human		4	AATTCTTCCTTCTGTTTTCGAT
TRAF3IP1-5F	gene screening	human		5	TTAGCTGGAGAGAAGGGAG
TRAF3IP1-5R	gene screening	human		5	TAGGCATAAAAGAAAACCAGTT
TRAF3IP1-6F	gene screening	human		6	TTATAGAAAATATCTTGGCATA
TRAF3IP1-6R	gene screening	human		6	CCCACAGAAAATCAGAG
TRAF3IP1-7F	gene screening	human		7	GCTTGAAAAATAAACCTGCT
TRAF3IP1-7R	gene screening	human		7	CACGCATGTGTATGTAACAG
TRAF3IP1-8F	gene screening	human		8	AAATCCCAGCTAAAACAA
TRAF3IP1-8R	gene screening	human		8	AAGTTATGTCCAGTCTTCAATA
TRAF3IP1-9F	gene screening	human		9	ATGTTAATGAAGCCGCTGAT
TRAF3IP1-9R	gene screening	human		9	ATGCCACCTCCTCTCACTT
TRAF3IP1-10F	gene screening	human		10	TCCTGTTTCTATTTAGTACCAT
TRAF3IP1-10R	gene screening	human		10	AGAGTCCACATTCACATTC
TRAF3IP1-11F	gene screening	human		11	GGGAGCTGACATGTGAC
TRAF3IP1-11R	gene screening	human		11	GCACTAAATAAATAGCAGCAG
TRAF3IP1-12F	gene screening	human		12	ACTTTCTGATTGGTCGGGTTA
TRAF3IP1-12R	gene screening	human		12	TGTCTGTTGGCCTATGGTGT
TRAF3IP1-13F	gene screening	human		13	TTAGATTCCTCTCTGCCGAC
TRAF3IP1-13R	gene screening	human		13	GGGGGAAAAAGAAGATTCA
TRAF3IP1-14F	gene screening	human		14	TTTTGAGATCCACAGAAGCAT

TRAF3IP1-14R	gene screening	human		14	CAGTGTGACCCAGACCAG
TRAF3IP1-15F	gene screening	human		15	TAGGTTTTTGGGATAGAGAAT
TRAF3IP1-15R	gene screening	human		15	AAAGATGCTCCAACTTGTAA
TRAF3IP1-16F	gene screening	human		16	GCCCTGTTCTGCCTTTGGACT
TRAF3IP1-16R	gene screening	human		16	CCACCCCAACCTGTTCCTG
TRAF3IP1-17F	gene screening	human		17	AAGAAGCCAACACACAAT
TRAF3IP1-17R	gene screening	human		17	TAACTAGCCAGTATTCCATCT
TRAF3IP1h-7F	cDNA verification	human	7		GCGGCGGTGGTGAGGCGGAC
TRAF3IP1h-156R	cDNA verification	human	156		TCATCTCGGCGTCTGTGTAG
TRAF3IP1h-563F	cDNA verification	human	563		TGAAAGAAGACCGCAAGCCA
TRAF3IP1h-923F	cDNA verification	human	923		GCTCAGGGGAGATGTCTAAA
TRAF3IP1h-1410F	cDNA verification	human	1410		GGTCAAACGGCAAGACAGCA
TRAF3IP1h-1917F	cDNA verification	human	1917		AGACTGTGCCGTGGAGCCCT
TRAF3IP1m-24F	cDNA verification	mouse	24		GACGCAGGAGGCTCTGGGCA
TRAF3IP1m-292R	cDNA verification	mouse	292		GTTCTTTCAGGTTCGTGCCC
TRAF3IP1m-563F	cDNA verification	mouse	563		AAGACAGCAAGCCTCGGGAG
TRAF3IP1m-1022F	cDNA verification	mouse	1022		TAAAACCATCAAAACGGCGA
TRAF3IP1m-1410F	cDNA verification	mouse	1410		CGGTGGGCTCGTGAAGAAGA
Flag-IFT54m-mutV125A-F	mutagenesis	mouse	V125A		CAGTGATGAGGCTGCGAAGAGAGTCTTAGCTG
Flag-IFT54m-mutV125A-R	mutagenesis	mouse			CAGCTAAGACTCTCTTCGCAGCCTCATCACTG
Flag-IFT54m-mutV125M-F	mutagenesis	mouse	V125M		CTCCAGTGATGAGGCAATGAAGAGAGTCTTAG
Flag-IFT54m-mutV125M-R	mutagenesis	mouse			CTAAGACTCTCTTCATTGCCTCATCACTGGAG
Flag-IFT54m-mutK155*-F	mutagenesis	mouse	K155*		CAACAAGAGTGGGTAGGAGGAAGAGTCCAGAATAC
Flag-IFT54m-mutK155*-R	mutagenesis	mouse			GTATTCTGGACTCTTCCTCCTACCCACTCTTGTTG
Flag-IFT54m-mutM458Mfs3X-F	mutagenesis	mouse	M458Mfs3X		GCAGACATTGACATGGTTAGGTGCCGTCAGGGGAGC
Flag-IFT54m-mutM458Mfs3X-R	mutagenesis	mouse			GCTCCCCTGACGGCACCTAACCATGTCAATGTCTGC
Flag-IFT54m-mutI520R-F	mutagenesis	mouse	I520R		CTCAGCTGTCAGAACGCGCAGATATTGATATGGTGCCGTCAG

Flag-IFT54m-mutI520R-R	mutagenesis	mouse			CTGACGGCACCATATCAATATCTGCGCGTTCTGACAGCTGAG
GFP-IFT54-mutM520R-R	mutagenesis	human	M520R		CCATTTCAATTTCTGATCTTTCTGAGAGCTGAGG
GFP-IFT54-mutM520R-F	mutagenesis	human			CCTCAGCTCTCAGAAAGATCAGAAATTGAAATGG
GFP-IFT54-mutV125M-F	mutagenesis	human	V125M		AGTGACGATGCGATGCGGAGGGTTTTAG
GFP-IFT54-mutV125M-R	mutagenesis	human			TAAAACCCTCCGCATCGCATCGTCACTAG
GFP-IFT54-mutR155*-F	mutagenesis	human	R155*		AGAATGTGTGAGAAGAAGAGTCCAGAG
GFP-IFT54-mutR155*-R	mutagenesis	human			ACTCTGGACTCTTCTTCTCACACATTC
IFT54 h qPCR F	qPCR	human	116	1/2	TCACGGAGGTGATTAGAATGACT
IFT54 h qPCR R	qPCR	human	242	3	ACAACCACGTCTATGGCCTTT
MAP4 h qPCR F	qPCR	human	1665	7	AGCACCCCTGGCTAAGGAT
MAP4 h qPCR R	qPCR	human	1896	8	CCCCGTTCCTGTGATGGTTT
MAP4 m qPCR F	qPCR	mouse	2774	12/13	GCCGGGCCAAAGTAGAGAAAA
MAP4 m qPCR R	qPCR	mouse	2843	13	GTGACTGCATTAGGTTCAGGC
Traf3ip1 shRNA # 461	shRNA	mouse			CCGGATGAGCTGCTTCAATTGATTGCTCGAGCAATCAATTGAAGCAGCTCATTTTTTG
Traf3ip1 shRNA # 462	shRNA	mouse			CCGGCATCTAGGTCCTCGACGTTAACTCGAGTTAACGTCGAGGACCTAGATGTTTTTG
Traf3ip1 shRNA # 463	shRNA	mouse			CCGGGAATACACAAAGAGGATAAACCTCGAGGTTTATCCTCTTTGTGTATTCTTTTTG

Table S1: List of forward and reverse primers used to perform PCR investigations and sequencing, as well as mutagenesis, quantitative Real-Time PCR and shRNA.

3) Discussion

3.1) The route of ciliary tubulin

Getting tubulin to its destined position at the ciliary tip is a long route. Examining mRNA by *in situ* hybridization revealed a localization of tubulin mRNA amongst others at the base of the cilium (Han et al., 1997). The specific localization of mRNAs is a cell-established mechanism to ensure the spatially restricted translation of proteins, leading to their destined position within different cell compartments (reviewed in (St Johnston, 2005)). Newly translated tubulin subunits have to acquire conformations that enables them to form αβ-heterodimers capable to form MTs. The cytosolic chaperonin containing TCP-1 (CCT) complex has been shown to ensure the proper folding of tubulin subunits (Yaffe et al., 1992). Tubulin undergoes a second quality control before its incorporation into the cilium. Another chaperone, the tubulin cofactor C (TBCC) domain-containing protein, localized at the transition fibers of the basal body, directly interacts with tubulin and helps in checking the GTPase activity of tubulin (Stephan et al., 2007; Tian et al., 1999). Further bioinformatics studies revealed a relationship of TBCC to human RP2, a protein involved in the eye disease retinis pigmentosa (RP). Therefore, it is supposed that loss or impairment of this quality control step could lead to various ciliopathies (Stephan et al., 2007). The IFT complex as well as the motors required for IFT also dock at the transition fibers (Deane et al., 2001; Dentler, 2005), bind ciliary tubulin via the tubulin-binding module in IFT81/74 (Bhogaraju et al., 2013a) and transport tubulin to the ciliary tip where it gets incorporated into the MT axoneme (Craft et al., 2015; Hao et al., 2011; Johnson and Rosenbaum, 1992; Lechtreck et al., 2013; Marshall and Rosenbaum, 2001; Rasala et al., 2013). In this study we identified the tubulin-binding ability of the CH domain in IFT54 (chapter II manuscript Fig. 3 and 6). If IFT54 indeed functions as a second tubulin-binding site within IFT *in vivo* still has to be verified.

In *Chlamydomonas reinhardtii*, the MTs in the ciliary axoneme are constantly turned over at the ciliary tip ('+ end') (Marshall and Rosenbaum, 2001). This process is likely similar to the dynamic turnover of cytoplasmic MTs, a process known as 'dynamic instability' (Mitchison and Kirschner, 1984). Furthermore, turned over tubulin subunits will be recycled and thus have to be transported back to the base of the cilium (Coyne and Rosenbaum, 1970; Marshall and Rosenbaum, 2001). The exact mechanism by which this tubulin turnover at the ciliary tip is achieved as well as the retrograde IFT and recycling of tubulin remains elusive.

In *Tetrahymena*, subunits of the cytosolic chaperonin CCT complex colocalize with tubulin at the ciliary tip (Seixas et al., 2003). Furthermore, mutational analysis revealed that CCT subunits are essential for assembly and maintenance of the axoneme structure of *Tetrahymena* cilia (Seixas et al., 2010). The CCT complex is a hetero-oligomeric complex containing both the Hsp60-related TCP-1 and Hsp70 chaperones (Lewis et al., 1992) and is known to mediate mainly the folding of actin and tubulin (reviewed in (Kubota et al., 1995)). Members of the Hsp70 family have been also detected in cilia of *Tetrahymena* and sea urchin embryos (Stephens, 1997; Williams and Nelsen, 1997) as well as at the tips of *Chlamydomonas reinhardtii* cilia (Bloch and Johnson, 1995). Furthermore, Hsp70 and Hsc70 are constitutively expressed in rat photoreceptor cells and localize to both the inner and outer segments (Bhowmick et al., 2009; Dean et al., 1999). Taken together, the CCT complex and Hsp70 proteins could be the main players in turnover of tubulin at the ciliary tip. However, further examinations are necessary to clarify this issue.

3.2) Do posttranslational modifications (PTMs) of tubulin serve as regulatory elements within cilia?

Cells are able to generate distinct MT subtypes due to the expression of different tubulin isoforms and through posttranslational modifications (PTMs). Phosphorylation, ubiquitylation, sumoylation and palmitoylation occur frequently on other proteins, but are not well studied in MTs (Westermann and Weber, 2003; Wloga and Gaertig, 2010). In contrast, (poly)glutamylation, (poly)glycylation, detyronisation and further cleavage to Δ2-tubulin are performed at the C-terminal acidic E-hooks of α- and/or β-tubulin. Acetylation takes place at certain lysines in the globular domain of α- and β-tubulin (figure 11) (reviewed in (Janke and Chloë Bulinski, 2011)).

All five tubulin PTMs are highly enriched in ciliary tubulin. Acetylation was the first PTM discovered in *Chlamydomonas reinhardtii* cilia (L'Hernault and Rosenbaum, 1983; 1985). Tubulin enters the cilium and gets modified within the cilium either prior to or at its addition to the growing MTs. Later studies revealed acetylation as a common PTM in cilia of various organisms (Piperno and Fuller, 1985). Tyrosinated tubulin can be found in the A- and B-tubules and the central MT pair of the ciliary axoneme. However, detyrosinated tubulin seems to be restricted to the B-tubule (Johnson, 1998). Assembly of cilia relies on tyrosinated tubulin, detyrosination of tubulin in the B-tubule occurs later and seem to enhance the interactions of dynein and the B-tubules that powers ciliary beating (Johnson, 1998).

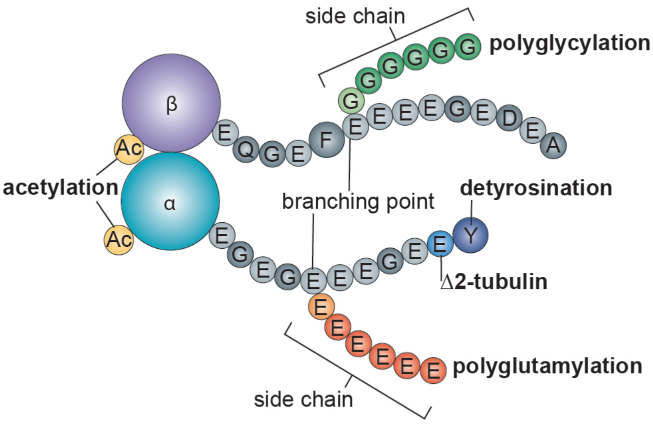

Figure 11: Schematic representation of different posttranslational modifications (PTMs) of a tubulin-heterodimer. The C-terminal tails of tubulin (E-hooks) are presented as amino acid sequences from murine α1A-tubulin (residues 441 to the end) and β2B -tubulin (residues 432 to the end). Removal of the last tyrosine of the α-tubulin tail results in detyrosinated tubulin, whereat further elimination of the glutamic acid generates Δ2-tubulin. Polyglycylation and polyglutamylation take place at the E-hooks of α- and β-tubulin on different glutamic acid residues. The globular part of α- and β-tubulin can be acetylated at Lys40 (α-tubulin) or Lys252 (β-tubulin) (adapted from (Janke and Chloë Bulinski, 2011)).

Δ2-tubulin is confined to very stable structures like the centrosome and primary cilia. Furthermore, Δ2-tubulin appears in sea urchin embryonic cilia during development and in the sperm flagella. Therefore, Δ2-tubulin was assumed to be a marker for the final stage of α-tubulin maturation (Paturle-Lafanechère et al., 1994). Polyglycylation was first discovered in axonemal tubulin of *Paramecium*, a unicellular ciliated protozoa (Redeker et al., 1994) and has been shown to be the predominant PTM in mammalian sperm cell flagella (Plessmann and Weber, 1997; Rüdiger et al., 1995).

Functional assays in human epithelial cells revealed a total loss of ciliary beating when an anti-glutamylation antibody was used, in contrast to only mild effects of an anti-glycylation antibody. These findings suggest only structural functions for polyglycylated tubulin in the ciliary axoneme, whereas polyglutamylation functions in cilia assembly and motility (Ikegami et al., 2010; Million et al., 1999). The same phenotype has been observed in sea urchin sperm flagella, supporting a role for polyglutamylated tubulin in dynein-based motility of cilia (Gagnon et al., 1996). Two independent studies link tubulin glutamylation, mediated by two conserved enzymes of the tubulin tyrosine ligase-like (TTLL) family (amongst others localized within cilia) on either α- or β-tubulin, to the regulation of IDA activity within cilia (Kubo et al., 2010; Suryavanshi et al., 2010). Furthermore, depletion of TTLLs lead to massive changes in glycylation or glutamylation of tubulin resulting in severe phenotypes in cilia structure or even loss of cilia (Pathak et al., 2011; Rogowski et al., 2009; Wloga et al., 2009).

Taken together, PTMs of tubulin are necessary for axonemal stabilization and motility regulations within cilia. But the question arises if tubulin PTMs serve as marker for ciliary tubulin as well. If yes, are tubulin PTMs necessary for the two tubulin-binding modules IFT81/74 (Bhogaraju et al., 2013a) and IFT54 (identified in this study (chapter II manuscript Fig. 3 and 6) in the IFT complex to recognize their tubulin cargo? Furthermore, the PTMs could also influence the binding affinity of the CH domains in the IFT proteins towards tubulin. Further examinations on this topic are crucial to understand the molecular role of tubulin PTMs in cilia assembly and maintenance in more detail.

3.3) Divergent evolution of the CH domains within the IFT complex

The CH domain is a small module composed of five to six α-helices and was identified in both signaling and cytoskeletal (actin/MT-binding) proteins (Castresana and Saraste, 1995; de Arruda et al., 1990). Nowadays, a couple of more CH-domain-containing proteins were discovered and it has been shown that they differ in their binding mode to actin and MTs (Gimona et al., 2002). In MT-binding proteins, like EB1 and Ndc80, normally only one CH domain (CH3) is present and the proteins form a complex with another CH-domain-containing-protein to fulfill their function (Ciferri et al., 2008; Hayashi and Ikura, 2003). In contrast, actinin4, an actin-binding protein, in which a tandem CH domain structure within the protein itself forms the actin-binding module (Galkin et al., 2010; Lee et al., 2008b). These two CH domains differ markedly in their sequence as well as in their binding affinity to actin. Whereas the amino-terminal CH domain (CH1) has intrinsic actin-binding ability, the carboxy-terminal CH domain (CH2) binds actin either with very low affinity or not at all (Gimona and Mital, 1998; Way et al., 1992; Winder et al., 1995).

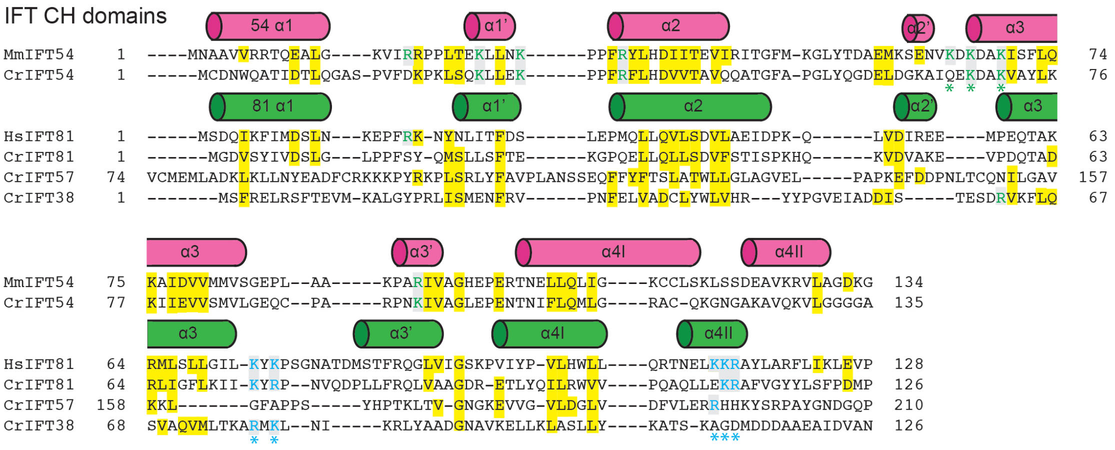

Figure 12: Structure based alignment (CrIFT81 and CrIFT54) and sequence alignment of the four CH domains of the IFT-B complex. The secondary structures of IFT54 and IFT81 are displayed above the sequence. Conserved residues are highlighted in yellow. Residues that abolish tubulin binding are marked with asterisks either in cyan for human IFT81 (Bhogaraju et al., 2013a) or in green for murine IFT54 (chapter II manuscript Fig. 6). Note that the tubulin-binding areas as well as the entire amino acid sequences of the four CH domains are not well conserved. Mus musculus (Mm), Homo sapiens (Hs), Chlamydomonas reinhardtii (Cr).

Within the IFT-B complex, four predicted α-helical domains in IFT81, IFT57, IFT54 and IFT38 have been classified as CH domains (Schou et al., 2014; Taschner et al., 2012). A recently published bioinformatics study (Schou et al., 2014) further grouped the CH domains in IFT81, IFT57 and IFT38 to the family of NN-CH domains (N-terminal CH like domain followed by a coiled coil region) based on their sequence and predicted structural similarity to the MT-binding founding members Ndc80 and Nuf2. Apart from IFT81/74 that has been already proven to serve as a tubulin-binding module via the CH domain in IFT81 and the positively charged N-terminal stretch of IFT74 (Bhogaraju et al., 2013a) less is known about the function of the other three predicted CH domains in the IFT machinery. The close structural relationship of the CH domains in IFT57 and IFT38 to the well known MT-binding proteins such as Ndc80 and Nuf2 strengthen the hypothesis that the thus far uncharacterized CH domains may serve as additional tubulin-binding modules in the process of IFT (Bhogaraju et al., 2014). Although IFT54 was not addressed in this bioinformatics study, previous publications already indicated the tubulin-binding ability for mammalian IFT54 (Ling and Goeddel, 2000). By solving the crystal structure of the N-terminal part of IFT54 we could show that IFT54 indeed adopts a CH domain fold and binds tubulin (chapter II manuscript Fig. 3 and 5). In contrast, the two putative NN-CH domains in IFT57 and IFT38 lost their tubulin-binding ability and mediate the binding to IFT172 and IFT80 (chapter II manuscript Fig. 3 and 7). Alignment studies revealed that the four CH domains in the IFT complex (in IFT81, IFT57, IFT54 and IFT38) are not well conserved (figure 12). Whereas the amino acids likely responsible for tubulin binding are conserved throughout IFT81 and IFT54, they are not present in IFT57 and IFT38. So it seems that IFT57 and IFT38 evolved divergently and execute different functions within the IFT process. If these functions are restricted to the interaction with IFT172 and IFT80 have to be addressed further.

3.4) Novel interactions between IFT-B proteins

As already mentioned in the introduction, the IFT-B complex consists of 16 different proteins. Within the IFT-B complex, the interactions between the nine ‘IFT-B core’ proteins are mapped (Lucker et al., 2010; Taschner et al., 2011; 2014) but less is known about interactions of the other seven IFT-B proteins with each other. An interaction between IFT20 and IFT54 was already reported (Follit et al., 2009; Omori et al., 2008) and could be proven in this study (chapter II manuscript Fig. 1B). The controversial IFT20/57 interaction (Baker et al., 2003; Krock and Perkins, 2008; Lucker et al., 2010) was also examined in this study, and could not be verified (chapter II manuscript Fig. 1E). But a novel interaction between IFT38 and IFT57 has been discovered in this study, undoubtedly linking IFT38 to the IFT-B complex (chapter II manuscript Fig 2). Furthermore, preliminary pull down experiments with recombinantly expressed proteins indicate an interaction of IFT20/54 and IFT38/57 as well as a mixture of both dimers with IFT80. The N-terminal β-propellers of IFT80 are sufficient to interact with IFT38/57 (figure 13A). Furthermore, the pentameric complex IFT20/38/54/57/80 seem to interact with IFT172, forming a hexameric complex (figure 13B).

(A) pull down experiments

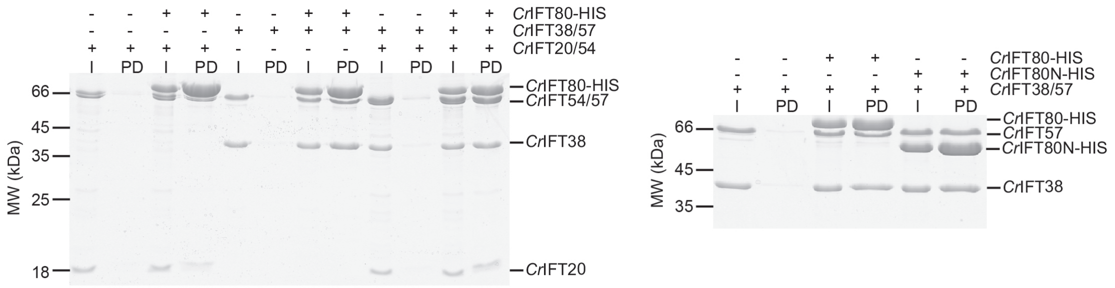

(B) size exclusion experiments

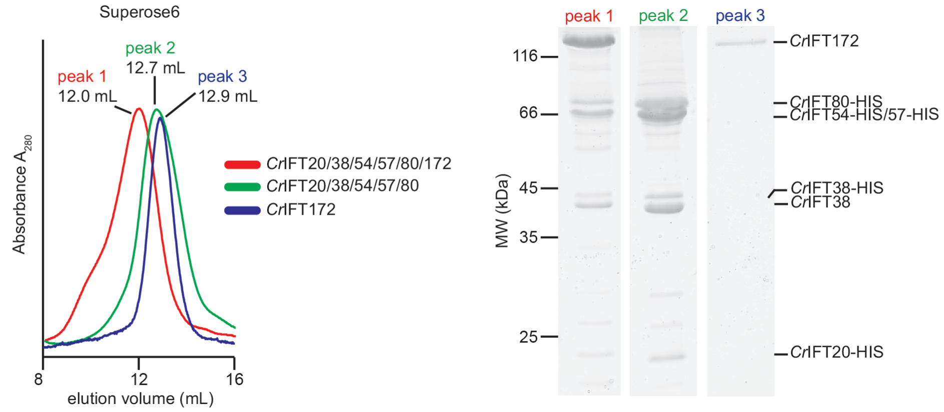

Figure 13: (A) Pull down experiments with recombinant purified IFT80 and IFT20/54, IFT38/57 and a mixture of both dimers indicate the formation of a pentameric complex (left). The binding of IFT38/57 to IFT80 is mediated via the β-propellers at the N-terminus of IFT80 (right). (B) Comparison of the size exclusion chromatography (SEC) profiles of IFT172 alone, the pentameric complex (identified in the pull down study above) and a hexameric complex revealed a shift in the elution profile to higher MW, indicating a stable complex between these six IFT-B proteins.

All the findings mentioned in chapter II as well as the preliminary results presented here (figure 13) are the first description of a stable subcomplex formed by the six IFT-B proteins IFT172, IFT80, IFT57, IFT54, IFT38 and IFT20. Therefore, we suggest to name the complex IFT-B2 and to rename the ‘IFT-B core’ IFT-B1 complex. Nevertheless, further interaction studies are necessary to map the exact binding regions between the IFT-B2 members. Another question is how the interaction between IFT-B1 and IFT-B2 is mediated. Do they directly interact with each other or is a yet unidentified adaptor protein necessary. In line with this, additional studies concerning the overall architecture of the IFT-B complex are crucial to understand the complex process of IFT.

4) Abbreviations

3D	Three-dimensional
β-cat	β-catenin
ADP	Adenosine diphosphate
AKT	Protein kinase B
APC/C	Anaphase-promoting complex/cyclosome
Arf	ADP-ribosylation factor
ASAP1	ArfGAP with SH3 Domain, Ankyrin Repeat and PH Domain 1
ATP	Adenosine triphosphate
BAR	Bin/amphiphysin/Rvs
BBS	Bardet-Biedl syndrome
Ca^{2+}	Calcium
CCT	Chaperonin containing TCP-1
CD	Circular dichroism spectroscopy
CH	Calponin Homology
COPI	Coat protein I
Cr	*Chlamydomonas reinhardtii*
CTM	Ciliary targeting motif
DIC	Differential interference contrast
DRC	Dynein regulatory complex
Dsh	Dishevelled
ERK	Extracellular signal-regulated kinases
FIP3	Family-interacting protein 3
GAP	GTPase activating protein
GC1	Guanylyl cyclase 1
GEF	GTPase exchange factor
GIFT	GldG, intraflagellar transport
Gli2/3	Glioma2/3
Gli3R	Glioma3 repressor
GPCR	G-protein-coupled receptor
GSH	Glutathione
GSK	Glycogen synthase kinase-3β

GTP	Guanosine triphosphate
HEK	Human embryonic kidney
Hh	Hedgehog
HIP-1	Huntington-interacting protein 1
Hsc	Heat shock cognate protein
Hsp	Heat shock protein
Htr6	Serotonin receptor 6
IDA	Inner dynein arm
IFT	Intraflagellar transport
JATD	Jeune asphyxiating thoracic dystrophy
LC-MS	Liquid chromatography-mass spectrometry
MEF	Mouse embryonic fibroblast
MEK	Mitogen activated protein kinase (MAPK)
MT	Microtubule
MW	Molecular weight
Ni^{2+}	Nickel
NRK	Normal rat kidney
NVP	Nodal vesicular parcel
ODA	Outer dynein arm
Orpk	Oak Ridge Polycystic Kidney
PC1/Pkd-1	Polycystin-1
PC2/Pkd-2/PKD-2	Polycystin-2
PCD	Primary cilia dyskinesia
PCP	Planar cell polarity
PDGF	Platelet-derived-growth factor
PDGFR	Platelet-derived-growth factor receptor
PKD	Polcystic kidney disease
Ptch-1	Patched-1
PTM	Post-translational modification
RP	Retinis pigmentosa
RPE	Retinal pigment epithelium
Shh	Sonic hedgehog
Smo	Smoothened
Sstr3	Somatostatin receptor 3

Sufu	Suppressor of fused
TBCC	Tubulin cofactor C
TCP-1	T-complex polypeptide-1
TGN	Trans Golgi network
TPR	Tetratricopeptide repeat
Tt	*Tetrahymena thermophile*
TTLL	Tubulin tyrosine ligase-like
TULP3	Tubby-like protein 3
WD	Tryptophan-aspartic
WT	wild type

5) References

Absalon, S., Blisnick, T., Kohl, L., Toutirais, G., Dore, G., Julkowska, D., Tavenet, A., and Bastin, P. (2008). Intraflagellar transport and functional analysis of genes required for flagellum formation in trypanosomes. Mol Biol Cell *19*, 929–944.

Adhiambo, C., Blisnick, T., Toutirais, G., Delannoy, E., and Bastin, P. (2009). A novel function for the atypical small G protein Rab-like 5 in the assembly of the trypanosome flagellum. J Cell Sci *122*, 834–841.

Ahmed, N.T., Gao, C., Lucker, B.F., Cole, D.G., and Mitchell, D.R. (2008). ODA16 aids axonemal outer row dynein assembly through an interaction with the intraflagellar transport machinery. J Cell Biol *183*, 313–322.

Anderson, R.G. (1972). The three-dimensional structure of the basal body from the rhesus monkey oviduct. J Cell Biol *54*, 246–265.

Arts, H.H., Bongers, E.M.H.F., Mans, D.A., van Beersum, S.E.C., Oud, M.M., Bolat, E., Spruijt, L., Cornelissen, E.A.M., Schuurs-Hoeijmakers, J.H.M., de Leeuw, N., et al. (2011). C14ORF179 encoding IFT43 is mutated in Sensenbrenner syndrome. J. Med. Genet. *48*, 390–395.

Badano, J.L., Mitsuma, N., Beales, P.L., and Katsanis, N. (2006). The ciliopathies: an emerging class of human genetic disorders. Annu Rev Genomics Hum Genet *7*, 125–148.

Baker, S., Freeman, K., Luby-Phelps, K., Pazour, G., and Besharse, J. (2003). IFT20 links kinesin II with a mammalian intraflagellar transport complex that is conserved in motile flagella and sensory cilia. J Biol Chem *278*, 34211–34218.

Banizs, B., Pike, M.M., Millican, C.L., Ferguson, W.B., Komlosi, P., Sheetz, J., Bell, P.D., Schwiebert, E.M., and Yoder, B.K. (2005). Dysfunctional cilia lead to altered ependyma and choroid plexus function, and result in the formation of hydrocephalus. Development *132*, 5329–5339.

Beales, P.L., Bland, E., Tobin, J.L., Bacchelli, C., Tuysuz, B., Hill, J., Rix, S., Pearson, C.G., Kai, M., Hartley, J., et al. (2007). IFT80, which encodes a conserved intraflagellar transport protein, is mutated in Jeune asphyxiating thoracic dystrophy. Nat. Genet. *39*, 727–729.

Beatson, S., and Ponting, C.P. (2004). GIFT domains: linking eukaryotic intraflagellar transport and glycosylation to bacterial gliding. Trends Biochem. Sci. *29*, 396–399.

Behal, R.H., Miller, M.S., Qin, H., Lucker, B.F., Jones, A., and Cole, D.G. (2012). Subunit interactions and organization of the Chlamydomonas reinhardtii intraflagellar transport complex A proteins. J Biol Chem *287*, 11689–11703.

Berbari, N., Kin, N., Sharma, N., Michaud, E., Kesterson, R., and Yoder, B. (2011). Mutations in Traf3ip1 reveal defects in ciliogenesis, embryonic development, and altered cell size regulation. Dev Biol.

Berbari, N.F., Johnson, A.D., Lewis, J.S., Askwith, C.C., and Mykytyn, K. (2008a). Identification of ciliary localization sequences within the third intracellular loop of G protein-coupled receptors. Mol Biol Cell *19*, 1540–1547.

Berbari, N.F., Lewis, J.S., Bishop, G.A., Askwith, C.C., and Mykytyn, K. (2008b). Bardet-Biedl syndrome proteins are required for the localization of G protein-coupled receptors to primary cilia. Proceedings of the National Academy of Sciences *105*, 4242–4246.

Berbari, N.F., O'Connor, A.K., Haycraft, C.J., and Yoder, B.K. (2009). The primary cilium as a complex signaling center. Curr Biol *19*, R526–R535.

Besharse, J.C., and Horst, C.J. (1990). The photoreceptor connecting cilium: a model for the transition zone. In Ciliary and Flagella Membranes, R.A. Bloodgood, ed. (Plenum Press), pp. 389–417.

Bhogaraju, S., Cajanek, L., Fort, C., Blisnick, T., Weber, K., Taschner, M., Mizuno, N., Lamla, S., Bastin, P., Nigg, E.A., et al. (2013a). Molecular Basis of Tubulin Transport Within the Cilium by IFT74 and IFT81. Science *341*, 1009–1012.

Bhogaraju, S., Taschner, M., Morawetz, M., Basquin, C., and Lorentzen, E. (2011). Crystal structure of the intraflagellar transport complex 25/27. Embo J.

Bhogaraju, S., Engel, B.D., and Lorentzen, E. (2013b). Intraflagellar transport complex structure and cargo interactions. Cilia 1–1.

Bhogaraju, S., Weber, K., Engel, B.D., Lechtreck, K.-F., and Lorentzen, E. (2014). Getting tubulin to the tip of the cilium: One IFT train, many different tubulin cargo-binding sites? Bioessays *36*, 463–467.

Bhowmick, R., Li, M., Sun, J., Baker, S.A., Insinna, C., and Besharse, J.C. (2009). Photoreceptor IFT complexes containing chaperones, guanylyl cyclase 1 and rhodopsin. Traffic *10*, 648–663.

Blacque, O., Li, C., Inglis, P., Esmail, M., Ou, G., Mah, A., Baillie, D., Scholey, J., and Leroux, M. (2006). The WD repeat-containing protein IFTA-1 is required for retrograde intraflagellar transport. Mol Biol Cell *17*, 5053–5062.

Blacque, O.E., Perens, E.A., Boroevich, K.A., Inglis, P.N., Li, C., Warner, A., Khattra, J., Holt, R.A., Ou, G., Mah, A.K., et al. (2005). Functional genomics of the cilium, a sensory organelle. Current Biology *15*, 935–941.

Blacque, O.E., Reardon, M.J., Li, C., McCarthy, J., Mahjoub, M.R., Ansley, S.J., Badano, J.L., Mah, A.K., Beales, P.L., Davidson, W.S., et al. (2004). Loss of C. elegans BBS-7 and BBS-8 protein function results in cilia defects and compromised intraflagellar transport. Genes Dev. *18*, 1630–1642.

Bloch, M.A., and Johnson, K.A. (1995). Identification of a molecular chaperone in the eukaryotic flagellum and its localization to the site of microtubule assembly. J Cell Sci *108 (Pt 11)*, 3541–3545.

Bornens, M. (2012). The centrosome in cells and organisms. Science *335*, 422–426.

Bos, J.L., Rehmann, H., and Wittinghofer, A. (2007). GEFs and GAPs: critical elements in the control of small G proteins. Cell *129*, 865–877.

Botilde, Y., Yoshiba, S., Shinohara, K., Hasegawa, T., Nishimura, H., Shiratori, H., and Hamada, H. (2013). Cluap1 localizes preferentially to the base and tip of cilia and is required for ciliogenesis in the mouse embryo. Dev Biol *381*, 203–212.

Brailov, I., Bancila, M., Brisorgueil, M.J., Miquel, M.C., Hamon, M., and Vergé, D. (2000). Localization of 5-HT(6) receptors at the plasma membrane of neuronal cilia in the rat brain. Brain Res. *872*, 271–275.

Brazelton, W.J., Amundsen, C.D., Silflow, C.D., and Lefebvre, P.A. (2001). The bld1 mutation identifies the Chlamydomonas osm-6 homolog as a gene required for flagellar assembly. Current Biology *11*, 1591–1594.

Bredrup, C., Saunier, S., Oud, M.M., Fiskerstrand, T., Hoischen, A., Brackman, D., Leh, S.M., Midtbø, M., Filhol, E., Bole-Feysot, C., et al. (2011). Ciliopathies with skeletal anomalies and renal insufficiency due to mutations in the IFT-A gene WDR19. Am. J. Hum. Genet. *89*, 634–643.

Breslow, D.K., Koslover, E.F., Seydel, F., Spakowitz, A.J., and Nachury, M.V. (2013). An in vitro assay for entry into cilia reveals unique properties of the soluble diffusion barrier. The Journal of Cell Biology *203*, 129–147.

Brokaw, C.J., and Kamiya, R. (1987). Bending patterns of Chlamydomonas flagella: IV. Mutants with defects in inner and outer dynein arms indicate differences in dynein arm function. Cell Motil Cytoskeleton *8*, 68–75.

Brown, J.M., Marsala, C., Kosoy, R., and Gaertig, J. (1999). Kinesin-II is preferentially targeted to assembling cilia and is required for ciliogenesis and normal cytokinesis in Tetrahymena. Mol Biol Cell *10*, 3081–3096.

Castresana, J., and Saraste, M. (1995). Does Vav bind to F-actin through a CH domain? FEBS Lett *374*, 149–151.

Cherfils, J., and Zeghouf, M. (2013). Regulation of small GTPases by GEFs, GAPs, and GDIs. Physiol. Rev. *93*, 269–309.

Christensen, S.T., Pedersen, S.F., Satir, P., Veland, I.R., and Schneider, L. (2008). The primary cilium coordinates signaling pathways in cell cycle control and migration during development and tissue repair. Ciliary Function in Mammalian Development *85*, 261–301.

Chuang, J.-Z., Zhou, H., Zhu, M., Li, S.-H., Li, X.-J., and Sung, C.-H. (2002). Characterization of a brain-enriched chaperone, MRJ, that inhibits Huntingtin aggregation and toxicity independently. J Biol Chem *277*, 19831–19838.

Ciferri, C., Pasqualato, S., Screpanti, E., Varetti, G., Santaguida, S., Reis, Dos, G., Maiolica, A., Polka, J., De Luca, J., De Wulf, P., et al. (2008). Implications for kinetochore-microtubule attachment from the structure of an engineered Ndc80 complex. Cell *133*, 427–439.

Cole, D., Diener, D., Himelblau, A., Beech, P., Fuster, J., and Rosenbaum, J. (1998). Chlamydomonas kinesin-II-dependent intraflagellar transport (IFT): IFT particles contain proteins required for ciliary assembly in Caenorhabditis elegans sensory neurons. J Cell Biol *141*, 993–1008.

Corbit, K.C., Aanstad, P., Singla, V., Norman, A.R., Stainier, D.Y.R., and Reiter, J.F. (2005). Vertebrate Smoothened functions at the primary cilium. Nature *437*, 1018–1021.

Corbit, K.C., Shyer, A.E., Dowdle, W.E., Gaulden, J., Singla, V., Chen, M.-H., Chuang, P.-T., and Reiter, J.F. (2008). Kif3a constrains beta-catenin-dependent Wnt signalling through dual ciliary and non-ciliary mechanisms. Nat Cell Biol *10*, 70–76.

Cortellino, S., Wang, C., Wang, B., Bassi, M.R., Caretti, E., Champeval, D., Calmont, A., Jarnik, M., Burch, J., Zaret, K.S., et al. (2009). Defective ciliogenesis, embryonic lethality and severe impairment of the Sonic Hedgehog pathway caused by inactivation of the mouse complex A intraflagellar transport gene Ift122/Wdr10, partially overlapping with the DNA repair gene Med1/Mbd4. Dev Biol *325*, 225–237.

Coyne, B., and Rosenbaum, J.L. (1970). Flagellar elongation and shortening in chlamydomonas. II. Re-utilization of flagellar proteins. J Cell Biol *47*, 777–781.

Craft, J.M., Harris, J.A., Hyman, S., Kner, P., and Lechtreck, K.F. (2015). Tubulin transport by IFT is upregulated during ciliary growth by a cilium-autonomous mechanism. The Journal of Cell Biology *208*, 223–237.

Czarnecki, P.G., and Shah, J.V. (2012). The ciliary transition zone: from morphology and molecules to medicine. Trends Cell Biol *22*, 201–210.

Dabdoub, A., and Kelley, M.W. (2005). Planar cell polarity and a potential role for a Wnt morphogen gradient in stereociliary bundle orientation in the mammalian inner ear. J. Neurobiol. *64*, 446–457.

Dacks, J.B., and Field, M.C. (2007). Evolution of the eukaryotic membrane-trafficking system: origin, tempo and mode. J Cell Sci *120*, 2977–2985.

de Arruda, M.V., Watson, S., Lin, C.S., Leavitt, J., and Matsudaira, P. (1990). Fimbrin is a homologue of the cytoplasmic phosphoprotein plastin and has domains homologous with calmodulin and actin gelation proteins. J Cell Biol *111*, 1069–1079.

Dean, D.O., Kent, C.R., and Tytell, M. (1999). Constitutive and inducible heat shock protein 70 immunoreactivity in the normal rat eye. Invest. Ophthalmol. Vis. Sci. *40*, 2952–2962.

Deane, J.A., Cole, D.G., Seeley, E.S., Diener, D.R., and Rosenbaum, J.L. (2001). Localization of intraflagellar transport protein IFT52 identifies basal body transitional fibers as the docking site for IFT particles. Current Biology *11*, 1586–1590.

DeCaen, P.G., Delling, M., Vien, T.N., and Clapham, D.E. (2013). Direct recording and molecular identification of the calcium channel of primary cilia. Nature *504*, 315–

318.

Delling, M., DeCaen, P.G., Doerner, J.F., Febvay, S., and Clapham, D.E. (2013). Primary cilia are specialized calcium signalling organelles. Nature *504*, 311–314.

Delmas, P., Nomura, H., Li, X., Lakkis, M., Luo, Y., Segal, Y., Fernández-Fernández, J.M., Harris, P., Frischauf, A.-M., Brown, D.A., et al. (2002). Constitutive activation of G-proteins by polycystin-1 is antagonized by polycystin-2. J Biol Chem *277*, 11276–11283.

Dentler, W. (2005). Intraflagellar transport (IFT) during assembly and disassembly of Chlamydomonas flagella. J Cell Biol *170*, 649–659.

Deretic, D., Williams, A.H., Ransom, N., Morel, V., Hargrave, P.A., and Arendt, A. (2005). Rhodopsin C terminus, the site of mutations causing retinal disease, regulates trafficking by binding to ADP-ribosylation factor 4 (ARF4). Proc Natl Acad Sci USA *102*, 3301–3306.

Devos, D., Dokudovskaya, S., Alber, F., Williams, R., Chait, B.T., Sali, A., and Rout, M.P. (2004). Components of coated vesicles and nuclear pore complexes share a common molecular architecture. PLoS Biol *2*, e380.

Dishinger, J.F., Kee, H.L., Jenkins, P.M., Fan, S., Hurd, T.W., Hammond, J.W., Truong, Y.N.-T., Margolis, B., Martens, J.R., and Verhey, K.J. (2010). Ciliary entry of the kinesin-2 motor KIF17 is regulated by importin-beta2 and RanGTP. Nat Cell Biol *12*, 703–710.

Duchateau, G.S., Graamans, K., Zuidema, J., and Merkus, F.W. (1985). Correlation between nasal ciliary beat frequency and mucus transport rate in volunteers. Laryngoscope *95*, 854–859.

Dwyer, N.D., Adler, C.E., Crump, J.G., L'Etoile, N.D., and Bargmann, C.I. (2001). Polarized dendritic transport and the AP-1 mu1 clathrin adaptor UNC-101 localize odorant receptors to olfactory cilia. Neuron *31*, 277–287.

Efimenko, E., Blacque, O.E., Ou, G., Haycraft, C.J., Yoder, B.K., Scholey, J.M., Leroux, M.R., and Swoboda, P. (2006). Caenorhabditis elegans DYF-2, an orthologue of human WDR19, is a component of the intraflagellar transport machinery in sensory cilia. Mol Biol Cell *17*, 4801–4811.

Efimenko, E., Bubb, K., Mak, H.Y., Holzman, T., Leroux, M.R., Ruvkun, G., Thomas, J.H., and Swoboda, P. (2005). Analysis of xbx genes in C. elegans. Development *132*, 1923–1934.

Eguether, T., San Agustin, J.T., Keady, B.T., Jonassen, J.A., Liang, Y., Francis, R., Tobita, K., Johnson, C.A., Abdelhamed, Z.A., Lo, C.W., et al. (2014). IFT27 links the BBSome to IFT for maintenance of the ciliary signaling compartment. Dev Cell *31*, 279–290.

Engel, B.D., Ludington, W.B., and Marshall, W.F. (2009). Intraflagellar transport particle size scales inversely with flagellar length: revisiting the balance-point length control model. J Cell Biol *187*, 81–89.

Fan, S., Whiteman, E.L., Hurd, T.W., McIntyre, J.C., Dishinger, J.F., Liu, C.J., Martens, J.R., Verhey, K.J., Sajjan, U., and Margolis, B. (2011). Induction of Ran GTP drives ciliogenesis. Mol Biol Cell *22*, 4539–4548.

Fan, Z.-C., Behal, R.H., Geimer, S., Wang, Z., Williamson, S.M., Zhang, H., Cole, D.G., and Qin, H. (2010). Chlamydomonas IFT70/CrDYF-1 is a core component of IFT particle complex B and is required for flagellar assembly. Mol Biol Cell *21*, 2696–2706.

Fisch, C., and Dupuis-Williams, P. (2011). Ultrastructure of cilia and flagella - back to the future! Biol Cell *103*, 249–270.

Fliegauf, M., Benzing, T., and Omran, H. (2007). When cilia go bad: cilia defects and ciliopathies. Nat Rev Mol Cell Biol *8*, 880–893.

Follit, J., San Agustin, J., Xu, F., Jonassen, J., Samtani, R., Lo, C., and Pazour, G. (2008). The Golgin GMAP210/TRIP11 anchors IFT20 to the Golgi complex. PLoS Genet *4*, e1000315.

Follit, J., Tuft, R., Fogarty, K., and Pazour, G. (2006). The intraflagellar transport protein IFT20 is associated with the Golgi complex and is required for cilia assembly. Mol Biol Cell *17*, 3781–3792.

Follit, J., Xu, F., Keady, B., and Pazour, G. (2009). Characterization of mouse IFT complex B. Cell Motil Cytoskeleton *66*, 457–468.

Fredriksson, L., Li, H., and Eriksson, U. (2004). The PDGF family: four gene products form five dimeric isoforms. Cytokine Growth Factor Rev. *15*, 197–204.

Fujiwara, M., Ishihara, T., and Katsura, I. (1999). A novel WD40 protein, CHE-2, acts cell-autonomously in the formation of C. elegans sensory cilia. Development *126*, 4839–4848.

Gagnon, C., White, D., Cosson, J., Huitorel, P., Eddé, B., Desbruyères, E., Paturle-Lafanechère, L., Multigner, L., Job, D., and Cibert, C. (1996). The polyglutamylated lateral chain of alpha-tubulin plays a key role in flagellar motility. J Cell Sci *109 (Pt 6)*, 1545–1553.

Galkin, V., Orlova, A., Salmazo, A., Djinovic-Carugo, K., and Egelman, E. (2010). Opening of tandem calponin homology domains regulates their affinity for F-actin. Nat Struct Mol Biol *17*, 614–616.

Gerdes, J.M., and Katsanis, N. (2008). Ciliary function and Wnt signal modulation. Ciliary Function in Mammalian Development *85*, 175–195.

Gervais, F.G., Singaraja, R., Xanthoudakis, S., Gutekunst, C.-A., Leavitt, B.R., Metzler, M., Hackam, A.S., Tam, J., Vaillancourt, J.P., Houtzager, V., et al. (2002). Recruitment and activation of caspase-8 by the Huntingtin-interacting protein Hip-1 and a novel partner Hippi. Nat Cell Biol *4*, 95–105.

Gibbons, I.R. (1963). STUDIES ON THE PROTEIN COMPONENTS OF CILIA FROM TETRAHYMENA PYRIFORMIS. Proc Natl Acad Sci USA *50*, 1002–1010.

Gibbons, I.R., and GRIMSTONE, A.V. (1960). On flagellar structure in certain flagellates. J Biophys Biochem Cytol *7*, 697–716.

Gilissen, C., Arts, H.H., Hoischen, A., Spruijt, L., Mans, D.A., Arts, P., van Lier, B., Steehouwer, M., van Reeuwijk, J., Kant, S.G., et al. (2010). Exome sequencing identifies WDR35 variants involved in Sensenbrenner syndrome. Am. J. Hum. Genet. *87*, 418–423.

Gillingham, A.K., and Munro, S. (2007). The small G proteins of the Arf family and their regulators. Annu Rev Cell Dev Biol *23*, 579–611.

Gilula, N.B., and Satir, P. (1972). The ciliary necklace. A ciliary membrane specialization. J Cell Biol *53*, 494–509.

Gimona, M., and Mital, R. (1998). The single CH domain of calponin is neither sufficient nor necessary for F-actin binding. J Cell Sci *111 (Pt 13)*, 1813–1821.

Gimona, M., Djinovic-Carugo, K., Kranewitter, W., and Winder, S. (2002). Functional plasticity of CH domains. FEBS Lett *513*, 98–106.

Goetz, S.C., and Anderson, K.V. (2010). The primary cilium: a signalling centre during vertebrate development. Nat. Rev. Genet. *11*, 331–344.

Guo, C., Xiong, S., Liu, G., Wang, Y., He, Q., Zhang, X., Zhang, Z., Ge, F., and Kitazato, K. (2010). Proteomic analysis reveals novel binding partners of MIP-T3 in human cells. Proteomics *10*, 2337–2347.

Haar, ter, E., Harrison, S.C., and Kirchhausen, T. (2000). Peptide-in-groove interactions link target proteins to the beta-propeller of clathrin. Proc Natl Acad Sci USA *97*, 1096–1100.

Han, J.W., Park, J.H., Kim, M., and Lee, J. (1997). mRNAs for microtubule proteins are specifically colocalized during the sequential formation of basal body, flagella, and cytoskeletal microtubules in the differentiation of Naegleria gruberi. J Cell Biol *137*, 871–879.

Han, Y.-G., Kwok, B.H., and Kernan, M.J. (2003). Intraflagellar transport is required in Drosophila to differentiate sensory cilia but not sperm. Current Biology *13*, 1679–1686.

Hanaoka, K., Qian, F., Boletta, A., Bhunia, A.K., Piontek, K., Tsiokas, L., Sukhatme, V.P., Guggino, W.B., and Germino, G.G. (2000). Co-assembly of polycystin-1 and -2 produces unique cation-permeable currents. Nature *408*, 990–994.

Hao, L., Thein, M., Brust-Mascher, I., Civelekoglu-Scholey, G., Lu, Y., Acar, S., Prevo, B., Shaham, S., and Scholey, J. (2011). Intraflagellar transport delivers tubulin isotypes to sensory cilium middle and distal segments. Nat Cell Biol *13*, 790–798.

Hayashi, I., and Ikura, M. (2003). Crystal structure of the amino-terminal microtubule-binding domain of end-binding protein 1 (EB1). J Biol Chem *278*, 36430–36434.

Haycraft, C.J., Swoboda, P., Taulman, P.D., Thomas, J.H., and Yoder, B.K. (2001). The C. elegans homolog of the murine cystic kidney disease gene Tg737 functions in a ciliogenic pathway and is disrupted in osm-5 mutant worms. Development *128*, 1493–1505.

Haycraft, C.J., Banizs, B., Aydin-Son, Y., Zhang, Q., Michaud, E.J., and Yoder, B.K. (2005). Gli2 and Gli3 localize to cilia and require the intraflagellar transport protein polaris for processing and function. PLoS Genet *1*, e53.

Haycraft, C.J., Schafer, J.C., Zhang, Q., Taulman, P.D., and Yoder, B.K. (2003). Identification of CHE-13, a novel intraflagellar transport protein required for cilia formation. Exp Cell Res *284*, 251–263.

Händel, M., Schulz, S., Stanarius, A., Schreff, M., Erdtmann-Vourliotis, M., Schmidt, H., Wolf, G., and Höllt, V. (1999). Selective targeting of somatostatin receptor 3 to neuronal cilia. Neuroscience *89*, 909–926.

Heuser, T., Raytchev, M., Krell, J., Porter, M.E., and Nicastro, D. (2009). The dynein regulatory complex is the nexin link and a major regulatory node in cilia and flagella. The Journal of Cell Biology *187*, 921–933.

Hou, Y., Qin, H., Follit, J.A., Pazour, G.J., Rosenbaum, J.L., and Witman, G.B. (2007). Functional analysis of an individual IFT protein: IFT46 is required for transport of outer dynein arms into flagella. J Cell Biol *176*, 653–665.

Houde, C., Dickinson, R.J., Houtzager, V.M., Cullum, R., Montpetit, R., Metzler, M., Simpson, E.M., Roy, S., Hayden, M.R., Hoodless, P.A., et al. (2006). Hippi is essential for node cilia assembly and Sonic hedgehog signaling. Dev Biol *300*, 523–533.

Huangfu, D., Liu, A., Rakeman, A.S., Murcia, N.S., Niswander, L., and Anderson, K.V. (2003). Hedgehog signalling in the mouse requires intraflagellar transport proteins. Nature *426*, 83–87.

Hudak, L.M., Lunt, S., Chang, C.-H., Winkler, E., Flammer, H., Lindsey, M., and Perkins, B.D. (2010). The intraflagellar transport protein ift80 is essential for photoreceptor survival in a zebrafish model of jeune asphyxiating thoracic dystrophy. Invest. Ophthalmol. Vis. Sci. *51*, 3792–3799.

Ibañez-Tallon, I., Pagenstecher, A., Fliegauf, M., Olbrich, H., Kispert, A., Ketelsen, U.-P., North, A., Heintz, N., and Omran, H. (2004). Dysfunction of axonemal dynein heavy chain Mdnah5 inhibits ependymal flow and reveals a novel mechanism for hydrocephalus formation. Hum Mol Genet *13*, 2133–2141.

Ikegami, K., Sato, S., Nakamura, K., Ostrowski, L.E., and Setou, M. (2010). Tubulin polyglutamylation is essential for airway ciliary function through the regulation of beating asymmetry. Proceedings of the National Academy of Sciences *107*, 10490–10495.

Inoue, H., Ha, V.L., Prekeris, R., and Randazzo, P.A. (2008). Arf GTPase-activating protein ASAP1 interacts with Rab11 effector FIP3 and regulates pericentrosomal localization of transferrin receptor-positive recycling endosome. Mol Biol Cell *19*, 4224–4237.

Iomini, C., Babaev-Khaimov, V., Sassaroli, M., and Piperno, G. (2001). Protein particles in Chlamydomonas flagella undergo a transport cycle consisting of four phases. J Cell Biol *153*, 13–24.

Ishikawa, H., Ide, T., Yagi, T., Jiang, X., Hirono, M., Sasaki, H., Yanagisawa, H., Wemmer, K.A., Stainier, D.Y., Qin, H., et al. (2014). TTC26/DYF13 is an intraflagellar transport protein required for transport of motility-related proteins into flagella. Elife *3*, e01566.

Ishikawa, H., Thompson, J., Yates, J.R., and Marshall, W.F. (2012). Proteomic analysis of mammalian primary cilia. Curr Biol *22*, 414–419.

Janke, C., and Chloë Bulinski, J. (2011). Post-translational regulation of the microtubule cytoskeleton: mechanisms and functions. Nat Rev Mol Cell Biol *12*, 773–786.

Jékely, G., and Arendt, D. (2006). Evolution of intraflagellar transport from coated vesicles and autogenous origin of the eukaryotic cilium. Bioessays *28*, 191–198.

Jin, H., White, S., Shida, T., Schulz, S., Aguiar, M., Gygi, S., Bazan, J., and Nachury, M. (2010). The conserved Bardet-Biedl syndrome proteins assemble a coat that traffics membrane proteins to cilia. Cell *141*, 1208–1219.

Johnson, K. (1998). The axonemal microtubules of the Chlamydomonas flagellum differ in tubulin isoform content. J Cell Sci *111 (Pt 3)*, 313–320.

Johnson, K.A., and Rosenbaum, J.L. (1992). Polarity of flagellar assembly in Chlamydomonas. J Cell Biol *119*, 1605–1611.

Jones, D.T. (1999). Protein secondary structure prediction based on position-specific scoring matrices. J Mol Biol *292*, 195–202.

Keady, B., Le, Y., and Pazour, G. (2011). IFT20 Is Required for Opsin Trafficking and Photoreceptor Outer Segment Development. Mol Biol Cell.

Keady, B., Samtani, R., Tobita, K., Tsuchya, M., San Agustin, J., Follit, J., Jonassen, J., Subramanian, R., Lo, C., and Pazour, G. (2012). IFT25 links the signal-dependent movement of Hedgehog components to intraflagellar transport. Dev Cell *22*, 940–951.

Kikuchi, T., Takasaka, T., Tonosaki, A., and Watanabe, H. (1989). Fine structure of guinea pig vestibular kinocilium. Acta Otolaryngol. *108*, 26–30.

Knodler, A., Feng, S., Zhang, J., Zhang, X., Das, A., Peranen, J., and Guo, W. (2010). Coordination of Rab8 and Rab11 in primary ciliogenesis. Proc Natl Acad Sci U S A *107*, 6346–6351.

Koulen, P., Cai, Y., Geng, L., Maeda, Y., Nishimura, S., Witzgall, R., Ehrlich, B.E., and Somlo, S. (2002). Polycystin-2 is an intracellular calcium release channel. Nat Cell Biol *4*, 191–197.

Kozminski, K., Beech, P., and Rosenbaum, J. (1995). The Chlamydomonas kinesin-like protein FLA10 is involved in motility associated with the flagellar membrane. J Cell Biol *131*, 1517–1527.

Kozminski, K., Johnson, K., Forscher, P., and Rosenbaum, J. (1993). A motility in the eukaryotic flagellum unrelated to flagellar beating. Proc Natl Acad Sci U S A *90*, 5519–5523.

Krock, B., and Perkins, B. (2008). The intraflagellar transport protein IFT57 is required for cilia maintenance and regulates IFT-particle-kinesin-II dissociation in vertebrate photoreceptors. J Cell Sci *121*, 1907–1915.

Kubo, T., Yanagisawa, H.-A., Yagi, T., Hirono, M., and Kamiya, R. (2010). Tubulin polyglutamylation regulates axonemal motility by modulating activities of inner-arm dyneins. Curr Biol *20*, 441–445.

Kubota, H., Hynes, G., and Willison, K. (1995). The chaperonin containing t-complex polypeptide 1 (TCP-1). Multisubunit machinery assisting in protein folding and assembly in the eukaryotic cytosol. Eur J Biochem *230*, 3–16.

Kulaga, H.M., Leitch, C.C., Eichers, E.R., Badano, J.L., Lesemann, A., Hoskins, B.E., Lupski, J.R., Beales, P.L., Reed, R.R., and Katsanis, N. (2004). Loss of BBS proteins causes anosmia in humans and defects in olfactory cilia structure and function in the mouse. Nat. Genet. *36*, 994–998.

Kunitomo, H., and Iino, Y. (2008). Caenorhabditis elegans DYF-11, an orthologue of mammalian Traf3ip1/MIP-T3, is required for sensory cilia formation. Genes Cells *13*, 13–25.

L'Hernault, S.W., and Rosenbaum, J.L. (1983). Chlamydomonas alpha-tubulin is posttranslationally modified in the flagella during flagellar assembly. J Cell Biol *97*, 258–263.

L'Hernault, S.W., and Rosenbaum, J.L. (1985). Chlamydomonas alpha-tubulin is posttranslationally modified by acetylation on the epsilon-amino group of a lysine. Biochemistry *24*, 473–478.

Lechtreck, K., Johnson, E., Sakai, T., Cochran, D., Ballif, B., Rush, J., Pazour, G., Ikebe, M., and Witman, G. (2009a). The Chlamydomonas reinhardtii BBSome is an IFT cargo required for export of specific signaling proteins from flagella. J Cell Biol *187*, 1117–1132.

Lechtreck, K.-F., Gould, T.J., and Witman, G.B. (2013). Flagellar central pair assembly in Chlamydomonas reinhardtii. Cilia *2*, 15.

Lechtreck, K.-F., Luro, S., Awata, J., and Witman, G.B. (2009b). HA-tagging of putative flagellar proteins in Chlamydomonas reinhardtii identifies a novel protein of intraflagellar transport complex B. Cell Motil Cytoskeleton *66*, 469–482.

Lee, E., Sivan-Loukianova, E., Eberl, D.F., and Kernan, M.J. (2008a). An IFT-A protein is required to delimit functionally distinct zones in mechanosensory cilia. Curr Biol *18*, 1899–1906.

Lee, S., Weins, A., Hayes, D., Pollak, M., and Dominguez, R. (2008b). Crystal structure of the actin-binding domain of alpha-actinin-4 Lys255Glu mutant implicated in focal segmental glomerulosclerosis. J Mol Biol *376*, 317–324.

Leroux, M.R. (2007). Taking vesicular transport to the cilium. Cell *129*, 1041–1043.

Lewis, V.A., Hynes, G.M., Zheng, D., Saibil, H., and Willison, K. (1992). T-complex polypeptide-1 is a subunit of a heteromeric particle in the eukaryotic cytosol. Nature *358*, 249–252.

Liem, K., Ashe, A., He, M., Satir, P., Moran, J., Beier, D., Wicking, C., and Anderson, K. (2012). The IFT-A complex regulates Shh signaling through cilia structure and membrane protein trafficking. J Cell Biol *197*, 789–800.

Liew, G.M., Ye, F., Nager, A.R., Murphy, J.P., Lee, J.S., Aguiar, M., Breslow, D.K., Gygi, S.P., and Nachury, M.V. (2014). The intraflagellar transport protein IFT27 promotes BBSome exit from cilia through the GTPase ARL6/BBS3. Dev Cell *31*, 265–278.

Ling, L., and Goeddel, D. (2000). MIP-T3, a novel protein linking tumor necrosis factor receptor-associated factor 3 to the microtubule network. J Biol Chem *275*, 23852–23860.

Liu, W., Murcia, N.S., Duan, Y., Weinbaum, S., Yoder, B.K., Schwiebert, E., and Satlin, L.M. (2005). Mechanoregulation of intracellular Ca2+ concentration is attenuated in collecting duct of monocilium-impaired orpk mice. Am. J. Physiol. Renal Physiol. *289*, F978–F988.

Lu, W., Peissel, B., Babakhanlou, H., Pavlova, A., Geng, L., Fan, X., Larson, C., Brent, G., and Zhou, J. (1997). Perinatal lethality with kidney and pancreas defects in mice with a targetted Pkd1 mutation. Nat. Genet. *17*, 179–181.

Lucker, B., Behal, R., Qin, H., Siron, L., Taggart, W., Rosenbaum, J., and Cole, D. (2005). Characterization of the intraflagellar transport complex B core: direct interaction of the IFT81 and IFT74/72 subunits. J Biol Chem *280*, 27688–27696.

Lucker, B., Miller, M., Dziedzic, S., Blackmarr, P., and Cole, D. (2010). Direct interactions of intraflagellar transport complex B proteins IFT88, IFT52, and IFT46. J Biol Chem *285*, 21508–21518.

Lyons, R.A., Saridogan, E., and Djahanbakhch, O. (2006). The reproductive significance of human Fallopian tube cilia. Hum. Reprod. Update *12*, 363–372.

Macnab, R.M. (2003). How bacteria assemble flagella. Annu. Rev. Microbiol. *57*, 77–100.

Marshall, W.F., and Rosenbaum, J.L. (2001). Intraflagellar transport balances continuous turnover of outer doublet microtubules: implications for flagellar length control. J Cell Biol *155*, 405–414.

Marszalek, J.R., Liu, X., Roberts, E.A., Chui, D., Marth, J.D., Williams, D.S., and Goldstein, L.S. (2000). Genetic evidence for selective transport of opsin and arrestin by kinesin-II in mammalian photoreceptors. Cell *102*, 175–187.

Masyuk, A.I., Masyuk, T.V., Splinter, P.L., Huang, B.Q., Stroope, A.J., and Larusso, N.F. (2006). Cholangiocyte cilia detect changes in luminal fluid flow and transmit them into intracellular Ca2+ and cAMP signaling. Gastroenterology *131*, 911–920.

Mazelova, J., Astuto-Gribble, L., Inoue, H., Tam, B., Schonteich, E., Prekeris, R., Moritz, O., Randazzo, P., and Deretic, D. (2009). Ciliary targeting motif VxPx directs assembly of a trafficking module through Arf4. Embo J *28*, 183–192.

McEwen, D.P., Jenkins, P.M., and Martens, J.R. (2008). Olfactory cilia: our direct neuronal connection to the external world. Ciliary Function in Mammalian Development *85*, 333–370.

McGrath, J., Somlo, S., Makova, S., Tian, X., and Brueckner, M. (2003). Two populations of node monocilia initiate left-right asymmetry in the mouse. Cell *114*, 61–73.

Million, K., Larcher, J., Laoukili, J., Bourguignon, D., Marano, F., and Tournier, F. (1999). Polyglutamylation and polyglycylation of alpha- and beta-tubulins during in vitro ciliated cell differentiation of human respiratory epithelial cells. J Cell Sci *112 (Pt 23)*, 4357–4366.

Mitchell, D.R. (2000). Chlamydomonas flagella. J. Phycol. *36*, 261–273.

Mitchison, T., and Kirschner, M. (1984). Dynamic instability of microtubule growth. Nature *312*, 237–242.

Mizuno, N., Taschner, M., Engel, B., and Lorentzen, E. (2012). Structural Studies of Ciliary Components. J Mol Biol.

Mochizuki, T., Wu, G., Hayashi, T., Xenophontos, S.L., Veldhuisen, B., Saris, J.J., Reynolds, D.M., Cai, Y., Gabow, P.A., Pierides, A., et al. (1996). PKD2, a gene for polycystic kidney disease that encodes an integral membrane protein. Science *272*, 1339–1342.

Morga, B., and Bastin, P. (2013). Getting to the heart of intraflagellar transport using Trypanosoma and Chlamydomonas models: the strength is in their differences. Cilia *2*, 16.

Morgan, D., Eley, L., Sayer, J., Strachan, T., Yates, L.M., Craighead, A.S., and Goodship, J.A. (2002). Expression analyses and interaction with the anaphase promoting complex protein Apc2 suggest a role for inversin in primary cilia and involvement in the cell cycle. Hum Mol Genet *11*, 3345–3350.

Moritz, O.L., Tam, B.M., Hurd, L.L., Peranen, J., Deretic, D., and Papermaster, D.S. (2001). Mutant rab8 Impairs docking and fusion of rhodopsin-bearing post-Golgi membranes and causes cell death of transgenic Xenopus rods. Mol Biol Cell *12*, 2341–2351.

Morris, R.L., and Scholey, J.M. (1997). Heterotrimeric kinesin-II is required for the assembly of motile 9+2 ciliary axonemes on sea urchin embryos. J Cell Biol *138*, 1009–1022.

Moyer, J.H., Lee-Tischler, M.J., Kwon, H.Y., Schrick, J.J., Avner, E.D., Sweeney, W.E., Godfrey, V.L., Cacheiro, N.L., Wilkinson, J.E., and Woychik, R.P. (1994). Candidate gene associated with a mutation causing recessive polycystic kidney disease in mice. Science *264*, 1329–1333.

Mukhopadhyay, S., Wen, X., Chih, B., Nelson, C.D., Lane, W.S., Scales, S.J., and Jackson, P.K. (2010). TULP3 bridges the IFT-A complex and membrane phosphoinositides to promote trafficking of G protein-coupled receptors into primary cilia. Genes Dev. *24*, 2180–2193.

Munro, N.C., Currie, D.C., Lindsay, K.S., Ryder, T.A., Rutman, A., Dewar, A., Greenstone, M.A., Hendry, W.F., and Cole, P.J. (1994). Fertility in men with primary ciliary dyskinesia presenting with respiratory infection. Thorax *49*, 684–687.

Murcia, N.S., Richards, W.G., Yoder, B.K., Mucenski, M.L., Dunlap, J.R., and Woychik, R.P. (2000). The Oak Ridge Polycystic Kidney (orpk) disease gene is required for left-right axis determination. Development *127*, 2347–2355.

Nachury, M., Loktev, A., Zhang, Q., Westlake, C., Peranen, J., Merdes, A., Slusarski, D., Scheller, R., Bazan, J., Sheffield, V., et al. (2007). A core complex of BBS proteins cooperates with the GTPase Rab8 to promote ciliary membrane biogenesis. Cell *129*, 1201–1213.

Nachury, M., Seeley, E., and Jin, H. (2010). Trafficking to the ciliary membrane: how to get across the periciliary diffusion barrier? Annu Rev Cell Dev Biol *26*, 59–87.

Nachury, M.V. (2014). How do cilia organize signalling cascades? Philos. Trans. R. Soc. Lond., B, Biol. Sci. *369*.

Nauli, S.M., Alenghat, F.J., Luo, Y., Williams, E., Vassilev, P., Li, X., Elia, A.E.H., Lu, W., Brown, E.M., Quinn, S.J., et al. (2003). Polycystins 1 and 2 mediate mechanosensation in the primary cilium of kidney cells. Nat. Genet. *33*, 129–137.

Nie, Z., Hirsch, D.S., Luo, R., Jian, X., Stauffer, S., Cremesti, A., Andrade, J., Lebowitz, J., Marino, M., Ahvazi, B., et al. (2006). A BAR domain in the N terminus of the Arf GAP ASAP1 affects membrane structure and trafficking of epidermal growth factor receptor. Current Biology *16*, 130–139.

Nigg, E.A., and Raff, J.W. (2009). Centrioles, centrosomes, and cilia in health and disease. Cell *139*, 663–678.

Nonaka, S., Tanaka, Y., Okada, Y., Takeda, S., Harada, A., Kanai, Y., Kido, M., and Hirokawa, N. (1998). Randomization of left-right asymmetry due to loss of nodal cilia generating leftward flow of extraembryonic fluid in mice lacking KIF3B motor protein. Cell *95*, 829–837.

Nonaka, S., Shiratori, H., Saijoh, Y., and Hamada, H. (2002). Determination of left-right patterning of the mouse embryo by artificial nodal flow. Nature *418*, 96–99.

O'Toole, E.T., Giddings, T.H., and Dutcher, S.K. (2007). Understanding microtubule organizing centers by comparing mutant and wild-type structures with electron tomography. Methods Cell Biol *79*, 125–143.

Okada, Y., Nonaka, S., Tanaka, Y., Saijoh, Y., Hamada, H., and Hirokawa, N. (1999). Abnormal nodal flow precedes situs inversus in iv and inv mice. Mol Cell *4*, 459–468.

Omori, Y., Zhao, C., Saras, A., Mukhopadhyay, S., Kim, W., Furukawa, T., Sengupta, P., Veraksa, A., and Malicki, J. (2008). Elipsa is an early determinant of ciliogenesis that links the IFT particle to membrane-associated small GTPase Rab8. Nat Cell Biol *10*, 437–444.

Ou, G., Blacque, O., Snow, J., Leroux, M., and Scholey, J. (2005a). Functional coordination of intraflagellar transport motors. Nature *436*, 583–587.

Ou, G., Qin, H., Rosenbaum, J., and Scholey, J. (2005b). The PKD protein qilin undergoes intraflagellar transport. Curr Biol *15*, R410–R411.

Ou, G., Koga, M., Blacque, O.E., Murayama, T., Ohshima, Y., Schafer, J.C., Li, C., Yoder, B.K., Leroux, M.R., and Scholey, J.M. (2007). Sensory ciliogenesis in Caenorhabditis elegans: assignment of IFT components into distinct modules based on transport and phenotypic profiles. Mol Biol Cell *18*, 1554–1569.

Palczewski, K., Kumasaka, T., Hori, T., Behnke, C.A., Motoshima, H., Fox, B.A., Le Trong, I., Teller, D.C., Okada, T., Stenkamp, R.E., et al. (2000). Crystal structure of rhodopsin: A G protein-coupled receptor. Science *289*, 739–745.

Park, T.J., Mitchell, B.J., Abitua, P.B., Kintner, C., and Wallingford, J.B. (2008). Dishevelled controls apical docking and planar polarization of basal bodies in ciliated epithelial cells. Nat. Genet. *40*, 871–879.

Pasek, R.C., Berbari, N.F., Lewis, W.R., Kesterson, R.A., and Yoder, B.K. (2012). Mammalian Clusterin associated protein 1 is an evolutionarily conserved protein required for ciliogenesis. Cilia *1*, 20.

Patel-King, R.S., Gorbatyuk, O., Takebe, S., and King, S.M. (2004). Flagellar radial spokes contain a Ca2+-stimulated nucleoside diphosphate kinase. Mol Biol Cell *15*, 3891–3902.

Pathak, N., Austin, C.A., and Drummond, I.A. (2011). Tubulin tyrosine ligase-like genes ttll3 and ttll6 maintain zebrafish cilia structure and motility. J Biol Chem *286*, 11685–11695.

Pathak, N., Obara, T., Mangos, S., Liu, Y., and Drummond, I.A. (2007). The zebrafish fleer gene encodes an essential regulator of cilia tubulin polyglutamylation. Mol Biol Cell *18*, 4353–4364.

Paturle-Lafanechère, L., Manier, M., Trigault, N., Pirollet, F., Mazarguil, H., and Job, D. (1994). Accumulation of delta 2-tubulin, a major tubulin variant that cannot be tyrosinated, in neuronal tissues and in stable microtubule assemblies. J Cell Sci *107 (Pt 6)*, 1529–1543.

Pazour, G., and Rosenbaum, J. (2002). Intraflagellar transport and cilia-dependent diseases. Trends Cell Biol *12*, 551–555.

Pazour, G.J. (2002). The intraflagellar transport protein, IFT88, is essential for vertebrate photoreceptor assembly and maintenance. J Cell Biol *157*, 103–114.

Pazour, G.J., Dickert, B.L., and Witman, G.B. (1999). The DHC1b (DHC2) isoform of cytoplasmic dynein is required for flagellar assembly. J Cell Biol *144*, 473–481.

Pazour, G.J., Dickert, B.L., Vucica, Y., Seeley, E.S., Rosenbaum, J.L., Witman, G.B., and Cole, D.G. (2000). Chlamydomonas IFT88 and its mouse homologue, polycystic kidney disease gene tg737, are required for assembly of cilia and flagella. J Cell Biol *151*, 709–718.

Pazour, G., Agrin, N., Leszyk, J., and Witman, G. (2005). Proteomic analysis of a eukaryotic cilium. J Cell Biol *170*, 103–113.

Pazour, G.J., San Agustin, J.T., Follit, J.A., Rosenbaum, J.L., and Witman, G.B. (2002). Polycystin-2 localizes to kidney cilia and the ciliary level is elevated in orpk mice with polycystic kidney disease. Current Biology *12*, R378–R380.

Pedersen, L., Geimer, S., and Rosenbaum, J. (2006). Dissecting the molecular mechanisms of intraflagellar transport in chlamydomonas. Curr Biol *16*, 450–459.

Pedersen, L., and Rosenbaum, J. (2008). Intraflagellar transport (IFT) role in ciliary assembly, resorption and signalling. Curr Top Dev Biol *85*, 23–61.

Pedersen, L., Geimer, S., Sloboda, R., and Rosenbaum, J. (2003). The Microtubule plus end-tracking protein EB1 is localized to the flagellar tip and basal bodies in Chlamydomonas reinhardtii. Curr Biol *13*, 1969–1974.

Pedersen, L., Miller, M., Geimer, S., Leitch, J., Rosenbaum, J., and Cole, D. (2005). Chlamydomonas IFT172 is encoded by FLA11, interacts with CrEB1, and regulates IFT at the flagellar tip. Curr Biol *15*, 262–266.

Perkins, L.A., Hedgecock, E.M., Thomson, J.N., and Culotti, J.G. (1986). Mutant sensory cilia in the nematode Caenorhabditis elegans. Dev Biol *117*, 456–487.

Peter, B.J., Kent, H.M., Mills, I.G., Vallis, Y., Butler, P.J.G., Evans, P.R., and McMahon, H.T. (2004). BAR domains as sensors of membrane curvature: the amphiphysin BAR structure. Science *303*, 495–499.

Pigino, G., Geimer, S., Lanzavecchia, S., Paccagnini, E., Cantele, F., Diener, D., Rosenbaum, J., and Lupetti, P. (2009). Electron-tomographic analysis of intraflagellar transport particle trains in situ. J Cell Biol *187*, 135–148.

Piperno, G., and Fuller, M.T. (1985). Monoclonal antibodies specific for an acetylated form of alpha-tubulin recognize the antigen in cilia and flagella from a variety of organisms. J Cell Biol *101*, 2085–2094.

Piperno, G., and Mead, K. (1997). Transport of a novel complex in the cytoplasmic matrix of Chlamydomonas flagella. Proc Natl Acad Sci USA *94*, 4457–4462.

Piperno, G., Huang, B., Ramanis, Z., and Luck, D.J. (1981). Radial spokes of Chlamydomonas flagella: polypeptide composition and phosphorylation of stalk components. J Cell Biol *88*, 73–79.

Piperno, G., Siuda, E., Henderson, S., Segil, M., Vaananen, H., and Sassaroli, M. (1998). Distinct mutants of retrograde intraflagellar transport (IFT) share similar morphological and molecular defects. J Cell Biol *143*, 1591–1601.

Plessmann, U., and Weber, K. (1997). Mammalian sperm tubulin: an exceptionally large number of variants based on several posttranslational modifications. J. Protein Chem. *16*, 385–390.

Porter, M.E. (1996). Axonemal dyneins: assembly, organization, and regulation. Curr Opin Cell Biol *8*, 10–17.

Porter, M.E., and Sale, W.S. (2000). The 9 + 2 axoneme anchors multiple inner arm dyneins and a network of kinases and phosphatases that control motility. J Cell Biol *151*, F37–F42.

Porter, M.E., Bower, R., Knott, J.A., Byrd, P., and Dentler, W. (1999). Cytoplasmic dynein heavy chain 1b is required for flagellar assembly in Chlamydomonas. Mol Biol Cell *10*, 693–712.

Praetorius, H.A., and Spring, K.R. (2001). Bending the MDCK cell primary cilium increases intracellular calcium. J. Membr. Biol. *184*, 71–79.

Praetorius, H.A., and Spring, K.R. (2003). Removal of the MDCK cell primary cilium abolishes flow sensing. J. Membr. Biol. *191*, 69–76.

Qin, H., Diener, D., Geimer, S., Cole, D., and Rosenbaum, J. (2004). Intraflagellar transport (IFT) cargo: IFT transports flagellar precursors to the tip and turnover products to the cell body. J Cell Biol *164*, 255–266.

Qin, H., Rosenbaum, J.L., and Barr, M.M. (2001). An autosomal recessive polycystic kidney disease gene homolog is involved in intraflagellar transport in C. elegans ciliated sensory neurons. Current Biology *11*, 457–461.

Qin, H., Wang, Z., Diener, D., and Rosenbaum, J. (2007). Intraflagellar transport protein 27 is a small G protein involved in cell-cycle control. Current Biology *17*, 193–202.

Qin, J., Lin, Y., Norman, R.X., Ko, H.W., and Eggenschwiler, J.T. (2011). Intraflagellar transport protein 122 antagonizes Sonic Hedgehog signaling and controls ciliary localization of pathway components. Proceedings of the National Academy of Sciences *108*, 1456–1461.

Ramelot, T.A., Raman, S., Kuzin, A.P., Xiao, R., Ma, L.-C., Acton, T.B., Hunt, J.F., Montelione, G.T., Baker, D., and Kennedy, M.A. (2009). Improving NMR protein structure quality by Rosetta refinement: a molecular replacement study. Proteins *75*, 147–167.

Rasala, B.A., Barrera, D.J., Ng, J., Plucinak, T.M., Rosenberg, J.N., Weeks, D.P., Oyler, G.A., Peterson, T.C., Haerizadeh, F., and Mayfield, S.P. (2013). Expanding the spectral palette of fluorescent proteins for the green microalga Chlamydomonas reinhardtii. Plant J. *74*, 545–556.

Redeker, V., Levilliers, N., Schmitter, J.M., Le Caer, J.P., Rossier, J., Adoutte, A., and Bré, M.H. (1994). Polyglycylation of tubulin: a posttranslational modification in axonemal microtubules. Science *266*, 1688–1691.

Richey, E.A., and Qin, H. (2012). Dissecting the sequential assembly and localization of intraflagellar transport particle complex B in chlamydomonas. PLoS ONE *7*, e43118.

Ringo, D.L. (1967). Flagellar motion and fine structure of the flagellar apparatus in Chlamydomonas. J Cell Biol *33*, 543–571.

Rix, S., Calmont, A., Scambler, P.J., and Beales, P.L. (2011). An Ift80 mouse model of short rib polydactyly syndromes shows defects in hedgehog signalling without loss or malformation of cilia. Hum Mol Genet *20*, 1306–1314.

Rogowski, K., Juge, F., van Dijk, J., Wloga, D., Strub, J.-M., Levilliers, N., Thomas, D., Bré, M.-H., Van Dorsselaer, A., Gaertig, J., et al. (2009). Evolutionary divergence of enzymatic mechanisms for posttranslational polyglycylation. Cell *137*, 1076–1087.

Rohatgi, R., Milenkovic, L., and Scott, M.P. (2007). Patched1 regulates hedgehog signaling at the primary cilium. Science *317*, 372–376.

Rosenbaum, J., and Witman, G. (2002). Intraflagellar transport. Nat Rev Mol Cell Biol *3*, 813–825.

Rual, J.-F., Venkatesan, K., Hao, T., Hirozane-Kishikawa, T., Dricot, A., Li, N., Berriz, G.F., Gibbons, F.D., Dreze, M., Ayivi-Guedehoussou, N., et al. (2005). Towards a proteome-scale map of the human protein-protein interaction network. Nature *437*, 1173–1178.

Rüdiger, M., Plessmann, U., Rüdiger, A.H., and Weber, K. (1995). Beta tubulin of bull sperm is polyglycylated. FEBS Lett *364*, 147–151.

Satir, P. (1968). Studies on cilia. 3. Further studies on the cilium tip and a “sliding filament” model of ciliary motility. J Cell Biol *39*, 77–94.

Sato, A., Khadka, D.K., Liu, W., Bharti, R., Runnels, L.W., Dawid, I.B., and Habas, R. (2006). Profilin is an effector for Daam1 in non-canonical Wnt signaling and is required for vertebrate gastrulation. Development *133*, 4219–4231.

Schafer, J.C., Winkelbauer, M.E., Williams, C.L., Haycraft, C.J., Desmond, R.A., and Yoder, B.K. (2006). IFTA-2 is a conserved cilia protein involved in pathways regulating longevity and dauer formation in Caenorhabditis elegans. J Cell Sci *119*, 4088–4100.

Schneider, L., Clement, C.A., Teilmann, S.C., Pazour, G.J., Hoffmann, E.K., Satir, P., and Christensen, S.T. (2005). PDGFRalphaalpha signaling is regulated through the primary cilium in fibroblasts. Current Biology *15*, 1861–1866.

Scholey, J. (2008). Intraflagellar transport motors in cilia: moving along the cell's antenna. J Cell Biol *180*, 23–29.

Scholey, J. (2012). Kinesin-2 motors transport IFT-particles, dyneins and tubulin subunits to the tips of Caenorhabditis elegans sensory cilia: Relevance to vision research? Vision Res.

Schou, K.B., Andersen, J.S., and Pedersen, L.B. (2014). A divergent calponin homology (NN-CH) domain defines a novel family: implications for evolution of ciliary IFT complex B proteins. Bioinformatics *30*, 899–902.

Sedmak, T., and Wolfrum, U. (2010). Intraflagellar transport molecules in ciliary and nonciliary cells of the retina. J Cell Biol *189*, 171–186.

Sedmak, T., and Wolfrum, U. (2011). Intraflagellar transport proteins in ciliogenesis of photoreceptor cells. Biol Cell *103*, 449–466.

Seixas, C., Casalou, C., Melo, L.V., Nolasco, S., Brogueira, P., and Soares, H. (2003). Subunits of the chaperonin CCT are associated with Tetrahymena microtubule structures and are involved in cilia biogenesis. Exp Cell Res *290*, 303–321.

Seixas, C., Cruto, T., Tavares, A., Gaertig, J., and Soares, H. (2010). CCTalpha and CCTdelta chaperonin subunits are essential and required for cilia assembly and maintenance in Tetrahymena. PLoS ONE *5*, e10704.

Shiba, T., Koga, H., Shin, H.-W., Kawasaki, M., Kato, R., Nakayama, K., and Wakatsuki, S. (2006). Structural basis for Rab11-dependent membrane recruitment of a family of Rab11-interacting protein 3 (FIP3)/Arfophilin-1. Proc Natl Acad Sci USA *103*, 15416–15421.

Signor, D., Wedaman, K.P., Orozco, J.T., Dwyer, N.D., Bargmann, C.I., Rose, L.S., and Scholey, J.M. (1999). Role of a class DHC1b dynein in retrograde transport of IFT motors and IFT raft particles along cilia, but not dendrites, in chemosensory neurons of living Caenorhabditis elegans. J Cell Biol *147*, 519–530.

Singla, V., and Reiter, J. (2006). The primary cilium as the cell's antenna: signaling at a sensory organelle. Science *313*, 629–633.

Sobkowicz, H.M., Slapnick, S.M., and August, B.K. (1995). The kinocilium of auditory hair cells and evidence for its morphogenetic role during the regeneration of stereocilia and cuticular plates. J. Neurocytol. *24*, 633–653.

Soding, J., Biegert, A., and Lupas, A.N. (2005). The HHpred interactive server for protein homology detection and structure prediction. Nucleic Acids Research *33*, W244–W248.

St Johnston, D. (2005). Moving messages: the intracellular localization of mRNAs. Nat Rev Mol Cell Biol *6*, 363–375.

Stayner, C., and Zhou, J. (2001). Polycystin channels and kidney disease. Trends Pharmacol. Sci. *22*, 543–546.

Stephan, A., Vaughan, S., Shaw, M.K., Gull, K., and McKean, P.G. (2007). An essential quality control mechanism at the eukaryotic basal body prior to intraflagellar transport. Traffic *8*, 1323–1330.

Stephens, R.E. (1997). Synthesis and turnover of embryonic sea urchin ciliary proteins during selective inhibition of tubulin synthesis and assembly. Mol Biol Cell *8*, 2187–2198.

Storm van's Gravesande, K., and Omran, H. (2005). Primary ciliary dyskinesia: clinical presentation, diagnosis and genetics. Ann. Med. *37*, 439–449.

Subota, I., Julkowska, D., Vincensini, L., Reeg, N., Buisson, J., Blisnick, T., Huet, D., Perrot, S., Santi-Rocca, J., Duchateau, M., et al. (2014). Proteomic analysis of intact flagella of procyclic Trypanosoma brucei cells identifies novel flagellar proteins with unique sub-localization and dynamics. Mol Cell Proteomics *13*, 1769–1786.

Summers, K.E., and Gibbons, I.R. (1971). Adenosine triphosphate-induced sliding of tubules in trypsin-treated flagella of sea-urchin sperm. Proc Natl Acad Sci USA *68*, 3092–3096.

Sun, Z., Amsterdam, A., Pazour, G.J., Cole, D.G., Miller, M.S., and Hopkins, N. (2004). A genetic screen in zebrafish identifies cilia genes as a principal cause of cystic kidney. Development *131*, 4085–4093.

Sung, C.H., Makino, C., Baylor, D., and Nathans, J. (1994). A rhodopsin gene mutation responsible for autosomal dominant retinitis pigmentosa results in a protein that is defective in localization to the photoreceptor outer segment. J. Neurosci. *14*, 5818–5833.

Sung, C.-H., and Leroux, M.R. (2013). The roles of evolutionarily conserved functional modules in cilia-related trafficking. Nat Cell Biol *15*, 1387–1397.

Suryavanshi, S., Eddé, B., Fox, L.A., Guerrero, S., Hard, R., Hennessey, T., Kabi, A., Malison, D., Pennock, D., Sale, W.S., et al. (2010). Tubulin glutamylation regulates ciliary motility by altering inner dynein arm activity. Curr Biol *20*, 435–440.

Swiderski, R.E., Nakano, Y., Mullins, R.F., Seo, S., and Bánfi, B. (2014). A mutation in the mouse ttc26 gene leads to impaired hedgehog signaling. PLoS Genet *10*, e1004689.

Tam, B., Moritz, O., Hurd, L., and Papermaster, D. (2000). Identification of an outer segment targeting signal in the COOH terminus of rhodopsin using transgenic Xenopus laevis. J Cell Biol *151*, 1369–1380.

Tanaka, Y., Okada, Y., and Hirokawa, N. (2005). FGF-induced vesicular release of Sonic hedgehog and retinoic acid in leftward nodal flow is critical for left-right determination. Nature *435*, 172–177.

Taschner, M., Bhogaraju, S., and Lorentzen, E. (2012). Architecture and function of IFT complex proteins in ciliogenesis. Differentiation *83*, S12–S22.

Taschner, M., Bhogaraju, S., Vetter, M., Morawetz, M., and Lorentzen, E. (2011).

Biochemical mapping of interactions within the intraflagellar transport (IFT) B core complex: IFT52 binds directly to four other IFT-B subunits. J Biol Chem *286*, 26344–26352.

Taschner, M., Kotsis, F., Braeuer, P., Kuehn, E.W., and Lorentzen, E. (2014). Crystal structures of IFT70/52 and IFT52/46 provide insight into intraflagellar transport B core complex assembly. The Journal of Cell Biology *207*, 269–282.

Tian, G., Bhamidipati, A., Cowan, N.J., and Lewis, S.A. (1999). Tubulin folding cofactors as GTPase-activating proteins. GTP hydrolysis and the assembly of the alpha/beta-tubulin heterodimer. J Biol Chem *274*, 24054–24058.

Tran, P.V., Haycraft, C.J., Besschetnova, T.Y., Turbe-Doan, A., Stottmann, R.W., Herron, B.J., Chesebro, A.L., Qiu, H., Scherz, P.J., Shah, J.V., et al. (2008). THM1 negatively modulates mouse sonic hedgehog signal transduction and affects retrograde intraflagellar transport in cilia. Nat. Genet. *40*, 403–410.

Tsao, C.-C., and Gorovsky, M.A. (2008). Different effects of Tetrahymena IFT172 domains on anterograde and retrograde intraflagellar transport. Mol Biol Cell *19*, 1450–1461.

van Dam, T.J.P., Townsend, M.J., Turk, M., Schlessinger, A., Sali, A., Field, M.C., and Huynen, M.A. (2013). Evolution of modular intraflagellar transport from a coatomer-like progenitor. Proceedings of the National Academy of Sciences *110*, 6943–6948.

Vassilev, P.M., Guo, L., Chen, X.Z., Segal, Y., Peng, J.B., Basora, N., Babakhanlou, H., Cruger, G., Kanazirska, M., Ye Cp, et al. (2001). Polycystin-2 is a novel cation channel implicated in defective intracellular Ca(2+) homeostasis in polycystic kidney disease. Biochem Biophys Res Commun *282*, 341–350.

Vetter, I.R., and Wittinghofer, A. (2001). The guanine nucleotide-binding switch in three dimensions. Science *294*, 1299–1304.

Wang, J., Morita, Y., Mazelova, J., and Deretic, D. (2012). The Arf GAP ASAP1 provides a platform to regulate Arf4- and Rab11-Rab8-mediated ciliary receptor targeting. Embo J *31*, 4057–4071.

Wang, Z., Fan, Z.-C., Williamson, S.M., and Qin, H. (2009). Intraflagellar transport (IFT) protein IFT25 is a phosphoprotein component of IFT complex B and physically interacts with IFT27 in Chlamydomonas. PLoS ONE *4*, e5384.

Warner, F.D. (1970). New observations on flagellar fine structure. The relationship between matrix structure and the microtubule component of the axoneme. J Cell Biol *47*, 159–182.

Warner, F.D., and Satir, P. (1973). The substructure of ciliary microtubules. J Cell Sci *12*, 313–326.

Warner, F.D., and Satir, P. (1974). The structural basis of ciliary bend formation. Radial spoke positional changes accompanying microtubule sliding. J Cell Biol *63*, 35–63.

Way, M., Pope, B., and Weeds, A.G. (1992). Evidence for functional homology in the F-actin binding domains of gelsolin and alpha-actinin: implications for the requirements of severing and capping. J Cell Biol *119*, 835–842.

Westermann, S., and Weber, K. (2003). Post-translational modifications regulate microtubule function. Nat Rev Mol Cell Biol *4*, 938–947.

Westlake, C.J., Baye, L.M., Nachury, M.V., Wright, K.J., Ervin, K.E., Phu, L., Chalouni, C., Beck, J.S., Kirkpatrick, D.S., Slusarski, D.C., et al. (2011). Primary cilia membrane assembly is initiated by Rab11 and transport protein particle II (TRAPPII) complex-dependent trafficking of Rabin8 to the centrosome. Proceedings of the National Academy of Sciences *108*, 2759–2764.

Williams, N.E., and Nelsen, E.M. (1997). HSP70 and HSP90 homologs are associated with tubulin in hetero-oligomeric complexes, cilia and the cortex of Tetrahymena. J Cell Sci *110 (Pt 14)*, 1665–1672.

Williamson, S.M., Silva, D.A., Richey, E., and Qin, H. (2012). Probing the role of IFT particle complex A and B in flagellar entry and exit of IFT-dynein in Chlamydomonas. Protoplasma *249*, 851–856.

Winder, S.J., Hemmings, L., Maciver, S.K., Bolton, S.J., Tinsley, J.M., Davies, K.E., Critchley, D.R., and Kendrick-Jones, J. (1995). Utrophin actin binding domain: analysis of actin binding and cellular targeting. J Cell Sci *108 (Pt 1)*, 63–71.

Witman, G.B., Carlson, K., Berliner, J., and Rosenbaum, J.L. (1972). Chlamydomonas flagella. I. Isolation and electrophoretic analysis of microtubules, matrix, membranes, and mastigonemes. J Cell Biol *54*, 507–539.

Witman, G.B., Plummer, J., and Sander, G. (1978). Chlamydomonas flagellar mutants lacking radial spokes and central tubules. Structure, composition, and function of specific axonemal components. J Cell Biol *76*, 729–747.

Wloga, D., and Gaertig, J. (2010). Post-translational modifications of microtubules. J Cell Sci *123*, 3447–3455.

Wloga, D., Webster, D.M., Rogowski, K., Bré, M.-H., Levilliers, N., Jerka-Dziadosz, M., Janke, C., Dougan, S.T., and Gaertig, J. (2009). TTLL3 Is a tubulin glycine ligase that regulates the assembly of cilia. Dev Cell *16*, 867–876.

Wood, C.R., and Rosenbaum, J.L. (2014). Proteins of the ciliary axoneme are found on cytoplasmic membrane vesicles during growth of cilia. Curr Biol *24*, 1114–1120.

Wu, G., D'Agati, V., Cai, Y., Markowitz, G., Park, J.H., Reynolds, D.M., Maeda, Y., Le, T.C., Hou, H., Kucherlapati, R., et al. (1998). Somatic inactivation of Pkd2 results in polycystic kidney disease. Cell *93*, 177–188.

Yaffe, M.B., Farr, G.W., Miklos, D., Horwich, A.L., Sternlicht, M.L., and Sternlicht, H. (1992). TCP1 complex is a molecular chaperone in tubulin biogenesis. Nature *358*, 245–248.

Yang, P., Diener, D.R., Yang, C., Kohno, T., Pazour, G.J., Dienes, J.M., Agrin, N.S., King, S.M., Sale, W.S., Kamiya, R., et al. (2006). Radial spoke proteins of Chlamydomonas flagella. J Cell Sci *119*, 1165–1174.

Yoder, B.K., Hou, X., and Guay-Woodford, L.M. (2002). The polycystic kidney disease proteins, polycystin-1, polycystin-2, polaris, and cystin, are co-localized in renal cilia. J Am Soc Nephrol *13*, 2508–2516.

Yoshiba, S., Shiratori, H., Kuo, I.Y., Kawasumi, A., Shinohara, K., Nonaka, S., Asai, Y., Sasaki, G., Belo, J.A., Sasaki, H., et al. (2012). Cilia at the node of mouse embryos sense fluid flow for left-right determination via Pkd2. Science *338*, 226–231.

Zimmermann, K.W. (1898). Beiträge zur Kenntniss einiger Drüsen und Epithelien. Arch. Mikrosk. Anat. *52*, 552–706.

Acknowledgements

Finally, I would like to thank all the people who contributed to this work and supported me over the last years.

A special thank you to my supervisor Dr. Esben Lorentzen for giving me the opportunity to conduct my thesis in his group. He has been always really helpful and patient in guiding me through the project and I could learn a lot from him.

I also would like to thank the members of my thesis advisory committee Prof. Dr. Elena Conti (MPIB), Dr. Dierk Niessing (Helmholtz Center, Munich) and Dr. Stefan Geimer (University of Bayreuth) for their scientific input and discussions on my project.

I sincerely thank my colleagues Mela (We share cause we care!), Marc (the most charming TA), Taschi (for always being accessible and patient in answering my questions), Steffi, André, Mayanka and my previous colleagues Michaela and Sagar for being the best labmates ever and creating such a great atmosphere in the lab. I am also deeply grateful to Julia, Carina V., Justine, Ira, Carina M., Dirk, Shun and Rajan and the remaining members of the Conti Department, Biertümpfel- and Mizuno-Lab not only for their support and input in scientific topics but also for making the department such a friendly place and for the free time we spend together.

My special thanks are extended to the staff of the MPIB crystallization facility (Jerôme Basquin, Dr. Karina Valer-Saldaña and Sabine Pleyer) for setting up so many plates for me, and the MPIB core facility (especially Lissy Weyher and Dr. Stephan Uebel) for technical support. I thank Jerôme Basquin, Dr. Masami Yamashita and Dr. Christian Benda for fruitful SLS trips, Dr. Claire Basquin and Dr. Jörg Tittor for biophysical measurements, Michaela Rode and Elfriede Eppinger for help with the insect cell culture, Peter Reichelt and Walter Erhardt for fixing every technical problem and Dr. Christophe Jung (LMU Munich) for introducing me to MST.

I also want to acknowledge my 'non-scientific' friends who supported me mentally and without whom this time would have been so much harder.

I sincerely thank my parents Thomas and Erika Weber and my sister Anne who supported me in every aspect of my life. Finally, a special thank you to Flo who always found the right words to brighten up my day. Thanks for bearing my moods over the last years. I am sure I would not have finished without your support.